Modélisation de la chimie arctique des halogènes et de ses impacts sur l'ozone et le mercure

Shaddy Ahmed

THÈSE

Pour obtenir le grade de

DOCTEUR DE L'UNIVERSITÉ GRENOBLE ALPES

École doctorale : STEP - Sciences de la Terre de lEnvironnement et des Planètes
Spécialité : Sciences de la Terre et de l'Univers et de l'Environnement
Unité de recherche : Institut des Géosciences de lEnvironnement

Modélisation de la chimie arctique des halogènes et de ses impacts sur l'ozone et le mercure

Modelling Arctic halogen chemistry and its impacts on ozone and mercury

Présentée par :

Shaddy AHMED

Direction de thèse :

Aurelien DOMMERGUE Enseignant chercheur, Université Grenoble Alpes	Directeur de thèse
Jennie L. THOMAS Chargée de recherche, Université Grenoble Alpes	Co-directrice de thèse

Rapporteurs :

Solène TURQUETY
PROFESSEUR DES UNIVERSITES, Sorbonne Université
Lucy CARPENTER
PROFESSEUR, University of York

Thèse soutenue publiquement le **2 décembre 2022**, devant le jury composé de :

Aurélien DOMMERGUE PROFESSEUR DES UNIVERSITES, Université Grenoble Alpes	Directeur de thèse
Solène TURQUETY PROFESSEUR DES UNIVERSITES, Sorbonne Université	Rapporteure
Lucy CARPENTER PROFESSEUR, University of York	Rapporteure
Paolo LAJ PHYSICIEN, Université Grenoble Alpes (Président)	Examinateur
Kerri PRATT PROFESSEUR ASSOCIE, University of Michigan	Examinatrice

Invités :

Jennie Thomas
CHARGE DE RECHERCHE, Institut des Géosciences de l'Environnement (IGE)

La science est faite d'erreurs, mais d'erreurs qu'il est bon de commettre, car elles mènent peu à peu à la vérité.

— Jules Verne, *Voyage au centre de la Terre (1864)*

Science is made up of mistakes, but mistakes that are good to make, because they lead little by little to the truth.

— Jules Verne, *Journey to the Center of the Earth (1864)*

Abstract

Halogens are an important component of Arctic atmospheric chemistry, responsible for the depletion of boundary layer ozone and mercury, oxidation of hydrocarbons, and impacts on nitrogen oxide chemistry and oxidative capacity. During spring, reactive halogens are photochemically activated on salty surfaces (e.g. land-based snow, snow on sea ice, aerosols) and released into the atmosphere. However, the interplay between polar chemical emissions, recycling, transport, and chemistry is complex and remains poorly understood. As a result, descriptions of such processes in atmospheric chemistry models are largely simplified or neglected. This thesis presents an investigation of the role of halogens (chlorine and bromine) on springtime Arctic boundary layer chemistry, through the development and use of atmospheric chemistry models.

First, a 1-dimensional model (PACT-1D) is used to study molecular halogen emissions from surface snow and the impact on oxidative chemistry within the boundary layer. The model is used to simulate reactive halogen chemistry observed during the spring 2009 OASIS (Ocean-Atmospheric-Sea ice-Snowpack) measurement campaign in Utqiaġvik, Alaska. Model results show that halogens can be confined to a very shallow layer near the surface, resulting in a large chemical reactivity gradient with altitude. Second, the 3-dimensional WRF-Chem model is used to investigate the interaction of halogens with ozone and mercury during Arctic spring. Several major WRF-Chem model developments are made in this work, including the addition of a new mercury chemical description. The model is evaluated with unique data from the central Arctic, obtained during the 2020 MOSAiC (Multidisciplinary drifting Observatory for the Study of Arctic Climate) expedition. Model results show that bromine emissions and recycling from surface snow and sea ice are necessary to capture ozone and mercury depletion events. This work

highlights a need for improved model descriptions of surface emissions to accurately represent boundary layer chemistry, and provides a basis for future model developments.

Keywords: Atmospheric chemistry, Arctic, Halogens, Ozone, Mercury, Snow, Sea Ice, Modelling

Résumé

Les composés halogénés sont des espèces chimiques clés de la réactivité de la basse atmosphère arctique. Ils sont responsables de l'appauvrissement de l'ozone et du mercure dans la couche limite, de l'oxydation des hydrocarbures et ont un impact sur la chimie des oxydes d'azote et la capacité oxydante. Au printemps, des halogènes réactifs sont générés via des mécanismes d'activation photochimique des surfaces salées (par exemple, la neige terrestre, la neige sur la glace de mer, les aérosols) et libérés dans l'atmosphère. Cependant les mécanismes d'émissions et de recyclage de ces composés, leur transport et leurs conséquences sur la chimie atmosphérique polaire sont très complexes et mal définis, ce qui conduit à des simplifications importantes dans les modèles de chimie atmosphérique. A travers le développement et l'utilisation de modèles de chimie atmosphérique, ces travaux de thèse proposent ainsi une étude du rôle des halogènes (chlore et brome) sur la chimie de la couche limite de l'Arctique au printemps.

Tout d'abord, nous avons développé et utilisé un modèle unidimensionnel (PACT-1D) pour étudier les émissions d'halogènes moléculaires de la neige de surface et leur impact sur la capacité oxydante dans la couche limite. Le modèle est utilisé pour simuler la chimie réactive des halogènes observée. Les résultats du modèle, appliqué aux observations menées au printemps 2009 pendant la campagne de mesures OASIS (Ocean-Atmospheric-Sea ice-Snowpack) à Utqiaġvik, Alaska montrent que le chlore peuvent être confinés dans une couche atmosphérique très fine près de la surface, ce qui entraîne un important gradient de réactivité chimique avec l'altitude. Deuxièmement, nous avons appliqué le modèle tridimensionnel WRF-Chem à l'étude des interactions entre les halogènes, l'ozone et le mercure pendant le printemps arctique. Plusieurs développements majeurs du modèle WRF-Chem ont été sont effectués dans cette thèse, notamment l'ajout

d'une nouvelle description chimique du mercure. Le modèle a ensuite ét évalué avec des données uniques du centre de l'Arctique, obtenues lors de l'expédition 2020 de MOSAiC (Multidisciplinary drifting Observatory for the Study of Arctic Climate). Les résultats du modèle ont montré que les émissions de brome et le recyclage de la neige de surface et de la glace de mer sont nécessaires pour mieux représenter les événements d'appauvrissement de l'ozone et du mercure. Nos travaux soulignent ainsi la nécessité d'améliorer les descriptions des émissions de surface dans les modèles afin de représenter avec précision la chimie de la couche limite en Arctique et fournissent une base pour les développements futurs des modèles.

Mots clés: Chimie atmosphérique, Arctique, Halogènes, Ozone, Mercure, Neige, Glace de mer, Modélisation

Acknowledgements

Over the past 3 years I have had the absolute pleasure of encountering and working with so many great minds and individuals, all of whom have made this experience truly extraordinary. It goes without saying but none of this would have been possible without the support and contributions of so many people.

First, I would like to express my thanks to my academic supervisors, Jennie and Aurélien, who gave me this opportunity and for believing in me. I thank you both for the continued support you provided me throughout my PhD and for always encouraging me to push and challenge myself. In the few years we have worked together I have learnt so much from you and it is clear that without your experience, knowledge, and trust this work could not have been possible. I would also like to thank the members of my thesis committee: Didier Voisin, Thorsten Bartels-Rausch, and Anna Jones. I am grateful for their wisdom and guidance that has shaped my PhD and provided me with the best possible chance for success.

I also thank Louis Marelle for the many hours spent debugging and helping me set up my model runs, as well as for reading the chapters of this thesis. I am grateful to Hélène Angot for all of our meaningful discussions about mercury chemistry and for always making yourself available to help answer any questions that I had. To some of my international colleagues, Jochen Stutz and Katie Tuite, I am thankful to you for teaching me the world of MATLAB programming, 1-D modelling, and for all of those early mornings you were up to discuss science with me.

I am grateful for the many friendships that I was able to build during my PhD. A special thanks to: Foteini, Alkuin, Edmond, Mohamed, Miloš, Bettina, Arianna, Rémy, Albane, Samuel, Aniket, Romane, Valeria, Anouk, and Lucille. I also wish to thank the

members of the wider atmospheric chemistry research community that I had the pleasure of meeting and discussing with (both remotely and in person).

To my family, your continued love, belief, and encouragement is a source of strength and I am grateful to you for always being by my side. Finally, to Madeleine – your patience and love has meant the world to me during this journey which I will forever cherish and I thank you for always being an inspiration to me.

Contents

List of Figures

List of Tables

Chapter 1

Introduction

Contents

General context

The Arctic is one of the most rapidly changing environments in the world and most prominent examples of global climate change. Surface temperatures in the region are rising two to three times faster than the global average, with sea ice extent quickly declining and predicted to experience at least one ice-free September before 2050 (Lee et al., 2021). Consequently, these changes are likely to: (i) reduce surface albedo via declining sea ice and snow cover; (ii) increase the frequency of extreme events (e.g. wildfires); (iii) accelerate melting permafrost; (iv) increase anthropogenic emissions via shipping and resource extraction; and (v) disrupt atmospheric chemistry cycles.

These changes have the potential to alter the chemical composition of the polar atmosphere, with implications for Arctic pollution, air quality, and climate. In particular, ozone and mercury pollution can detrimentally impact local ecosystems and human health, making our understanding of the current and future state of the Arctic a major scientific and policy issue (AMAP, 2021). Halogen chemistry (chlorine, bromine, iodine) is central in determining the fate of both ozone and mercury in the atmosphere, yet, the effects of future warming on halogen emissions and chemistry are difficult to predict. Chemical transport models are useful tools for addressing such questions by exploring the complex interconnected nature of the atmosphere. However, many models are currently unable to represent key processes in the Arctic atmosphere due to simplified or missing model descriptions. This thesis aims to address some of the current model deficiencies in the representation of Arctic halogen, ozone, and mercury chemistry.

1.1 Overview of the Earth's atmosphere

Earth's atmosphere is divided into several layers based on their unique chemical and physical characteristics. The lowest atmospheric layer is the troposphere, which can extend to an altitude between 8–18 km from the surface, depending on latitude and season. Above the troposphere is the stratosphere; this layer extends to an altitude of $\sim$50 km. These two layers are most important for atmospheric chemists as they hold over 99.9 % of Earth's atmospheric mass (Jacob, 1999). The lowermost portion of the troposphere that is directly influenced by the planetary surface is known as the *planetary boundary layer* (PBL). The height of the PBL can typically range between 100–2000 m, depending on the atmospheric conditions (e.g. temperature, winds) and topographical features of the environment (Stull, 1988). PBL dynamics is important in modulating surface chemical concentrations, as it can determine the volume within which chemical species are dispersed. During sunlit periods, solar radiation warms the surface generating turbulent eddies that increase vertical mixing and the height of the PBL. In the absence of sunlight (e.g. at night), atmospheric conditions become more stable due to cooling of the surface, which dampens turbulent mixing and reduces the height of the PBL. Under these stable conditions, chemical species can be trapped near the surface due to a suppression in vertical mixing. This has important consequences for surface chemistry and air quality, as gases and pollutants can accumulate near the surface.

Broadly, the chemical composition of the atmosphere is determined by the balance between the rate of production versus the rate of removal for a particular chemical species. At a given location, this can be described by four main processes: chemistry, transport, emissions, and deposition. Chemical production (or loss) is governed by the availability of reactants and by the atmospheric conditions (e.g. temperature, radiation). Transport of air masses can redistribute long-lived chemical species globally. Emissions are influenced by both natural and anthropogenic activity, releasing compounds directly into the atmosphere. Deposition can remove species from the atmosphere, via both dry and wet processes, and transfer these species to the ground. All of these terms can be expressed mathematically in the form of the continuity equation (1.1), describing the conservation of mass for a species, i (Jacob, 1999):

$$\frac{\partial C_i}{\partial t} = -\nabla \cdot F + P_i - L_i \tag{1.1}$$

where $\frac{\partial C_i}{\partial t}$ is the change in concentration of species i with respect to time (t), $\nabla \cdot F$ is the net flux in or out of a given volume, P_i is the total production (sum of chemical production and emissions), and L_i is the total loss (sum of chemical loss and deposition). The atmospheric lifetime (τ) of a species, which is the average time a species remains in the atmosphere, can be represented by its total atmospheric mass (M_i) and the rate of its production (or loss), as:

$$\tau = \frac{M_i}{P_i} = \frac{M_i}{L_i} \tag{1.2}$$

assuming steady state conditions (sources and sinks are equal) (Seinfeld and Pandis, 2006).

1.2 Specificities of the polar regions

The polar regions (Arctic and Antarctic) are cold and remote environments that exhibit several unique characteristics, in terms of climate and geography, which distinguishes them from other regions of the Earth. These distinct features have important implications for polar atmospheric chemistry, the central research theme of this thesis. This thesis will focus on the chemical processes occurring in the Arctic atmosphere, but, these cycles are also equally relevant to the Antarctic. The key physical and chemical conditions that characterize the Arctic and Antarctic are described below.

1.2.1 Physical and meteorological conditions

The Arctic region (defined as 60° N to 90° N) consists of the Arctic Ocean and is surrounded by landmasses, whereas the Antarctic is a continent surrounded by ocean. A large fraction of the Arctic Ocean is ice-covered year-round, with a maximum sea ice extent during spring (March–April) and a minimum in autumn (September). Sea ice is a crucial component of the cryosphere as it reflects visible radiation (due to high albedo), modulates gas and heat exchange between the Arctic Ocean and atmosphere, and provides

a surface for chemical reactions and re-emission of deposited chemical species. Total sea ice extent has gradually declined over the past few decades, accelerated by rising global temperatures, and is projected to be ice-free in the month of September before the end of the 21st century (Lee et al., 2021). Figure 1.1 shows the rate of sea ice decline (in September) over the past 40 years, declining at a rate of approximately 13 % per decade. The reduction of Arctic sea extent has many far-reaching consequences on the global climate, such as the exacerbation of Arctic warming due to a reduction in surface albedo. Arctic atmospheric chemistry is also affected by changes in emissions (e.g. increased Arctic shipping, more open water emissions) and by a reduction in snow cover. Snow (on land and sea ice) is a porous multiphase medium which can exchange trace gases between the surface and the overlying atmosphere. It is a key component of the cryosphere as it facilitates the production and release of a number of chemical species to the atmosphere. One example is the formation of nitrogen oxides (NO_x=NO+NO_2) in the interstitial air of surface snow, previously measured in the Arctic (Honrath et al., 1999, 2002). Many chemical reactions within the porous snowpack, including NO_x production, are driven by photochemistry when sunlight resumes at the end of polar night (Bartels-Rausch et al., 2014; Grannas et al., 2007).

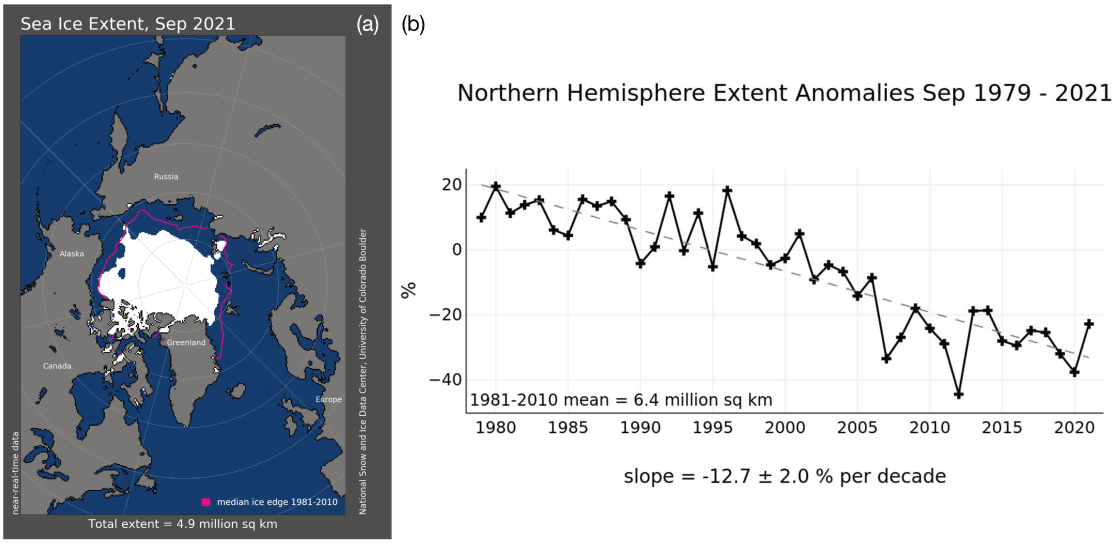

Figure 1.1: (a) Monthly Arctic sea ice extent in September 2021. Magenta line indicates the 30-year (1981–2010) median extent for September. (b) Time series of the mean Arctic sea ice extent anomaly in September compared to the September 1981–2010 mean. Image/photo courtesy of the National Snow and Ice Data Center, University of Colorado, Boulder.

Because of the Arctic's high latitude, the amount of available sunlight varies drastically depending on the season, with complete darkness during winter and all-day sunlight in summer. The transition from polar night to polar sunrise in spring can have several effects, including: changes in the surface energy budget, the initiation of photoactive processes and chemistry, and impacts on boundary layer dynamics and atmospheric stability. The cold climate and relatively homogeneous snow/ice surface of the polar regions can often produce very stable conditions, known as surface temperature inversions (Anderson and Neff, 2008). Temperature inversions are phenomena common to polar regions and are present when there is a reversal of the adiabatic lapse rate, causing air temperature to increase with altitude. This can occur when a warm air mass resides above a cooler one, hindering vertical mixing between the two layers. Within the inversion layer, typically 10–100 m above the surface, conditions are stable further trapping pollutants and gases very close to the surface. Another important feature of the Arctic is the presence of sea ice leads and the impact they have on convective mixing of air masses. Leads are naturally occurring cracks in sea ice that can cause large sensible and latent heat fluxes from the sea ice surface to the atmosphere, due to temperature gradients between the warmer ocean surface and cooler polar atmosphere. These temperature gradients cause strong convective mixing in the atmosphere above the lead, resulting in strong ventilation of air within the boundary layer. In such cases, air masses that are depleted in chemical species, such as ozone or mercury, can be replenished by downward mixing of air from the free troposphere, resulting in rapid changes in surface chemical concentrations (Moore et al., 2014).

1.2.2 Arctic air pollution

A key difference between the Arctic and Antarctic is the proximity of the Arctic to the surrounding landmasses, unlike the Antarctic which is surrounded by the Southern Ocean. Anthropogenic emissions released from industrialized activities and open fires in the Northern Hemisphere can therefore be transported long distances from the mid-latitudes to the Arctic. This can bring large amounts of gaseous and particulate pollutants to the Arctic, impacting local air quality. This is exemplified with the build up of Arctic haze;

a fog-like accumulation of atmospheric aerosols (e.g. sulphate) and other air pollutants (e.g. organic matter) which typically occurs during late winter/early spring (Quinn et al., 2007). Local emissions are believed to be low compared to the pollution transported from the mid-latitudes due to the remote nature of the Arctic. However, local sources such as Arctic shipping routes can be an important source of local pollutants (e.g. NO_x, sulphur dioxide (SO_2)) which are projected to increase as new shipping routes are made accessible by the continuing decline of sea ice (Corbett et al., 2010; Mudryk et al., 2021; Stephenson et al., 2018). Natural (re-)emissions from snow, sea ice, and the open ocean also contribute to the release of chemical species to the polar atmosphere, influencing surface layer chemistry where most long-term Arctic observations are made. The combination of atmospheric conditions, chemical emissions, and transport result in atmospheric chemistry cycles that are unique to the Arctic.

This thesis focuses on the chemical fate of two major pollutants: tropospheric ozone (O_3) and mercury (Hg). Tropospheric O_3 (hereinafter referred to as ozone) is an important greenhouse gas with a positive radiative forcing, estimated at approximately 0.40 W m^{-2} (Myhre et al., 2013). O_3 is also a harmful air pollutant which can cause respiratory problems and affects millions of people globally each year (Anenberg et al., 2010). Mercury is a toxic contaminant and a worldwide concern due to its adverse effects on human health. Arctic communities and ecosystems are particularly vulnerable due to its bioaccumulation in aquatic food chains (AMAP, 2015). In an effort to reduce human exposure to Hg, an international agreement was reached in 2013 by the United Nations Environment Program (UNEP) called the Minamata Convention on Mercury (United Nations Environment Programme, 2013). This agreement was formally ratified in 2017 and aims to protect human health and the environment by reducing emissions of Hg and Hg-containing compounds.

In the Arctic, the atmospheric cycles of both ozone and mercury are controlled by halogens. However, the exact role that halogens play in these chemical cycles are still not completely defined. As a result, it is currently difficult for models to accurately predict the chemical transformations and lifetimes of ozone and mercury in the polar atmosphere.

1.3 Arctic atmospheric chemistry

The chemical composition of the Arctic atmosphere is regulated by a combination of chemistry, emissions, transport, and deposition. During spring, polar sunrise initiates many photochemical reactions involving ozone, mercury, halogens, and NO_x. These chemical cycles ultimately impact the oxidative capacity of the atmosphere (HO_x = OH+HO_2), controlling the chemical lifetimes of numerous trace gases. The coupled nature between these reaction cycles is illustrated in Figure 1.2. Chemistry within the troposphere can exhibit marked differences in behaviour compared to the stratosphere, as each is subject to different atmospheric conditions (e.g. temperature, UV radiation). This thesis is focused only on chemistry occurring within the troposphere. An overview of the Arctic-relevant chemical cycles (bromine, chlorine, ozone, and mercury) investigated in this thesis is given below. Examples of detailed reviews of Arctic atmospheric chemistry can be found in Abbatt et al. (2012); Barrie and Platt (1997); Platt and Hönninger (2003); Saiz-Lopez and von Glasow (2012); Simpson et al. (2007, 2015). Note, although iodine can also participate in these chemical cycles, it has not been addressed in this thesis. Reviews for Arctic iodine chemistry can be found elsewhere (e.g., Carpenter, 2003; Saiz-Lopez et al., 2012, 2014). Similarly, chemistry in the Antarctic is not discussed in this thesis, however previous works are highlighted in the following sections where relevant.

1.3.1 Tropospheric ozone

O_3 is one of the most studied compounds in the atmosphere for its role as both a greenhouse gas and harmful air pollutant. Downward transport of stratospheric ozone is a known source in the global tropospheric ozone budget (Shapiro et al., 1987). In addition, O_3 is chemically produced in the troposphere via reactions between NO_x and volatile organic compounds (VOCs), released from anthropogenic emissions. This is estimated to represent the main source of tropospheric O_3 (Myhre et al., 2013). O_3 is the major source of hydroxyl radicals (OH); the primary atmospheric oxidant that determines the chemical lifetimes of most species (Finlayson-Pitts and Pitts, 1999). OH radicals are produced following the photodissociation of O_3 under shortwave UV radiation:

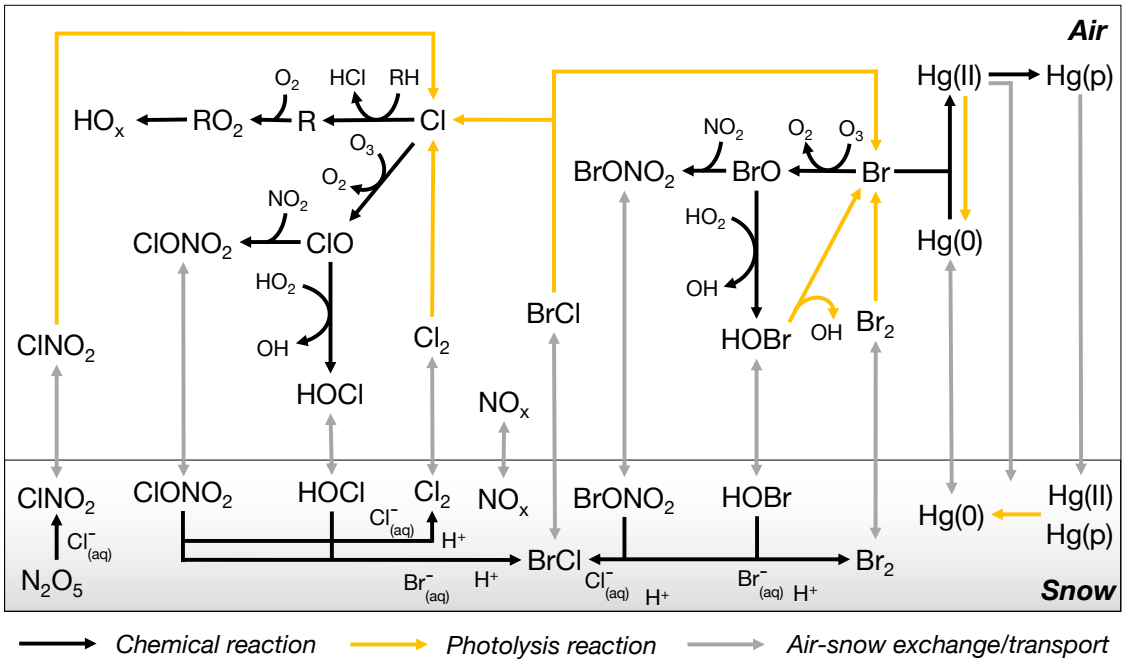

Figure 1.2: Simplified schematic of the Arctic chlorine, bromine, ozone, and mercury chemical mechanisms investigated in this thesis. The species depicted in snow here are representative of gas-phase compounds in the interstitial air between snow grains.

$$O_3 + h\nu \xrightarrow{(\lambda<330\ \text{nm})} O(^1D) + O_2, \tag{R1.1}$$

$$O(^1D) + H_2O \rightarrow 2OH \tag{R1.2}$$

OH is highly reactive with an average chemical lifetime of 1–2 seconds in the troposphere (Lelieveld et al., 2016). Key chemical reactions of OH include trace gases such as VOCs, CH_4, and carbon monoxide (CO), summarized by reactions (R1.3) and (R1.4):

$$RH + OH \rightarrow R + H_2O, \tag{R1.3}$$

$$R + O_2 \rightarrow RO_2 \tag{R1.4}$$

where R represents a carbon chain (e.g. CH_3). The products of this oxidation pathway are peroxyl radicals (RO_2), including the hydroperoxyl radical (HO_2), which impact the overall oxidative capacity of the atmosphere. Under polluted conditions, emission-generated NO_x may react with RO_2 and HO_2 species to form tropospheric O_3 (Crutzen, 1970). First,

NO can be converted to NO_2 via reaction with HO_2 and regenerate an OH radical:

$$NO + HO_2 \rightarrow NO_2 + OH \tag{R1.5}$$

Photodissociation of NO_2, under visible and ultraviolet radiation, then leads to the production of O_3, following reactions (R1.6) and (R1.7):

$$NO_2 + h\nu \xrightarrow{(\lambda<430\ \text{nm})} NO + O(^3P), \tag{R1.6}$$

$$O(^3P) + O_2 \xrightarrow{M} O_3 \tag{R1.7}$$

where M is a third body (typically O_2 or N_2). These reactions summarize the main processes involved in the production of tropospheric ozone. As shown by reactions (R1.3)–(R1.7), the rate of tropospheric ozone formation is largely determined by the abundance of VOCs, NO_x, and available sunlight. This is particularly important in polluted regions, where emissions of ozone precursors are high, severely impacting local air quality. In remote regions, such as the Arctic, long-range transport from the mid-latitudes and stratosphere-troposphere exchange of O_3 are the main sources of boundary layer ozone (Liang et al., 2011).

1.3.2 Boundary layer ozone depletion

Background mixing ratios of O_3 in the Arctic boundary layer range between 30–40 parts per billion by volume (ppbv or 10^{-9} mol mol^{-1}) during winter. In spring, O_3 can experience periods of depletion to almost 0 ppbv (Barrie et al., 1988). These episodic events, known as "Ozone Depletion Events" (ODEs), were first discovered in the Arctic in the 1980s and have since been regularly observed during spring (Barrie et al., 1988; Bottenheim et al., 1986; Oltmans, 1981; Oltmans and Komhyr, 1986). In the Antarctic, boundary layer ozone depletion was also observed to occur during austral spring, first reported in the 1990s (Wessel et al., 1998). The onset of ODEs coincides with polar sunrise and their duration and intensity can vary depending on both chemical (e.g. oxidant concentrations) and physical factors (e.g. boundary layer stability). Numerous observations of ODEs

have shown that these events can last anywhere between a few hours to several weeks depending on the scale of depletion (Jacobi et al., 2010). Similarly, ODEs can extend several hundreds of kilometers horizontally in the Arctic and up to 1 km vertically from the surface (Ridley et al., 2003). During these events, an anti-correlation between ozone and filterable bromine was first reported by Barrie et al. (1988), suggesting a halogen-driven chemical mechanism to explain their occurrence. Many studies have since followed this initial investigation, with strong evidence now attributing Arctic ODEs to halogen chemistry (Simpson et al., 2007).

1.3.3 Atmospheric mercury

Mercury is present globally and emitted to the atmosphere from natural sources (e.g. volcanoes) and anthropogenic activities (e.g. coal combustion, gold mining) (AMAP, 2011; Lindberg and Stratton, 1998). Gaseous elemental mercury (Hg(0)), the main form of atmospheric Hg, is transported worldwide due to its relatively long atmospheric lifetime (6 months to 1 year) (Selin, 2009). Hg(0) can be oxidized to divalent gaseous mercury (Hg(II)) and particulate mercury (Hg(p)), which are readily deposited to environmental surfaces (e.g. land, oceans) via dry and wet processes (Lindqvist and Rodhe, 1985; Lu et al., 2001). Briefly, oxidation of Hg(0) to Hg(II) can be summarized by reactions (R1.8) and (R1.9):

$$\mathrm{Hg(0)} + Y \xleftrightarrow{\mathrm{M}} Y\mathrm{Hg^{I}} \tag{R1.8}$$

$$Y\mathrm{Hg^{I}} + Z \xrightarrow{\mathrm{M}} Y\mathrm{Hg^{II}}Z \tag{R1.9}$$

where Y and Z = Br, Cl, OH. Determining the exact kinetics and speciation of these reactions however is an ongoing research challenge (Subir et al., 2011). As a result, the main oxidation pathway of Hg(0) globally remains a subject of discussion (Gustin et al., 2015, 2021; Jaffe et al., 2014)

1.3.4 Boundary layer mercury depletion

Similar to ozone, surface Hg(0) experiences depletion during spring in the Arctic boundary layer, first observed in 1995 (Schroeder et al., 1998). Following this discovery, depletion of boundary layer Hg(0) was also reported in the Antarctic during austral spring (Ebinghaus et al., 1998). Background levels of Hg(0) in the Arctic are typically around 1.4 ng m^{-3} and depletion events are defined as Hg(0) concentrations below 1.0 ng m^{-3} (Cobbett et al., 2007; Steffen et al., 2005). Atmospheric mercury depletion events (AMDEs) are highly correlated and coincident with ODEs, implicating bromine as the major oxidant driving Hg(0) depletion (Wang et al., 2019). During AMDEs, Hg(II) and Hg(p) concentrations increase as Hg(0) is oxidized, simultaneously increasing the amount of Hg deposited to the cryosphere (Steffen et al., 2014). Importantly, deposited Hg to snow surfaces can be re-emitted back into the atmosphere (as Hg(0)) under sunlit conditions (Durnford and Dastoor, 2011). Alternatively, Hg can remain within the snow and be redistributed to the Arctic Ocean during snowmelt. Here, it can be transformed into more toxic forms such as methylmercury (MeHg); a highly toxic contaminant harmful to marine and human organisms (AMAP, 2015). The exact amount of Hg(0) re-emitted from the Arctic snowpack is however uncertain, with estimates ranging between 40–90 % of deposited Hg (Durnford and Dastoor, 2011). This large variability highlights the complexity of Hg(0) re-emission from snow which can be influenced by several variables, including: snow chemical composition, UV radiation, snow temperatures, and snow age (Mann et al., 2014, 2015b, 2018). Changes in the Arctic climate could therefore impact the Hg cycle, including its transfer to the Arctic Ocean and contamination of aquatic ecosystems. A better understanding of the full polar mercury cycle is currently needed to predict the long-term impacts of future warming on the fate of Arctic Hg.

1.3.5 Bromine chemistry

Bromine is considered to be the most well-understood halogen in Arctic atmospheric chemistry, playing a central role in ODEs and AMDEs. The first measurements of bromine monoxide (BrO), a key species in the bromine/ozone cycle, were made by Long Path-Differential Optical Absorption Spectrometry (LP-DOAS) (Hausmann and Platt, 1994;

Tuckermann et al., 1997). Instrumental techniques have since improved, enabling more detailed investigations of bromine chemistry in the Arctic. Techniques including multi-axis DOAS (MAX-DOAS) and chemical ionization mass spectrometry (CIMS) have been employed at both ground-level and onboard aircrafts during many Arctic field campaigns (e.g., Koo et al., 2012; Liao et al., 2011, 2012a,b; Neuman et al., 2010; Pratt et al., 2013). These advances have allowed the characterization of more inorganic bromine species (such as molecular bromine (Br_2), hypobromous acid (HOBr), and bromine chloride (BrCl)) at higher temporal resolution than previously possible (Foster et al., 2001; Liao et al., 2012b; Spicer et al., 2002). This has enabled a more detailed understanding of their diurnal profiles, revealing that Br_2 experiences a peak in concentrations at night, before being photolyzed after sunrise (Liao et al., 2012b; McNamara et al., 2020; Wang and Pratt, 2017; Wang et al., 2019). Satellite retrievals have also helped probe the spatial distribution of Arctic bromine, particularly BrO, revealing a strong correlation between BrO and sea ice cover (e.g., Bougoudis et al., 2020; Chance, 1998; Richter et al., 1998; Salawitch et al., 2010; Wagner et al., 2001).

The springtime depletion of ozone and mercury by bromine can be summarized by the following chemical reactions. First, the reaction cycle is initiated by photolysis of Br_2 which has a very short photochemical lifetime ($<$ 1 min):

$$Br_2 \xrightarrow{h\nu} 2Br \tag{R1.10}$$

Bromine atoms can then quickly react with O_3 (forming BrO), or with Hg(0) (to form Hg(II)):

$$Br + O_3 \rightarrow BrO + O_2 \tag{R1.11}$$

$$Br + Hg(0) \xleftrightarrow{M} HgBr, \tag{R1.12}$$

$$Br + HgBr \xrightarrow{M} HgBr_2, \tag{R1.13}$$

BrO can further react with HO_2 to produce HOBr which is an important species involved in the autocatalytic regeneration of Br_2:

$$BrO + HO_2 \rightarrow HOBr + O_2 \tag{R1.14}$$

HOBr may be photolyzed to reform Br atoms whilst also converting one HO_2 molecule to OH:

$$HOBr \xrightarrow{h\nu} Br + OH \tag{R1.15}$$

Under high BrO concentrations, BrO can self-react to reform Br_2, restarting the reaction cycle:

$$BrO + BrO \rightarrow Br_2 + O_2 \tag{R1.16}$$

Alternatively, under high NO_x conditions, reaction between BrO and NO_2 can result in the formation of bromine nitrate ($BrONO_2$):

$$BrO + NO_2 \xrightarrow{M} BrONO_2 \tag{R1.17}$$

Recycling of reactive bromine on surfaces is crucial in sustaining high bromine concentrations which allows the depletion of ozone and mercury to proliferate. This recycling occurs via reactions (R1.18) and (R1.19), where HOBr and $BrONO_2$ activate aqueous bromide on salty surfaces (e.g. snow, sea ice, aerosols):

$$HOBr_{(g)} + Br^-_{(aq)} + H^+_{(aq)} \xrightarrow{\text{surface}} Br_{2(g)} + H_2O_{(l)} \tag{R1.18}$$

$$BrONO_{2(g)} + Br^-_{(aq)} \xrightarrow{\text{surface}} Br_{2(g)} + NO_3^- \tag{R1.19}$$

These reactions release two bromine atoms (as Br_2) into the atmosphere, resulting in an exponential increase in reactive bromine concentrations (Simpson et al., 2007). This is known as the "bromine explosion" and it is the reason why reactive bromine concentrations are sustained in the Arctic atmosphere capable of depleting ozone and mercury to near-zero levels.

The source of bromine in the Arctic originates from seawater containing bromide (Br^-), which is transferred onto on snow, sea ice, and aerosols. This is then activated and released to the atmosphere as Br_2, following reactions (R1.18) and (R1.19). Whilst several different bromine activation mechanisms have been proposed, all methods involve heterogeneous surface reactions, converting Br^- into reactive bromine. Surfaces involved in bromine recycling and activation include surface snow on land and sea ice, blowing snow, and aerosols. The amount of bromine released to the atmosphere is dependent on

several physical and chemical conditions. Firstly, surfaces must be acidic and enriched with bromide, as reaction (R1.18) exhibits a strong pH dependence, shown by previous laboratory and field experiments (Abbatt et al., 2012; Pratt et al., 2013; Wren et al., 2013). The initiation of the bromine chemical cycle is driven by photochemistry, therefore, the amount of available solar radiation will strongly influence bromine emissions. Laboratory and field experiments have shown a strong correlation between solar radiation and bromine production, with peak production under irradiated conditions (Custard et al., 2017; Pratt et al., 2013; Wren et al., 2013). The presence of ozone gas in snow was also shown to increase Br_2 production in these same studies. This is consistent with the bromine chemical mechanism as higher ozone concentrations would favour the formation of BrO, sustaining bromine recycling through the bromine explosion. In addition, surface observations of BrO in the Arctic have indicated a negative correlation between temperature and BrO abundance (Burd et al., 2017). Measurements suggested that recycling and emission of BrO can occur up to temperatures of 0 °C, but above freezing, BrO recycling is hindered due to the onset of snowmelt. The physical properties of the snowpack (e.g. morphology, liquid water content, gas transport and ventilation) may also impact the release of bromine to the atmosphere, however, their impacts on bromine emissions are still poorly understood (Bartels-Rausch et al., 2014). Boundary layer stability is another important factor that can impact the vertical distribution of bromine (Anderson and Neff, 2008). Stable atmospheric conditions (e.g. low-level temperature inversions) can concentrate reactive bromine close to the ground, limiting its transport to the free troposphere (Peterson et al., 2015; Simpson et al., 2017).

1.3.6 Chlorine chemistry

The bromine and chlorine cycles operate in conjunction and are directly linked through interhalogen reactions, and, indirectly via their impacts on the oxidative capacity (see Figure 1.2). Chlorine plays a different role to bromine in the Arctic, with only a minor contribution to surface ozone depletion in the boundary layer (Platt and Hönninger, 2003). The main source of atmospheric chlorine is from oceanic sea salt, in the form of chloride (Cl^-), activated on surfaces. Chloride is present in greater quantities than bromide in sea

salt, and can react with inorganic bromine (e.g. HOBr) promoting the formation of BrCl on surfaces (Simpson et al., 2007):

$$HOX_{(g)} + Y^-_{(aq)} + H^+_{(aq)} \xrightarrow{\text{surface}} XY_{(g)} + H_2O_{(l)} \quad \text{(R1.20)}$$

$$XONO_{2(g)} + Y^-_{(aq)} + H^+_{(aq)} \xrightarrow{\text{surface}} XY_{(g)} + NO^-_{3(aq)} \quad \text{(R1.21)}$$

where X and Y = Br or Cl. Once BrCl is formed, it can be readily photolyzed releasing both Br and Cl atoms to the atmosphere (R1.22), or react on surfaces to produce Br_2 (R1.23) (Hu et al., 1995):

$$BrCl \xrightarrow{h\nu} Br + Cl \quad \text{(R1.22)}$$

$$BrCl_{(g)} + Br^-_{(aq)} \xrightarrow{\text{surface}} Br_{2(g)} + Cl^-_{(aq)} \quad \text{(R1.23)}$$

Under polluted conditions, reactive nitrogen species (e.g. dinitrogen pentoxide (N_2O_5)) may also activate chloride by forming nitryl chloride ($ClNO_2$) which is an important nighttime reservoir and Cl precursor (McNamara et al., 2019). This reaction is as follows:

$$N_2O_5 + Cl^-_{(aq)} \rightarrow ClNO_2 + NO^-_{3(aq)} \quad \text{(R1.24)}$$

The production of Cl atoms in the Arctic is dominated by Cl_2 and $ClNO_2$ photolysis:

$$Cl_2 \xrightarrow{h\nu} 2Cl \quad \text{(R1.25)}$$

$$ClNO_2 \xrightarrow{h\nu} Cl + NO_2 \quad \text{(R1.26)}$$

Importantly, Cl atoms are highly efficient atmospheric oxidants, reacting with VOCs and CH_4 up to three orders of magnitude quicker than the more abundant OH radical (Atkinson et al., 2006). This makes chlorine an important reactive species even in low quantities. Measurements at Utqiaġvik, Alaska revealed that Cl_2 concentrations could sometimes reach as high as 400 pptv (parts per trillion by volume or 10^{-12} mol mol^{-1}) during spring (Liao et al., 2014). VOC oxidation by Cl results in the formation of RO_2, ultimately

impacting HO_x concentrations and the oxidative capacity of the atmosphere:

$$Cl + RH \xrightarrow{+ O_2} RO_2 + HCl \quad \text{(R1.27)}$$

Production mechanisms of Cl_2 are analogous to Br_2, with surface observations in the Arctic indicating a strong correlation to ozone and sunlight, suggesting both are prerequisites for Cl_2 production (Custard et al., 2016, 2017; Liao et al., 2014). Cl_2 has a slightly longer photochemical lifetime than Br_2 (approximately 10 minutes), resulting in distinct differences between their respective diurnal profiles. Arctic surface Br_2 measurements have recorded maximum Br_2 concentrations at night and a minimum during the day, whilst Cl_2 exhibits the inverse diurnal profile (daytime maxima and nighttime minima) (Custard et al., 2016; Liao et al., 2012b, 2014; McNamara et al., 2019; Wang and Pratt, 2017). Measurements of inorganic chlorine species in the Arctic are still relatively rare, with open questions regarding their vertical and spatial distribution in the Arctic boundary layer.

1.4 Atmospheric chemistry modelling

In remote regions (such as the Arctic), measurement data can often be sparse or incomplete, and chemical transport models can help us to predict the composition of the atmosphere. Specifically, CTMs are helpful in understanding the complex interactions between competing processes and the non-linear feedbacks present in atmospheric chemistry cycles, such as the bromine explosion. Models are fundamentally based on mathematical expressions of atmospheric processes, designed to quantitatively understand the evolution of chemical concentrations with time. This is done by numerically solving the continuity equation (1.1) to simulate the changes in production, loss, and transport, of a chemical species.

Atmospheric chemistry models represent the Earth (or regions of the Earth) in smaller boxes (grid cells) and can operate on different spatial and temporal timescales. One way to classify atmospheric models is according to their dimensionality (i.e. the number of dimensions in which a computed variable is a function of). Box models (0-D), column

models (1-D), and regional/global models (3-D) differ fundamentally in the complexity of their descriptions of an atmospheric system, resulting in different uses and applications (Figure 1.3). As the dimensions and size of a model domain increases, the number of processes to be resolved grows drastically, increasing the computational cost of a model simulation. Descriptions of processes in models are therefore often simplified or approximated through model parameterizations, as a way of reducing the overall computational load. Consequently, there is always a trade-off between model complexity and computational cost that must be considered before any modelling exercise.

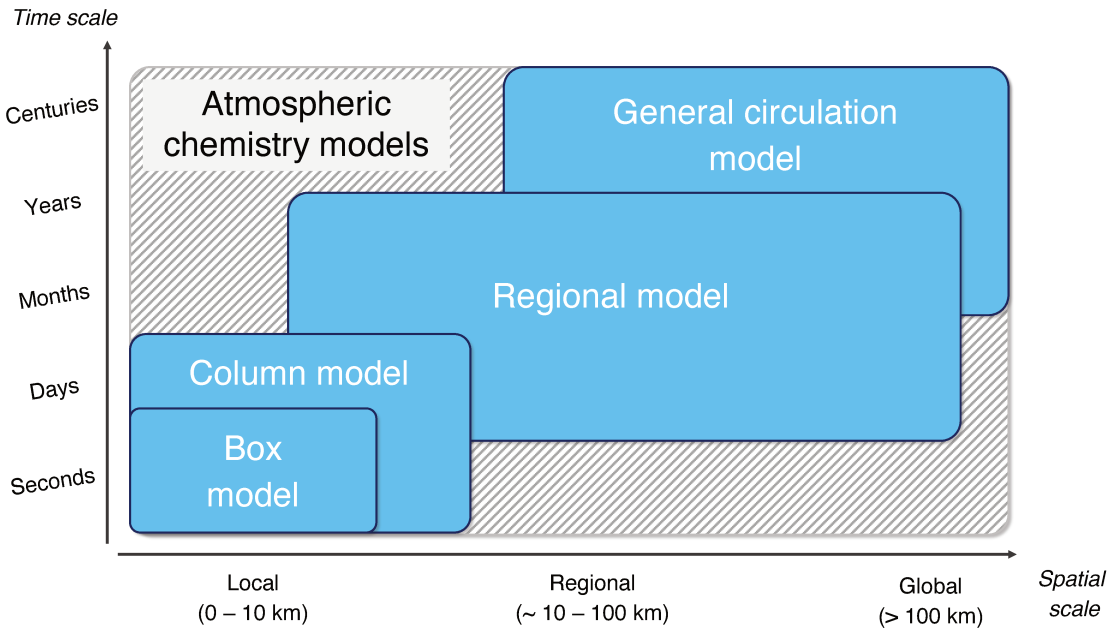

Figure 1.3: Types of atmospheric chemistry models and examples of their typical use cases.

The underlying framework of CTMs can be characterized by two main categories: *Eulerian* and *Lagrangian* models. Both types of models are used in this thesis and are briefly described below. Eulerian models use a fixed coordinate system in which the atmosphere is divided into grid cells stationary in space. Chemical concentrations are computed in each model grid cell (assumed to be well-mixed within a grid cell) and transported in and out of each cell at the cell boundaries. These types of models are generally used for large-scale climate applications and atmospheric chemistry studies. On the other hand, Lagrangian models (also known as trajectory or particle dispersion models) employ a moving frame of reference, in which air parcels are tracked over time. These mod-

els simulate chemical concentrations as infinitesimally small air parcels moving through space continuously. One advantage of Lagrangian models is the ability to accurately simulate advection as there is no numerical diffusion, unlike in Eulerian models. This preserves sharp gradients of species (e.g. within a plume) whereas these gradients are smoothed out in Eulerian models. Conversely, Eulerian models are often computationally less expensive than Lagrangian models (depending on the application and model resolution).

In this thesis, a combination of modelling tools are used, including: Lagrangian modelling (Chapter 3), 1-D modelling (Chapter 4), and 3-D regional modelling (Chapter 5). These models were specifically chosen to address particular aspects of the polar atmospheric chemistry cycles, from surface snow chemistry and emissions, to regional scale chemistry and air mass transport.

1.4.1 State-of-the-art in Arctic atmospheric chemistry modelling

Many models that exist today offer differing insights into the behaviour of physical and chemical processes due to differences in model descriptions and complexity. It is therefore important to first assess the current state-of-the-art in atmospheric chemistry modelling to identify model shortcomings and limitations. At the start of this thesis project, many models still struggled to accurately represent key aspects of polar atmospheric chemistry. For example, model predictions of boundary layer ozone in Arctic spring can be incorrect due to missing or simplified descriptions of bromine chemistry and emissions (Monks et al., 2015). No regional model using both surface snow and blowing snow emissions of Arctic bromine could be found prior to the beginning of this thesis. This motivated the study of Marelle et al. (2021), in which I jointly collaborated, to develop a regional model with descriptions of both bromine emission mechanisms and study their combined impact on Arctic ozone. Additionally, the effects of using hourly-calculated bromine oxidant concentrations on polar springtime mercury chemistry have seldom been explored. This research gap was one of issues addressed in this thesis (presented in Chapter 5).

Model intercomparison studies are extremely valuable in providing comprehens-

ive assessments of the current state-of-the-art and highlighting key model deficiencies. For example, the POLARCAT Model Intercomparison Project (POLMIP) evaluated 3-D model representation of Arctic atmospheric chemistry, motivated by a growing number of observations in the Arctic (Emmons et al., 2015). In total, 11 global and regional chemical transport models were evaluated against ground-based, aircraft, and satellite observations. Large differences were found between models in the concentrations of reactive nitrogen species (NO_y) and VOCs, which were often negatively biased and therefore underestimated ozone formation in the troposphere. Furthermore, a comparison of surface ozone concentrations revealed most models failed to capture ODEs during spring, as a result of missing/simplified descriptions of halogen chemistry and emissions (Monks et al., 2015). Another example is the assessment of aerosols in atmospheric models, conducted as part of the AeroCom project. Clouds and aerosols are two of the largest uncertainties in atmospheric models, with important impacts on the global radiative balance. Aerosol chemistry is also an essential component of halogen activation and chemistry during polar spring (Abbatt et al., 2012). Currently, model predictions of Arctic aerosols show large inter-model variability due to differences in model descriptions of aerosol processes (Sand et al., 2017).

Similarly, model representation of mercury chemistry in global models was recently evaluated against a network of ground-based observations (Angot et al., 2016; Travnikov et al., 2017). This work was conducted as part of the Mercury Modeling Task Force under the Global Mercury Observation System (GMOS) project. In the model evaluation of Angot et al. (2016), four contemporary mercury models (ECHMERIT, GEM-MACH-HG, GEOS-Chem, GLEMOS) were evaluated with monthly-averaged surface mercury measurements in the polar regions. Results showed that models were generally able to capture the annual cycle of mercury in the Arctic. However, model performance in spring is difficult to assess, due to the use of monthly-averaged data which hides the daily variations of mercury during AMDEs. This is crucial as spring is when most atmospheric Hg is deposited to the cryosphere (Steffen et al., 2014). In addition, most mercury models are currently faced with the limitation of using monthly mean oxidant concentrations (e.g. Br), which neglects the diurnal variability of these species needed to accurately simulate

mercury oxidation chemistry.

Lower dimensional models (e.g. box models and column models) have also been useful in investigating small-scale processes, such as snow chemistry and snow-atmosphere exchange of trace gases. Specifically, these types of models have been used to understand how Arctic snow acts as a chemical source of NO_x and halogens, to complement surface chemical measurements (e.g., Custard et al., 2015; Thomas et al., 2011, 2012; Thompson et al., 2015; Toyota et al., 2014b; Wang and Pratt, 2017; Wang et al., 2020). However, due to the complexity of the snowpack and uncertainties surrounding snow chemistry and transport, developments of fully coupled snow-atmosphere models have been limited (Domine et al., 2013). Continued model developments are therefore necessary to improve the representation of physical (e.g. snow-atmosphere exchange) and chemical (e.g. halogen emissions and chemistry) processes in the Arctic. More specifically, these improvements are needed to refine our understanding of how the interconnected cycles of halogens, ozone, and mercury operate during Arctic spring.

1.5 Objectives of this thesis

There are several knowledge gaps that remain to be addressed regarding the coupled Arctic halogen, ozone, and mercury cycles. In this thesis, I focus on developing our understanding of these cycles by using a combination of chemical transport modelling tools to study the relevant emission, chemical, and transport processes in the Arctic. Efforts to address these knowledge gaps are crucial for better understanding cryosphere-atmosphere interactions, and predicting the impacts of a warming climate on Arctic atmospheric chemistry. Specifically, I aim to answer the following questions:

1. Using Lagrangian transport models, what can we learn about the geographical origin and transport pathways of observed ozone-depleted and mercury-enriched air masses in the Arctic? What is the influence of exposure to sea ice on atmospheric mercury and ozone?

2. What are the quantifiable impacts of halogen emissions from snow on boundary layer chemistry and oxidative capacity? What combination of emissions, chemistry,

and transport can explain surface chlorine and VOC observations in the Arctic?

3. What is the vertical extent of bromine and chlorine chemistry in the Arctic boundary layer?

4. Can regional modelling be used to accurately represent springtime ozone and mercury depletion events in the central Arctic on an hourly timescale?

5. How does mercury redox chemistry impact deposition rates in the Arctic? What are the relative amounts of mercury re-emission and retention in the Arctic snowpack?

To answer these research questions, two main modelling tools (1-D and 3-D models) have been developed and used in this work, described in Chapter 2. Chapter 3 presents an investigation of ozone transport and mercury emission sources using trajectory modelling, based on measurements from two different Arctic campaigns. In Chapter 4, 1-D modelling is used to study the impact of halogen emissions from snow on boundary layer chemistry. The model is evaluated with field measurements from the spring 2009 OASIS (Ocean-Atmosphere-Sea Ice-Snowpack) campaign at Utqiaġvik, Alaska. Chapter 5 presents a regional Arctic modelling study, using a 3-D model developed in this thesis, to explore the coupled chemical cycles of bromine, ozone, and mercury. Model performance is assessed with measurements made in the central Arctic during the 2020 MOSAiC (Multidisciplinary drifting Observatory for the Study of Arctic Climate) expedition. Finally, the conclusions and future perspectives are discussed in Chapter 6.

Chapter 2

Developing atmospheric chemistry modelling tools

Contents

Introduction

Predicting changes in the chemical composition of the atmosphere can be achieved by using chemical transport models. Atmospheric models are particularly suited to considering many processes simultaneously and assessing their combined impact on atmospheric composition. Their widespread usage has enabled advancements in many areas of atmospheric chemistry research, including air quality prediction and in complementing measurement-based studies. As discussed in Chapter 1, different types of models possess distinct strengths and limitations, often characteristic to their foundational framework. The choice of an atmospheric chemistry model is therefore largely dependent on the research question(s) to be investigated.

A central research theme to this thesis is boundary layer chemistry in the Arctic. As our understanding of certain boundary layer processes grows (e.g. chemical emissions, reactivity, transport), this necessitates model developments to improve the representation of these processes. In this thesis, a combination of one-dimensional (1-D) and three-dimensional (3-D) models are developed and used to address the research objectives mentioned in Chapter 1. Specifically, 1-D modelling is used to study near-surface halogen emissions and reactivity, and 3-D modelling is used to investigate the regional impacts of springtime halogen chemistry on mercury and ozone. This chapter describes the two main atmospheric chemistry models developed and used in this thesis.

2.1 One-dimensional column modelling

Column models (or 1-D models) calculate chemical concentrations with respect to time in the vertical dimension, assuming horizontally homogeneous layers. A key advantage of one-dimensional modelling is the high vertical model resolution, which can resolve processes at a much finer resolution than regional or global models at a lower computational cost. The vertical resolution of 1-D models can range from as low as the centimetre scale up to the kilometre scale. These models are therefore useful for studying fine-scale processes and for developing parameterizations to be incorporated into 3-D models.

A number of 1-D models have been developed and applied to a broad range of re-

search questions to better understand different components of atmospheric chemistry. For example, the 1-D model MISTRA has been used in several studies, exploring topics such as marine boundary layer chemistry (von Glasow et al., 2002a,b), volcanic plume modelling (Aiuppa et al., 2007), and snow-atmosphere chemical interactions in the Arctic (Thomas et al., 2011, 2012). Another example is the 1-D model PHANTAS, developed to study air-snow chemistry and exchange processes in the polar boundary layer (Toyota et al., 2014b,a).

In this thesis, the Platform for Atmospheric Chemistry and Transport in One-dimension (PACT-1D) model is developed to investigate the impact of halogen emissions from snow on springtime boundary chemistry in the Arctic. Specifically, the model is used to study atmospheric chemistry during the OASIS 2009 measurement campaign at Utqiaġvik, Alaska. One of the reasons for using a 1-D model in this work was to provide flexibility in developing parameterizations of halogen emissions by performing numerous model simulations. This is something that can be done efficiently with a 1-D model at much lower computational cost than in a 3-D model. Consequently, the model parameterizations derived from the 1-D model can later be applied and tested in regional/global models.

2.1.1 Platform for Atmospheric Chemistry and Transport in One Dimension (PACT-1D) model description

PACT-1D is a vertical column model which solves both chemical kinetics and vertical transport with time. This is done by numerically solving the continuity equation (equation 1.1). Chemistry is calculated online in the model and the atmospheric physics and dynamics are provided as inputs. The first description and use of PACT-1D can be found in Tuite et al. (2021), which investigated surface nitrous acid (HONO) formation chemistry in Pasadena, California. PACT-1D is an open source model and publicly available at Ahmed et al. (2022b) (https://doi.org/10.5281/zenodo.6045999). Several processes are considered by the model, including: (i) gas-phase chemistry (including photolysis), (ii) heterogeneous chemistry on aerosols, (iii) vertical diffusion, (iv) deposition, and (v) chemical emissions.

The gas-phase chemical mechanism is based on the Regional Atmospheric Chemistry Mechanism version 2 (RACM2) (Goliff et al., 2013). This mechanism lists the set of chemical species, reactions, and rate expressions to be simulated by the model. PACT-1D uses the Kinetic PreProcesseor (KPP) to compute the kinetic rates of all gas-phase reactions and is done on a separate internal timestep (Sandu and Sander, 2006). Photolysis rates are provided as inputs to the model, derived from external model output, which are then passed to KPP. For example, the Tropospheric Ultraviolet-Visible (TUV) radiation model is one such model which calculates photolysis rate coefficients for different photodissociation reactions (https://www2.acom.ucar.edu/modeling/tropospheric-ultraviolet-and-visible-tuv-radiation-model). These values are calculated in TUV based on user input (e.g. location, time, surface albedo) to capture the atmospheric conditions for the radiation calculations.

In addition, PACT-1D considers both non-reactive uptake of gases to aerosols and heterogeneous surface reactions on aerosols. The model does not explicitly solve aerosol physics and therefore considers heterogeneous reactions as surface reactions, with aerosol concentrations and radii provided as inputs. Reactive uptake rates of gases to aerosols are described in the model following equation (2.1):

$$k_{\text{het}} = \frac{1}{4} S \nu \gamma J \tag{2.1}$$

where k_{het} is heterogeneous reaction rate, S is the aerosol surface area (assuming perfectly spherical aerosol droplets), ν is the mean molecular speed, γ is the reactive uptake probability, and J is a correction factor for diffusion limitations of gas molecules close to the aerosol surface. Aerosol surface area is calculated based on the mean aerosol radius and number concentration, which is provided as input to the model. J is calculated according to Fuchs and Sutugin (1971), as:

$$J = \frac{0.75\gamma(1+Kn)}{Kn^2 + Kn + (0.283Kn \times \gamma) + 0.75\gamma} \tag{2.2}$$

where Kn is the Knudsen number which represents the ratio of the mean free path to the aerosol radius.

Vertical transport of gases is solved numerically using the Crank-Nicolson method, following equation (2.3) (Brasseur and Jacob, 2017):

$$\frac{\partial}{\partial t}C_{(i,z,t)} = \frac{1}{\rho_{(i,z,t)}}\frac{\partial}{\partial z}\left(\rho_{(i,z,t)}K_{D(i,z,t)}\frac{\partial}{\partial z}C_{(i,z,t)}\right) + R_{(i,1,t)} \tag{2.3}$$

where $C_{(i,z,t)}$ is the concentration of species i at altitude z and time t, $\rho_{(i,z,t)}$ is the air density, $K_{D(i,z,t)}$ is the sum of eddy diffusivity $\left(K_{(z,t)}\right)$ and molecular diffusion $\left(D_{(i,z,t)}\right)$, and $R_{(i,1,t)}$ is the loss of species in the lowest model level (deposition). Vertical exchange (eddy diffusion) coefficients, $K_{(z,t)}$, are also provided as model input from surface measurements or parameterizations, which vary with altitude and time. One approach to estimate K_z is based on the first-order parameterization of Pielke and Mahrer (1975), which has been applied in previous 1-D modelling studies (Cao et al., 2016; Herrmann et al., 2019),. This parameterization uses an empirical polynomial equation, described by equation (2.4):

$$K_z = \begin{cases} \dfrac{z}{L_0}K_{SL}, & \text{if } 0 \le z \le L_0 \\ K_{FT} + \left(\dfrac{L-z}{L-L_0}\right)^2 \left[K_{SL} - K_{FT} + (z-L_0)\left(\dfrac{K_{SL}}{L_0} + 2\dfrac{K_{SL}-K_{FT}}{L-L_0}\right)\right], & \text{if } L_0 \le z \le L \\ K_{FT}, & \text{if } L \le z \end{cases} \tag{2.4}$$

In equation (2.4), L is height of the boundary layer and L_0 is the height of the surface layer (assumed to be 10 % of the boundary layer height). L (and L_0) can be estimated using different parameterization schemes (e.g. Pollard et al., 1973; Zilitinkevich et al., 2002; Zilitinkevich and Baklanov, 2002; Neff et al., 2008) or based on measurement data (e.g. turbulent flux measurements). K_{SL} is the estimated turbulent diffusion coefficient at the top of the surface layer, calculated as $K_{SL} = \kappa u_* L_0$, where $\kappa = 0.41$ is the von Karman constant and u_* is the friction velocity. K_{FT} is the turbulent diffusion coefficient in the free troposphere, assumed to be constant and equal to 1.0 $cm^2\ s^{-1}$. In the lowest model levels near the surface (e.g. below 1 m), K_z is set close to the molecular diffusion

coefficient ($\sim$ 0.1–0.01 $cm^2\ s^{-1}$). Snowpack chemistry is not explicitly described in this version of the model and is simplified using parameterizations for surface snow emissions and recycling reactions. This is described in more detail in section 2.1.2.

Deposition to the surface (R in equation (2.3)) is treated by calculating the molecular collisions of each species with the ground and applying a non-reactive uptake probability (α). This approach allows the deposition rates of different species to be calculated without prescribing a deposition velocity. Chemical emissions $\left(E_{(i,z,t)}\right)$ are provided as input to the model, for specific model levels and times. Emissions can therefore be applied for specific species, varying with altitude and time. More complex descriptions of surface chemistry and emissions can also be specifically developed using a parameterized approach, as is presented in this work (see section 2.1.2).

PACT-1D is based on a modular framework with options for different routines (e.g. vertical diffusion, halogen chemistry, chemical timestep, model output frequency), allowing for routines to be easily activated or deactivated between different model simulations. One benefit of this modular system is that sensitivity analyses can be performed efficiently without major changes to the model code. Another advantage is that PACT-1D can be configured to run as a 0-D box model, by simply deactivating the vertical diffusion routine, for particular case studies.

2.1.2 PACT-1D model developments

Prior to this work, no publicly available 1-D model existed that was capable of addressing the research questions posed in this thesis. Furthermore, the version of PACT-1D available at the start of this thesis did not include key model capabilities for studying halogen surface chemistry. A number of developments were therefore first made to the PACT-1D model code for the purposes of this investigation. Mainly, the developments involve the addition of a new halogen chemical mechanism and a surface snow emission parameterization for molecular halogens (Cl_2 and Br_2). Some additional technical modifications were also performed to modularize the code and improve usability, but, discussion of these updates are excluded from here. All model developments made in this work are included in the public version of the code at Ahmed et al. (2022b)

(https://doi.org/10.5281/zenodo.6045999).

Halogen gas-phase and heterogeneous chemistry

Gas-phase chlorine and bromine reactions were added to the existing PACT-1D chemical mechanism, via KPP. Chemical rate expressions for these new reactions were obtained from IUPAC (2009) and Burkholder et al. (2019). In total, 63 gas-phase halogen reactions (including 13 photolysis reactions) have been included in this work. As previously described, photolysis rates are calculated outside of PACT-1D, using the TUV model, before being passed into KPP. The TUV model was also updated to calculate photolysis rates of particular halogen reactions (not described here). Heterogeneous surface reactions of halogens on aerosols are also added to the model (14 reactions). The reactive uptake coefficients (γ in equation (2.1)) for these reactions are based on recommended values obtained from IUPAC (2009) and Burkholder et al. (2019). In some cases, the range of values reported for γ may be large depending on factors such as the surface type and temperature. In these cases, values of γ were chosen for low temperatures appropriate for snow/ice surfaces (where possible). More details are provided in Chapter 4 and in the model mechanism at Ahmed et al. (2022b) (https://doi.org/10.5281/zenodo.6045999).

Deposition of halogens

Dry deposition is calculated by considering the number of molecular collisions of each gas with the surface. Deposition of 8 halogens species is added to the model, treated by assuming a non-reactive uptake to snow and ice surfaces. The mass accommodation coefficient (α) is used to estimate the efficiency of non-reactive uptake to surfaces for each particular species, set using values from Burkholder et al. (2019). Values of α are added for the following species: Cl_2, HOCl, HOBr, $BrONO_2$, $ClONO_2$, BrCl, HCl, and BrCl. These values are listed in the model code at Ahmed et al. (2022b) (https://doi.org/10.5281/zenodo.6045999).

Emissions and recycling of halogens

Emissions of molecular halogens have been measured from the Arctic snowpack and were found to depend on several factors. There is strong evidence that emission from snow is driven by solar radiation, with peak emissions under irradiated conditions, reported in both field and laboratory studies (Custard et al., 2017; Pratt et al., 2013; Wren et al., 2013). The presence of ozone gas within the snow was also found to favour the production and release of halogens, likely through the halogen explosion mechanism. Additionally, lower pH values in snow have shown enhanced halogen production, indicative of heterogeneous halogen recycling (Abbatt et al., 2012; Pratt et al., 2013; Wren et al., 2013).

Emissions and recycling of chlorine and bromine from surface snow are added to PACT-1D following two methods. First, primary emissions of Cl_2 and Br_2 are described based on available solar radiation and ambient ozone concentrations. As mentioned, these two variables have been shown to be highly correlated with surface emissions of molecular halogens from snow (Custard et al., 2017; Pratt et al., 2013; Wren et al., 2013). Second, recycling and re-emission of Cl_2 and Br_2 on the surface is included, following the deposition of reactive halogen species (HOX and $XONO_2$, where X = Cl, Br). A surface heterogeneous conversion probability is applied for this recycling, with the sensitivity of the chosen values explored in Chapter 4. The exact parameterizations used for these surface halogen emissions are described in detail in Chapter 4.

2.2 Three-dimensional regional modelling

Developments in 3-D atmospheric modelling have increased the number and complexity of processes considered in models, advancing our knowledge of the coupled Earth climate system. 3-D models are among the most sophisticated chemical transport models, capable of simulating atmospheric chemistry and dynamics simultaneously over the entire globe. These models are fundamentally based on the same general form of the continuity equation (equation (1.1)), with added terms to represent the treatment of advection and turbulent transport.

Broadly, 3-D atmospheric chemistry models are designed in two main configura-

tions. Models that do not generate their own meteorological variables (e.g. winds, temperature, humidity) and use data from external meteorological models are known as "offline" models. In contrast, models that resolve meteorology by numerically solving equations for conservation of mass, momentum, and energy, (together with the chemistry) are referred to as "online" models. The advantage of online models is that the interactions between chemistry and dynamics are fully coupled and accounted for (e.g. the impacts of aerosol concentrations on radiative transfer and cloud formation).

3-D models also vary in terms of their horizontal resolution, applicable to local, regional, and global scale applications. For investigations focused on a particular location of Earth, regional models can be an ideal choice for these research problems. This is because regional models are able to simulate highly resolved processes (e.g. aerosol chemistry) at lower computational cost than global models. In addition, regional models are typically capable of higher vertical resolution compared to global models, simulating as many as tens of model levels within the planetary boundary layer which is important for representing near-surface processes. In the case of simulating Arctic boundary layer chemistry, a detailed representation of both chemistry and dynamics is needed, at a sufficient horizontal and vertical model resolution. For these reasons, an online 3-D regional model was chosen to address the research objectives of this thesis.

2.2.1 Weather Research and Forecasting (WRF) model

The Weather Research and Forecasting model (WRF) is the core 3-D model used in this thesis. WRF is a mesoscale meteorological model developed and maintained by the US National Oceanic and Atmospheric Administration (NOAA), in collaboration with other global research institutes and organizations (Grell et al., 2005). The model is a numerical weather prediction system, designed for both operational forecasting and for atmospheric research applications. WRF has been widely used in many different studies within the atmospheric research community. The model is based on two dynamical cores which deal with the meteorological and physical processes; the Advanced Research WRF (ARW) core and the Nonhydrostatic Mesoscale Model (NMM) core (Skamarock et al., 2019). The work presented in this thesis is based on the WRF ARW core.

The framework of WRF is highly modular, with options for different meteorological schemes (e.g. boundary layer, microphysics, radiative transfer) defined within subroutines. The WRF model grid uses a terrain-following coordinate system (or sigma coordinate), based on user-defined pressure levels, which allows the model to conform to the surface terrain. Initial and boundary conditions for meteorology are provided to WRF from analyses (e.g. National Centers for Environmental Prediction (NCEP) Final Analysis (FNL) data), reanalyses (e.g. ECMWF Reanalysis version 5 (ERA5)), or other model output (e.g. global models). These input data are often on a coarser resolution than the desired model resolution of the WRF grid. Dynamical downscaling is technique used by many high resolution regional models, such as WRF, to extrapolate these coarsely resolved meteorological data to finer spatial resolution. Meteorological conditions from such datasets may also be used to gently force the dynamical model variables toward a physical reference state (i.e. the forcing dataset). This technique provides a more realistic representation of the atmospheric conditions and is common amongst CTMs, known as "nudging" or "Newtonian relaxation". Two types of nudging can be employed by the WRF model; grid nudging and spectral nudging. Grid nudging is a processes in which forcing is applied in every grid cell toward the reference state (Stauffer and Seaman, 1990). Alternatively, spectral nudging allows forcing to be applied only on the large-scale processes, whilst maintaining small-scale variability (von Storch et al., 2000). The model may also be run in a configuration without nudging toward any pre-defined meteorology; this is known as a "free-running" simulation.

Meteorological model setup

The selected meteorological options for simulations performed in this thesis have been chosen based on previous testing of boundary layer representation in the Arctic (Marelle et al., 2017, 2021), and are described below. To model the entire Arctic, a horizontal model resolution of 100×100 km is used, with a vertical resolution of 72 levels, up to 50 hPa. This work uses NCEP FNL (National Centers for Environmental Prediction, 2000) to initialise the model and to constrain the lateral boundaries for meteorological variables (e.g. air temperature, humidity, winds). NCEP FNL data is provided on a 1×1

degree grid, and boundary conditions of these input data are updated in WRF every 6 hours. Spectral nudging is applied within and above the boundary layer in WRF, nudged towards NCEP-FNL data. A dynamical timestep of 5 minutes is used for the simulations in this work.

To compute vertical mixing and boundary layer stability, the Mellor–Yamada Nakanishi Niino Level 2.5 Scheme (MYNN2, Nakanishi and Niino (2009)) is used together with the MYNN surface layer scheme (Nakanishi, 2001). Additionally, land surface processes are represented by the unified Noah Land Surface Model (Noah-LSM). Noah-LSM is responsible for computing land-based variables such as soil moisture, skin temperature, and snowpack depth to improve predictions of the land-atmosphere interactions (Tewari et al., 2004). Radiative transfer calculations in the longwave and shortwave are treated following the Rapid Radiative Transfer Model for Global applications (RRTMG) scheme (Iacono et al., 2008). This model considers the radiative effects of all significant atmospheric gases, and absorption and scattering properties of aerosols, liquid and ice clouds. Cloud microphysics are represented in WRF using the bulk Morrison two-moment microphysics scheme, which calculates the mass mixing ratios and number concentrations of water and ice clouds (Morrison et al., 2009). This allows for the prediction of cloud formation, cloud properties, grid-scale precipitation, as well as aerosol activation in clouds and wet removal. An additional parameterization is used to resolve sub-grid scale cumulus clouds, represented by the KF-CuP (Kain-Fritsch + Cumulus Potential) scheme (Berg et al., 2015). KF-CuP is based on the Kain-Fritsch convective parameterization (Kain and Fritsch, 2004; Kain, 2004) and the cumulus potential scheme (Berg and Stull, 2005), recommended for simulations with horizontal resolutions coarser than 10 km. Both the Morrison two-moment and KF-CuP schemes are coupled to aerosols in the model to account for aerosol-cloud interactions.

2.2.2 WRF coupled with chemistry (WRF–Chem) model

The WRF model coupled with chemistry (WRF–Chem) is used in this thesis to perform regional simulations of Arctic atmospheric chemistry (Fast et al., 2000; Grell et al., 2005). WRF–Chem is a fully coupled online model as it performs chemical and meteorological

calculations simultaneously to predict atmospheric composition. Chemistry (gas-phase and aerosol chemistry) is calculated within subroutines of the WRF-Chem code, represented by different mechanisms of varying complexity. The chemical component of WRF-Chem is consistent with the meteorological component of WRF, both using the same model grid, timestep, transport, and physics schemes. Applications of WRF-Chem have included hindcast atmospheric chemistry studies and regional air quality forecasting, where consideration of meteorological-chemical feedbacks are important. The options and inputs used for the chemistry-related settings in this investigation are described below.

Chemistry and aerosol scheme

Gas-phase chemistry in WRF-Chem is also calculated by KPP, as in the PACT-1D model. Chemical rates are calculated on an internal KPP timestep, which can differ to the dynamical timestep of the model. A number of chemical mechanisms have been developed and exist within WRF-Chem that define the set of gas-phase reactions calculated by the model. This investigation extends a recent development of the SAPRC-99 (Statewide Air Pollution Research Center, 1999 version; Carter (2000)) chemical mechanism, which includes halogen gas-phase chemistry (Marelle et al., 2021), by adding a number of mercury redox reactions (see section 2.2.3). Photolysis rates are calculated using the Fast-J photolysis scheme, based on the species absorption cross sections and modelled actinic flux, before being passed into KPP (Wild et al., 2000).

Aerosols in WRF-Chem are represented by the MOSAIC (Model for Simulating Aerosol Interactions and Chemistry) model and is coupled to the chemical mechanism. MOSAIC uses a sectional approach to represent aerosols in 8 discrete size bins, with radii ranging between 39 nm and 10 μm. Aerosol particles within the same size bin are assumed to be internally mixed and therefore have the same chemical composition, and different bins are externally mixed. Chemical concentrations and aerosol number concentrations are calculated by MOSAIC within each grid cell, for a number of aerosol species, including: sulfate (SO_4^{2-}), ammonium (NH_4^+), nitrate (NO_3^{2-}), sodium (Na^+), calcium (Ca^{2+}), Cl^-, black carbon (BC), organic aerosol (OA), and other inorganics (OIN).

Aerosol-cloud interactions are also treated explicitly in MOSAIC, with both interstitial and cloud-borne aerosols treated explicitly.

Dry deposition velocities of gas-phase and aerosol species are calculated following the Wesley resistance scheme (Wesely, 1989). These values are calculated within each grid cell based on the surface type, local meteorology, and chemical properties of the species (e.g. Henry's law constant). For aerosols, dry deposition also includes gravitational settling, which is an important removal process for large aerosols. Wet removal of gases and aerosols is considered for both in-cloud (rainout) and below-cloud (washout) processes (Easter et al., 2004). Rainout describes the scavenging of gases and aerosols by cloud droplets (within clouds), whereas washout is the removal of aerosols and gases by impaction during precipitation (below clouds).

Chemical initial & boundary conditions and emission inventories

Before running WRF-Chem, a number of inputs are provided to the model that describe chemical emissions, initial, and boundary concentrations during the simulation. For this investigation, initial and boundary chemical concentrations of trace gases and aerosols are obtained from the global model CAM-Chem. This data is publicly available, hosted by NCAR, for the purposes of providing boundary conditions to regional models. CAM-Chem is run using a 0.9×1.25 degree horizontal model resolution with 56 vertical levels, and model output data for boundary conditions are available every 6 hours. Chemistry in the CAM-Chem model is based on the MOZART-T1 (Model for Ozone and Related chemical Tracers) mechanism, with the full list of chemical species provided in (Emmons et al., 2020).

Anthropogenic emissions are obtained from the global ECLIPSEv6b dataset (Evaluating the Climate and Air Quality Impacts of Short-Lived Pollutants version 6b), created with the GAINS model (Greenhouse gas – Air pollution Interactions and Synergies). Emission fields include: sulfur dioxide (SO_2), NO_x, ammonia (NH_3), non-methane VOCs (nmVOCs), BC, organic carbon (OC), organic matter (OM), particulate matter ($PM_{2.5}$ and PM_{10}), carbon monoxide (CO), and CH_4. These data are provided on a global grid at 0.5×0.5 degree horizontal model resolution. ECLIPSEv6b accounts for emissions from a

number of sectors including: energy; agriculture; waste; transport; residential and industrial combustion; and international shipping. Anthropogenic emissions of Hg species are also included in this work, from the global anthropogenic mercury emissions inventory for 2015. This was prepared as part the 2018 AMAP/UNEP Global Mercury Assessment (GMA, AMAP/UN Environment (2019)). Emissions of elemental mercury (Hg(0)), gaseous oxidized mercury (Hg(II)), and particulate mercury (Hg(p)) are globally gridded on a 0.25×0.25 degree horizontal resolution grid. These emissions are divided into four distinct sectors: fuel combustion; industrial sectors; waste from intentional use; and artisanal and small-scale gold mining (Steenhuisen and Wilson, 2019, 2022).

Biogenic emissions are calculated in WRF-Chem online by the MEGAN model (Model of Emissions of Gases and Aerosols from Nature, Guenther et al. (2012)). MEGAN calculates emission fluxes of biogenic compounds released naturally from terrestrial ecosystems. Emission fluxes are calculated based on climatological inputs of land surface, vegetation types, and leaf area index, as well as WRF predicted surface temperature. Biomass burning emissions are also included in WRF-Chem from the FINNv2.5 inventory (Fire inventory from NCAR version 2.5) (Wiedinmyer et al., 2011, 2022). FINNv2.5 includes emission estimates of trace gases and particulate matter, based on satellite observations of fire size and burned area from the MODIS and VIIRS instruments. Emissions are provided on a daily resolution and gridded on a 0.1×0.1 global grid. This work also includes oceanic emissions of DMS, based on the emission scheme of Nightingale et al. (2000) and Saltzman et al. (1993), with monthly DMS concentrations derived from the Lana et al. (2011) climatology. DMS chemistry and emissions are not part of the standard WRF-Chem model and have been added in previous work by Marelle et al. (2016, 2017).

2.2.3 WRF-Chem model developments

Currently, halogen chemistry is not included in the chemical gas-phase mechanisms of the main distributed version of WRF-Chem. Several recent studies have worked on developing WRF-Chem by including halogen chemistry and bromine activation to study Arctic ozone depletion events (Herrmann et al., 2021; Marelle et al., 2021). These stud-

ies have included polar bromine emissions and recycling mechanisms from snow and sea ice, based on previous modelling works (Toyota et al., 2011; Yang et al., 2008). Notably, Marelle et al. (2021) was the first study to implement and test descriptions of both surface snow and blowing snow bromine emissions simultaneously in the same 3-D model (WRF-Chem). Briefly, 3-D model descriptions of surface bromine emissions are parameterized as a function of both reactive bromine and ozone deposition fluxes, with different efficiencies under sunlit and dark conditions (Falk and Sinnhuber, 2018; Herrmann et al., 2021; Marelle et al., 2021; Toyota et al., 2011). This approach differs slightly to the one developed in the 1-D model (see Chapter 4) due to limitations in representing surface chemistry and processes in a 3-D model. The version of WRF-Chem published in Marelle et al. (2021) therefore represented the state-of-the-art in regional modelling of Arctic halogen chemistry at the beginning of this thesis and was the basis for all subsequent WRF-Chem model developments in this work.

To investigate the coupled chemical cycles of halogens, ozone, and mercury, several developments to the WRF-Chem model were first needed. The current version of WRF-Chem used does not include any descriptions of mercury chemistry and are therefore added in this work. Mainly, the model developments include: (i) mercury gas-phase and heterogeneous chemistry, (ii) mercury dry and wet deposition, and (iii) mercury re-emission from land-based snow and snow on sea ice. These updates are briefly summarised here and are described in more detail in Chapter 5. The WRF-Chem model version developed in this thesis is publicly available at Ahmed et al. (2022a) (https://doi.org/10.5281/zenodo.7137482). This new model was developed not only for the purposes of this investigation, but to also provide the research community with a tool for future applications in polar mercury studies.

Mercury gas-phase and heterogeneous chemistry

A new mercury chemical mechanism, including gas-phase and heterogeneous redox chemistry, is added to KPP in the WRF-Chem model. This new mechanism, *saprc99_mosaic_8bin_vbs2_aq_mercury*, is an extension of the SAPRC99 mechanism, which also includes halogen chemistry from a recent development of WRF-Chem

Table 2.1: New Hg species added to WRF-Chem 4.3.3. Hg(0) is elemental mercury, Hg(p) is particulate-bound mercury, and HgX represents the unspeciated Hg(II) gas volatilizing from Hg(p) and is treated as a photostable complex ($HgCl_2$).

Hg(0)	HgBr	HgBrO	HgCl
HgClO	HgOH	HgOHO	$HgBr_2$
HgBrOH	$HgBrNO_2$	$HgBrHO_2$	HgBrBrO
HgBrClO	HgBrCl	HgClOH	$HgClNO_2$
$HgClHO_2$	HgClBrO	HgClClO	HgOHOH
$HgOHNO_2$	$HgOHHO_2$	HgOHBrO	HgOHClO
Hg(p)	HgX		

(Marelle et al., 2021). Mercury chemical reactions added here are based on an improved mercury mechanism tested in the global model GEOS-Chem (Shah et al., 2021). The list of newly added mercury species in WRF-Chem is shown in Table 2.1. In total, 26 Hg chemical species are added.

The redox mechanism implemented can be summarized as follows. Hg(0) is oxidized via OH, Br, and Cl to form an intermediate Hg(I) species, which can before be reduced back to Hg(0) (via photoreduction or thermal dissociation), or oxidized to Hg(II). Once a Hg(II) species is formed, this may be deposited to the surface, undergo photoreduction back to Hg(0), or participate in heterogeneous chemistry on aerosols and liquid clouds forming Hg(p). In the particle phase, a fraction of Hg(p) can be volatilized to release Hg(II) in the gas phase. This unspeciated Hg(II) gas is denoted as HgX in the model and is treated as a photostable species. Photolysis rate coefficients for Hg(I) and Hg(II) are calculated with the Fast-J photolysis scheme, using absorption cross sections reported in previous computational studies. The full chemical mechanism developed here is provided online at Ahmed et al. (2022a) (https://doi.org/10.5281/zenodo.7137482). In total, 38 gas-phase, 18 photolysis, and 18 heterogeneous mercury reactions were added in this work.

Mercury deposition

Dry and wet deposition of Hg(0), Hg(p), and all Hg(II) species is included. Hg(0) dry deposition is treated based on the Wesley resistance scheme in WRF-Chem, with relevant parameters and values described in Chapter 5. Dry deposition velocities of Hg(I) are assumed to be zero as these species are unstable and short-lived. Hg(II) and Hg(p) dry deposition velocities are assumed to be 1.0 cm s^{-1} and 0.1 cm s^{-1} respectively, based on observational estimates to snow (Zhang et al., 2009). For wet removal, Hg(II) and Hg(p) are scavenged by both washout and rainout processes, assuming a similar solubility as nitric acid (HNO_3), as in previous modelling studies (Gencarelli et al., 2014).

Hg(0) re-emission from snow and sea ice

Re-emission of Hg(0) from the Arctic snowpack has been measured in multiple studies during spring (Durnford and Dastoor, 2011). Observed re-emission fluxes from snow report large ranges (40–90 % of total deposited mercury re-emitted), with re-emission found to be influenced by several factors, including: solar radiation, snow temperature, chemical composition of snow, and snowpack ventilation. Here, a simplified paramterization is added to describe Hg(0) re-emission from land-based snow and snow on sea ice. Deposited reactive mercury (Hg(II) and Hg(p)) is stored in a surface snow reservoir in the model, and, under sunlit conditions is re-released as Hg(0). The rate of this re-emission is based on reported net reduction rates of oxidized mercury in snow (Durnford and Dastoor, 2011). A temperature threshold of 0 °C is also added, in which re-emission of Hg(0) is only active in grid cells below this temperature. The specific parameterizations developed are described in detail in Chapter 5.

Chapter 3

Modelling air-mass histories to interpret Arctic ozone and mercury observations

Contents

Preface

The first research objective of this thesis is to understand the origin and transport of ozone-depleted and mercury-enriched air masses, based on Arctic observations. This aims to address two key questions relevant for Arctic atmospheric chemistry. First, how are air masses of ozone-depleted air transported in the Arctic and where do they originate from? Second, what are the key emission source regions that explain the summertime peak in Hg(0) concentrations observed in the Arctic? By characterizing the air mass histories arriving at measurement sites, we are able to understand the contribution of different surface types (e.g. land, sea ice, open ocean), and consequently, the potential exposure to emissions and chemistry during transport.

This chapter presents results from two atmospheric transport models, using back trajectory analysis, to understand air mass histories of ozone and mercury observations in the Arctic. Two case studies are explored in this chapter. First, air mass trajectories of ozone measurements from the coastal Arctic in spring 2012 are characterized to assess the origins of ozone-depleted air. Measurement data during periods of background and depleted ozone are separated to examine the origins and emission sensitivity to sea ice. Second, back trajectories from Arctic mercury observations are evaluated to understand the source of the summertime Hg(0) maximum. The work presented in this chapter is based on work contributed to two co-authored publications.

Co-author contributions to:

1. Marelle, L., Thomas, J. L., Ahmed, S., Tuite, K., Stutz, J., Dommergue, A., Simpson, W. R., Frey, M. M., and Baladima, F. (2021). Implementation and impacts of surface and blowing snow sources of Arctic bromine activation within WRF-Chem 4.1.1. *Journal of Advances in Modeling Earth Systems*, 13:e2020MS002391. doi: 10.1029/2020MS002391

2. Araujo, B. F., Osterwalder, S., Szponar, N., Lee, D., Petrova, M. V., Pernov, J. B., Ahmed, S., Heimbürger-Boavida, L.-E., Laffont, L., Teisserenc, R., Tananaev, N., Nordstrom, C., Magand, O., Stupple, G., Skov, H., Steffen, A., Bergquist, B., Pfaff-

huber, K. A., Thomas, J. L., Scheper, S., Petäjä, T., Dommergue, A., and Sonke, J. E. (2022). Mercury isotope evidence for Arctic summertime re-emission of mercury from the cryosphere. *Nature Communications*, 13(1):4956. doi: 10.1038/s41467-022-32440-8

3.1 Introduction to trajectory and particle dispersion modelling

As discussed in Chapter 1, Eulerian and Lagrangian models have different advantages and the selection of a model is largely based on the research question to be investigated. Often, Eulerian and Lagrangian models work complementary to one another. The models described in the previous chapter are based on a Eulerian fixed frame of reference. To understand air mass history however, Lagrangian models are more suited to explore such questions. An extensive review of applying air-mass history analysis to observations can be found in Fleming et al. (2012).

These types of models have been applied in many previous studies to address a broad range of research questions. For example, their application to studying the transport and origin of ozone depleted air masses in the Arctic has been well documented (e.g., Bottenheim and Chan, 2006; Bottenheim et al., 2009; Halfacre et al., 2014; Jacobi et al., 2010). Briefly, there are several types of Lagrangian models available with varying degrees of complexities. The most simple form of Lagrangian model is a trajectory model. This type of model simulates the transport of a particle (or particles) within an air mass which retains its identity along a single line (or trajectory). In this approach, the path of an air mass is determined by the mean wind vector and the effects of turbulent diffusion are neglected. Another type are Lagrangian models are stochastic models, also known as Lagrangian particle dispersion models (LPDMs). LPDMs simulate the transport of air parcels by calculating the random turbulent flow of particles via a stochastic (Markov) process. This method can capture the effects of turbulent diffusion and simulate the random dispersion of thousands of particles. LPDMs are therefore the most sophisticated, but most computationally expensive, type of Lagrangian model. Semi-Lagrangian (or hybrid) approaches also exist in which the transport of particles is simulated using a Lagrangian framework, but, concentrations are calculated in a fixed Eulerian grid.

This chapter presents results from both a hybrid trajectory model and a LPDM. These tools are used to analyze two Arctic cases of ozone and mercury observations, to better understand the influence of (re-)emission sources in the Arctic during their transport to

the measurement sites. First, I describe the case study of Arctic ozone transport during depletion events in spring 2012. Second, I explore air mass histories of summertime Hg(0) observations in the Arctic to characterize the likely source regions for Hg(0) re-emission.

3.2 Depleted ozone air mass origin

The case study presented in this section is part of the published work of Marelle et al. (2021). To provide the context for my contribution in this research study, I introduce the general aims and key results from the paper first. The WRF-Chem model was developed and used to study Arctic ozone depletion events in spring 2012. Bromine and chlorine chemistry were added to the WRF-Chem 4.1.1 model version, as well as polar bromine emissions and recycling mechanisms from snow and sea ice. This study was the first to implement and test descriptions of both surface snow and blowing snow bromine activation simultaneously in the same 3-D model. The model was used to study ozone depletion and bromine chemistry at multiple Arctic sites, including the central Arctic using O-buoy measurements (Halfacre et al., 2014; Knepp et al., 2010; Simpson et al., 2009). Results from this work indicated that both surface snow and blowing snow emissions were important in initiating ODEs, but the surface snow emission mechanism dominated during spring 2012.

The WRF-Chem simulations were performed by the lead author of this study, Louis Marelle. As part of this study, I contributed by performing back trajectory simulations using the Lagrangian particle dispersion model FLEXPART-WRF. The aim of my analysis was to complement the WRF-Chem model results by simulating air mass histories from Utqiaġvik, Alaska, to understand the origins of observed ozone-rich and ozone-depleted air masses. My contribution in this work included setting up FLEXPART-WRF for the specific spring 2012 case, performing the model simulations, and analysing the model output.

3.2.1 FLEXPART-WRF model description

FLEXPART-WRF is an extension of the FLEXPART Lagrangian particle dispersion model (Stohl et al. 2005), driven by meteorological fields from WRF. The model cal-

culates the transport and dispersion of a large number of particles, described as infinitesimally small air parcels, to predict the transport of air in the atmosphere. Each particle (or air parcel) has an associated mass and the model output can be gridded onto a regular grid. The model can be run in two configurations: forward or backward in time

When running FLEXPART-WRF forward in time, particles are released from a single or multiple source locations at a given time or at particular intervals. FLEXPART-WRF then simulates the long-range transport and dispersion of these particles. After a given time, the concentration and distribution of these tracers originating from the point source can be estimated in space on a regular grid. One application of this method is to investigate the transport of a pollution plume from a known source.

Alternatively, the model can be run backward in time to predict air mass history. In this configuration, the point of arrival (receptor) is known and the origin of the air mass (source) is predicted; this is known as a source-receptor relationship. FLEXPART-WRF also computes the potential emission sensitivity (PES), which describes the length of time particles have spent at a particular location as they move backwards in time. This provides information regarding the possible emission contributions an air mass has been exposed to during transport.

3.2.2 FLEXPART-WRF model analysis

FLEXPART-WRF was used in the context of this study to identify the air mass origins of ozone-rich and ozone-depleted air masses, measured at Utqiaġvik, Alaska in spring 2012. Long-term surface measurements of ozone at Utqiaġvik, Alaska are available on an hourly resolution, provided by NOAA-ESRL; https://www.esrl.noaa.gov/gmd/ozwv/surfoz/data.html). In April 2012, several ODEs were observed at Utqiaġvik station (Figure 3.1), followed by periods of ozone recovery. Here, I use FLEXPART-WRF to better understand how the transport and origins of these observed ozone-depleted air masses differ from ozone-rich air. Ozone-depleted air is defined here as periods when measurements of O_3 were below 10 ppbv, and ozone-rich air is when O_3 exceeded 30 ppbv.

The meteorological fields driving FLEXPART-WRF are used from the WRF-Chem

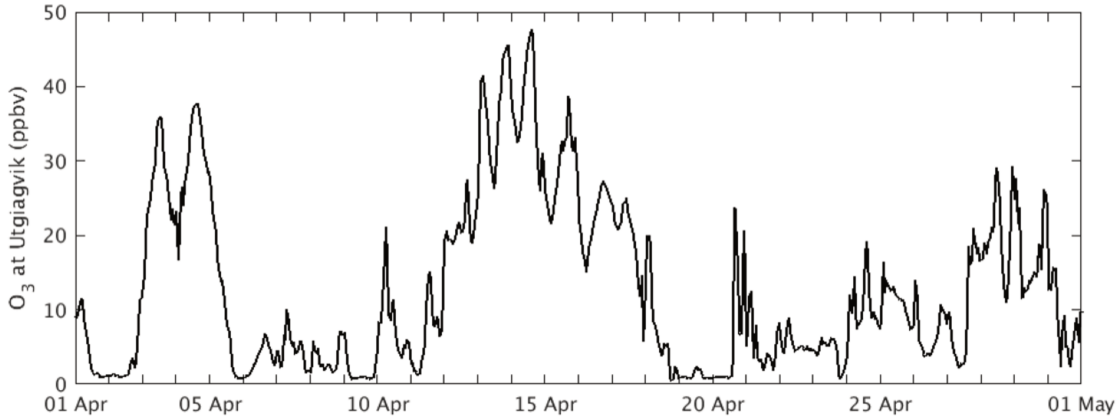

Figure 3.1: Hourly surface O_3 measurements at Utqiaġvik, Alaska between April 1 2012 – May 1 2012. Data obtained from NOAA at https://www.esrl.noaa.gov/gmd/ozwv/surfoz/data.html

simulation. Two back trajectory simulations were performed for April 2012: one for ozone-depleted observations ($[O_3] < 10$ ppbv) and one for ozone-rich observations ($[O_3] > 30$ ppbv). In each case, a fixed number of particles were released for every hour that O_3 measurements were within these thresholds. In total, 100,000 particles were released for each case. For the ozone-depleted simulation, this corresponded to 388 releases. In the ozone-rich case, this included a total of 68 releases. FLEXPART-WRF was then run for 7 days backward in time, from Utqiaġvik, Alaska, to track the origin of air masses and study the source-receptor relationships.

Figure 3.2 shows the mean PES for ozone-depleted (Figure 3.2a) and ozone-rich (Figure 3.2b) air masses, up to 7 days before arriving at the measurement site. For periods when ozone was depleted (Figure 3.2a), the surface (0–100 m) PES column shows that air originated almost exclusively from over sea ice regions. Ozone-depleted air would have therefore been exposed to emissions of bromine from sea ice, as evidenced by the high PES values over sea ice regions. In contrast, for non-depleted periods (Figure 3.2b), the 0-5000 m PES column indicates that high ozone air originated from both land-based and sea ice covered. This also shows that ozone-rich air was subject to long-range transport, having originated from the Canadian Arctic before arriving to the measurement site.

To further understand the vertical origin of these air masses, the mean altitudes of air arriving at Utqiaġvik are evaluated in Figure 3.3 for the two cases. It can be clearly seen

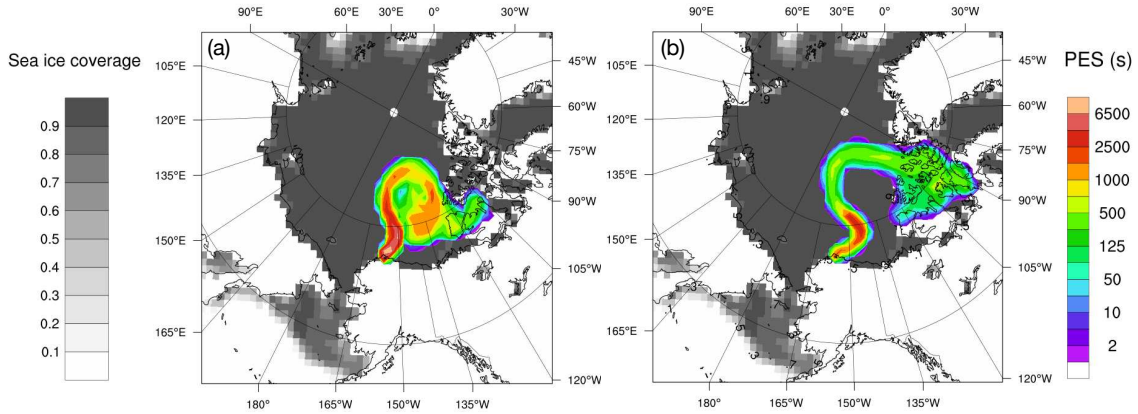

Figure 3.2: FLEXPART-WRF 7-day backwards trajectory potential emission sensitivity (PES). (a) 0–100 m PES for particle releases during depleted ozone ($[O_3] < 10$ ppbv) periods, (b) 0–5000 m PES for particle releases during ozone rich ($[O_3] > 30$ ppbv) periods. WRF-predicted sea ice coverage for April 2012 is shown in grey.

in this figure that the mean altitude of ozone-depleted air (red curve) resided much closer to the surface than the ozone-rich air (blue curve), up to 7 days before arrival. Depleted air was often below 750 m in altitude from the surface for several days prior to measurement, indicating higher sensitivity to surface emissions. Coupled with the PES from Figure 3.2a, it is evident that the arriving air masses were subject to surface emissions from sea ice for several days before measurement. For ozone-rich air, it typically arrived to the measurement site from higher altitudes (up to 1500 m) in the 7 days before observation. This suggests that ozone-rich air was mixed down from the free troposphere and therefore less influenced by emissions from the surface. These results are also in agreement with previous studies, suggesting an important role for the sea ice surface in releasing reactive bromine and depleting ozone (Bottenheim et al., 2009; Halfacre et al., 2014; Jacobi et al., 2010).

3.3 Mercury re-emission source regions

This section is based on contributed analysis to the study of Araujo et al. (2022). Before detailing my individual contributions to this study, I first highlight the context, aims, and key results from the paper.

Observations of Arctic Hg(0) seasonality have regularly recorded springtime minima

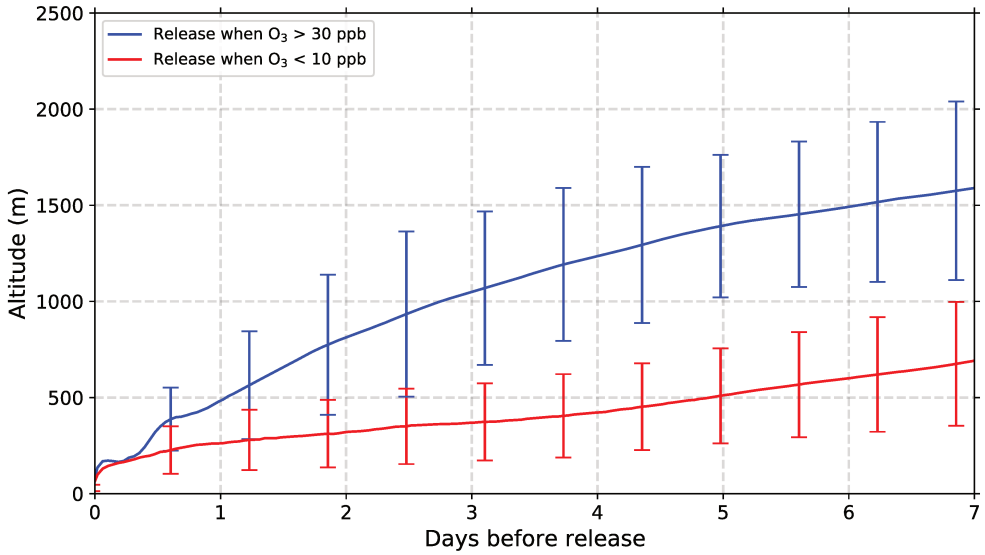

Figure 3.3: FLEXPART-WRF 7-day backwards mean air mass altitude (above sea level) for ozone-rich (blue) and ozone-depleted (red) air. Root-mean-square values are indicated by the error bars.

(during depletion events), followed by a summertime maxima in Hg(0) concentrations (Durnford et al., 2010; Fisher et al., 2012; Skov et al., 2020). The cause of springtime depletion events of Hg(0) have been well established for many years (Brooks et al., 2006; Lindberg et al., 2002; Schroeder et al., 1998; Skov et al., 2004; Wang et al., 2019), however, the origin of the summertime Hg(0) peak is less well understood. Several sources have been proposed to account for the Hg(0) maximum during spring, including: a riverine Hg flux to the Arctic Ocean followed by marine evasion to the atmosphere (Fisher et al., 2012; Sonke et al., 2018; Zhang et al., 2015); Hg(0) re-emission from snow and sea ice following Hg deposition during spring depletion events (Hirdman et al., 2009; Lindberg et al., 2002); and long-range atmospheric transport from Asia to the Arctic (Durnford et al., 2010).

The work of Araujo et al. (2022) aimed to better constrain the sources of the summertime Hg(0) maximum, using an ensemble of Arctic atmospheric Hg(0) measurements. Briefly, isotopic measurements of atmospheric Hg(0) were made between 2018 and 2019 at three Arctic coastal sites (Alert, Villum, and Zeppelin research stations). Observations of Hg(0) at each station recorded increases in summertime atmospheric Hg(0) concentra-

tions, peaking between June and July. High isotopic signatures of Hg(0) associated with AMDEs (e.g. Δ^{199}Hg) were also recorded at the start of the summer period, suggesting a dominant cryospheric Hg(0) source from deposited Hg in spring. To support these findings, I performed an analysis on back trajectory model data from the HYSPLIT model, to characterize the air mass origins during summer 2018. It is important to note that previous studies that suggested a terrestrial source for the Hg(0) summer maximum (Fisher et al., 2012, 2013; Sonke et al., 2018; Steffen et al., 2005; Zhang et al., 2015) did not include back trajectory analysis. Assessing air mass histories can provide additional information regarding the source regions of measurements, as demonstrated in the previous case study with FLEXPART-WRF.

3.3.1 HYSPLIT model description

The HYSPLIT (Hybrid Single Particle Lagrangian Integrated Trajectory) model was used in this work to perform this analysis. HYSPLIT is an atmospheric transport model, developed by NOAA, used to simulate air mass trajectories (Rolph et al., 2017; Stein et al., 2015). It can operate as both a simple trajectory model and a more sophisticated dispersion model. Similar to FLEXPART-WRF, HYSPLIT can be used to compute both back trajectories and forward trajectories, for similar research applications. HYSPLIT is a widely applied model in atmospheric research and simulations can be performed interactively on the web at https://www.ready.noaa.gov/HYSPLIT.php. The model is driven by meteorological input data derived from several sources, including global and regional model data or reanalyses.

3.3.2 HYSPLIT model analysis

Measurements of Hg(0) at Alert, Zeppelin and Villum between 2018 and 2019 were made continuously at a time resolution of 5–15 minutes. Isotopic Hg measurements were also made at the same locations and the mean monthly values for Hg(0) and isotopic Hg are shown in Figure 3.4 (reproduced from Araujo et al. (2022)). In June, mean Hg(0) concentrations in the Arctic were observed to increase (red curve), followed by a peak in July, and a decline beginning in August. The isotopic signature of Δ^{199}Hg is one which

is associated with re-emission from snow, particularly following AMDEs (Sherman et al., 2011). Δ^{199}Hg also exhibits a seasonal variation (black line), with an increase in June, coinciding with the onset of the summer increase in Hg(0) concentrations. To further understand these observations and to characterize the origins of Hg(0)-enriched air in the Arctic, back trajectory analysis using HYSPLIT was performed.

The HYSPLIT simulations were performed by Stefan Osterwalder, running for 10 days backward in time for the months of June, July, and August in 2018. Trajectories were released from each measurement site (Zeppelin, Villum, and Alert) every 2 hours during the sampling periods. HYSPLIT simulations were driven by meteorological input data from the Global Data Assimilation System (GDAS), provided every 3 hours. In Figure 3.5, I analyze the HYSPLIT model output by plotting the air residence maps for the combined back trajectories during June, July, and August 2018 The air residence maps represent the trajectories within the atmospheric boundary layer.

In June, the highest air residence times are clearly located over sea ice and snow covered regions (Figure 3.5d), representing 62 % of air mass origins (see also Figure 3.4a, grey line). This coincides with the rise in measured Hg(0) concentration and the distinct isotopic signatures associated with AMDE re-emissions (Figure 3.4a). During the July peak of Hg(0), air masses begin to shift from sea ice and land-based snow (39 %) to the open ocean close to Greenland (51 %). In August, mean Hg(0) concentrations begin to fall as well the air residence time over sea ice and continental snow (25 %). Importantly, Figures 3.5d–f do not show high residence times of boundary layer air over the Siberian coastal waters, where most terrestrial Hg inputs to the Arctic Ocean occur (Sonke et al., 2018). Therefore, by combining the analyses of air mass histories and the isotopic measurements of Arctic Hg(0) during summer, there is evidence for a cryospheric source of summertime Hg(0) released from deposited Hg during AMDEs in spring.

3.4 Conclusions

The work presented here demonstrates the application of transport and dispersion modelling in two unique case studies. In the each case, I aimed to understand the influence of cryospheric emissions on surface chemical observations made at coastal Arctic sites.

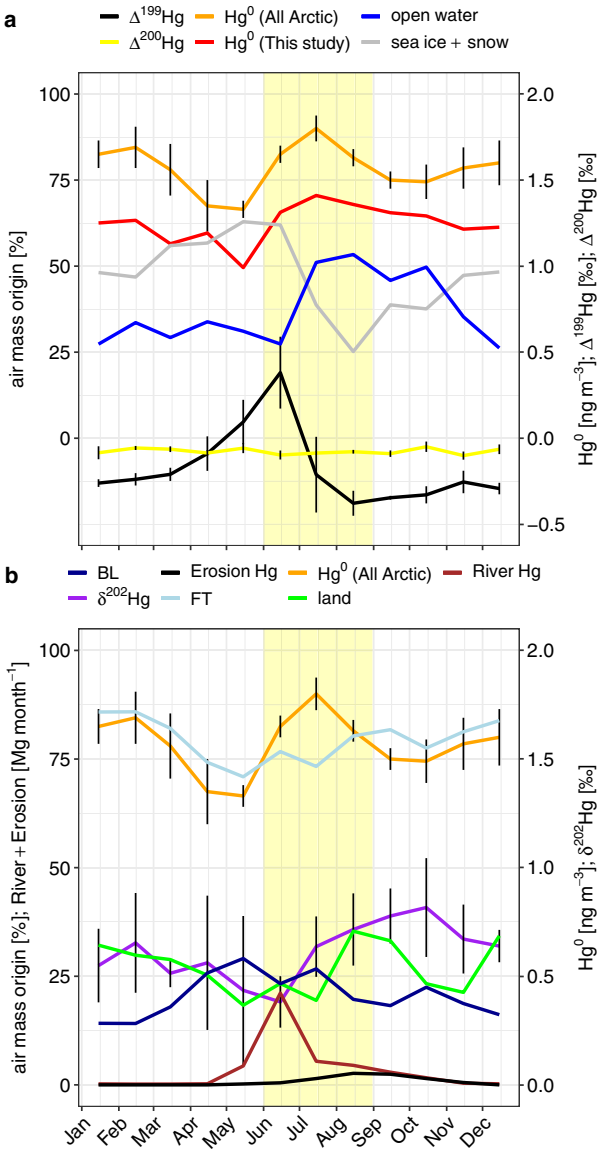

Figure 3.4: Mean monthly Hg in the Arctic and air mass origins. (a) Mean monthly atmospheric Hg(0) observations at Zeppelin (Svalbard), Alert (Canada), and Amderma (Russia) stations between 2000 to 2009 (orange line), mean monthly Hg(0) (red line), Δ^{199}Hg (black line), Δ^{200}Hg (yellow line) concentrations at Zeppelin, Alert, and Villum between 2018 to 2019. The air mass origin contributions, calculated from HYSPLIT 10-day back trajectories, from Zeppelin, Alert, and Villum within the boundary layer over open water (blue line) and sea ice and continental snow (grey line). (b) Mean monthly δ^{202}Hg concentration (purple line), air mass origins over land (green line), free troposphere (light blue line), and the boundary layer (dark blue line). The monthly pan-Arctic Hg inputs from rivers (burgundy line) and coastal erosion (black line). Error bars for Δ^{199}Hg and δ^{202}Hg represent two standard deviations from the mean and Hg(0) error bars represent one standard deviation. Yellow shaded region indicates the summer period. Reproduced from Araujo et al. (2022).

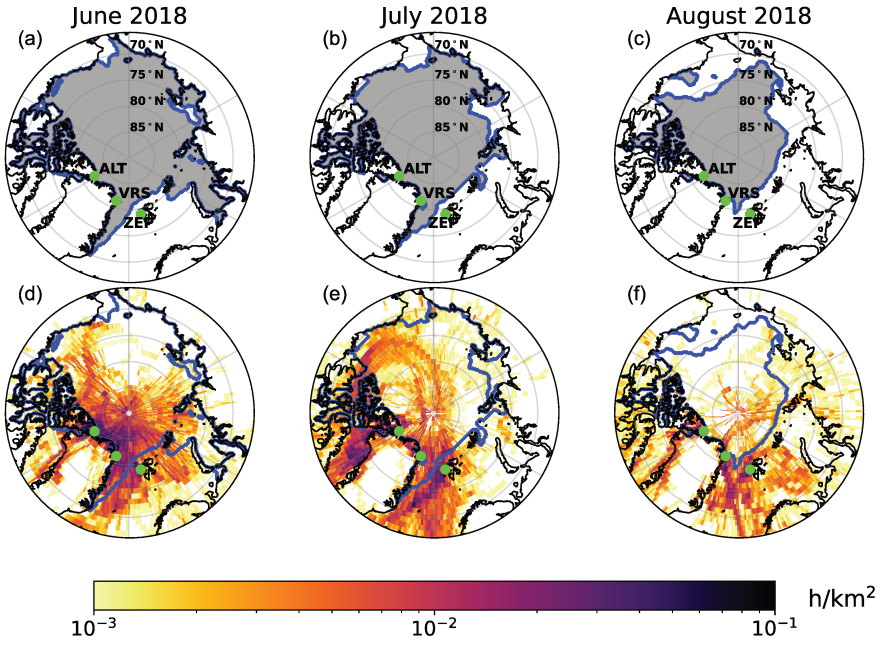

Figure 3.5: (a) – (c) Arctic sea ice extent from June to August 2018 from the National Snow and Ice Data Center (Fetterer et al., 2017). (d) – (f) Air residence maps calculated from combined HYSPLIT 10-day back trajectories from ALT, VRS, and ZEP for June to August 2018. Air residence maps represent trajectories within the boundary layer. ALT = Alert, Canada, VRS = Villum Research Station, Station Nord, Greenland, ZEP = Zeppelin Station, Svalbard.

For ozone, springtime measurements at Utqiaġvik showed several depletion episodes during spring 2012. Using FLEXPART-WRF back trajectory analysis, I characterized the origins of ozone-depleted air masses and found that they originated almost exclusively from sea ice regions. The mean altitude of air depleted in ozone also travelled close to the surface (within 750 m) in the 7 days before arriving at the measurement site. This suggests that these air masses were subject to bromine emissions from sea ice, with little influence from downward mixing of tropospheric air masses. For mercury, the source of the summertime Hg(0) maximum remains an ongoing topic of discussion. The HYSPLIT back trajectory analysis presented here shows a high residence time of boundary layer air over sea ice and snow-covered land, during June (62 %) and July (39 %), when Hg(0) concentrations peak in the Arctic. Moreover, the air residence maps and isotopic evidence do not suggest a large terrestrial source of Hg(0), but support a cryospheric source of re-emitted Hg deposited during AMDEs in spring.

These two cases exemplify the cryosphere-atmosphere interactions, present in the Arctic, that can greatly impact atmospheric chemical composition. Better understanding the contribution of cryospheric emissions to the polar atmosphere is needed to more accurately simulate near-surface atmospheric chemistry. The next two chapters aim to explore how (re-)emission processes of halogens and Hg(0), from snow and sea ice, impact polar boundary layer chemistry.

Chapter 4

The role of snow in controlling halogen chemistry and boundary layer oxidation during Arctic spring: A 1D modelling case study

Contents

Preface

To address research objectives 2 and 3 of this thesis (outlined in Chapter 1), it was necessary to study the links between surface chemistry, where most chemical measurements are made, and the overlying atmosphere. A 1-D model was the tool of choice to answer these questions. However, prior to this investigation, no publicly available 1-D model existed that was able to sufficiently address these research aims. This motivated a need for a publicly available 1-D model, capable of simulating surface chemistry and transport. The two research questions investigated in this chapter are:

- What are the quantifiable impacts of halogen emissions from snow on boundary layer chemistry and oxidative capacity? What combination of emissions, chemistry, and transport can explain surface chlorine and VOC observations in the Arctic?

- What is the vertical extent of bromine and chlorine chemistry in the Arctic boundary layer?

Arctic surface observations made during the 2009 Ocean-Atmosphere-Sea Ice-Snowpack (OASIS) campaign, included a large number of chemical measurements, including halogens and VOCs. In particular, high Cl_2 concentrations were observed during spring ($[Cl_2] > 400$ pptv), indicating a highly reactive surface layer (Liao et al., 2014). However, observations of VOC chemical lifetimes were not consistent with the predicted lifetimes based on the Cl atom concentrations (Hornbrook et al., 2016). This presented an ideal case study to explore the interplay between halogen snow emissions, chemistry, and transport. Finally, the broader goal of this work was to also develop parameterizations of halogen emissions from surface snow that can later be applied and tested in 3-D regional models.

After: Ahmed, S., Thomas, J. L., Tuite, K., Stutz, J., Flocke, F., Orlando, J. J., Hornbrook, R. S., Apel, E. C., Emmons, L. K., Helmig, D., Boylan, P., Huey, L. G., Hall, S. R., Ullmann, K., Cantrell, C. A., and Fried, A. (2022c). The Role of Snow in Controlling Halogen Chemistry and Boundary Layer Oxidation During Arctic Spring: A 1D Modeling

Case Study. *Journal of Geophysical Research: Atmospheres*, 127(5):e2021JD036140. doi: 10.1029/2021JD036140

Abstract

Reactive chlorine and bromine species emitted from snow and aerosols can significantly alter the oxidative capacity of the polar boundary layer. However, halogen production mechanisms from snow remain highly uncertain, making it difficult for most models to include descriptions of halogen snow emissions and to understand the impact on atmospheric chemistry. We investigate the influence of Arctic halogen emissions from snow on boundary layer oxidation processes using a one-dimensional atmospheric chemistry and transport model (PACT-1D). To understand the combined impact of snow emissions and boundary layer dynamics on atmospheric chemistry, we model Cl_2 and Br_2 primary emissions from snow and include heterogeneous recycling of halogens on both snow and aerosols. We focus on a two-day case study from the 2009 Ocean-Atmosphere-Sea Ice-Snowpack (OASIS) campaign at Utqiaġvik, Alaska. The model reproduces both the diurnal cycle and high quantity of Cl_2 observed, along with the measured concentrations of Br_2, BrO, and HOBr. Due to the combined effects of emissions, recycling, vertical mixing, and atmospheric chemistry, reactive chlorine is typically confined to the lowest 15 m of the atmosphere, while bromine can impact chemistry up to and above the surface inversion height. Upon including halogen emissions and recycling, the concentration of HO_x (HO_x = OH+HO_2) at the surface increases by as much as a factor of 30 at mid-day. The change in HO_x due to halogen chemistry, as well as chlorine atoms derived from snow emissions, significantly reduce volatile organic compound (VOC) lifetimes within a shallow layer near the surface.

4.1 Introduction

Halogen chemistry has a large impact on tropospheric chemistry in the polar regions (e.g., Abbatt et al., 2012; Barrie et al., 1988; Oltmans et al., 2012; Simpson et al., 2007, 2015; Steffen et al., 2008, 2013). Recently, new evidence of active Arctic chlorine chemistry has been attributed mainly to photochemical activation of chloride present in surface snow (Custard et al., 2017; Liao et al., 2014). Molecular chlorine (Cl_2) and nitryl chloride ($ClNO_2$), emitted from snow and aerosols, are sources of atomic chlorine (Cl) following

their photolysis (McNamara et al., 2019, 2021). The highly reactive nature of Cl atoms makes it important even in trace amounts as Cl atoms react with volatile organic compounds (VOCs) up to three orders of magnitude faster than the more abundant hydroxyl radical (OH) (Atkinson et al., 2006). Active chlorine chemistry occurs simultaneously with reactive bromine chemistry each spring (e.g., Abbatt et al., 2012; Barrie et al., 1988; Simpson et al., 2007, 2015). The latter causes both ozone (O_3) and mercury depletion (Hg^0) in the lowest part of the atmosphere (e.g., Oltmans et al., 2012; Steffen et al., 2008, 2013).

Halogens in the Arctic atmosphere ultimately originate from the ocean as halides (Cl^- and Br^-), which are activated on salty surfaces such as snow on sea ice, continental snow and aerosols (Abbatt et al., 2012). Chlorine and bromine species impact atmospheric chemistry within the polar boundary layer via reactions (R4.1)–(R4.9) (where X, Y = Cl or Br) (Abbatt et al., 2012; Simpson et al., 2015). Cl_2 photolyzes very quickly during the day (R4.1), with a photolysis lifetime of approximately 10 minutes, producing Cl atoms that rapidly react with ozone (R4.2) or VOCs (including methane) ((R4.3) and (R4.4)) (Atkinson et al., 2006). Reactions (R4.3) and (R4.4) constitute the major reaction pathways of Cl atoms (Platt and Hönninger, 2003). This produces organic peroxy radicals (RO_2), including the methylperoxy radical (CH_3O_2), which ultimately contribute to hydroperoxyl radical formation (HO_2). HO_2 production, driven by chlorine chemistry, can impact HO_x chemistry (HO_x = OH+HO_2) by decreasing the OH/HO_2 ratio, as well as affecting the reactive bromine cycle (Piot and von Glasow, 2009; Rudolph et al., 1999; Thompson et al., 2015). Molecular bromine (Br_2) is photolyzed very rapidly (photolysis lifetime $<$ 1 minute) to produce bromine atoms (Br) which can lead to efficient ozone destruction and formation of bromine monoxide (BrO) (Wang et al., 2019). However, Br atoms react appreciably only with a few specific VOCs such as ethyne and the aldehydes and not with methane ((R4.3) and (R4.4) only occur for Cl). Br atoms can also react with elemental mercury to deplete near-surface atmospheric $Hg_{(0)}$ levels and produce more reactive forms of mercury (Hg(II)) (Steffen et al., 2008, 2013; Wang et al., 2019). Subsequent reaction of BrO with HO_2 forms HOBr (R4.5), which can be photolyzed to re-form Br and OH (R4.6). The net result of reactions (R4.5) and (R4.6) is the regenera-

tion of a Br atom, which can facilitate further ozone depletion, and the conversion of HO_2 to OH, increasing the oxidative capacity of the atmosphere. At high BrO concentrations, Br_2 is also regenerated in the gas phase via self-reaction of BrO (R4.7).

$$X_2 \xrightarrow{h\nu} 2X \tag{R4.1}$$

$$X + O_3 \rightarrow XO + O_2 \tag{R4.2}$$

$$Cl + RH + O_2 \rightarrow RO_2 + HCl \tag{R4.3}$$

$$Cl + CH_4 \rightarrow CH_3 + HCl \tag{R4.4}$$

$$XO + HO_2 \rightarrow HOX + O_2 \tag{R4.5}$$

$$HOX \xrightarrow{h\nu} X + OH \tag{R4.6}$$

$$BrO + BrO \rightarrow Br_2 + O_2 \tag{R4.7}$$

Figure 4.1a highlights the typical diurnal behaviour of surface molecular halogen concentrations, snow emissions, solar radiation, and the boundary layer height observed during Arctic spring. Measured diurnal cycles of Cl_2 have shown a double-peaked profile, with peaks in the morning and late afternoon, followed by concentrations dropping below 0.8 parts per trillion by volume (pptv) after midnight (Custard et al., 2016; Liao et al., 2014; McNamara et al., 2019). At sunrise, increased solar radiation drives photochemistry within the snow interstitial air which leads to the release of halogens to the overlying atmosphere via diffusion and wind pumping (Bartels-Rausch et al., 2014; Grannas et al., 2007; Pratt et al., 2013; Thomas et al., 2011; Toyota et al., 2014b). Boundary layer mixing modulates surface Cl_2 concentrations, with Cl_2 decreasing during the day due to a combination of its fast photolytic loss (R4.1) and the effects of boundary layer mixing. Solar heating of the lower atmosphere can cause turbulent mixing of the surface layer, mixing species away from the surface, and increasing the height of the boundary layer (Anderson and Neff, 2008). Low light conditions (i.e., night and early morning) cause a reduction in the photochemical loss of Cl_2 (R4.1) and a collapse of the boundary layer. This effect has previously been demonstrated to drive evening increases of reactive nitrogen species

(NO_x = NO + NO_2) at the surface in both the Arctic and Antarctic (Frey et al., 2015; Honrath et al., 1999, 2002; Thomas et al., 2011).

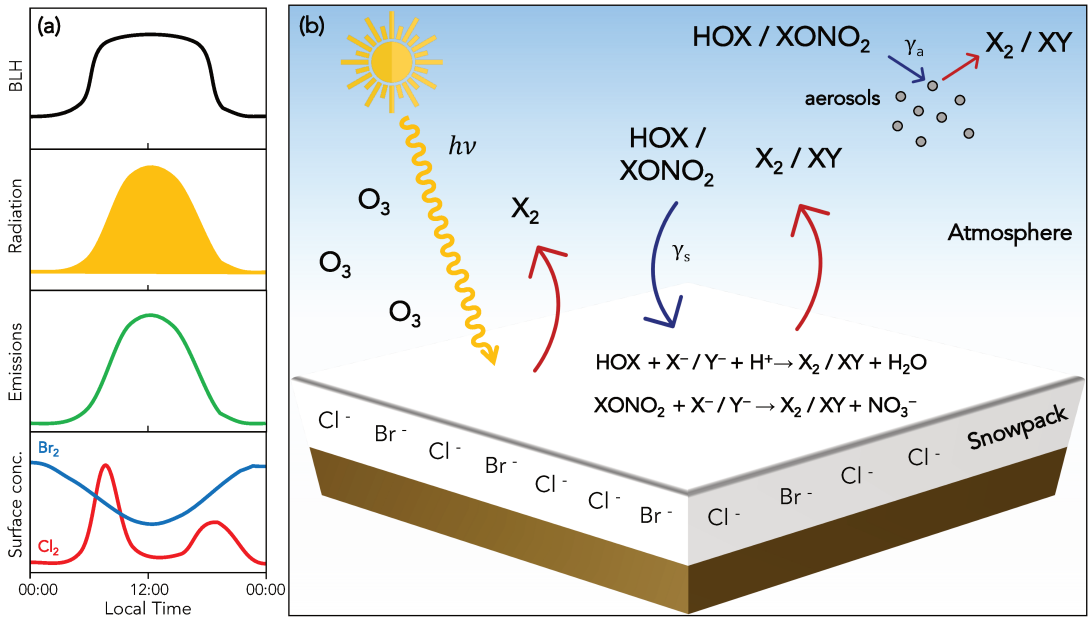

Figure 4.1: (a) Diurnal evolution of boundary layer height (BLH), solar radiation, chemical snowpack emissions, and surface concentrations of Cl_2 and Br_2 for an "average" day in the Arctic during spring (not drawn to scale). (b) Schematic of key polar halogen emissions from the continental snowpack (X = Cl, Br). Blue arrows represent loss processes and red arrows indicate production. Primary production of halogens is based on ozone and the availability of sunlight. Molecular halogens are also emitted via surface snow and aerosol recycling reactions, dependent on the heterogeneous reactive uptake coefficients γ_s and γ_a, on surface snow and aerosols, respectively.

Figure 4.1b illustrates some of the key known emission sources of halogens from surface snow in the Arctic. Heterogeneous reactions involving hypohalous acids (e.g., HOCl and HOBr) (R4.8) and halogen nitrates (e.g., $ClONO_2$ and $BrONO_2$) (R4.9), have been recognized as a source of molecular halogens on halide-containing snow and aerosol surfaces (Aguzzi and J. Rossi, 1999; Deiber et al., 2004; Finlayson-Pitts et al., 1989; Hu et al., 1995; Pratte and Rossi, 2006). Bromine chloride (BrCl) is another product formed via reactions (R4.8) and (R4.9) on snow and aerosols, linking the chlorine and bromine chemical cycles (McNamara et al., 2020). BrCl can then be photolyzed, re-forming Br and Cl atoms, as in reaction (R4.1).

$$HOX + X^-/Y^- + H^+ \xrightarrow{\text{surface}} X_2/XY + H_2O \qquad \text{(R4.8)}$$

$$XONO_2 + X^-/Y^- \xrightarrow{\text{surface}} X_2/XY + NO_3^- \quad \text{(R4.9)}$$

At present, detailed descriptions of chlorine snow emissions remain absent from most 3D numerical models. Bromine mechanisms are included in some 3D models, but remain under discussion as to the source and recycling mechanisms involving snow (Falk and Sinnhuber, 2018; Fernandez et al., 2019; Herrmann et al., 2021; Marelle et al., 2021; Toyota et al., 2011). Snow is a very complex photochemical medium and the release of halogens is determined by many uncertain processes/variables, including: snow physics; snow/ice chemistry (including photochemistry); gas transport within snow; and impurity concentrations and locations (Bartels-Rausch et al., 2014; Domine et al., 2008; Grannas et al., 2007; McNeill et al., 2012). As a result, modelling snow-covered environments using a first principles approach remains challenging and uncertain (Domine et al., 2013). Zero-dimensional box models are often used to study the effects of halogens on boundary layer chemistry under Arctic conditions (Custard et al., 2015; Liao et al., 2012b, 2014; McNamara et al., 2020; Piot and von Glasow, 2009; Thompson et al., 2015; Wang and Pratt, 2017). An inherent limitation of 0D models, however, is the absence of the vertical dimension necessary for simulating vertical transport and capturing concentration gradients in the atmosphere. Additionally, the physical conditions that characterise the polar regions (low temperatures, limited sunlight during winter, high albedo, etc.) can often create stable low-level temperature inversions resulting in shallow boundary layers (Kahl, 1990). This can greatly impact the vertical distribution of chemical species by acting as a barrier to vertical mixing and transport. One-dimensional models are therefore extremely useful tools which can include these processes to help us better understand the interactions between snow and the atmosphere (Cao et al., 2016; Herrmann et al., 2019; Lehrer et al., 2004; Piot and von Glasow, 2008; Thomas et al., 2011, 2012; Toyota et al., 2014b; Wang et al., 2020).

The first observations of high Cl_2 levels within the Arctic boundary layer were reported in spring 2009, during the Ocean-Atmosphere-Sea Ice-Snowpack (OASIS) campaign at Utqiaġvik, Alaska (Liao et al., 2014). Cl_2 mixing ratios of up to 400 pptv were observed and an average noontime Cl atom concentration of 2×10^5 atoms cm^{-3} was estimated from these observations. Daytime Cl_2 mixing ratios were highly correlated with sunlight

and surface ozone levels (r^2 value = 0.86), indicating both are key requirements for Cl_2 production. Measurements of VOCs made during the campaign showed a clear impact of chlorine chemistry on VOC oxidation processes (Hornbrook et al., 2016). Measurement-derived estimates of Cl atom concentration suggested the presence of a highly reactive surface layer, which led to an overprediction of VOC production and loss rates compared to the observations (Hornbrook et al., 2016). Interactions between radical chemistry, atmospheric mixing, and snow emissions need to be better understood in order to fully explain these observations and the impacts of halogens on boundary layer oxidation processes.

In this work, we address the following questions:

1. What combination of factors, including vertical mixing, land-based snow emissions/recycling, and chemistry explain observations of halogens in the Arctic surface layer?

2. How are halogens vertically distributed within the polar boundary layer?

3. What is the impact of halogen chemistry on boundary layer oxidation processes as a function of altitude?

We answer these questions using an updated version of the Platform for Atmospheric Chemistry and vertical Transport in 1-dimension (PACT-1D) model (Tuite et al., 2021), which includes descriptions of halogen chemistry, emissions, and recycling. We compare our model with surface measurements of chemical species, including Cl_2 and Br_2, recorded during the 2009 OASIS campaign at Utqiaġvik, Alaska. In section 4.2, we introduce the measurements used from the campaign and the new model halogen updates are described in section 4.3. The model configuration used in this work is presented in section 4.4, followed by the model results and a discussion in section 4.5. Finally, the conclusions and perspectives are presented in section 4.6.

4.2 OASIS 2009 campaign measurements

In this study, we use measurements taken during the OASIS campaign, which was conducted between March and April 2009 near Utqiaġvik, Alaska. The measurement site was located approximately 5.5 km northeast of the town of Utqiaġvik (71.323 N, 156.663 W; 8 m above sea level) and was chosen for the prevailing northeasterly winds arriving from over the Beaufort Sea. A map of the study site can be found in Boylan et al. (2014) and Hornbrook et al. (2016). Observations from this campaign were chosen due to the extensive chemical and meteorological measurements available, including direct measurements of Cl_2, Br_2, BrO, and a large number of VOCs. A summary of the measurements used in this study is given in Table 4.1 with the respective instruments/techniques used during OASIS. Meteorological measurements (temperature, winds, relative humidity) were made from two tower stations set up at the field site at several heights. At one of the tower stations, turbulent flux measurements were made using ultrasonic anemometers located at 4 heights (0.6 m, 1.8 m, 3.2 m, and 6.2 m above ground level (AGL)). Inorganic halogens (including Cl_2, Br_2, BrO and HOBr), as well as OH and HO_2, were measured using chemical ionization mass spectrometers (CIMS) at 1.5 m AGL (Hornbrook et al., 2011; Liao et al., 2011, 2012b, 2014; Mauldin III et al., 1998; Tanner et al., 1997). Surface ozone and NO_x measurements were made using a chemiluminescence instrument on a second tower station, operated by the National Center for Atmospheric Research (NCAR), at 3 different heights (0.6 m, 1.5 m and 5.4 m AGL) (Helmig et al., 2012; Villena et al., 2011; Weinheimer et al., 1998). Additionally, measurements of formaldehyde (HCHO) made by a Difference Frequency Generation Tunable Diode Laser Absorption Spectrometer (Barret et al., 2011; Weibring et al., 2007, 2010), and 18 VOCs measured by a Trace Organic Gas Analyzer (TOGA) (Hornbrook et al., 2016) were made at these same heights. Balloon soundings were also launched during the campaign to record vertical profiles of ozone (Helmig et al., 2012; Oltmans et al., 2012). Carbon monoxide (CO) measurements were made using a CO infrared absorption analyzer (Parrish et al., 1994). Aerosol physical properties (size distribution and number concentration) were measured using an optical particle counter and two scanning mobility particle sizers (Woo et al., 2001). Finally, actinic flux measurements made by CCD Actinic Flux Spectroradiomet-

Table 4.1: Measurements from the OASIS 2009 campaign used in this study.

Measurement	Method	Reference
Meteorology and turbulent fluxes	Ultrasonic anemometers	Boylan et al. (2014)
Cl_2, Br_2, BrO, HOBr	Chemical Ionization Mass Spectrometers (CIMS)	Liao et al. (2011, 2012b, 2014)
OH, HO_2	Chemical Ionization Mass Spectrometers (CIMS)	Hornbrook et al. (2011), Mauldin III et al. (1998), Tanner et al. (1997)
NO, NO_2, O_3	Chemiluminescence	Helmig et al. (2012), Villena et al. (2011), Weinheimer et al. (1998)
HCHO	Difference Frequency Generation Tunable Diode Laser Absorption Spectrometer	Weibring et al. (2007, 2010)
CO	IR absorption CO analyzer	Parrish et al. (1994)
VOCs[a]	Trace Organic Gas Analyzer (TOGA)	Hornbrook et al. (2016)
Aerosol number density and radius	Optical Particle Counter (OPC) and Scanning Mobility Particle Sizers (SMPS)	Woo et al. (2001)
Actinic flux	CCD Actinic Flux Spectroradiometers (CAFS)	Shetter and Müller (1999)

[a]See Table 1 in Hornbrook et al. (2016)

ers (CAFS) were used to calculate photolysis frequencies of 35 different reactions using a modified version of the Tropospheric Ultraviolet and Visible (TUV) radiation model version 4.4 (Madronich and Flocke, 1999; Shetter and Müller, 1999). Data from this campaign are available through the National Science Foundation (NSF) Arctic Data Center at https://arcticdata.io/ (Apel, 2009; Cantrell, 2009; Fried, 2009; Guenther, 2009; Hall, 2009; Smith et al., 2009; Weinheimer, 2009).

4.3 Description of halogen chemistry within PACT-1D

The Platform for Atmospheric Chemistry and vertical Transport in 1-Dimension (PACT-1D) is the vertical column model used in this work to study Arctic halogen emissions and

their impact on oxidation processes during the OASIS campaign. A full description of this model is given in Tuite et al. (2021). Chlorine and bromine gas-phase and heterogeneous reactions are added to this version of the model. Snow emissions and recycling mechanisms of chlorine and bromine have also been implemented and are described in the following sections.

4.3.1 Gas-phase and aerosol heterogeneous halogen chemistry

We update the existing PACT-1D mechanism to include additional chlorine and bromine gas-phase and heterogeneous reactions. The chemical mechanism in PACT-1D is based on the Regional Atmospheric Chemistry Mechanism version 2 (RACM2) (Goliff et al., 2013) using the Kinetic PreProcessor (KPP) (Sandu and Sander, 2006). The additional gas-phase bromine reactions are added following the implementation of Marelle et al. (2021) and are listed in the model chemical mechanism (Ahmed et al., 2022b). Reactive and non-reactive heterogeneous uptake reactions of halogens on aerosols are also added to the model (Table 4.2). We do not include a full description of aerosol aqueous-phase chemistry within the model. We track particulate chloride and bromide as separate species that undergo heterogeneous chemistry to ensure mass balance, which are tracked in the model. We do this by first initialising the concentration of aerosol-phase chloride and bromide to the chloride and bromide concentrations in fresh sea salt aerosols and then track release and reactive and non reactive uptake. Second-order heterogeneous reactions consuming aerosol-phase halide ions are treated as pseudo first-order reactions, following Marelle et al. (2021), maintaining mass conservation of each species.

4.3.2 Snow emission and recycling of Cl_2 and Br_2

Emissions of molecular halogens from snow have been identified as a key source of Arctic halogen production (Custard et al., 2017; Pratt et al., 2013). Cl_2 and Br_2 production from continental snow have been reported to be a function of both solar radiation and ozone concentration (Custard et al., 2017; Liao et al., 2014; Liu et al., 2017). Halogen species deposited to the snow surface can also undergo recycling mechanisms to re-emit reactive halogens back into the atmosphere (Abbatt et al., 2012; Toyota et al., 2011). We therefore

Table 4.2: Heterogeneous reactions and reaction uptake coefficients on aerosols (γ_a).

Reaction	Heterogeneous reactive uptake (γ_a)	Reference
$HOCl + Cl^-_{(aq)} \rightarrow Cl_2$	2×10^{-4}	Ammann et al. (2013)
$HOCl + Br^-_{(aq)} \rightarrow BrCl$	2×10^{-4}	Ammann et al. (2013)
$ClONO_2 + Cl^-_{(aq)} \rightarrow Cl_2 + HNO_{3(aq)}$	0.03	Aguzzi and J. Rossi (1999)
$ClONO_2 + Br^-_{(aq)} \rightarrow BrCl + HNO_{3(aq)}$	0.05	Aguzzi and J. Rossi (1999)
$ClONO_2 \rightarrow HOCl + HNO_{3(aq)}$	0.03	Aguzzi and J. Rossi (1999)
$HOBr + Br^-_{(aq)} \rightarrow Br_2$	0.05	Pratte and Rossi (2006), IUPAC (2009)
$HOBr + Cl^-_{(aq)} \rightarrow BrCl$	0.05	Pratte and Rossi (2006), IUPAC (2009)
$BrONO_2 + Br^-_{(aq)} \rightarrow Br_2$	0.06	Deiber et al. (2004)
$BrONO_2 + Cl^-_{(aq)} \rightarrow BrCl$	0.04	Deiber et al. (2004)
$BrONO_2 \rightarrow HOBr + HNO_{3(aq)}$	0.04	Deiber et al. (2004)
$N_2O_5 + Cl^-_{(aq)} \rightarrow ClNO_2 + HNO_{3(aq)}$	0.02	Burkholder et al. (2019)
$N_2O_5 + Br^-_{(aq)} \rightarrow BrNO_2 + HNO_{3(aq)}$	0.011	Seisel et al. (1998)
$Cl_2 + Br^-_{(aq)} \rightarrow BrCl + Cl^-_{(aq)}$	0.2	Burkholder et al. (2019)
$OH + HCl \rightarrow 0.5 * Cl_2$	0.1	Knipping et al. (2000), Laskin et al. (2006)

add four parameterizations to describe emissions of chlorine and bromine in this version of PACT-1D. We include (1) an emission of chlorine and bromine as a function of the available solar radiation and the surface ozone concentration, and (2) a recycling source of X_2 from the surface conversion of $XONO_2$ and HOX (where X = Cl, Br) on snow. In both cases, the exact parameterizations are determined by comparing modelled and observed halogen concentrations.

The emission of chlorine is parameterized as follows:

$$E^{primary}_{Cl_2} = F_{(p,Cl)} \times (J_{Cl_2})^{0.5} \times [O_3] \tag{4.1}$$

$$E_{\mathrm{Cl_2}}^{recycling} = \gamma_{(snow,\mathrm{Cl})} \times (D_{\mathrm{ClONO_2}} + D_{\mathrm{HOCl}}) \tag{4.2}$$

where $E_{\mathrm{Cl_2}}^{primary}$ and $E_{\mathrm{Cl_2}}^{recycling}$ are the snow emission fluxes of Cl_2, $F_{(p,\mathrm{Cl})}$ is a correction factor which includes a scaling term and the height of the lowest model level (0.01 cm) in units of cm $s^{-\frac{1}{2}}$, $J_{\mathrm{Cl_2}}$ is the calculated photolysis rate of Cl_2, $[O_3]$ is the measured O_3 concentration (in molec cm^{-3}), $\gamma_{(snow,\mathrm{Cl})}$ is the probability of heterogeneous conversion on snow to re-form Cl_2 (between 0 and 1), and $D_{\mathrm{ClONO_2}}$ and D_{HOCl} are the model-calculated deposition rates of $ClONO_2$ and HOCl, respectively. In the case of primary chlorine emissions (equation (4.1)), different values of $F_{(p,\mathrm{Cl})}$ were tested in order to reproduce the Cl_2 measurement data in the model (Figure A.1). Observed ambient concentrations of Cl_2 showed a double peaked profile, with an increase in the early morning following sunrise, and a second peak in the late afternoon before falling to almost zero at night. The best-fit primary emission flux for chlorine is found to be a function of $J_{\mathrm{Cl_2}}$ to the power of 0.5, with $F_{(p,\mathrm{Cl})} = 0.2$ cm $s^{-\frac{1}{2}}$. It is also well known that $ClONO_2$ and HOCl are converted on ice surfaces to re-form Cl_2 (IUPAC, 2009). However, within snow there are a number of complex physical and chemical processes that make these recommendations not directly applicable for snow. We therefore performed a series of sensitivity tests varying $\gamma_{(snow,\mathrm{Cl})}$ between 0 and 1, and found the best fit value of 0.1 for chlorine recycling on snow (Figure A.2).

For bromine, the emission sources are described as:

$$E_{\mathrm{Br_2}}^{primary} = F_{(p,\mathrm{Br})} \times J_{\mathrm{Br_2}} \times [O_3] \tag{4.3}$$

$$E_{\mathrm{Br_2}}^{recycling} = \gamma_{(snow,\mathrm{Br})} \times (D_{\mathrm{BrONO_2}} + D_{\mathrm{HOBr}}) \tag{4.4}$$

where $E_{\mathrm{Br_2}}^{primary}$ and $E_{\mathrm{Br_2}}^{recycling}$ are the snow emission fluxes of Br_2, $F_{(p,\mathrm{Br})}$ is a correction factor which includes a scaling term and the height of the lowest model level (0.01 cm) in units of cm, $J_{\mathrm{Br_2}}$ is the calculated photolysis rate of Br_2, $\gamma_{(snow,\mathrm{Br})}$ is the heterogeneous conversion efficiency on snow to re-form Br_2 (between 0 and 1), and $D_{\mathrm{BrONO_2}}$ and D_{HOBr} are the model-calculated deposition rates of $BrONO_2$ and HOBr, respectively. For brom-

ine, we found that the observations of bromine species are best described using primary emissions (equation (4.3)) as a function of J_{Br_2}, with $F_{(p,Br)} = 0.01$ cm (equivalent to the lowest model level height and a scaling factor of 1). The conversion of $BrONO_2$ and HOBr on ice to re-form Br_2 is known to be more efficient than for chlorine (IUPAC, 2009), which in part facilitates the well known bromine explosion chemistry (Abbatt et al., 2012). We tested a range of possible conversion efficiencies for these reactions and found $\gamma(snow, Br) = 0.6$ best reproduces the observations (Figure A.3). For both equations (4.2) and (4.4), it is assumed that there is an infinite supply of Cl^- and Br^- in the snow. We do not include conversion of N_2O_5 on snow to form reactive bromine and chlorine due to the low NO_x concentrations compared to pollution influence.

There are large uncertainties in describing both the primary emission flux (equations (4.1) and (4.3)) from land-based snow, as well as the recycling of both bromine and chlorine species on snow (equations (4.2) and (4.4)), which must be considered in future work that use or further refine these parameterizations. First, there are significant uncertainties in vertical transport near the snow surface and in the lowest portion of the atmosphere (∼below 10 m). Therefore, as future work refines our knowledge of these vertical transport processes, we will need to revisit the values used for $F_{(p,Cl)}$, $F_{(p,Br)}$, $\gamma_{(snow,Cl)}$ and $\gamma_{(snow,Br)}$. Secondly, the main factors driving molecular halogen production from the snowpack are still highly uncertain, with more work needed to improve our understanding. In addition, descriptions of halogen emissions from land-based snow within 3D models remain limited. Bromine emissions triggered from ozone deposition to snow on sea ice is the main process considered by the bromine emissions/recycling scheme of Toyota et al. (2011). Here, we use ambient ozone concentrations rather than ozone deposition as the trigger for both bromine and chlorine on land-based snow, as suggested from observations. Our equations can be re-formulated as a function of the ozone deposition rate (which is directly dependant on ozone concentration) to be more consistent with equations proposed for snow on sea ice. Finally, production of BrCl from Arctic snow has been measured following irradiation of the snowpack, with multiphase reactions on snow also predicted to be significant contributors of BrCl production (Custard et al., 2017; McNamara et al., 2020). However, flux estimates of BrCl from snow remain

uncertain and measurements of BrCl were not available during our selected simulation period (see section 4.4.1). We therefore only include BrCl production via heterogeneous reactions on aerosols (Table 4.2), but, this must be updated in future work to also include BrCl emissions from continental snow.

4.4 Model setup

4.4.1 Selection of OASIS simulation period

The model was set up for the dates of 18 – 19 March 2009 during the campaign; these dates were selected due to the high Cl_2 concentrations recorded and the limited influence from local pollution sources (Figure A.4). The average daytime (06:00-20:00) Cl_2 mixing ratio for the two days was 59 pptv and surface ozone levels remained above 10 parts per billion by volume (ppbv), indicating that there was not a major ozone depletion event during this period. Ozonesonde data from profiles launched at the start and just after our modelling case study showed that ozone was well distributed within the lower atmosphere with no significant ozone gradients as a function of altitude (Figure 4c in Oltmans et al. (2012) and Figure 13a in Helmig et al. (2012)). Average background levels of NO_x and CO over the entire campaign were recorded at $\sim$ 84 pptv and $\sim$ 160 ppbv, respectively (Villena et al., 2011). Measurements of NO_x and CO between 18 – 19 March do not suggest polluted conditions, with CO levels close to the average background measurements ($\sim$ 160 ppbv), however NO_x levels were above the average background levels (50 – 500 pptv). Influence from nearby anthropogenic sources was likely to be minimal during this period as winds arriving at the measurement site originated from the Arctic Ocean (north through northeast) for most of 18 and 19 March. Considering these criteria, the period between 18 – 19 March best met the requirements for our modelling case study.

Figure 4.2a and 4.2b show the state of sea ice north of Utqiaġvik, on the 18 and 19 March, respectively. A key feature of Figure 4.2a and 4.2b is the presence of sea ice leads close to the measurement site. Sea ice leads are visible on both days which are important as they can induce convective mixing of air masses, impacting the concentration of species recorded at the measurement site (Moore et al., 2014). This has been shown

to replenish ozone-depleted air masses to near-background concentrations (Moore et al., 2014) as well as influencing the vertical distribution of BrO by mixing it higher in the atmosphere (Simpson et al., 2017).

4.4.2 Model configuration

We set up the vertical model grid (Figure 4.3a) using a total of 112 levels, with a logarithmic spacing for the lowest 1 m of the grid down to a lower boundary of 1×10^{-4} m. The model levels are linearly spaced up to 100 m, by 1-m increments, followed by a non-linear spacing to an upper boundary of 3000 m. This highly resolved vertical model grid allows us to analyse the impacts of halogen emissions on chemistry very close to the surface.

The 1D model is driven by input data obtained from the measurements (where possible), model output data and calculated explicitly from parameterizations. The atmospheric dynamics (temperature, pressure, relative humidity) are calculated using the 3D Weather Research and Forecasting (WRF) meteorological model (Skamarock et al., 2019) for Utqiaġvik, Alaska, and used to drive the 1D model physics in combination with the OASIS ground measurements. We use a WRF set up specifically optimised for the Arctic, described in Marelle et al. (2017), with the model domain centered at Utqiaġvik (domain shown in Figure 4.3b). A horizontal resolution of 25 km $\times$ 25 km is used with a vertical resolution of 50 levels, up to a pressure of 50 hPa. To validate the use of the WRF simulated meteorology, we compare WRF calculated temperatures at Utqiaġvik with surface measurements from OASIS and available vertical temperature profiles in Figure 4.4. The Integrated Global Radiosonde Archive (IGRA, Durre et al. (2006)) provides radiosonde data twice a day at 00:00 and 12:00 UTC (15:00 and 03:00 AKST, UTC-9, respectively) which we use to compare with our model results. Figure 4.4 shows that we are able to obtain very good agreement of both the surface and vertical temperature profiles in WRF compared to the observations.

The eddy diffusion coefficients (K_z) in the model are calculated following the parameterization described in Cao et al. (2016) and used in Herrmann et al. (2019). We calculate these values as measurement data of eddy diffusion coefficients during this period

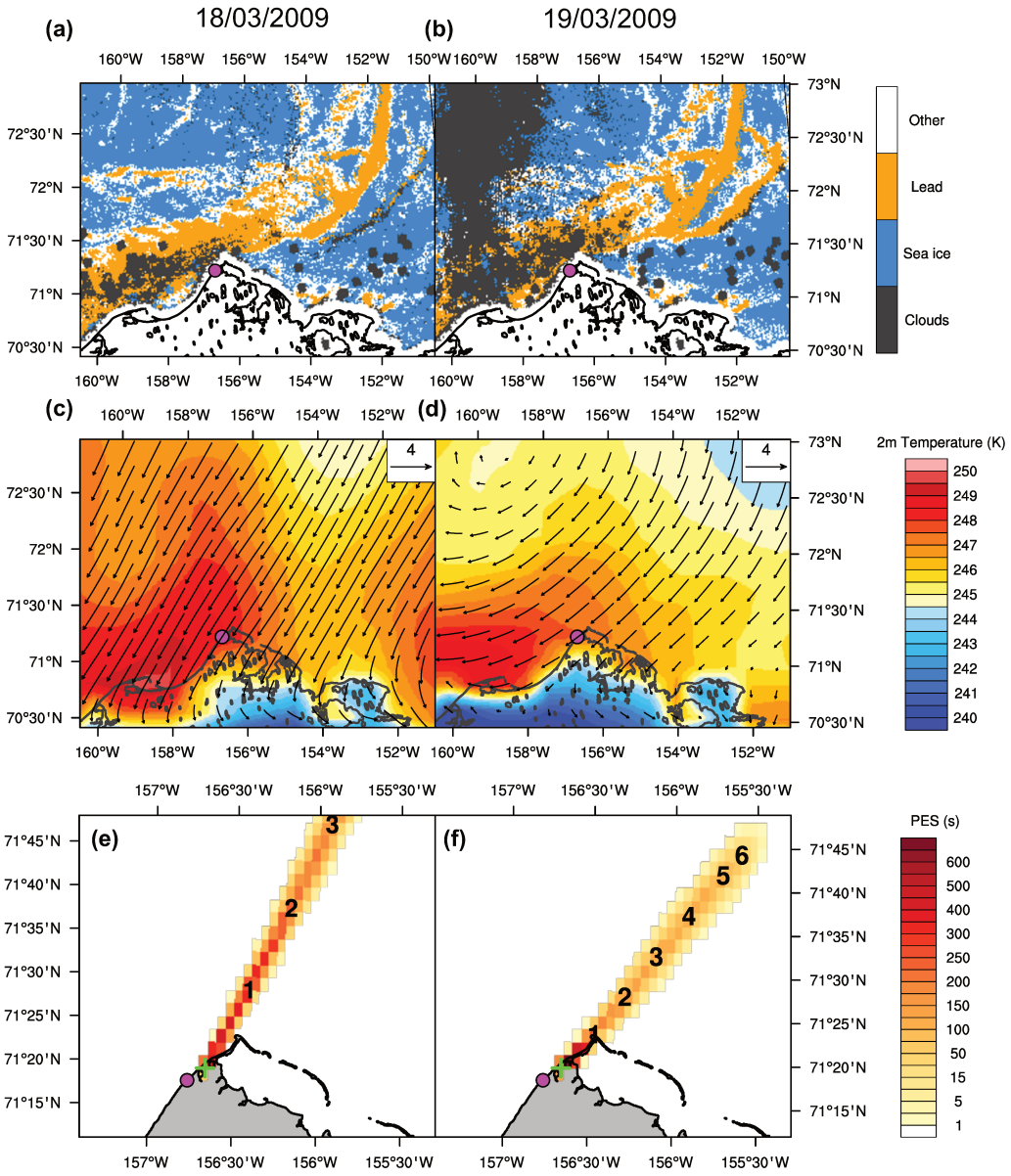

Figure 4.2: (a) Daily Arctic sea ice cover and leads from Willmes and Heinemann (2015) over Northern Alaska on 18/03/2009 and (b) 19/03/2009 with the town of Utqiaġvik marked in magenta. Areas shaded in white represent either land cover or data artifacts. (c) 2-m temperature from WRF over Utqiaġivk at local noon on 18/03/09 and (d) 19/03/09 with 10-m wind speed and wind directions displayed as arrows. (e) FLEXPART-WRF 6-hour backwards surface (0-100 m) potential emission sensitivity (PES) from the measurement site (marked by the green cross) on 18/03/09 – 10:00 AKST and (f) 19/03/09 – 18:00 AKST. Numbers represent hourly intervals since release.

were sparse. Vertical K_z profiles are calculated using the measured friction velocities (u_*) at 1.8 m AGL, with the estimated surface inversion height (SIH) derived from the tower

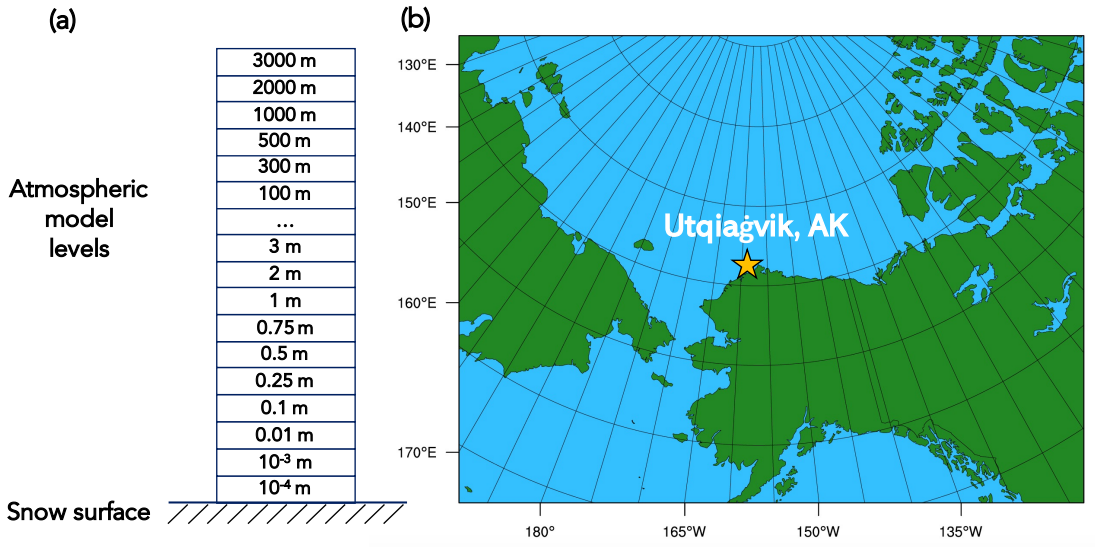

Figure 4.3: (a) PACT-1D model grid used with numbers representing the upper model level height in metres above the snow surface. A total of 112 vertical model levels were used. (b) 3D WRF model domain centred on Utqiaġvik, Alaska with a 25 × 25 km horizontal resolution and 50 vertical levels up to a pressure of 50 hPa.

turbulent flux measurements. A comparison was made between the calculated K_z values and the available measurement data which showed that calculated values were approximately a factor of 3 greater than the observations. Above the surface inversion layer, we assume a fixed value of $K_z = 1$ cm^2 s^{-1}, following Cao et al. (2016). In our model runs, we calculate the SIH using a description based on eddy viscosity scaling, following equation (4.5) (Zilitinkevich et al., 2002; Zilitinkevich and Baklanov, 2002):

$$\mathrm{SIH} = C_s^2 (u_* L / |f|)^{0.5} \tag{4.5}$$

where C_s is an empirical constant (estimated as 0.7), u_* is the measured friction velocity, L is the calculated Obukhov length from the measurements and f is the Coriolis parameter (equal to 1.38×10^4 at the latitude of the study site).

Chemical concentrations in the model are initialised using both observations and CAM-chem model data (Buchholz et al., 2019a; Emmons et al., 2020). Aerosol surface area and number concentration are fixed to the observations for the duration of the run throughout the boundary layer. To supplement the 35 reactions reported in the CAFS data set, additional photolysis rates were added using the TUV radiation model (version

5.0). Each of these additional rates is scaled to the reported NO_2 photolysis rate (J_{NO_2}). Chemical emission of NO_2 is also included in the model and is scaled as a function of J_{NO_2}. These emissions are added to the lowest model level, to simulate photochemical production from snow, and scaled to align with the NO_x levels measured during the simulation period. The 24-hour average NO_2 emission flux we use is 1.71×10^{13} molecules m^{-2} s^{-1}, in reasonable agreement with previous Arctic NO_x flux measurements (Honrath et al., 2002). All input data are provided on 15 minute time resolution and the model is run using a 20-second time step.

4.5 Results and discussion

We study the impact of halogen emissions on oxidation processes during OASIS by performing the following model runs: a reference simulation without halogen emissions from snow (NOSURF); a model run with surface snow emissions and recycling of halogens active (BASE); and several sensitivity runs (FIXO3, AERO, BLD). The model runs are summarised in Table 4.3 and are discussed in detail in the following section. In all model runs, we include heterogeneous chemistry on aerosols, which participates in active recycling of halogen species in all cases. We present the results and discussion in seven sub-sections. First, we present the meteorological conditions at the measurement site during the modelled period (section 4.5.1), followed by an analysis of the NOSURF (section 4.5.2) and BASE runs (section 4.5.3). We discuss in detail the results of the sensitivity tests performed (section 4.5.4), the influence of snow emissions on the vertical extent of halogen concentrations (section 4.5.5) and a comparison of the snow emission fluxes with other estimates (section 4.5.6). Finally, we analyse the impacts on boundary layer oxidation processes (section 4.5.7).

4.5.1 Meteorological conditions and air mass history

The measurements during OASIS were made approximately 5.5 kilometres northeast of Utqiaġvik, Alaska, near the Arctic Ocean (Barret et al., 2011; Boylan et al., 2014; Helmig et al., 2012; Hornbrook et al., 2016; Liao et al., 2012b, 2014; Villena et al., 2011). Figure 4.2a and 4.2b show the sea ice cover and lead information over Northern Alaska on

Table 4.3: Description of the model runs performed in this study.

Model run	Description
NOSURF	Run with halogen snowpack emission routines deactivated.
BASE	Run with halogen snowpack emission and recycling routines active.
FIXO3	BASE run + O_3 fixed to the observations.
AERO	BASE run + heterogeneous recycling efficiency on aerosols increased by a factor of 10.
BLD	BASE run + surface inversion height estimated using expression from Pollard et al. (1973).

18 and 19 March 2009, respectively. Lead information is obtained from the dataset of Willmes and Heinemann (2015) who used thermal-infrared data retrieved from MODIS and applied a binary segmentation procedure to identify leads (Willmes and Heinemann, 2016). During March, the sample location was snow covered and the surrounding ocean largely covered by sea ice, typically reaching its annual maximum in spring. Sea ice leads are clearly visible during the simulation period north of Utqiaġvik, which are known to be important for inducing convective mixing that influences atmospheric chemistry (Moore et al., 2014; Simpson et al., 2017). Meteorological conditions, such as wind speed, wind direction and surface temperature, can also alter surface chemical concentrations via impacts on boundary layer dynamics. Winds on both days were recorded arriving from the northeast, over the Beaufort Sea, carrying clean air masses to the measurement site. During this period, wind speeds were moderate to weak (< 5 m s^{-1}) (Figure A.4), lower than much of the campaign period, and surface temperatures were close to the March average. A strong low-level temperature inversion was also observed for the duration of these two days, indicating stable boundary layer conditions, which is likely to inhibit vertical mixing of species between the inversion layer top and the overlying atmosphere (Figure A.5).

We use the regional meteorological model WRF (setup described in section 4.4.2) to both drive the 1D model atmospheric physics and to understand the regional meteor-

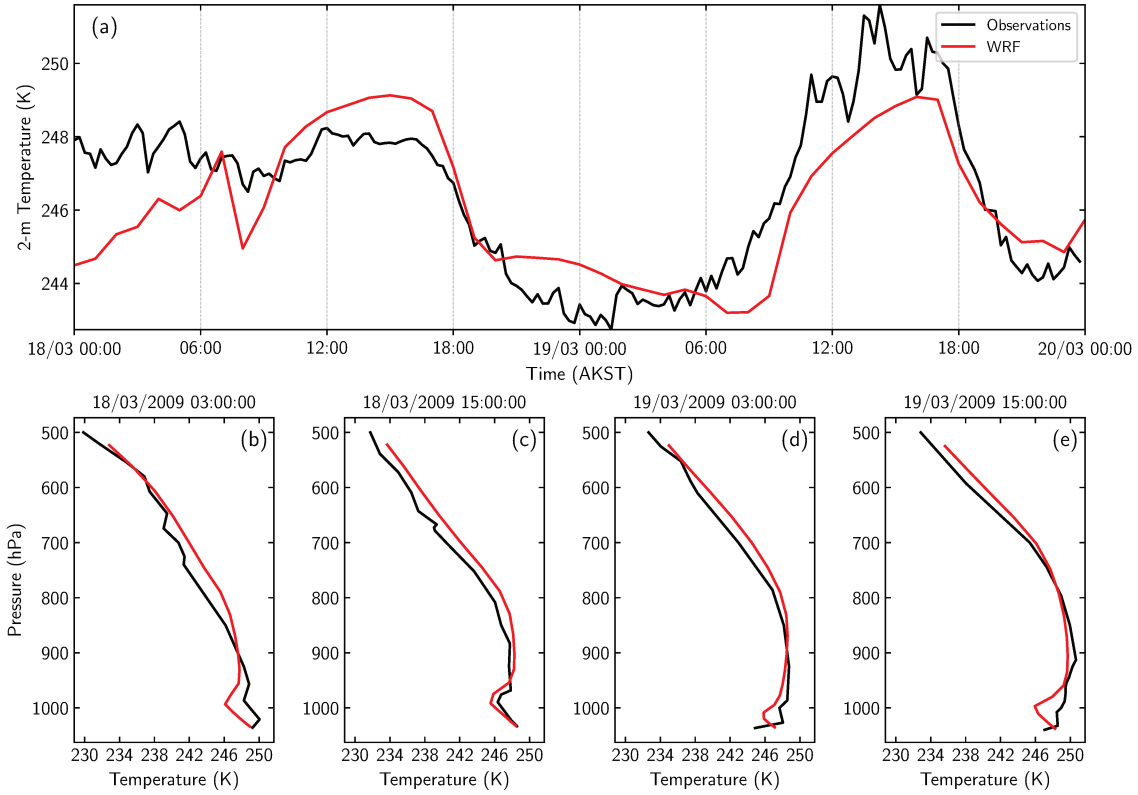

Figure 4.4: Temperature comparison between the WRF model (red) and measurements (black) at Utqiaġvik, Alaska during the simulation period. (a) 2-m temperature from WRF and surface measurements from OASIS. (b) - (e) Vertical temperature profiles from WRF and NOAA IGRA radiosondes released every 12 hours during the simulation period (dates and times are in Alaska standard time).

ological conditions during the sampling period. Simulated 2-m temperature and 10-m winds over Northern Alaska are shown in Figure 4.2c and 4.2d on 18 and 19 March 2009 (local noon) respectively. The wind direction from WRF on both days captures the northern/northeasterly winds measured at the site, as well as the weaker wind speeds on 19 March. This analysis allows us to next identify the origin for air arriving at the measurement site, using the Lagrangian particle dispersion model, FLEXPART-WRF (Brioude et al., 2013). FLEXPART-WRF is driven by the meteorological conditions simulated by WRF and is run in backward mode to simulate air mass histories for the modelled period. These simulations are performed by releasing a total of 100,000 air parcels at the time when Cl_2 maxima were observed for each day (10:00 and 18:00 local time for 18 and 19 March, respectively) and run backwards in time for 6 hours. Figure 4.2e and 4.2f, show the calculated surface ($0 - 100$ m) potential emission sensitivities (PES) near the meas-

urement site. The PES indicates the air mass origin near the surface and represents the length of time the air mass is sensitive to surface emissions. In Figure 4.2e and 4.2f, we show that air masses on these days were unaffected by either the town of Utqiaġvik or Prudhoe Bay (southeast of Utqiaġvik, not shown on map). Transport of air masses over sea ice, including leads, may impact the halogen concentrations measured at the site. On both days, the PES shows (Figure 4.2e and 4.2f) that air passes over leads (Figure 4.2a and 4.2b) just before arrival at Utqiaġvik. Moore et al. (2014) showed that the rapid recovery of depleted mercury and ozone, which are both tied to the abundance of bromine, can be explained by lead-initiated convection bringing higher concentrations of Hg^0 and ozone from aloft. This also indicates that high concentrations of bromine in these air masses are likely diluted over leads during the induced convective mixing, as shown by Simpson et al. (2017). Due to the air mass origins and lead locations, and the relatively short lifetimes of Cl_2 and Br_2, our case is expected to be particularly sensitive to local snow emissions and so we assume that this provides the main source of Cl_2 and Br_2 for our case study (see section 4.5.2).

4.5.2 Model results without snow emissions or recycling

A model simulation without halogen emissions from snow or surface recycling (NOSURF) was first performed as a reference simulation. The results from this simulation are compared to measured species at 1.5 m AGL in Figure 4.5 (blue curve). The halogen species (Cl_2, BrO, and HOBr) in this simulation remain negligible for the duration of the simulation, with the exception of Br_2 which is initialised as described below, showing that additional sources of both chlorine and bromine are required to explain the observations. Surface Br_2 is initialised to the average midnight value (15 pptv) that was recorded during OASIS (Liao et al., 2012b), which fell rapidly to zero after 08:00 on the first day, indicative of photochemical loss. No significant levels of Br_2 after this period are modelled, suggesting that bromine recycling solely on aerosols is not efficient enough to replenish measured levels of Br_2 and other bromine species. Local snow emissions of Br_2 are therefore necessary to replenish bromine levels during the simulation period.

Surface measurements of both NO and NO_2 were higher than the background aver-

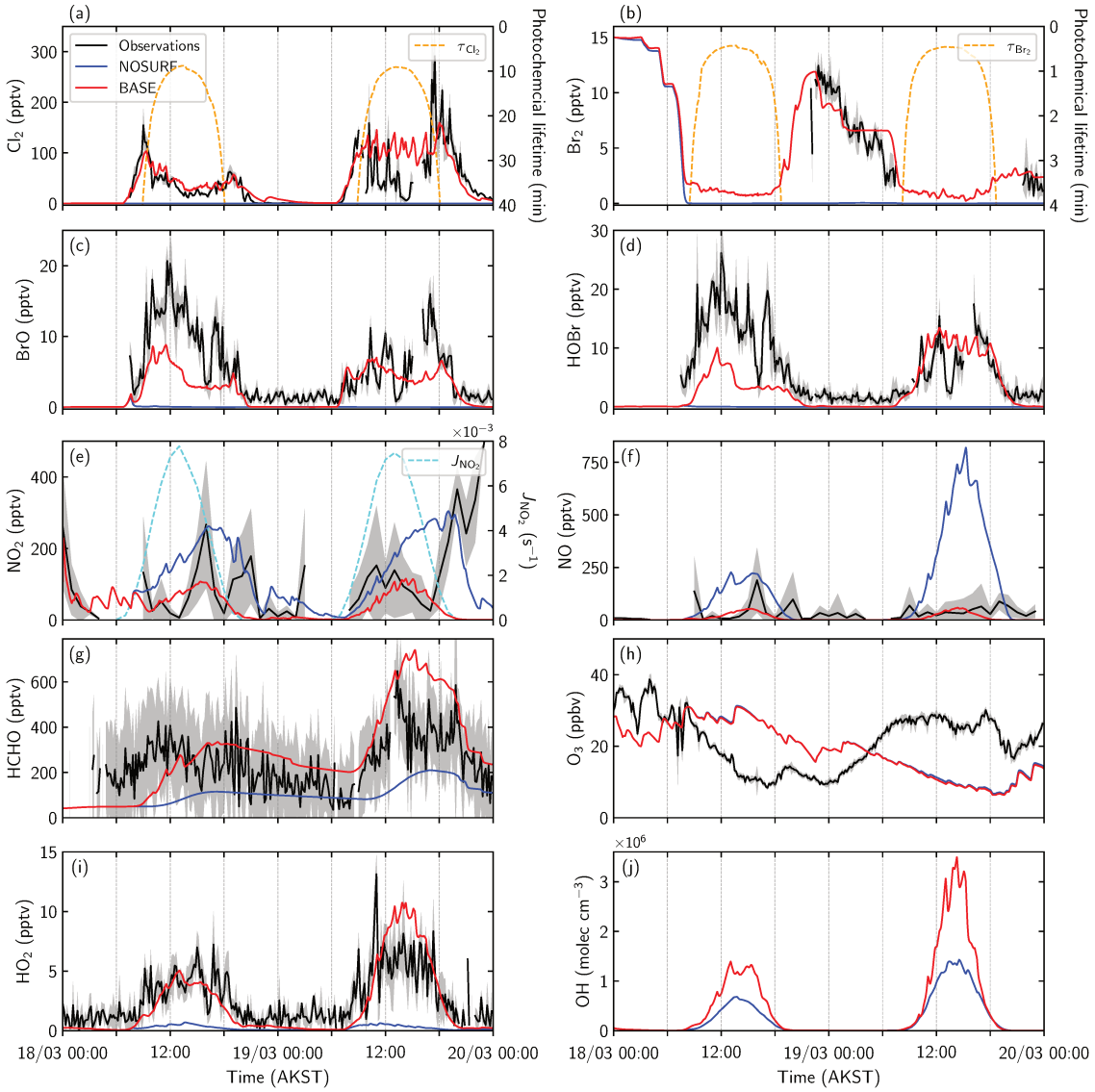

Figure 4.5: Model comparison with observations at 1.5 m above ground level during 18 and 19 March 2009. NOSURF (blue) and BASE (red) runs are compared with the 10-minute averaged measurements (black). NO_x measurements are plotted as an hourly average. Grey shaded areas represent the standard deviation of the average from the instantaneous measurements. Photochemical lifetimes of Cl_2 (τ_{Cl_2}) and Br_2 (τ_{Br_2}) (orange) and the calculated photolysis rate of NO_2 (J_{NO_2}) (cyan) are also plotted.

age ($\sim$ 82 pptv), reaching daytime peaks of close to 250 pptv and over 400 pptv at night on 19 March. These measurements were likely impacted by both local background NO_x emissions from snow (Honrath et al., 1999, 2002) and transient point sources. We filtered out the extreme elevated point sources of pollution (above 500 pptv), and use an hourly average of NO and NO_2 concentrations to smooth out sharp peaks arising from local point sources. The observations (Figure 4.5e and 4.5f) show some remaining sharp peaks

of NO_x on both days, likely caused by these local emission sources, which are difficult to estimate. In addition, a large increase of NO_2 on the evening of 19 March was recorded, corresponding with a change of wind direction and air mass, bringing air from more polluted regions to the measurement site. Stable conditions and low wind speeds may have also facilitated the build-up of higher NO_x concentrations near the surface on these two days. The impact of these local point sources, and of advected polluted air masses, are therefore difficult to simulate in the model to represent the true NO_x concentrations observed at the measurement site. Modelled values reach and even exceed the measured daytime peaks, with a large overestimation in NO on day 2, before falling to lower than 100 pptv at night. The low concentration of modelled halogens would certainly contribute to the overestimation of NO_x concentrations via halogen oxide limited reactions with NO and NO_2. Changes in the surface ozone levels over the two days are not fully captured by either the NOSURF or BASE simulations. This is possibly due to sea ice leads and convective mixing of ozone down from the free troposphere to the surface. The model currently does not account for the impact of sea ice leads on convective mixing of air masses, and would require further testing to include. Finally, we find a general underestimation of both HCHO and HO_2 levels, indicating missing oxidants and oxidation chemistry, and a predicted midday OH concentration between $0.7 - 1.5 \times 10^6$ molecules cm^{-3} for the two days.

4.5.3 Model results with halogen emissions from snow and surface recycling

When snow and recycling emissions of halogens are active (BASE run), we obtain much better agreement with the measured surface mixing ratios compared to the NOSURF run. Measured Cl_2 levels reached up to 150 and 300 pptv on 18 and 19 March 2009 respectively (10 minute average). Figure 4.5 (red curve) shows the model performs well, capturing both the timing and intensity of the morning and late afternoon Cl_2 peaks on the first day, with some discrepancies on day 2. Early morning increase of Cl_2 was recorded after sunrise, suggesting a photochemical production mechanism, which is captured by the model on both days. Daytime levels of modelled Cl_2 on day 2 are overpredicted,

by up to 100 pptv, with the difference possibly explained by weak vertical mixing and a shallow daytime boundary layer. The effects of this on surface chemical concentrations are discussed in more detail in section 4.5.5. Nighttime Cl_2 mixing ratios fall to near-zero levels in the model, which is consistent with the measurements on both days. Our model results show that the nighttime (20:00-06:00) reduction of Cl_2 at 1.5 m is largely explained by depositional loss to the ground (see section 4.5.5). Together, vertical transport and deposition represent the dominant nighttime loss processes ($\sim 94\%$) for Cl_2 at 1.5 m. Heterogeneous uptake of Cl_2 on aerosols and reaction with bromide has also been suggested as a potential Cl_2 sink (and a source of BrCl) (Hu et al., 1995; McNamara et al., 2020; Wang and Pratt, 2017). We find that the reaction of Cl_2 with bromide on aerosols accounts for nearly 5% of nighttime removal of Cl_2 at 1.5 m, which comprises the majority (95%) of the nighttime chemical loss for Cl_2.

Modelled bromine species (Br_2, BrO, and HOBr; Figure 4.5b, 4.5c, and 4.5d, respectively) are also in close agreement with the measurements, with a slight underestimation of BrO and HOBr on day 1. Daytime measurements of Br_2 on these two days are missing due to unstable background Br_2 measurements that led to observations below the detection limit (2.0 pptv) (Liao et al., 2012b). We find that modelled daytime levels of Br_2 are close to this 2 pptv detection limit, due its very fast photochemical loss. At night, we find an accumulation of the photolabile Br_2, via the surface recycling mechanism, which provides reactive bromine for the following day. This is consistent with the average diurnal profile measured for Br_2 during OASIS (Liao et al., 2012b), as well as other Arctic measurement campaigns during spring (McNamara et al., 2020; Wang et al., 2019). Modelled BrO and HOBr diurnal profiles are also in agreement with the observations, with peaks at noon on the first day, indicative of production via Br atoms, and near zero at night. On day 2, a second peak for both BrO and HOBr is recorded in the late afternoon, coinciding with the evening peak of Cl_2. This suggests that the second peak in halogen species could possibly be due to a change in the boundary layer meteorology (e.g., collapse of the boundary layer) rather than chemical production.

The model captures the general trend of NO_x (Figure 4.5e and 4.5f) and we obtain better agreement with the observations in the BASE run, however, the model does not

capture some peaks which may be due to advection of more polluted air masses (e.g., evening of 19 March) or transient point sources. Simulated NO_x levels are highly affected by the presence of halogen emissions, with both NO and NO_2 levels reduced in the BASE run compared to NOSURF. Halogens can react with NO_x to produce halogen nitrites and nitrates (e.g., $ClNO_2$, $ClONO_2$, $BrONO_2$), which act as an important reservoir to sustain reactive halogen chemistry. These species can release halogens back into the atmosphere either directly via photolytic destruction, or by chemical reactions on aerosols and surface snow. O_3 levels in the BASE run also show a steady decline over the two days, with O_3 changes dominated by vertical mixing and deposition to the ground in our particular simulation period (Figure 4.5h). Modelled HCHO (Figure 4.5g) and HO_2 (Figure 4.5i) are also in better agreement with the observations following the addition of halogen emissions. We find an increase in the daytime HO_x (HO_x = OH+HO_2) levels by roughly $20-30$ times compared to the NOSURF run, indicating much more active HO_x chemistry, which can be attributed to halogen chemistry. Overall, we show that halogen emissions from snow and snow-surface recycling are necessary to reproduce surface concentrations of several key species measured during OASIS, with a considerable impact on HO_x concentrations and oxidative chemistry.

4.5.4 Model sensitivity runs

We investigate the effects of different model uncertainties on surface chemical concentrations by performing 3 sensitivity tests. The aim of these runs is to explore uncertainties in both the chemical and dynamical mechanisms in our model and their associated impacts on surface concentrations. Specifically, we test whether changes in the modelled ozone concentration, halogen recycling on aerosols, or boundary layer dynamics impact the conclusions drawn from this modelling study. Descriptions of the runs performed are included in Table 4.3 and are summarised here, followed by a discussion of the results compared with the surface observations (Figure 4.6).

1. **FIXO3**: We first address the impact of ozone on halogen concentrations by fixing the modelled ozone to the measurements within the boundary layer (Figure 4.6, dashed green curve). Bromine levels in this run are greatly affected by the change

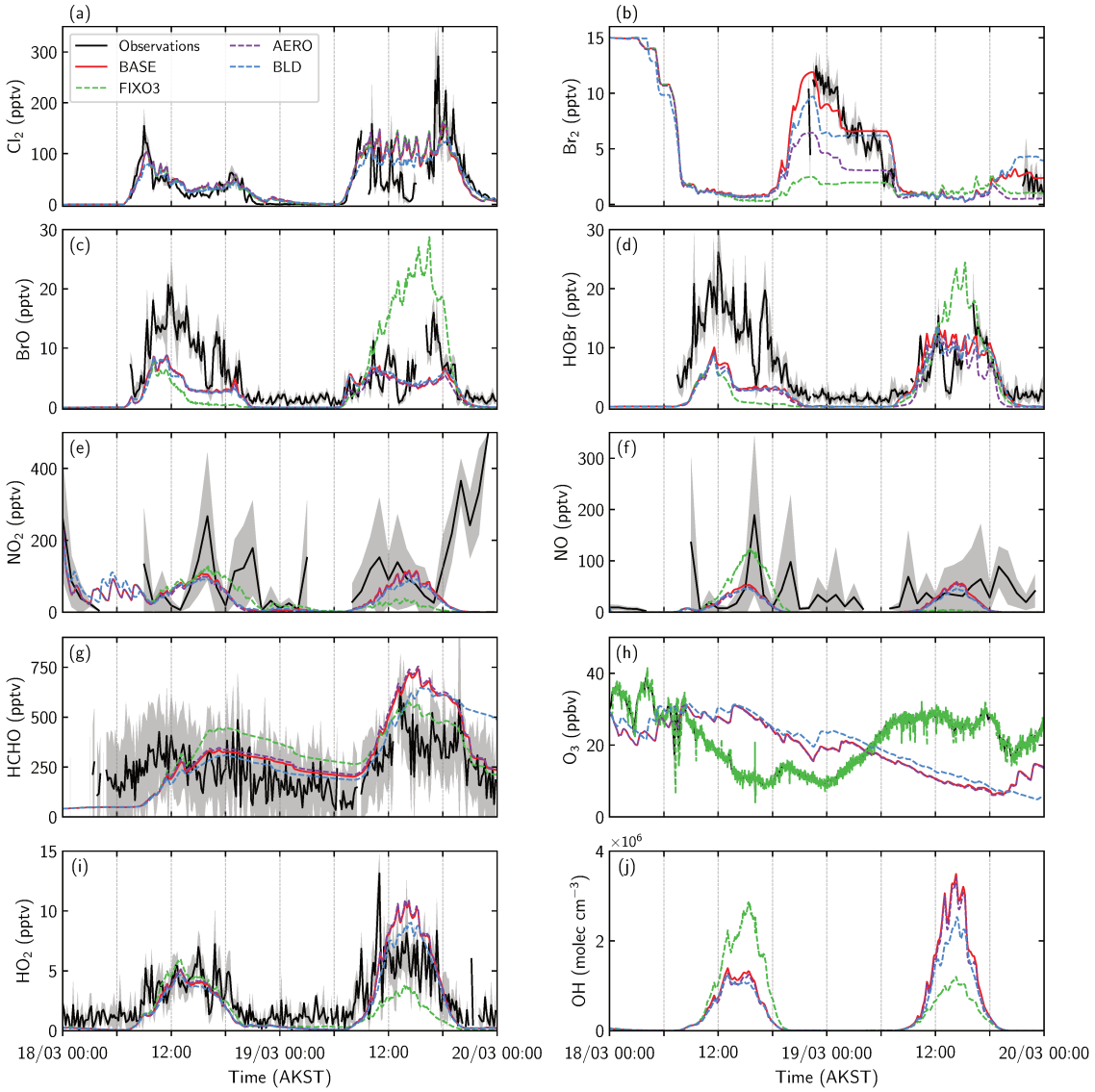

Figure 4.6: Model comparison of sensitivity runs with observations at 1.5 m above ground level during 18 and 19 March 2009. BASE (red), FIXO3 (dashed green), AERO (dashed purple) and BLD (dashed blue) runs are compared with the 10-minute averaged measurements (black). NO_x measurements are plotted as an hourly average. Grey shaded areas represent the standard deviation of the average from the instantaneous measurements.

in ozone availability due to the reaction with Br atoms (R4.2). On 18 March, BrO and HOBr are both underestimated in this run compared to the observations, followed by an overestimation on 19 March (when there was more ozone available). Nighttime Br_2 levels are underestimated by $\sim$ 10 pptv compared to the observations and BASE run, with this difference likely explained by the lower levels of BrO on day 1, resulting in less $BrONO_2$ formation and recycling to re-form Br_2. The day-

time HO_2 concentration on day 2 is approximately 68% lower than the BASE run, due to increased BrO levels and subsequent loss via reaction (R4.5). The results from this run point to potential inaccuracies in the emission parameterizations of bromine, uncertainties in the downward mixing of ozone in the model from above the boundary layer, or, to the missing treatment of advected air masses, all of which require further exploration and testing.

2. **AERO**: To test whether heterogeneous recycling on aerosols could contribute a significant source of halogens, we increase the heterogeneous reactive uptake coefficients for Cl_2, Br_2 and BrCl formation reactions by a factor of 10 (Figure 4.6, dashed purple curve). This test fails to show a significant increase in the halogen concentrations at the surface, indicating that recycling on aerosols contribute only a minor source of reactive halogens at 1.5 m. Interestingly, nighttime Br_2 levels decreased by up to 5 pptv when compared to the BASE run, caused by lower $BrONO_2$ levels ($\sim$ 25% reduction) as it was more efficiently recycled on aerosols. We also evaluate the difference in the vertical distribution of halogens between the AERO and BASE run (Figure A.6). The modelled vertical distribution of halogens in the BASE run is discussed in detail in section 4.5.5. We find differences of less than 10 pptv between halogens in the AERO run and the BASE run within the lowest 50 m of the model, and see no differences above this height. Specifically, we find an increase in Cl_2 concentrations of several pptv in the AERO run and a small decrease for each modelled bromine species.

3. **BLD**: We explore uncertainties in the boundary layer dynamics by testing a different expression to calculate the SIH from the meteorological measurements (Figure 4.6, dashed blue curve). The expression used in this run (equation (4.6)) was originally developed for a stable mixed layer over the ocean by Pollard et al. (1973), and was found to also be applicable to the South Pole by Neff et al. (2008):

$$\mathrm{SIH} = 1.2u_*(fN_B)^{-0.5} \tag{4.6}$$

$$N_B = \sqrt{\frac{g}{T}\frac{\partial\theta}{\partial z}} \tag{4.7}$$

where u_* is the measured friction velocity, f is the Coriolis parameter (equal to 1.38×10^4 at the latitude of the study site), N_B is the Brunt-Vaisala frequency, g is the acceleration due to gravity, T is the absolute temperature and $\partial\theta/\partial z$ is the potential temperature gradient. This results in a SIH which is several metres greater than previously used for the BASE run (Figure A.5), leading to some key differences in the modelled chemical species. Most notably, we see a reduction in daytime Cl_2 levels at 1.5 m, by up to 60 pptv, on day 2 compared to the BASE run due to an increased SIH. This shows how sensitive surface concentrations can be to small changes in the boundary layer conditions, with significant uncertainties in vertical transport near the snow surface and lower atmosphere. This is discussed in more detail in section 4.5.5.

In summary, the sensitivity runs performed here do not significantly improve model agreement with the observations. However, these sensitivity tests show that modelled surface concentrations are influenced by a number of parameters, which require better understanding of specific processes in order to constrain halogen emissions. Changes in ozone and boundary layer dynamics (vertical mixing) had the largest impacts on halogen concentrations, as well as influencing surface NO_x and HO_x levels. We find that uncertainties in heterogeneous reactions on aerosols do not explain the underestimation of BrO and HOBr on day 1, and represent only a minor source contribution of halogens in our model case. Additional studies designed to investigate these processes and reduce known uncertainties for the Arctic region are needed to further evaluate the source contributions of halogens from snow.

4.5.5 Vertical influence of snow emissions and recycling on halogens

In this section, we use the BASE run to understand the vertical distributions of Cl_2 and Br_2 (Figure 4.7a and 4.7b respectively). No vertically resolved measurements were available for either species, therefore, no direct comparison can be made to the model results. We find that the majority of modelled Cl_2 (approximately 97%) is confined to the lowest 15 m of the atmosphere and rapidly decreases with altitude. This implies highly active chlorine chemistry at the surface. Very little Cl_2 is present above 15 m, indicating a strong

vertical gradient in chemical reactivities, with the vertical distribution of Cl_2 influenced by the height of the surface inversion. During the campaign, the surface layer height ranged from as low as a few metres up to several hundreds of metres and was estimated to be very shallow (< 50 m) during the simulation period (Boylan et al., 2014). Low-level temperature inversions and shallow boundary layers are a common phenomena in cold polar regions and are frequently characterised by stable conditions and low wind speeds. Typically, solar heating of the surface generates a turbulent well-mixed daytime boundary layer, creating a larger volume in which chemical species can be distributed. This simultaneously increases the vertical transport of species away from the surface and results in decreasing concentrations of chemical species that would otherwise build up near the surface. The diurnal evolution of the surface layer can be seen following this behaviour on the first day but not on the second. We are therefore able to capture the daytime reduction in surface Cl_2 levels on day 1, following the morning peak, but overestimate Cl_2 levels on day 2. This high daytime Cl_2 concentration is simulated when the wind speed and estimated SIH were very low (< 1 m s^{-1} and < 10 m, respectively), confining Cl_2 to a very shallow layer close to the surface. The BLD sensitivity test also shows similar behaviour of the surface layer on the second day, however estimated a SIH several metres higher during the day, resulting in a reduction of Cl_2 at this time (Figures S5 and S7). Differences in the SIH estimates between equations (4.5) and (4.6) are discussed in detail by Boylan et al. (2014), but further evaluation is beyond the scope of this study.

The modelled vertical distribution of Br_2, presented in Figure 4.7b, shows that Br_2 is present up to and above the SIH during the simulation. During sunlit hours, Br_2 is found only within the first few metres of the model, whereas at night, Br_2 is more abundant (approx. 10 pptv) reaching up to 40 m in height. Previous studies have examined the vertical distribution of bromine in the Arctic via surface-based measurements of BrO (Peterson et al., 2015; Simpson et al., 2017). Peterson et al. (2015) found that the percentage of BrO within the lower troposphere (< 200 m) was highly dependent on atmospheric stability. During stable conditions, higher BrO mixing ratios were measured close to the surface, with less BrO distributed within the lower troposphere, compared to unstable conditions which were associated with more vertically distributed BrO events. Simpson

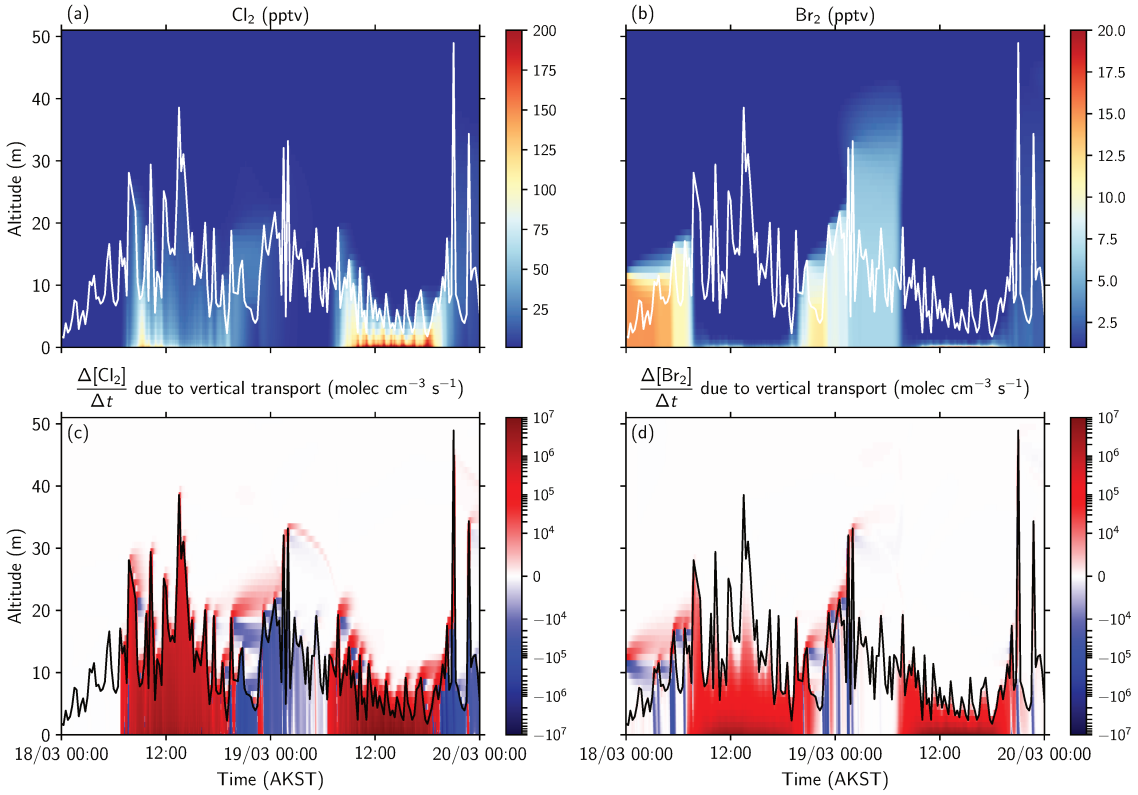

Figure 4.7: Modelled vertical distributions of (a) Cl_2 and (b) Br_2 during 18 and 19 March 2009 in the BASE run. White trace indicates the model prescribed surface inversion height. Modelled concentration change of (c) Cl_2 and (d) Br_2 due to vertical transport and deposition with respect to time. Black trace indicates the prescribed surface inversion height. Positive values represent upward transport and negative values indicate downward transport.

et al. (2017) also observed shallow layer events of BrO during stable conditions, and during lead opening events, found that BrO was lofted above the surface via lead-induced convective mixing. Air that had travelled over sea ice, arriving at the measurement site with very low ozone representing ODE conditions and very active bromine chemistry, are not specifically investigated here. However, there are some similarities between what we investigate regarding land-based snow emissions of both bromine and chlorine and what is known about bromine activation from snow on sea ice, where atmospheric boundary layer stability is similar. During the simulation, we find that both BrO and HOBr are present within and above the SIH, reaching heights of up to 40 m during the day (Figure A.8). This is in agreement with the findings of Peterson et al. (2015), as the stable conditions recorded between 18 – 19 March would suggest a shallow layer event of BrO. However, it

is also important to note that the air masses arriving at the site could have possibly experienced some lead-induced convective mixing (see Figure 4.2), which would mix bromine to higher altitudes and this is not considered in the model.

In Figure 4.7c and 4.7d, we plot the changes in concentration of Cl_2 and Br_2 due to transport and deposition, respectively. The change in both Cl_2 and Br_2 concentrations, due to vertical transport, is highest during the day following release from snow and transport into the atmosphere. During the night, Cl_2 is mainly transported downward to the surface and lost via deposition to the ground. Deposition in the model is calculated using an approach of molecular collisions with the ground and applying a non-reactive uptake probability (α) (Tuite et al., 2021). This allows us to calculate deposition of different species without prescribing a deposition velocity. For Cl_2, we set $\alpha = 5 \times 10^{-5}$, following the lower limit recommendation of Burkholder et al. (2019). On 19 March, transport of Cl_2 is clearly limited by the height of the inversion layer, with Cl_2 transport not exceeding more than 15 m altitude, thereby concentrating Cl_2 at the surface. Figure 4.7d shows that the upward transport of Br_2 is at its maximum during the day on 18 and 19 March. Daytime Br_2 concentrations are confined to the first few metres above ground, indicating that daytime Br_2 is lost via its fast photolytic destruction. Vertically resolved measurements of halogens above the Arctic snow surface are highly desirable for further model evaluation and development.

4.5.6 Modelled halogen snow emission fluxes compared to previous estimates

Here, we compare the surface emission fluxes of Cl_2 and Br_2 estimated in this work to previous flux estimates. The model emission flux contributions of Cl_2 and Br_2 are shown in Figure 4.8a and 4.8b, respectively. Our modelled emissions of both Cl_2 and Br_2 peak at solar noon on each day, coinciding with increased radiation at the snow surface, before falling to zero at night. The peak fluxes are similar to previously reported halogen emission fluxes measured from the Arctic snowpack (Custard et al., 2017), while the exact timing of emissions differs. During February 2014, snowpack flux estimates of Arctic Br_2 and Cl_2 were calculated, based on vertical gradient measurements, for the first time near

Utqiaġvik. Estimates of these fluxes ranged between $0.7 - 12 \times 10^8$ and $0.02 - 1.4 \times 10^9$ molecules cm^{-2} s^{-1} for Br_2 and Cl_2, respectively. We modelled midday fluxes for Cl_2 of 4.3×10^9 and 7.2×10^9 molecules cm^{-2} s^{-1} for 18 and 19 March, respectively, with the primary photochemical snow emission mechanism the main contributor to Cl_2 emissions. This is several times higher than the values reported by Custard et al. (2017). This may in part be explained by increased available sunlight during March compared to February (when the flux measurements were made), enhancing halogen production. Additionally, ambient concentrations of Cl_2 were much lower in February 2014 than those measured in March 2009, with daytime values ranging between $5 - 20$ pptv in February 2014 and 59 pptv for the simulation period. Both of these reasons would suggest higher snow emission fluxes of halogens between $18 - 19$ March 2009 than estimated previously.

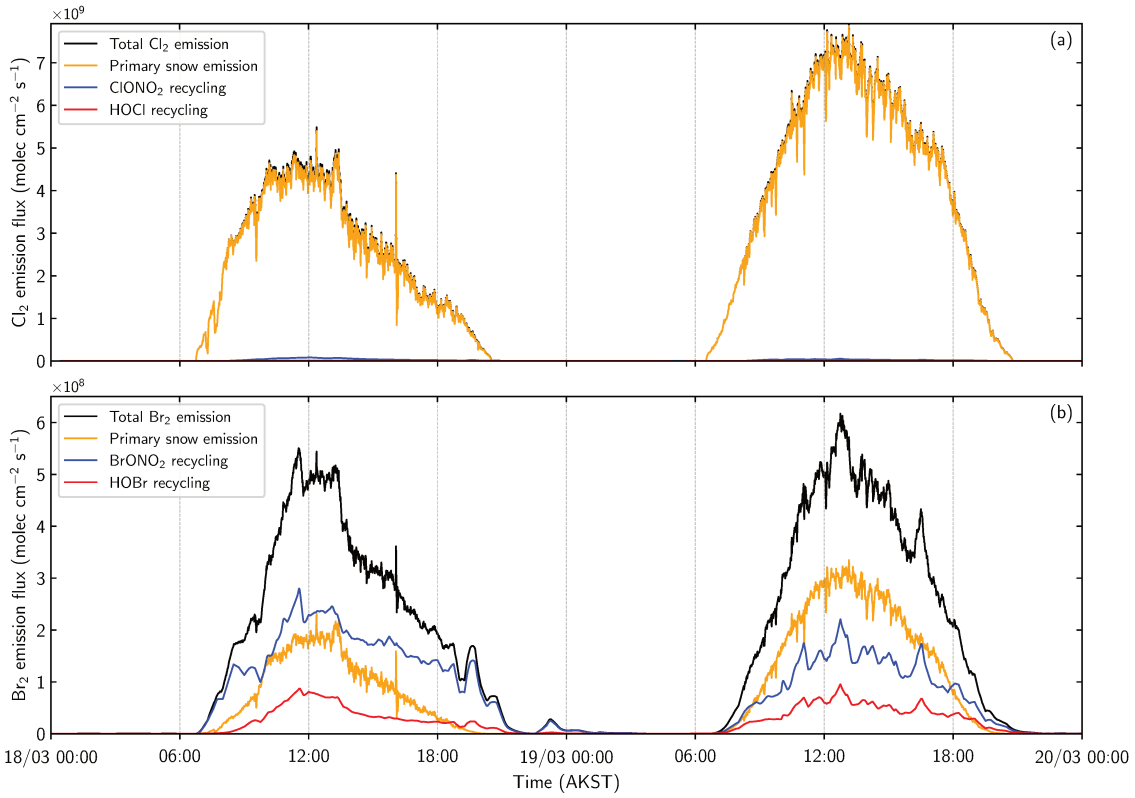

Figure 4.8: Snow emission and recycling fluxes of (a) Cl_2 and (b) Br_2 in the BASE run. The total emission flux (black) for each species is plotted together with the primary snow emission flux (orange) and recycling fluxes of $XONO_2$ (blue) and HOX (red), where X = Cl and Br.

During the OASIS campaign, Liao et al. (2014) estimated an average peak production of Cl_2 of 2.2×10^6 molecules cm^{-3} s^{-1} using 0D box modelling. Assuming a 15 m

mixing layer, this corresponds to an average emission flux of 3.3×10^9 molecules cm^{-2} s^{-1}. This is slightly lower than the value we report here, which is likely due to our focus on an extremely high Cl_2 event during the campaign. Similarly, Wang and Pratt (2017) conducted a 0D box modelling study to simulate halogen snowpack production during March 2012 near Utqiaġvik. A peak Cl_2 production rate of $2.9 - 3.2 \times 10^8$ molecules cm^{-2} s^{-1} was reported (assuming a 10 m effective mixing height), with ambient Cl_2 concentrations ranging between $0 - 20$ pptv for the modelled periods. The lower ambient Cl_2 concentrations during March 2012 suggest that solar radiation is not the driving factor for differences between Cl_2 emission fluxes during February and March. Other factors such as atmospheric stability, vertical mixing, and snowpack chemistry are also likely to play a role in controlling molecular halogen emission fluxes from snow. Production of Cl_2 via snow surface recycling of HOCl and $ClONO_2$ was also minimal over the two days, with almost no production of Cl_2 at night, which explains the difference in the nighttime concentrations of Cl_2 and Br_2. There are uncertainties to the efficiency of this recycling (see section 4.3.2), however, sensitivity tests showed no significant increase in Cl_2 when the recycling efficiency of these species was increased (Figure A.2).

Figure 4.8b shows the modelled Br_2 emission fluxes, with midday values calculated at 4.9×10^8 and 5.0×10^8 molecules cm^{-2} s^{-1} for 18 and 19 March, respectively. These are in close agreement with the range reported by Custard et al. (2017) and are higher than those modelled by Wang and Pratt (2017) of 2.1×10^8 and 3.5×10^6 molecules cm^{-2} s^{-1} for 15 March and 24 March 2012 respectively. Both primary photochemical and snow recycling emissions of Br_2 are important production mechanisms and contribute significantly to the total Br_2 emission flux. Surface recycling of $BrONO_2$ is the main source of Br_2 on day 1, highlighting the influence of NO_x on bromine chemistry. This mechanism drives the accumulation of Br_2 at night, as this emission source remains significant later into the evening on day 1 compared to the primary snow emission, which falls to zero after sunset. Previous box modelling studies have shown that even under low NO_x levels (< 100 pptv), formation of $BrONO_2$ is significant (Liao et al., 2012b; Thomas et al., 2012; Wang and Pratt, 2017), and under high NO_x levels (> 700 pptv) formation of both BrO and HOBr are suppressed, whereas the rate of $BrONO_2$ formation remained largely unaffected (Cus-

tard et al., 2015). Due to the difficulty of measuring $BrONO_2$, no measurements have yet been reported in the Arctic to the best of our knowledge. Future work remains to compare the partitioning of HOBr and $BrONO_2$ under different NO_x conditions.

4.5.7 Boundary layer VOC oxidation processes

We have shown (in section 4.5.3) that with the addition of halogen emissions (BASE run), we obtain good agreement with the measured HO_2 concentration at the surface and predict an increase in OH (Figure 4.5). To further understand the links between halogens, HO_x cycling and oxidative chemistry, we analyse the major HO_x production and loss reactions, as well as VOC chemical lifetimes with respect to OH and Cl. First, we compare the difference in modelled HO_x concentrations between the NOSURF and BASE runs, as well as the change in partitioning of OH/HO_2 between the two runs.

Figure 4.9a shows the modelled HO_x and Cl atom concentrations in the NOSURF and BASE runs at 1.5 m AGL. We see a clear impact of halogens on surface HO_x concentrations, with up to a 30 times increase at the surface when the halogen snow and recycling emissions are active. This increase is largest within the daytime surface layer, coinciding with the high levels of simulated chlorine atoms, and is shown in Figure 4.9b as a ratio of HO_x between the BASE and NOSURF runs. Modelled Cl atom concentration at noon is higher than the average concentration predicted during the campaign of 2.0×10^5 atoms cm^{-3} (Liao et al., 2014). We calculate values of 2.9×10^5 and 1.1×10^6 atoms cm^{-3} for 18 and 19 March at noon, respectively. Our higher values can partly be explained by the overestimation of modelled Cl_2 on day 2, as well as the higher Cl_2 levels observed during this period compared to the campaign average Cl_2 levels.

Figure 4.9c shows the calculated OH/HO_2 ratio at 1.5 m AGL in the NOSURF and BASE model runs. We find a significant shift in the OH/HO_2 ratio towards HO_2 in our BASE run following the addition of halogen emissions compared to the NOSURF run. This difference is largest during the day, within the lowest 40 m of the atmosphere, with up to an order of magnitude difference, as shown in Figure 4.9d. This shift towards HO_2 in the BASE run can be explained by two main reasons. Firstly, with the chlorine sources active in the BASE run, HO_2 formation via Cl-mediated VOC oxidation is greatly increased,

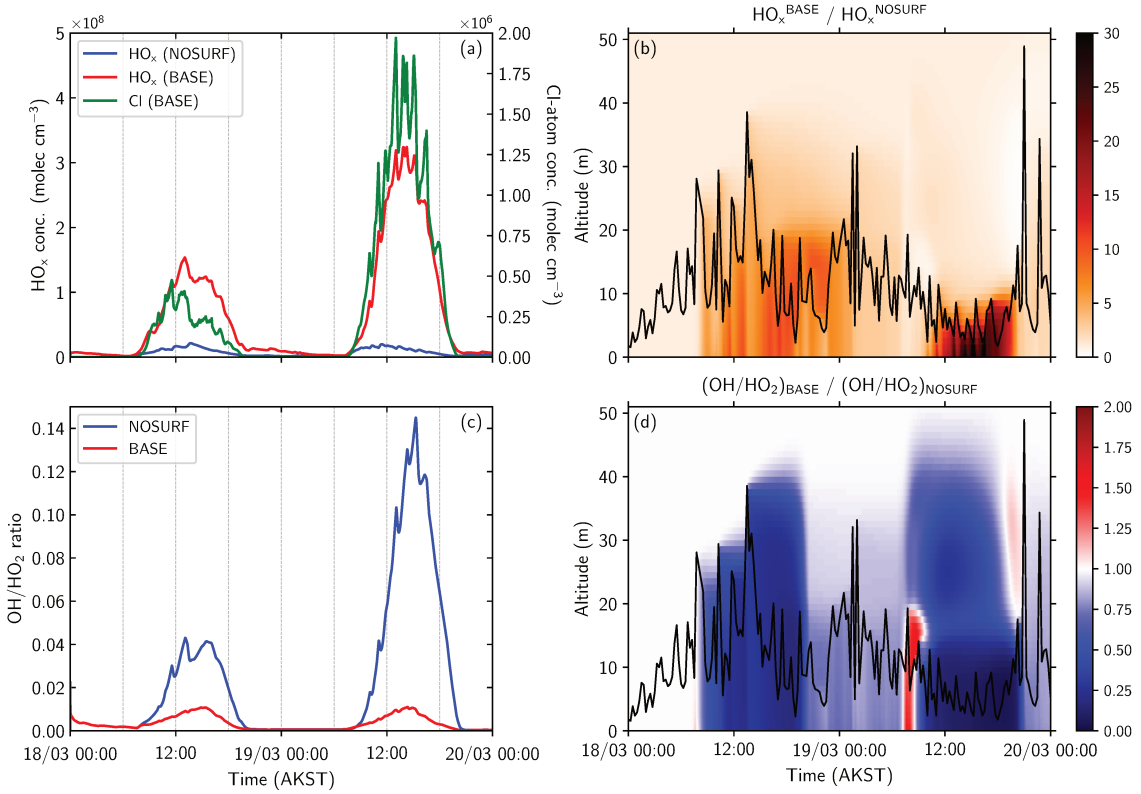

Figure 4.9: (a) Modelled HO_x concentrations at 1.5 m above ground level in the NOSURF (blue) and BASE (red) runs and Cl atom concentration (green). (b) HO_x concentration in the BASE run divided by the HO_x concentration in the NOSURF run as a function of altitude. (c) OH/HO_2 ratio at 1.5 m above ground level in the NOSURF (blue) and BASE runs (red). (d) OH/HO_2 ratio in the BASE run divided by the OH/HO_2 ratio in the NOSURF run as a function of altitude.

skewing the ratio towards HO_2. This is in support of previous studies, which have suggested that HO_2 can be increased by the presence of chlorine, shifting the OH/HO_2 ratio significantly towards HO_2 (Piot and von Glasow, 2009; Rudolph et al., 1999; Thompson et al., 2015). Secondly, as the model was not constrained to any observations, the addition of halogen sources had a significant impact on the NO_x concentrations. Surface NO_x levels in the NOSURF run were several times greater than the BASE run, which greatly impacted OH formation. Thomas et al. (2012) showed that modelled surface concentrations of OH double with the inclusion of snowpack NO_x sources and bromine chemistry. This was mainly driven by the NO + HO_2 reaction under conditions where the halogen concentrations were significantly lower than those measured at Utqiaġvik during OASIS. In order to further understand HO_x cycling in our model, we analyse the major production

and loss reactions of both OH and HO_2.

HO_x chemical budget

The main HO_x production and loss reactions at two heights (1.5 and 50.5 m) above the snow are shown in Figure 4.10. A clear chemical reactivity gradient is shown, with rates at 1.5 m approximately an order of magnitude greater than at 50.5 m, due to increased HO_x and Cl atom concentrations in the lower atmosphere. The principal OH production source in the model is the HO_2 recycling reaction with NO, at both the surface and above the boundary layer at 50.5 m AGL. Halogen-influenced OH production is clearly shown at 1.5 m, accounting for almost a quarter of surface OH production, with photolysis of HOBr (R4.6) contributing 14% and reactions involving chlorine comprising nearly 10%. This is a significant direct impact of snow-sourced halogens on the OH concentration. Snow emissions of other species, such as nitrous acid (HONO) and hydrogen peroxide (H_2O_2), could also be important sources of OH which may not be fully represented by our simulations due to missing snow emissions of these species in our model runs. At 50.5 m, modelled halogen concentrations are low with limited contribution to OH production at this height. Reaction between ozone and HO_2 is the second most important pathway for OH production at this height and is particularly important as it continues to convert HO_2 to OH for several hours after sunset. OH is lost via a multitude of reactions with organics, which can both recycle OH back into HO_2 and act as a source of CH_3O_2 and RO_2. Mainly, OH loss is dominated by the reaction with CO, accounting for approximately a quarter of OH loss at both heights, which is also an important source of HO_2.

At 1.5 m, the main HO_2 production reaction is the CH_3O_2 + NO reaction (25%), followed by CO + OH (16%). CH_3O_2 is formed following oxidation of VOCs and methane by OH and Cl, with the rate constant of Cl + CH_4 roughly an order of magnitude greater than OH + CH_4. Figure 4.11 shows the major production reactions of CH_3O_2 in our BASE run, with Cl + CH_4 responsible for almost two-thirds (64%) of surface CH_3O_2 production, whereas OH + CH_4 accounts for only 5%. At 50.5 m above the surface, production via Cl + CH_4 is negligible due to the low abundance of Cl atoms. Therefore, we can determine that snow emissions of chlorine drive the increase of surface HO_2 levels via

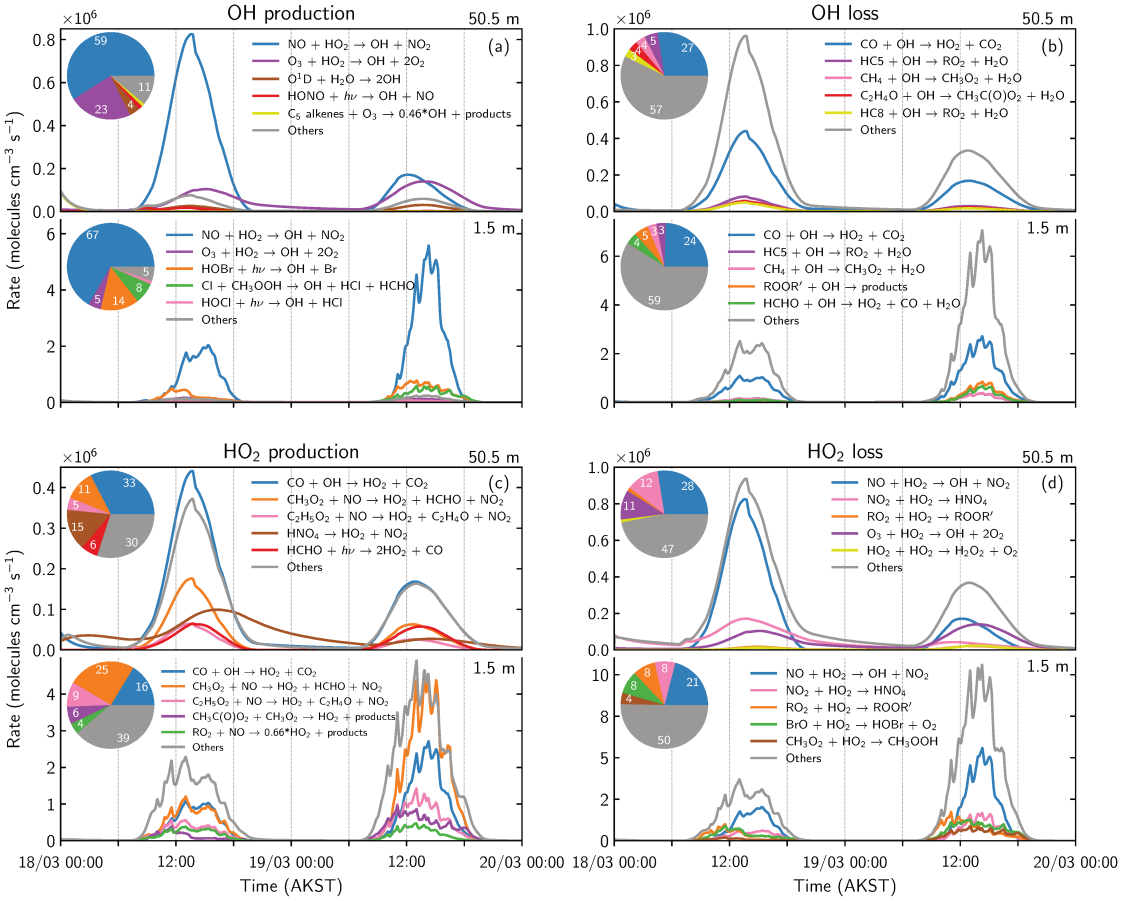

Figure 4.10: BASE simulation modelled (a) OH production (b) OH loss (c) HO_2 production, and (d) HO_2 loss each at 1.5 m and 50.5 m above the snow surface. The five largest contributing reactions are shown for each with the percentage contributions shown as a pie chart.

CH_3O_2 formation. Consequently, this reaction cycle can also accelerate bromine recycling and ozone depletion, via (R4.5), linking together the chlorine and bromine chemical cycles. This effect is seen at 1.5 m, with BrO constituting 8% of HO_2 loss, with minimal contribution at 50.5 m.

In summary, it can be clearly seen that halogen emissions from snow make a significant contribution to HO_x production and loss reactions close to the surface. Chlorine and bromine chemical cycles are linked via peroxy radical formation, enhancing HO_x chemistry within the boundary layer, which can significantly impact VOC reactivity and lifetimes.

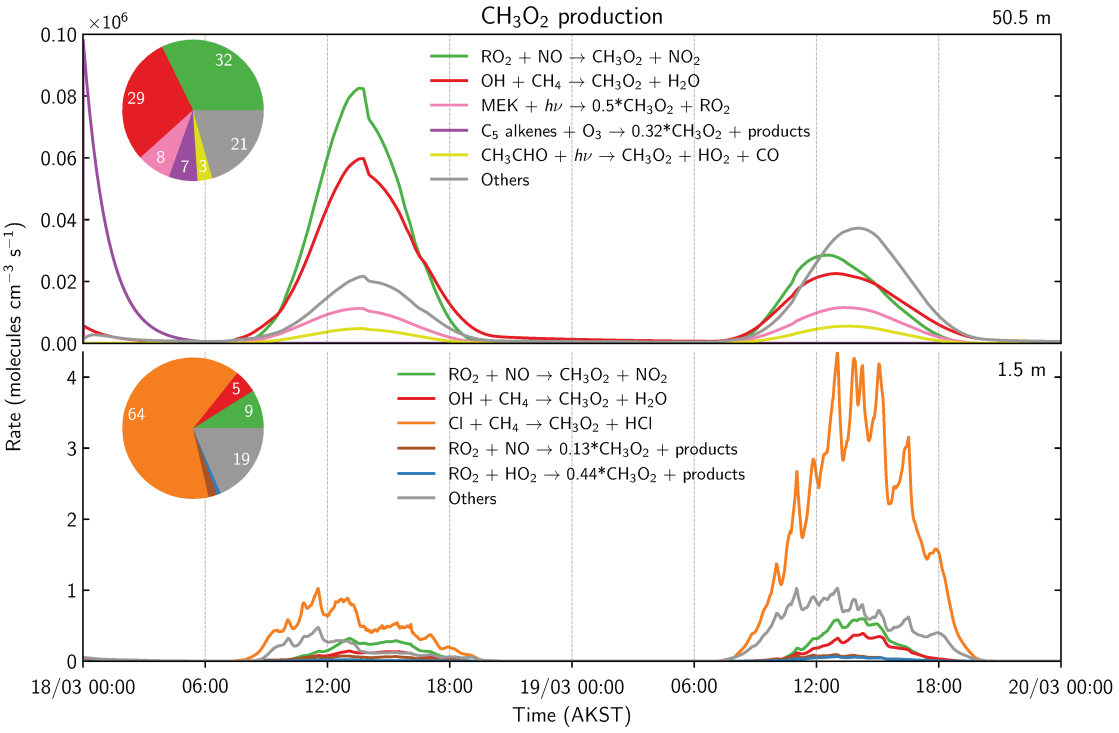

Figure 4.11: Modelled production reactions of CH_3O_2 at 1.5 m and 50.5 m above the snow surface. The five largest contributing reactions are shown for each with the percentage contributions shown as a pie chart.

VOC chemical lifetimes

VOCs were measured during the campaign and the impact of Cl and Br atoms on VOC concentrations are discussed in detail in Hornbrook et al. (2016). The influence of chlorine chemistry on VOCs was determined during the campaign by recording the ratio of isobutane to n-butane (iC_4/C_4), as both alkanes react at similar rates with OH, but n-butane reacts approximately 1.5 times faster with Cl. iC_4/C_4 rose over the course of the campaign, indicating increased Cl atom processing (and Cl_2 production) with increased availability of sunlight as spring progressed. Table 4.4 shows the simulated OH and Cl atoms concentrations at 1.5 m and 50.5 m AGL used to calculate the chemical lifetimes (τ) of several VOCs presented in Table 4.5. For computational efficiency, some species within the RACM2 mechanism with similar reactivities are lumped together and treated as one species, such as propane and other similar organic compounds (HC3), as well as for pentane (HC5) and octane (HC8). At the surface, Cl atoms are abundant and rapidly oxidise VOCs, typically on the order of several hours, compared to OH which is generally

Table 4.4: OH and Cl concentrations at 1.5 m and 50.5 m, at 12:00 AKST and 48-hour average in the NOSURF and BASE runs.

	1.5 metres		**50.5 metres**	
Species	12:00 AKST	48-hour average	12:00 AKST	48-hour average
	(molecules cm^{-3})		(molecules cm^{-3})	
$[OH]_{NOSURF}$	6.98×10^5	2.37×10^5	3.23×10^5	1.04×10^5
$[OH]_{BASE}$	1.22×10^6	4.57×10^5	3.21×10^5	1.04×10^5
$[Cl]_{BASE}$	7.19×10^5	2.65×10^5	22	7

on the order of days. As previously shown, surface OH concentration increases following the addition of halogen emissions, resulting in a reduction of VOC lifetimes by roughly 43% compared to the NOSURF run. This is a significant increase in the reactivity and processing of VOCs via OH due to the presence of halogens. At 50.5 m above the surface, this difference is minimal as levels of halogen radicals are very low, demonstrating the impact of chlorine chemistry close to the ground. We also see a clear gradient in chemical lifetimes with height and would expect longer lived VOCs above the boundary layer to act as a reservoir and replenish surface VOC concentrations by downward transport.

Indeed, as shown in Hornbrook et al. (2016), the VOCs sampled indicated more important halogen influence on atmospheric chemistry between the early hours of 18 March and 19 March. These VOC observations are likely a mix of local chemistry that is represented within our 1D model and chemistry that occurred while air masses resided over sea ice prior to sampling. Hornbrook et al. (2016) used ethyne levels to show there was a fairly consistent, but moderately low, Br atom influence atmospheric chemistry on 18 March. At the same time, measured acetaldehyde, propanal, and butanal decreased by approximately 50%, 75% and 90% respectively (see Figure 14 in Hornbrook et al. (2016)). As well, the butanal observations indicated a gradient between the lowest sampling height, 0.6 m, and the other two sampling heights at 1.5 and 5.4 m, in which the mixing ratio nearest the snow surface reached levels as low as half that at the higher sampling inlets, consistent with Cl atom chemistry near the surface. Overall, our results show that measurements above the Arctic snow surface can be highly influenced by halogen chemistry

directly or indirectly via increases in HO_x concentration, resulting in a highly reactive surface layer. Deriving accurate Cl atom concentrations from VOC measurements can therefore be challenging, as surface VOC and Cl atom concentrations are dependent on vertical mixing, surface halogen emissions, and chemistry.

In a well-mixed system, downward transport of VOCs can replenish concentrations at the surface, potentially resulting in an underestimation of the derived Cl atom concentration at the ground.

4.6 Conclusions and perspectives

In this study, we examined the role of Arctic halogen emissions from snow on boundary layer oxidation processes using an updated version of the PACT-1D model. Snow emissions of Cl_2 and Br_2 were added to the model, including primary production from land-based surface snow and heterogeneous recycling on aerosols and snow. We compared the model against observations from the 2009 OASIS campaign at Utqiaġvik, Alaska, when high atmospheric Cl_2 levels were observed ($18-19$ March). The modelled halogen concentrations showed excellent agreement with the observations upon the addition of halogen emissions. The main conclusions of our study can be summarised as follows:

- Surface Arctic halogen observations are reproduced by the model when including the combined effects of halogen emissions from snow, vertical mixing and atmospheric chemistry. Primary emissions of Cl_2 from snow, parameterized using solar irradiance and measured surface ozone concentration, can describe surface observations of Arctic Cl_2. Modelled Br_2 levels are in good agreement with observations when using a combination of both primary emissions from snow and heterogeneous surface recycling of $BrONO_2$ and HOBr. Sensitivity analyses showed that increased heterogeneous recycling of halogens on aerosols could not explain surface observations and only provided a minor source of reactive halogens in our model simulations (AERO simulation).

- Boundary layer dynamics, vertical mixing, chemistry and emissions all strongly impact halogen vertical distribution. During the day, Cl_2 is confined to within the

Table 4.5: VOC lifetimes at 1.5 m and 50.5 m with respect to OH and Cl, at 12:00 AKST and 48-hour average in the NOSURF and BASE runs. Units h, d, and y represent time in hours, days, and years, respectively. HC3, HC5, and HC8 represent lumped hydrocarbon species with similar reactivities and average carbon chains of 3, 5, and 8, respectively.

	12:00 AKST			48-hour average		
Species	τ_{OH}^{NOSURF}	τ_{OH}^{BASE}	τ_{Cl}^{BASE}	τ_{OH}^{NOSURF}	τ_{OH}^{BASE}	τ_{Cl}^{BASE}
1.5 metres						
HC3	9.7 d	5.5 d	2.8 h	28.5 d	14.8 d	7.5 h
HC5[a]	4.4 d	2.5 d	1.6 h	13.1 d	6.8 d	4.4 h
HC8[a]	1.8 d	1.0 d	1.1 h	5.2 d	2.7 d	3.0 h
Ethane	139 d	79.4 d	7.1 h	1.1 y	212 d	19.3 h
Ethene	1.7 d	23.4 h	2.0 h	5.0 d	2.6 d	5.3 h
Acetaldehyde	20.9 h	12.0 h	4.8 h	2.6 d	1.3 d	13.1 h
Acetone	112 d	64.0 d	11.6 d	329 d	171 d	31.9 d
MEK	15.9 d	9.1 d	9.2 h	46.9 d	24.3 d	1.0 d
Aldehydes ($\geq C_3$)	15.7 h	9.0 h	3.0 h	1.9 d	1.0 d	8.1 h
Toluene	2.2 d	1.2 d	6.5 h	6.4 d	3.3 d	17.8 h
50.5 metres						
HC3	20.8 d	20.9 d	10.3 y	64.6 d	64.6 d	32.4 y
HC5[a]	9.5 d	9.6 d	6.0 y	29.7 d	29.7 d	18.9 y
HC8[a]	3.8 d	3.9 d	4.2 y	11.9 d	11.9 d	13.1 y
Ethane	295 d	297 d	26.6 y	2.5 y	2.5 y	83.5 y
Ethene	3.7 d	3.7 d	7.4 y	11.5 d	11.5 d	23.1 y
Acetaldehyde	1.9 d	1.9 d	18.0 y	5.9 d	5.9 d	56.6 y
Acetone	241 d	243 d	1042 y	2.1 y	2.1 y	3275 y
MEK	34.4 d	34.6 d	34.2 y	107 d	107 d	108 y
Aldehydes ($\geq C_3$)	1.4 d	1.4 d	11.1 y	4.4 d	4.4 d	34.9 y
Toluene	4.7 d	4.8 d	24.4 y	14.7 d	14.7 d	76.8 y

[a]Reactions of HC5 and HC8 with Cl were not included in the chemical mechanism. We therefore calculate approximate chemical lifetimes using the rate constants of n-pentane and isopentane (in equal proportions) with Cl for HC5 and n-octane and iso-octane (in equal proportions) with Cl for HC8. Rate constants are obtained from Calvert et al. (2015) at 248 K.

lowest 15 m of the atmosphere on both days of the simulation period. Stable conditions during this period resulted in a shallow surface layer, hindering vertical mixing and impacting surface concentrations. In particular, changes in the model vertical mixing and boundary layer dynamics result in a reduction of up to 60 pptv of Cl_2 at 1.5 m during the day (BLD simulation).

- HO_x radical concentration is increased by up to a factor of 30 with the inclusion of halogen emissions in the model. The increase in OH was primarily driven by elevated HOBr levels and its subsequent photolysis (R4.6). A significant contributor of HO_2 production is the CH_3O_2 radical formed via the Cl + CH_4 reaction (R4.4). This also caused a decrease in the modelled OH/HO_2 ratio which is attributable to chlorine chemistry.

- Increased HO_x radicals and a high Cl atom concentration near the surface significantly increases chemical reactivity within a shallow layer near the surface. Modelled VOC lifetimes, with respect to OH, are reduced by approximately 43% due to the presence of halogens (BASE run). Cl atoms concentrated near the surface rapidly react with VOCs, but this reactivity becomes much weaker with height and negligible over 15 m above the surface.

We have proposed two model parameterizations for Cl_2 and Br_2 emissions from land-based snow that have been applied to understanding observations during OASIS. Toyota et al. (2011) and recently Marelle et al. (2021) have considered bromine activation, triggered from snow on sea ice, with different efficiency in sunlit compared to dark conditions. In these studies, land-based snow sustains bromine chemistry via conversion of deposited HOBr, $BrONO_2$, and HBr to form Br_2 via reaction of trace quantities of bromide that is assumed to be present in all land-based snow. This is likely too simplified, but works, due to the fact that activated bromine in the atmosphere is lost via deposition and other processes away from the coasts, which also turns off the land-based snow source of Br_2. Here we propose a slightly different approach, which is consistent with our prior modelling study at Summit, Greenland (Thomas et al., 2011) that showed trace amounts of bromide in snow can be activated via photochemistry without enhanced

atmospheric bromine already present. This approach is also consistent with the chamber studies presented in Pratt et al. (2013), which showed that land-based snow can release reactive bromine without the need for any other triggers than ozone and sunlight. Land-based snow as a primary source of activated bromine should be tested in 3D regional models using this proposed parameterization, however we note this may not be important regionally compared to the quantities of bromine that are released from snow on sea ice and sea salt aerosols. Physical changes in the snowpack or other properties tied to temperature also influence bromine release from snow on sea ice. For example, Burd et al. (2017) have shown that over the Arctic Ocean atmospheric bromine chemistry is quickly deactivated upon warming to near freezing temperatures and that bromine chemistry is reactivated upon fresh snowfall. The deactivation of bromine release from snow on sea ice upon reaching near freezing temperatures is already included in some models (Marelle et al., 2021; Toyota et al., 2011). At present, less is known on how temperature changes (including related changes in snow physics, impurity locations, etc.) influence bromine release from land-based snow. The inland snow source of reactive bromine is already partially considered in the Toyota et al. (2011) land-based snow treatment which considers all snow to have reactive bromide available for release upon HBr, $BrONO_2$, and HOBr deposition. However, the exact description of how this works is not known and hypotheses should be tested in models and further characterised via observations in the future.

Our modelling work suggests that some description of chlorine emissions from snow is needed to capture the atmospheric chemistry occurring near the surface during Arctic spring. Coastal Arctic surface stations where chlorine has been observed are also the same stations where all long term observations of VOCs, aerosols, and ozone are made. Therefore, understanding and modelling how chlorine contributes to atmospheric chemistry at these locations is essential. We have proposed a model parameterization of chlorine release from land-based snow that depends on available sunlight and ozone. This description needs to be tested during other periods of the year and under different conditions. How this chlorine source depends on other parameters, such as snow chlorine content, snow properties, etc., is currently not known due to very limited observations of activated chlorine in the Arctic atmosphere. There is also some evidence that chlorine emissions

should be considered from snow on sea ice (e.g. Peterson et al. (2019)). The regional and seasonal sensitivity to potential snow emissions of chlorine needs to be explored with model sensitivity studies using reasonable hypotheses and with dedicated observations in the future.

One of the most important conclusions from our study is that the vertical extent of a highly oxidising layer with active chlorine chemistry may only extend to 15 metres above the snow surface. This is much smaller than the vertical resolution of most regional and global models. The effects of this highly oxidising layer on new particle formation, aerosol processing, VOC chemistry, and other atmospheric chemistry processes need to be explored and eventually included in models. One possibility is to implement sub-grid scale parameterizations of these processes with regional and global chemical models in the future. The influence of bromine chemistry vertically and with respect to the presence of aerosols and mesoscale weather systems has been relatively well characterised (Blechschmidt et al., 2016; Burd et al., 2017; Liao et al., 2012a; Oltmans et al., 2012; Peterson et al., 2017; Simpson et al., 2017). However, less is known from observations regarding whether there is active chlorine chemistry above the surface. More observations are needed to quantify both bromine and chlorine chemistry above the surface in order to understand how to best include these effects within models.

Acknowledgments

This work was supported by the Ecole Doctorale Sciences de la Terre, de l'Environnement et des Planètes (ED105) of Université Grenoble Alpes. We also acknowledge support by the CNRS INSU LEFE-CHAT program under the grant Brom-Arc. This material is based upon work supported by the National Center for Atmospheric Research, which is a major facility sponsored by the National Science Foundation under Cooperative Agreement No. 1852977. Support for Detlev Helmig and Patrick Boylan from the NSF grant 0902165 is acknowledged. Additional support to NCAR under the NSF grants 0806437 and 0732556 are also acknowledged. We thank the entire OASIS team involved in the campaign and the collection of data with special thanks to: Jin Liao, Andrew Weinheimer, Jim Smith, Roy Mauldin, James Walega, Petter Weibring and Dirk Richter. We also thank colleagues

Aurélien Dommergue, Didier Voisin, Pierre Rampal, Anna Jones and Thorsten Bartels-Rausch for meaningful scientific discussions.

Data Availability Statement

The code for the model and input files are all publicly available on Zenodo as Ahmed et al. (2022b) (https://doi.org/10.5281/zenodo.6045999). The model outputs for the BASE run can also be found on Zenodo at https://doi.org/10.5281/zenodo.5654628. The data for this campaign are publicly available through the NSF Arctic Data Center at https://arcticdata.io/.

Chapter 5

Modelling the coupled mercury, ozone, and bromine cycles in the central Arctic spring atmosphere during MOSAiC with WRF-Chem

Contents

Preface

Following the study of local scale halogen emissions and chemistry in PACT-1D, it was also important to assess the regional impacts of halogen chemistry on the polar ozone and mercury cycles. At the start of this PhD project, very few regional models were available that could accurately depict the springtime depletion of ozone and mercury in the Arctic. Most available models were limited in some aspects, such as: missing descriptions of halogen activation processes, simplified mercury redox chemical mechanisms, poor representation of boundary layer dynamics, assumptions of monthly averaged oxidant concentration, and low spatial/temporal resolution. This gap in the mercury modelling community highlighted a need for an Arctic-focused model, capable of studying the interconnected halogen, ozone, and mercury cycles during polar springtime. In addition, recent measurements of Hg(0), O_3, and BrO were obtained simultaneously in the central Arctic, during the Multidisciplinary drifting Observatory for the Study of Arctic Climate (MOSAiC) expedition. This presented a rare opportunity to study these coupled cycles in the central Arctic, and, assess model performance where observations have generally remained sparse.

These factors have inspired the work presented in this chapter, to address the following research objectives of the thesis:

- Can regional modelling be used to accurately represent springtime ozone and mercury depletion events in the central Arctic on an hourly timescale?
- How does mercury redox chemistry impact deposition rates in the Arctic? What are the relative amounts of mercury re-emission and retention in the Arctic snowpack?

In addition, a secondary goal of this work was to provide the research community with an improved model to study Arctic Hg chemistry at high resolution in future studies. The model version developed and used in this chapter is publicly available at Ahmed et al. (2022a) (https://doi.org/10.5281/zenodo.7137482)

This chapter is in review for publication in *Elementa: Science of the Anthropocene*.

After: Ahmed, S., Thomas, J. L., Angot, H., Dommergue, A., Archer, S. D., Bariteau, L., Beck, I., Benavent, N., Blechschmidt, A.-M., Blomquist, B., Boyer, M., Christensen, J. H., Dahlke, S., Dastoor, A., Helmig, D., Howard, D., Jacobi, H.-W., Jokinen, T., Lapere, R., Laurila, T., Quéléver, L. L. J., Richter, A., Ryjkov, A., Mahajan, A. S., Marelle, L., Pfaffhuber, K. A., Posman, K., Rinke, A., Saiz-Lopez, A., Schmale, J., Skov, H., Steffen, A., Stupple, G., Stutz, J., Travnikov, O., Zilker, B. (in review). Modelling the coupled mercury, ozone, and bromine cycles in the central Arctic spring atmosphere during MOSAiC with WRF-Chem. *Elementa: Science of the Anthropocene*.

Abstract

Near surface mercury (Hg(0)) and ozone (O_3) depletion events occur in the lowest part of the atmosphere during Arctic spring. Mercury depletion is the first step in a process that transforms long-lived Hg(0) to more reactive forms within the Arctic that are deposited to the cryosphere, ocean, and other surfaces, which can ultimately get integrated into the Arctic food web. Depletion of both mercury and ozone occur due to the presence of reactive halogen radicals that are released from snow, ice, and aerosols. In this work, we add a detailed description of the Arctic atmospheric mercury cycle to our recently published version of WRF-Chem 4.3.3 that includes Arctic bromine and chlorine chemistry and activation/recycling on snow and aerosols. The major advantage of our modelling approach is the online calculation of bromine concentrations and emission/recycling that is required to simulate the hourly and daily variability of Arctic mercury depletion. We use this model to study coupling between reactive cycling of Hg, O_3, and bromine during the Multidisciplinary drifting Observatory for the Study of Arctic Climate (MOSAiC) spring season in 2020 and evaluate results compared to land based, ship based, and remote sensing observations. The model predicts that Hg(0) oxidation is largely driven by bromine chemistry and that particulate mercury (Hg(p)) is the major form of oxidized mercury. The model predicts that the majority (74 %) of oxidized mercury deposited to land-based snow is re-emitted to the atmosphere as Hg(0), while a minor fraction (4 %) of oxidized mercury that is deposited to sea ice is re-emitted during spring. Our work demonstrates that hourly differences in bromine/ozone chemistry in the atmosphere must be considered to capture the springtime Arctic mercury cycle including its integration into the cyrosphere and ocean.

5.1 Introduction

Each spring halogens released from snow, sea ice, and sea salt aerosols cause the depletion of boundary layer ozone (O_3) and mercury (Hg) in the Arctic (Abbatt et al., 2012; Barrie, 1986; Barrie et al., 1988; Bottenheim et al., 1990; Lindberg et al., 2001; Oltmans, 1981; Schroeder et al., 1998; Simpson et al., 2007; Skov et al., 2004; Wang et al., 2019). Deple-

tion occurs when halogens and other radicals in the atmosphere oxidize Hg(0) to Hg(II), which is much shorter-lived, and is directly taken up onto aerosols, snow, ice and the open ocean (Douglas et al., 2012; Selin, 2009). Oxidized mercury present in particles is also removed to ice, snow, and the ocean via both wet and dry deposition. Once deposited to the Arctic Ocean, mercury can undergo transformation to more toxic forms, including methylmercury, that are harmful to ecosystems and human health (Driscoll et al., 2013). The main form of atmospheric Hg is long-lived, gaseous elemental mercury (Hg(0)), emitted from both anthropogenic (e.g., coal burning and artisanal gold mines) and natural sources (e.g., volcanoes) (AMAP, 2011; Lindberg and Stratton, 1998). Anthropogenic Hg sources in the Arctic are estimated to be less than 1 % of global Hg emissions to air, with most Arctic Hg(0) originally from emissions from distant sources (Dastoor et al., 2022b; Durnford et al., 2010; Skov et al., 2020). Understanding the fate of Arctic Hg that involves air-surface exchange processes remain a challenge, including: integration of mercury from the atmosphere into the cryosphere and ocean; storage of oxidized mercury in snow and ice; and photochemical re-emissions of mercury back to the atmosphere.

Developing models that describe diurnal variation and cycling of mercury in the lowest part of the Arctic atmosphere has remained a challenge because of the complexity of chemical and physical processes involved. In addition, closely coupled chemical cycles, such as halogens, have recently been improved within Arctic atmospheric models (e.g., Falk and Sinnhuber, 2018; Fernandez et al., 2019; Herrmann et al., 2022; Marelle et al., 2021; Swanson et al., 2022; Toyota et al., 2011; Yang et al., 2008, 2010, 2019). Figure 5.1 illustrates the main chemical processes of Hg in the Arctic boundary layer. During atmospheric mercury depletion events (AMDEs), Hg(0) is oxidized forming gaseous oxidized mercury (GOM or Hg(II)) and particulate mercury species (Hg(p)), which are deposited to the cryosphere via dry and wet processes (Ariya et al., 2015; Brooks et al., 2006; Lindqvist and Rodhe, 1985; Skov et al., 2006). AMDEs are linked to high concentrations of reactive bromine (e.g., Br_2, Br, BrO, HOBr, and $BrONO_2$), activated from trace amounts of oceanic bromide on snow and ice surfaces (Brooks et al., 2006; Lu et al., 2001; Stephens et al., 2012; Sommar et al., 2007; Wang et al., 2019). This occurs simultaneously with the well-studied depletion of surface ozone, known as ozone depletion events (ODEs) (Abbatt

et al., 2012; Barrie et al., 1988; Platt and Hönninger, 2003; Simpson et al., 2007, 2015). Upon deposition of Hg to snow, a fraction can be photoreduced and re-emitted back into the atmosphere as Hg(0) (e.g., Brooks et al., 2006; Dommergue et al., 2010; Douglas and Blum, 2019; Durnford and Dastoor, 2011; Ferrari et al., 2008; Kirk et al., 2006; Poulain et al., 2004; Skov et al., 2006; Sommar et al., 2007; Steffen et al., 2013). Chemical transformation between Hg(0), Hg(II), and Hg(p) can occur rapidly and is driven by several factors including oxidant and aerosol concentrations, air temperature, and solar radiation (Ariya et al., 2015). Currently, many models are limited in capturing the behaviour of Hg in Arctic spring due to: (1) uncertainties in the mercury chemical mechanism; (2) use of offline-calculated oxidant concentrations including reactive bromine; (3) a lack of detailed halogen chemistry/emission processes over snow and sea ice; and/or (4) poorly represented Arctic boundary layer meteorology (Angot et al., 2016; Travnikov et al., 2017).

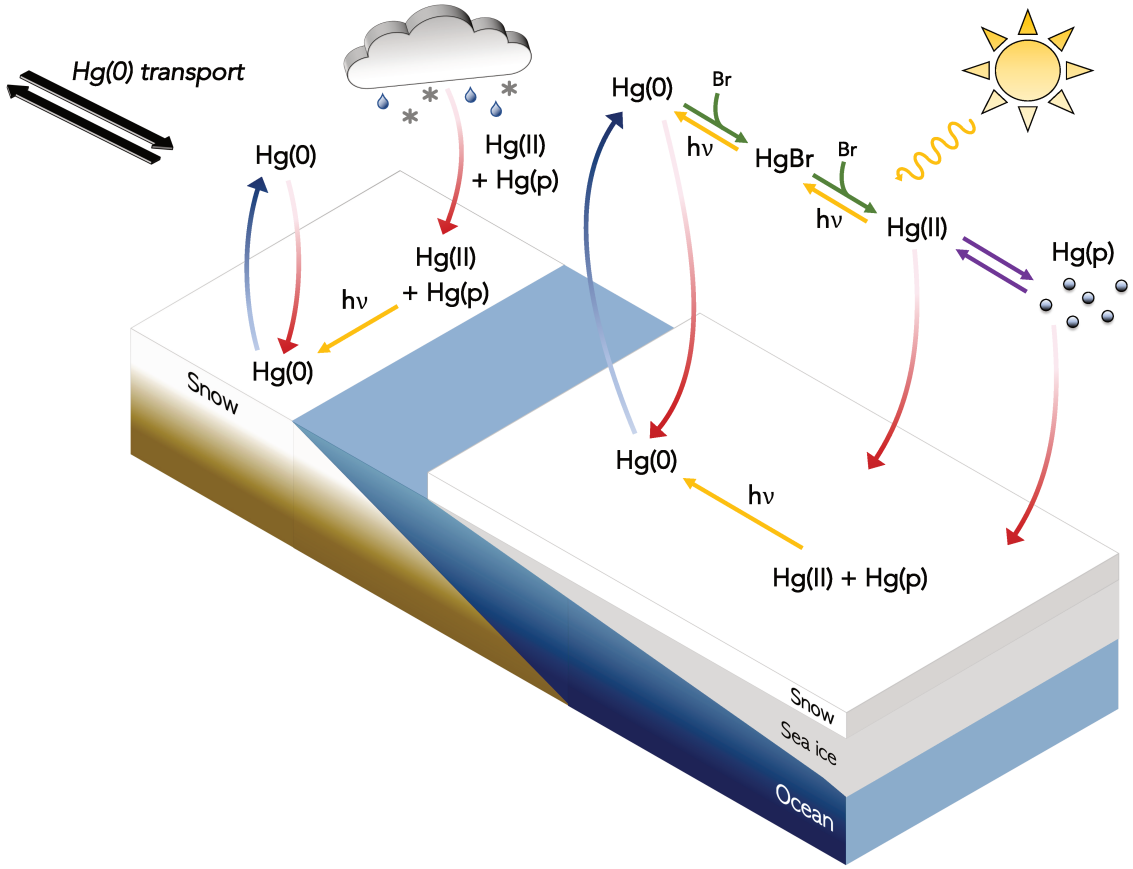

Figure 5.1: Overview schematic of Arctic Hg chemical processes represented in WRF-Chem. Hg(0) denotes gaseous elemental mercury, Hg(II) is gaseous oxidized mercury, and Hg(p) represents particulate mercury.

Bromine is a central species in Arctic O_3 and Hg(0) depletion and is considered to be the major oxidant driving AMDEs (Wang et al., 2019). Elevated Br concentrations in the Arctic are known to occur due to the uptake and emission of reactive bromine on surfaces, which occurs via autocatalytic process on snow, ice, and aerosols known as the "bromine explosion" (Simpson et al., 2007, 2015). Two main bromine activation mechanisms in the Arctic have been proposed and tested in 3D chemical transport models. The first method, proposed by Toyota et al. (2011), involves the activation of bromide in the top layer of the snowpack, triggered by ozone deposition or heterogeneous recycling of HOBr and $BrONO_2$ (Falk and Sinnhuber, 2018; Fernandez et al., 2019; Herrmann et al., 2021; Marelle et al., 2021; Swanson et al., 2022; Toyota et al., 2011). The second method involves the release of bromine from sea salt aerosols (SSA), formed via sublimation of lofted blowing snow, as proposed by Yang et al. (2008) (Huang and Jaeglé, 2017; Huang et al., 2018, 2020; Rhodes et al., 2017; Yang et al., 2008, 2010, 2019, 2020). Both mechanisms have been shown to have important impacts on reactive bromine and ozone concentrations in the Arctic, thus necessary to consider in models for springtime chemistry.

Descriptions of mercury in models often differ in their treatment of physical and chemical processes, partly due to current knowledge gaps (Ariya et al., 2015). Multi-model intercomparisons are therefore useful to assess the impacts of different model parameterizations on the behaviour of atmospheric Hg (Angot et al., 2016; Dastoor et al., 2022a; Travnikov et al., 2017). Arctic-focused model intercomparisons have shown that several models are capable of simulating the seasonality in surface Hg(0) concentrations (spring minima and summer maxima), however, can underestimate the amplitude of the seasonal variation (Angot et al., 2016; Dastoor et al., 2022a). Several factors are likely to contribute to this disparity, which underscore some of the limitations of current global models. First, most global models that include Hg chemistry use monthly-averaged oxidant fields to simulate Hg(0) oxidation (Durnford et al., 2012; Holmes et al., 2010; Horowitz et al., 2017; Shah et al., 2021; Song et al., 2015). For the purpose of studying springtime mercury chemistry, this approach is inadequate as it neglects the diurnal variability of oxidants, including bromine, in the Arctic (Angot et al., 2016). Secondly,

the low spatial and temporal resolution of global models may not sufficiently resolve the local chemistry and emissions occurring that contribute to AMDEs during spring (Toyota et al., 2014b). Bromine production mechanisms from snow and sea ice can therefore be inaccurately represented, which are crucial for polar atmospheric chemistry. In comparison to global models, regional models are computationally less expensive at high spatial resolution and can calculate oxidant concentrations online, making them ideal tools for studying AMDEs.

Here, we update our Arctic specific version of the regional Weather Research and Forecasting model coupled with Chemistry (WRF-Chem) model (Marelle et al., 2021) to include the atmospheric mercury cycle described in (Shah et al., 2021). This version of WRF-Chem 4.3.3 currently includes detailed bromine emissions from both Arctic surface snow and blowing snow, previously shown to improve model representation of Arctic ODEs (Marelle et al., 2021). In this dedicated Arctic study, we investigate the impacts of polar bromine activation on springtime Hg and O_3 chemistry and depletion, during spring 2020. To evaluate the model, we compare with data from Arctic stations and from the central Arctic obtained on board the Research Vessel (RV) *Polarstern* during the Multidisciplinary drifting Observatory for the Study of Arctic Climate (MOSAiC) campaign in spring 2020 (Shupe et al., 2022). The new mercury developments and WRF-Chem model setup are presented in Section 5.2, with the observations used to evaluate the model described in Section 5.3. In Section 5.4, we evaluate the model against meteorological and chemical observations from MOSAiC. Section 5.5 assess the model performance compared to other Arctic observations, as well as a discussion of the simulated pan-Arctic impacts. Finally, the outcomes and conclusions are presented in Section 5.6.

5.2 WRF-Chem model

5.2.1 Implementation of mercury chemistry in WRF-Chem

We extend the work of Marelle et al. (2021) by including Hg gas-phase chemistry and photolysis, heterogeneous uptake to aerosols and liquid clouds, dry and wet deposition processes, and Hg(0) re-emission from continental snow and snow on sea ice. These up-

dates are based largely on the latest developments in other Hg chemical transport models (e.g., Amos et al., 2012; Fisher et al., 2012, 2013; Gencarelli et al., 2014; Holmes et al., 2010; Horowitz et al., 2017; Shah et al., 2021), which are implemented in the WRF-Chem model here. The model developments presented in this study are publicly available as Ahmed et al. (2022a).

Hg gas-phase chemistry and photoreduction

Atmospheric Hg(0) oxidation is understood to proceed via several pathways, however the relative importance of each oxidant on the global Hg budget remains a subject of debate (Ariya et al., 2015; Subir et al., 2011). Determining the kinetics and speciation of oxidized mercury is an ongoing analytical challenge due to very low atmospheric Hg(II) concentrations (picograms per cubic meter, pg m^{-3}) and limitations in instrument sensitivity (Hynes et al., 2009; Subir et al., 2011). Here, we include gas-phase oxidation of Hg(0) via Br, Cl, and OH, to the SAPRC-99 (Statewide Air Pollution Research Center, 1999 version; Carter (2000)) chemical mechanism in WRF-Chem, following the chemistry scheme of Shah et al. (2021). We have used the SAPRC-99 chemical mechanism for this study due to the demonstrated performance of this setup for Arctic ozone inland (see Figure 15 from Petäjä et al. (2020)) and during bromine-mediated ozone depletion events (see Figures 3 & 4 from Marelle et al. (2021)). Chemical concentrations (including oxidants such as OH and Br) are calculated online in the WRF-Chem model. Hg gas-phase reactions are added to a previously developed chemical mechanism (Marelle et al., 2021), which includes chlorine and bromine gas-phase chemistry, using the Kinetic PreProcessor (KPP, Sandu and Sander (2006)). Hg(0) oxidation is treated as a two-step process, first forming a Hg(I) intermediate, which can be reduced to Hg(0) (via photoreduction or thermal dissociation), before undergoing further oxidation to Hg(II) (Goodsite et al., 2004, 2012). The full list of oxidized Hg species included in the model is listed in Table 5.1 (column 1).

The role of atmospheric Hg(II) reduction on the global Hg cycle is also uncertain, as rate constants are largely based on theoretical estimates yet to be experimentally verified (Balabanov et al., 2005; Dibble et al., 2012, 2020; Francés-Monerris et al., 2020;

Table 5.1: Modelled tropospheric Hg budget in the model domain during the simulation period (March 14 – April 14 2020). Percent contributions of each Hg(I) and Hg(II) species are represented as a fraction of the total Hg(I) and Hg(II) budget. HgX denotes gas-phase Hg(II) volatilized from Hg(p) (treated as $HgCl_2$ in the model).

Species	**Budget (Mg)**	**Percent contribution (%)**
Hg(0)	**927**	**95.6**
Hg(I)	**1.34×10^{-4}**	**$<$ 0.1 (100)**
HgBr	9.69×10^{-5}	72.3
HgBrO	2.49×10^{-5}	18.6
HgOHO	8.94×10^{-6}	6.7
HgOH	3.34×10^{-6}	2.5
HgClO	2.98×10^{-9}	$<$ 0.1
HgCl	2.50×10^{-9}	$<$ 0.1
Hg(II)	**42.8**	**4.4 (100)**
Hg(p)	27.1	63.2
HgX	15.0	35.1
HgOHOH	0.567	1.3
HgBrOH	0.165	0.4
HgBrBrO	1.44×10^{-3}	$<$ 0.1
$HgBr_2$	1.35×10^{-3}	$<$ 0.1
HgBrClO	1.90×10^{-4}	$<$ 0.1
HgBrCl	2.01×10^{-4}	$<$ 0.1
HgClClO	1.78×10^{-4}	$<$ 0.1
HgOHClO	1.42×10^{-4}	$<$ 0.1
HgClOH	1.28×10^{-4}	$<$ 0.1
$HgBrNO_2$	9.10×10^{-5}	$<$ 0.1
HgOHBrO	6.68×10^{-5}	$<$ 0.1
HgClBrO	6.41×10^{-5}	$<$ 0.1
$HgBrHO_2$	5.63×10^{-5}	$<$ 0.1
$HgOHNO_2$	5.54×10^{-5}	$<$ 0.1
$HgClNO_2$	5.53×10^{-5}	$<$ 0.1
$HgClHO_2$	4.43×10^{-5}	$<$ 0.1
$HgOHHO_2$	4.06×10^{-5}	$<$ 0.1
Total	970	100

Gómez Martín et al., 2022; Goodsite et al., 2004, 2012; Khiri et al., 2020; Saiz-Lopez et al., 2018, 2019; Sitkiewicz et al., 2019). Recent modelling studies have shown that atmospheric Hg(II) reduction must be considered in models to match observational estimates of total gaseous mercury lifetime against deposition (Horowitz et al., 2017; Shah et al., 2021; Zhang and Zhang, 2022). We therefore add to WRF-Chem photoreduction reactions of Hg(I) and Hg(II) species, following the implementation of Shah et al. (2021). Photochemical rates are calculated using the FastJ photolysis scheme in WRF-Chem (Wild et al., 2000), from computationally-derived quantum yields (ϕ) and absorption cross sections (σ) of Hg(I) and Hg(II) species. For Hg(I), we use $\phi = 0$ for non-dissociative transitions in the wavelength range of 270 – 460 nm, and $\phi = 1$ for transitions in the 460 – 800 nm range, as in Saiz-Lopez et al. (2019). Values of σ for Hg(I) species are also taken from Saiz-Lopez et al. (2019). For Hg(II), values of ϕ are taken from Francés-Monerris et al. (2020) and σ values are taken from Saiz-Lopez et al. (2018). We do not include the photoreduction of Hg(p) as the rate of this reaction remains highly uncertain.

Heterogeneous uptake and gas-particle partitioning

Surface uptake of gas-phase Hg(II) onto aerosols and clouds is an important process for the formation of Hg(p) in the Arctic, particularly during spring (Steffen et al., 2013, 2014). Uptake and volatilization of Hg(II) to/from surfaces is a complex process influenced by several variables including: temperature, fine particle concentration, and aerosol chemical composition (Subir et al., 2012). We use a parameterized approach to represent Hg heterogeneous chemistry in WRF-Chem, using the 8-bin sectional aerosol scheme MOSAIC (Model for Simulating Aerosol Interactions and Chemistry, not related to the MOSAiC expedition) (Zaveri et al., 2008). We include the heterogeneous uptake of all Hg(II) species on aerosols and liquid clouds. This process is treated as a kinetic process with the uptake rate, k_{het}, calculated for each aerosol size bin and summed to obtain a total heterogeneous uptake rate, following equation (5.1) (Jacob, 2000; Schwartz, 1986):

$$k_{\text{het}} = \sum_{i}^{n=8} A_i \left(\frac{r_i}{D_g} + \frac{4}{\nu \alpha} \right)^{-1} \tag{5.1}$$

where k_{het} is the total reactive uptake rate (s^{-1}), A_i and r_i are the effective mean aerosol surface area (cm^2/cm^3_{air}) and aerosol radius (cm) for aerosols in size bin i, D_g is the diffusion coefficient ($cm^2\ s^{-1}$), ν is the mean molecular speed (cm s^{-1}) and α is the mass accommodation coefficient (unitless). We assume $\alpha = 0.1$ for uptake of all Hg(II) species onto aerosols and liquid clouds, following Shah et al. (2021). For liquid clouds, we calculate the uptake rate in a similar way to equation (1), using the average cloud droplet surface area and radius for A and r, respectively (see Figure B.1 for average modelled surface values). For computational efficiency, Hg(p) is not explicitly modelled in the aerosol-phase and is treated here as an additional gas-phase species.

We also include the conversion of Hg(p) on aerosols back to gas-phase Hg(II) via volatilization. This process is parameterized based on the empirical gas-particle equilibrium of Amos et al. (2012) and is considered only for fine-mode aerosols ($\leq 2.5\ \mu$m), corresponding to the first 6 MOSAIC aerosol size bins. This empirical equilibrium, described by Amos et al. (2012), defines the ratio of Hg(II) and Hg(p) available as a function of particulate matter ($PM_{2.5}$) concentration and air temperature. Volatilized Hg(II) gas, denoted as HgX, is treated in the model as $HgCl_2$, which does not photolyze at tropospheric wavelengths (Saiz-Lopez et al., 2018).

Dry and wet deposition of mercury

The transformation between Hg(0), Hg(II), and Hg(p) has important consequences on the dry and wet deposition rates of Hg over the Arctic (Zhang et al., 2009). We include dry deposition for all added Hg species (Hg(0), Hg(II), and Hg(p)), excluding Hg(I) species as they are thermally unstable and short-lived intermediates. Dry deposition of Hg(0) is calculated based on the Wesley resistance scheme (Wesely, 1989) and is implemented using four species-specific parameters: the Henry's law constant (H^*); the Henry's law temperature correction factor (DHR); a surface reactivity factor (f_0); and the molecular diffusivity (dvj). For Hg(0), we use values of $H^* = 0.11$ mol m^{-3} hPa^{-1} and DHR = 4800 K from Clever et al. (1985), $f_0 = 1.0 \times 10^{-5}$ from Selin et al. (2008), and dvj = 0.071 cm^{-2} s^{-1} based on the inverse square root of the molar mass of Hg(0). Henry's law constants for Hg(II) species are less well known and so we assume a dry deposition velocity of

0.1 cm s^{-1} for all Hg(II) species based on estimates of reactive gaseous mercury dry deposition to ice surfaces (Lindberg et al., 2002; Skov et al., 2006; Zhang et al., 2009). Measurements of the dry deposition velocity of Hg(p) currently remain limited, however previous results have shown that Hg(p) deposits several times slower than Hg(II) (Poissant et al., 2004; Zhang et al., 2012). We therefore assume a dry deposition velocity of 0.01 cm s^{-1} for Hg(p), but we note that this assumption should be revised in future work as more measurements become available.

We also add to the model wet removal of Hg(II) and Hg(p) considering both in-cloud (washout) and below-cloud (rainout) scavenging. Hg(II) is highly soluble however the Henry's law constants for each individual species remain relatively unknown. We therefore assume the wet scavenging rates of Hg(II) and Hg(p) to be equal to that of HNO_3, based on similarities in solubility and on previous Hg modelling work (Gencarelli et al., 2014; Seigneur et al., 2004). This assumption is an imperfect simplification and should be revised in future developments of the model.

Hg(0) re-emission from snow and sea ice

The fate of deposited Hg(II) to the Arctic snowpack remains a major scientific question, with reported Hg(0) re-emission ranging between 40–90 % of deposited Hg(II) during AMDEs (Brooks et al., 2006; Dommergue et al., 2010; Douglas and Blum, 2019; Durnford and Dastoor, 2011; Ferrari et al., 2008; Kirk et al., 2006; Lalonde et al., 2002; Poulain et al., 2004; Skov et al., 2006; Sommar et al., 2007; Steffen et al., 2013). The amount of Hg(0) re-emitted can depend on several factors including the chemical composition of snow, the amount of solar radiation, snow temperature, liquid water content of snow, and snowpack ventilation and gas transport (Dommergue et al., 2007; Ferrari et al., 2005; Lalonde et al., 2003; Mann et al., 2015a,b, 2018; Poulain et al., 2004; Steffen et al., 2002, 2013). Here, we add a description of Hg(0) re-emission from both land-based snow and snow on sea ice. Total reactive mercury (RM = Hg(II)+ Hg(p)) that has been deposited to the snow surface is tracked in the model and stored as a surface reservoir. We assume 60% of deposited RM at the surface is photoreducible and available for re-emission under sunlit conditions, following Holmes et al. (2010) and Fisher et al. (2012). The sensitivity

of this value is tested by performing a simulation with 100 % of RM in snow available for re-emission. The rate of Hg(0) re-emission from land-based snow and snow on sea ice is parameterized in the model following equations (5.2) and (5.3), respectively:

$$R_{\mathrm{Hg^0}}^{\mathrm{snow}} = k_{\mathrm{red}}^{\mathrm{snow}} \times \cos(\mathrm{SZA}) \times f_{\mathrm{snow}} \tag{5.2}$$

$$R_{\mathrm{Hg^0}}^{\mathrm{sea\ ice}} = k_{\mathrm{red}}^{\mathrm{sea\ ice}} \times \cos(\mathrm{SZA}) \times f_{\mathrm{sea\ ice}} \tag{5.3}$$

where $R_{\mathrm{Hg^0}}^{\mathrm{snow}}$ and $R_{\mathrm{Hg^0}}^{\mathrm{sea\ ice}}$ are the rates of Hg(0) re-emission ($\mathrm{s^{-1}}$) from land-based snow and snow on sea ice, respectively. $k_{\mathrm{red}}^{\mathrm{snow}}$ and $k_{\mathrm{red}}^{\mathrm{sea\ ice}}$ are the net reduction rate constants of RM ($\mathrm{s^{-1}}$) from land-based snow and snow on sea ice, respectively, cos(SZA) is the cosine of the solar zenith angle (dimensionless), and f_{snow} and $f_{\mathrm{sea\ ice}}$ are the fractions of each grid cell ($0-1$, dimensionless) covered by snow or sea ice, respectively. For land-based snow, we use $k_{\mathrm{red}}^{\mathrm{snow}} = 2.5 \times 10^{-5}$ $\mathrm{s^{-1}}$ (0.09 $\mathrm{h^{-1}}$), following Poulain et al. (2004), and for snow on sea ice we assume a lower value of $k_{\mathrm{red}}^{\mathrm{sea\ ice}} = 2.8 \times 10^{-7}$ $\mathrm{s^{-1}}$ (0.001 $\mathrm{h^{-1}}$) based on a mid-range value from observational estimates (Durnford and Dastoor, 2011), following Fisher et al. (2012). Current estimates of k_{red} in Arctic snow samples have a large variability, with reported values ranging from 7×10^{-6} to 0.6 $\mathrm{h^{-1}}$ (Poulain et al., 2004; Dommergue et al., 2007; Mann et al., 2015b, 2018). Part of this variability can be explained by differences in measurement techniques, with some values reporting gross Hg(II) photoreduction rate constants, thereby neglecting the effects of in-snow Hg(0) oxidation (e.g., Mann et al., 2015b, 2018). The values of k_{red} used here are therefore tentative estimates to be examined further in future studies. A temperature dependence is applied for Hg(0) re-emissions, where re-emission is only active for snow-covered grid cells with a skin temperature below 0 °C. We also apply a fractional sea ice cutoff of 75 % for Hg(0) re-emission, in which grid cells below this sea ice threshold do not re-emit Hg(0), following similar descriptions of Br_2 emissions in Marelle et al. (2021).

5.2.2 Model setup

Model domain and simulation period

We set up the model for the dates between March 1, 2020 and April 14, 2020 during leg 3 of the MOSAiC expedition. In mid to late April 2020, warm air intrusions were observed reaching the *Polarstern*, transporting pollution from southern latitudes to the central Arctic (Dada et al., 2022). We therefore excluded this period from our model simulation as these events require a detailed evaluation of pollution transport which is beyond the scope of this study. The first 2 weeks of model output are considered spin-up and are not included in the analysis (see section 5.4.2). A horizontal resolution of 100 $\times$ 100 km is used to encompass the entire Arctic (model domain shown in Figure 5.2) with a vertical resolution of 72 levels up to a pressure of 50 hPa. Details about the model setup are given below and are selected based on extensive testing for the Arctic from previous studies (Marelle et al., 2017, 2021). A summary of the specific model chemistry and physics options selected are given in Table 5.2.

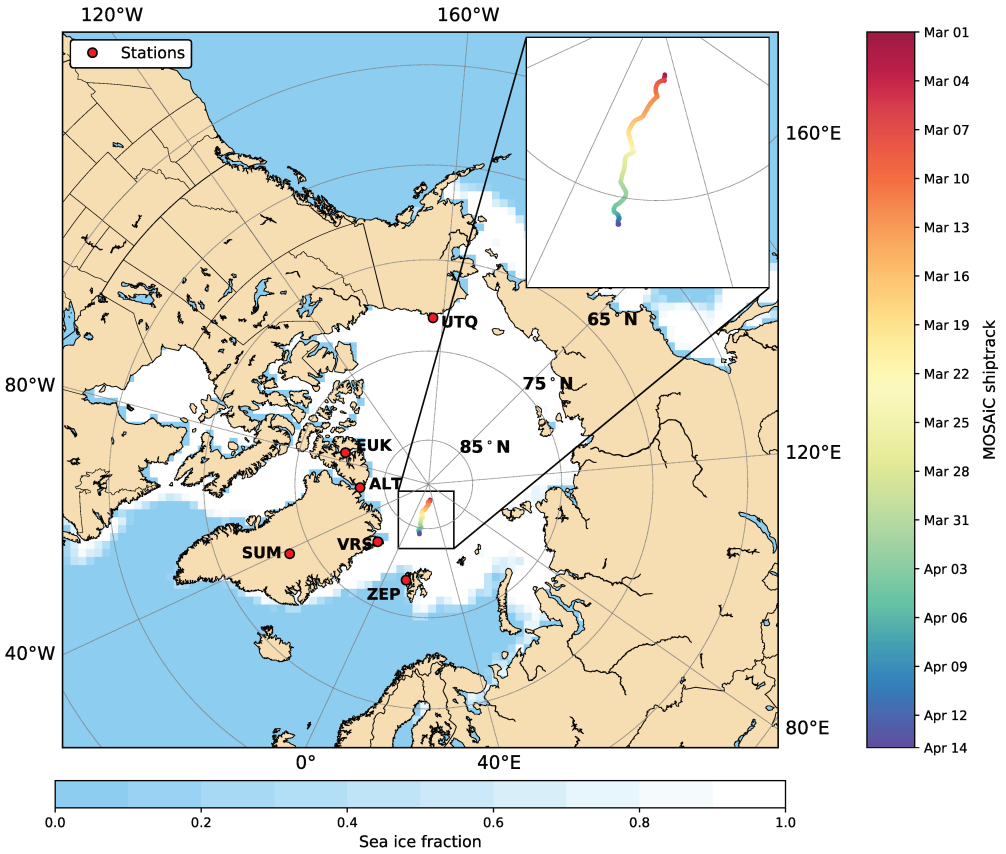

Figure 5.2: WRF-Chem model domain with sea ice fraction at the beginning of the simulation (1 March 2020). The MOSAiC Polarstern shiptrack between March 1 – April 14 2020 is shown. Stations used for the model comparison are indicated with red markers (UTQ = Utqiaġvik, Alaska; EUK = Eureka, Canada; ALT = Alert, Canada; VRS = Villum Research Station, Station Nord, Greenland; SUM = Summit, Greenland; and ZEP = Zeppelin Observatory, Svalbard).

Initial and boundary conditions

Initial and boundary conditions for meteorology are obtained from the National Centers for Environmental Prediction Final Analysis (NCEP FNL, National Centers for Environmental Prediction (2000)) and we apply spectral nudging within and above the boundary layer. The boundary layer scheme and land surface model used are the Mellor–Yamada Nakanishi Niino Level 2.5 Scheme (MYNN, Nakanishi and Niino (2009)) and the Noah Land Surface Model (NoahLSM, Tewari et al. (2004)) respectively. These options are selected as they were found to give the best representation of boundary layer dynamics in the Arctic from a number of different WRF dynamics configurations (Marelle et al.,

Table 5.2: WRF-Chem 4.3.3 model namelist options and inputs.

Physics and meteorology	**Model option**
Planetary boundary layer	MYNN 2.5 level TKE scheme (Nakanishi and Niino, 2009)
Surface layer	MYNN (Nakanishi and Niino, 2009)
Land surface	Noah LSM (Tewari et al., 2004)
Microphysics	Morrison (Morrison et al., 2009)
SW radiation	RRTMG (Iacono et al., 2008)
LW radiation	RRTMG (Iacono et al., 2008)
Cumulus parameterization	KF-CuP (Berg et al., 2015)
Meteorology initial and boundary conditions	NCEP FNL (National Centers for Environmental Prediction, 2000)
Chemistry and aerosol	**Model option**
Gas-phase chemistry	SAPRC-99(Carter, 2000; Marelle et al., 2021)
Aerosols	MOSAIC 8 bins (Zaveri et al., 2008) with VBS-2 SOA formation & aq. chem.
Photolysis	Fast-J (Wild et al., 2000)
Chemical initial and boundary conditions	CAM-Chem (Buchholz et al., 2019b; Emmons et al., 2020)
Hg(0) initial and boundary conditions	Global model ensemble
Emissions	**Model input**
Hg emissions	Global Mercury Assessment 2018 (GMA) (Steenhuisen and Wilson, 2019, 2022)
Anthropogenic emissions	ECLIPSEv6b (Klimont et al., 2017)
Fire emissisions	FINNv2.5 (Wiedinmyer et al., 2011, 2022)
Biogenic emissions	MEGAN (Guenther et al., 2012)

2021). Furthermore, we include an additional sea ice thickness variable from the TOPAZ4b model to better simulate surface temperatures over sea ice (E.U. Copernicus Marine Service Information, 2022).

Chemical concentration initial and boundary conditions are set using data from the global CAM-Chem model (Buchholz et al., 2019b; Emmons et al., 2020). We also include an initial and boundary concentration of atmospheric Hg(0), obtained from model output simulated by an ensemble of four chemical transport models (see section 5.3.4). More details about the model ensemble and its performance in the Arctic can be found in Dastoor et al. (2022a). Concentrations of RM are initialized as zero and are allowed to reach a natural equilibrium during the model spin-up period.

Interactive halogen emissions and recycling

We consider bromine emissions from snow/ice and aerosols using both surface snow and blowing snow sources of reactive bromine emissions and recycling, as described in Marelle et al. (2021). These are interactive parameterizations within the model that calculate Br_2 emissions online. Specifically, the surface snow mechanism calculates the emission of Br_2 following the deposition of ozone to the snowpack over sea ice (Toyota et al., 2011). This is accelerated under sunlit conditions compared to dark conditions. The blowing snow mechanism calculates the release of Br_2 and sea salt aerosols from the sublimation of lofted snow under windy conditions (wind speeds >7 m s^{-1}) (Yang et al., 2008, 2019). Finally, heterogeneous recycling of bromine on all frozen surfaces is also considered in this work, following Marelle et al. (2021). These interactive bromine emissions were evaluated in Marelle et al. (2021) by comparing with Arctic ozone observations, including in the central Arctic from ice-tethered buoys (O-Buoys; Halfacre et al. (2014); Knepp et al. (2010)), showing a good representation of springtime ozone depletion.

Emission inventories

Biogenic emissions are calculated online using the Model of Emissions of Gases and Aerosols from Nature (MEGAN, Guenther et al. (2012)). Fire emissions are obtained from

the Fire INventory from NCAR version 2.5 (FINNv2.5, Wiedinmyer et al. (2011, 2022)) and anthropogenic emissions are from the global ECLIPSEv6b inventory (Evaluating of the Climate and Air Quality Impacts of Short-Lived Pollutants version 6b, Klimont et al. (2017)). ECLIPSEv6b includes revised international shipping emissions compared to previous versions of the inventory, relevant for capturing local Arctic emission sources. We further add anthropogenic emissions of Hg(0), Hg(II), and Hg(p) from the global anthropogenic mercury emissions inventory for 2015 (Steenhuisen and Wilson, 2022). This inventory was prepared as part of the 2018 AMAP/UNEP Global Mercury Assessment (GMA, AMAP/UN Environment (2019)) and groups emissions into four distinct sectors: fuel combustion; industrial sectors; waste from intentional use; and artisanal and small-scale gold mining (Steenhuisen and Wilson, 2019, 2022). To include anthropogenic emissions of gas-phase Hg(II) in the model, we assume that these emissions are evenly distributed between each gas-phase Hg(II) species in the model.

5.3 Measurement data

5.3.1 MOSAiC observations

The MOSAiC expedition took place on board the *Polarstern* icebreaker, between October 2019 and September 2020, and is the largest scientific exploration of the Arctic to date. A comprehensive suite of measurements were made during drift through the Arctic Ocean to better understand the links between the atmosphere, sea ice, and ocean (Nicolaus et al., 2022; Rabe et al., 2022; Shupe et al., 2022). This extensive dataset provides a unique insight into the chemical behaviour of the atmosphere in the central Arctic. More details about the MOSAiC campaign can be found in Shupe et al. (2022). For the purpose of our modelling study, we use a subset of meteorological and chemical observations made during MOSAiC which are introduced below.

Meteorological observations

Continuous surface meteorological measurements were made onboard the *Polarstern* at various locations and heights. Measurements of air temperature and relative humidity

were made at a height of 29 m above sea level using a Vaisala HMP155 probe. Wind speed and wind direction were measured at 39 m above sea level using an ultrasonic anemometer. The meteorological measurement data used here to evaluate the WRF-Chem model are available at Schmithüsen (2021).

Radiosondes (model Vaisala RS41-SGP) measuring temperature, humidity, and winds were routinely launched every 6 hours throughout the whole expedition (Maturilli et al., 2021). During synoptic events of special interest, such as major storms, the launch frequency was enhanced up to three-hourly. The launches were performed from the helicopter deck of the *Polarstern*, approximately 12 m above the sea level, so the data do not capture the lowermost part of the boundary layer. Furthermore, polluted data may exist in the lowermost $\sim$100 m, in cases when the sonde flew through the ship's exhaust fan, or when it was otherwise influenced by the ship's presence.

Elemental mercury (Hg(0)) observations

As described in Angot et al. (2022b), Hg(0) measurements were performed in the University of Colorado sea-container laboratory using a Tekran 2537B analyzer. Only Hg(0) was collected and analyzed (as opposed to total gaseous mercury (TGM)) as cation-exchange membranes were used to remove potential divalent Hg species. All instruments located within this container were automatically backflushed with zero-air when wind direction was more than $\pm$130 degrees from the ship bow to prevent any contamination of the sampling line by the ship exhaust. This explains the presence of gaps in the Hg(0) time series. The Hg(0) dataset can be accessed at Angot et al. (2022a).

Ozone observations

Ozone ambient air mole fractions were monitored in three different sea-container laboratories using commercial instruments. The three individual ozone time series were cross-evaluated and used to generate the hourly-averaged merged dataset used in this study. This merged dataset limits gaps in the ozone time series (as opposed to the Hg(0) time series, see above). More information can be found in Angot et al. (2022b). The O_3 dataset can be accessed at Angot et al. (2022c).

BrO observations

The Multi-Axis Differential Optical Absorption Spectroscopy (MAX-DOAS) technique (Lohberger et al., 2004; Plane and Saiz-Lopez, 2006; Platt and Stutz, 2008) was used to make observations of BrO during the MOSAiC expedition. The instrument (Prados-Roman et al., 2015) has an external telescope used to collect scattered sunlight connected to an indoor spectrometer using an optical fibre. The outdoor unit consisted of a telescopic lens (focal length of 200 mm, diameter 50.8 mm), which focused light onto an optical fibre. The optical fibre was connected to the indoor unit consisting of a spectrometer (Princeton Instruments SP500i) and a Charge-Coupled Device detector (camera CCD Princeton Instruments Pixis 400B). The instrument was placed at a height of 15 m from the sea surface and an inclinometer was used to correct the measured elevation angles using the actual pitch and roll of the instrument during the expedition. The solar spectra were then analysed using the QDOAS software (Fayt et al., 2011) to retrieve the absorption due to the oxygen dimer (O_4) and BrO at different viewing elevation angles, using the zenith spectra as a reference (see Figure B.2). The resulting Differential Slant Column Densities (DSCDs) are the difference of the slant column densities (SCDs) in the viewing direction and the SCD in the zenith direction. The DOAS retrieval settings are given in Table B.1 and an example of the DOAS fit can be found in Benavent et al. (2022). The AC-2 radiative transfer model (Benavent, 2020), was then used to derive mixing ratios of BrO by estimating the path length from the O_4 DSCDs. This is a two-step process where the O_4 DSCDs are used to estimate the light path length and subsequently the mixing ratio of BrO is estimated. Considering that in most cases BrO was above the detection limit only at the lowermost angles (< 3 degrees), an average mixing ratio across the first kilometer is computed due to lack of information above it. Photographs of sky conditions were used to filter the data for blowing snow and broken cloud cover to avoid multiple scattering effects, which can lead to the incorrect conversion of DSCDs into mixing ratios.

5.3.2 Arctic stations

Mercury observations

TGM measurements at Villum Research Station (Station Nord, Greenland), Zeppelin Observatory (Svalbard), and the Dr. Neil Trivett Global Atmosphere Watch Observatory (Alert, Nunavut, Canada) were performed using Tekran 2537 instruments and are part of ongoing long-term monitoring efforts (e.g., MacSween et al., 2022). Teflon inlet filters were used to remove gaseous oxidized mercury (GOM) during sampling, but it is possible that small amounts of GOM are measured by the analyzers. It is assumed that this contribution is small, relative to the overall Hg(0) signal, and therefore these measurements are henceforth referred to as Hg(0). Hg(II) and Hg(p) measurements at Alert were made using a Tekran 1130/1135 speciation unit, sampled at a 2h time resolution and reported on a 3h time interval (Steffen et al., 2014). More information on the instrumental setup and quality control procedures can be found elsewhere (Angot et al., 2016; Berg et al., 2013; Skov et al., 2020; Steffen et al., 2014).

Ozone observations

Surface ozone data from Villum (Greenland) and Zeppelin (Svalbard) were retrieved from the EBAS database (http://ebas-data.nilu.no/default.aspx). All measurements were performed using commercial UV absorption instruments (detection limit of 1 ppb). Surface ozone data from Utqiaġvik (Alaska), Summit (Greenland), and the Polar Environment Atmospheric Research Laboratory (Eureka, Nunavut, Canada) were provided by the NOAA Global Monitoring Laboratory (https://www.esrl.noaa.gov/gmd/ozwv/surfoz/data.html). These measurements are also performed using a commercial UV absorption instrument. More information can be found in Platt et al. (2022).

5.3.3 Satellite BrO observations

Satellite BrO data of the high-resolution TROPOspheric Monitoring Instrument (TROPOMI) on the Sentinel-5 Precursor (S5P) satellite was used to retrieve total BrO columns by applying the method from Seo et al. (2019). To obtain the tropospheric BrO Slant

Column Density (SCD), the stratospheric part was removed from the total column using the stratospheric correction method described in Theys et al. (2011). It requires stratospheric ozone and NO_2 columns from TROPOMI and the tropopause height, which was taken from the NCEP Reanalysis 1 product (Kalnay et al., 1996). The tropospheric BrO Vertical Column Densities (VCDs) were obtained from the tropospheric SCDs using an air mass factor suitable for a surface BrO layer of 400 m thickness over a bright surface. As a result, boundary layer BrO over dark surfaces such as open oceans may be underestimated.

5.3.4 Global model ensemble output

Simulations for the MOSAiC year (Oct 2019 – Sept 2020) were performed with the multi-model ensemble (GLEMOS, GEOS-Chem, GEM-MACH-Hg, and DEHM) used for the recent Global Mercury Assessment (AMAP/UN Environment, 2019) and Arctic Monitoring and Assessment Programme reports (AMAP, 2021). A description of the four models can be found in Dastoor et al. (2022a), along with a full evaluation of their performances in the Arctic. A subset of this simulation (March – April 2020) was used to provide initial boundary conditions of Hg(0) in the model simulation presented here.

5.4 Model evaluation with MOSAiC observations

We evaluate the hourly model outputs against meteorological and chemical measurements made onboard the *Polarstern* during MOSAiC. We use several metrics to provide a comparison between the model and observations, including: the Pearson correlation coefficient (r), root-mean-square error (RMSE), and mean bias error (MBE). Performance metrics between the model and the MOSAiC observations are given in Table 5.3.

5.4.1 Simulated meteorological conditions during MOSAiC

Polar boundary layer stability is crucial in modulating atmospheric chemical composition near the surface via impacts on vertical mixing, surface emissions, and chemistry. Accurately modelling boundary layer structure is therefore necessary to investigate surface

Table 5.3: Goodness-of-fit statistics between model and observations for chemical and meteorological variables observed along the MOSAiC shiptrack. Correlation coefficients (r), root mean square error (RMSE), and mean bias error (MBE).

Variable	r	**RMSE**	**MBE**
Surface air temperature	0.85	2.67 K	1.95 K
Vertical air temperature			
05:00	0.97	0.59 K	−0.14 K
11:00	0.94	0.57 K	−0.20 K
17:00	0.94	0.58 K	−0.08 K
23:00	0.96	0.42 K	−0.08 K
Relative humidity	0.31	9.49 %	−7.69 %
Wind speed	0.97	1.03 m s^{-1}	−0.15 m s^{-1}
Wind direction	0.77	78.2 °	−1.68 °
Hg(0)	0.81	0.24 ng m^{-3}	−0.09 ng m^{-3}
O_3	0.82	6.53 ppb	0.35 ppb
BrO	0.42	11.85 ppt	9.78 ppt

chemistry and air-snow exchange processes. We evaluate the meteorological configuration of the model by comparing the simulated boundary layer meteorology with observations obtained onboard the *Polarstern*. Figure 5.3 shows the comparison between the simulated and observed meteorology for several variables including air temperature, relative humidity, wind speed, and wind direction. Simulated variables are extracted at the nearest model grid cell to the location of the ship. Modelled air temperatures are largely in good agreement with the observations (Figure 5.3a, r = 0.85), despite a mean positive bias (MBE = 1.95 K) slightly overestimating both warm and cold periods. The model also shows good performance in simulating surface wind speeds and wind directions (r = 0.97 and r = 0.77, respectively), with the exception of relative humidity (r = 0.31), which is biased low (MBE = −7.69 %).

To evaluate the vertical structure of the boundary layer, we compare the average simulated and observed temperature profiles above the *Polarstern* in Figure 5.4. Radiosondes

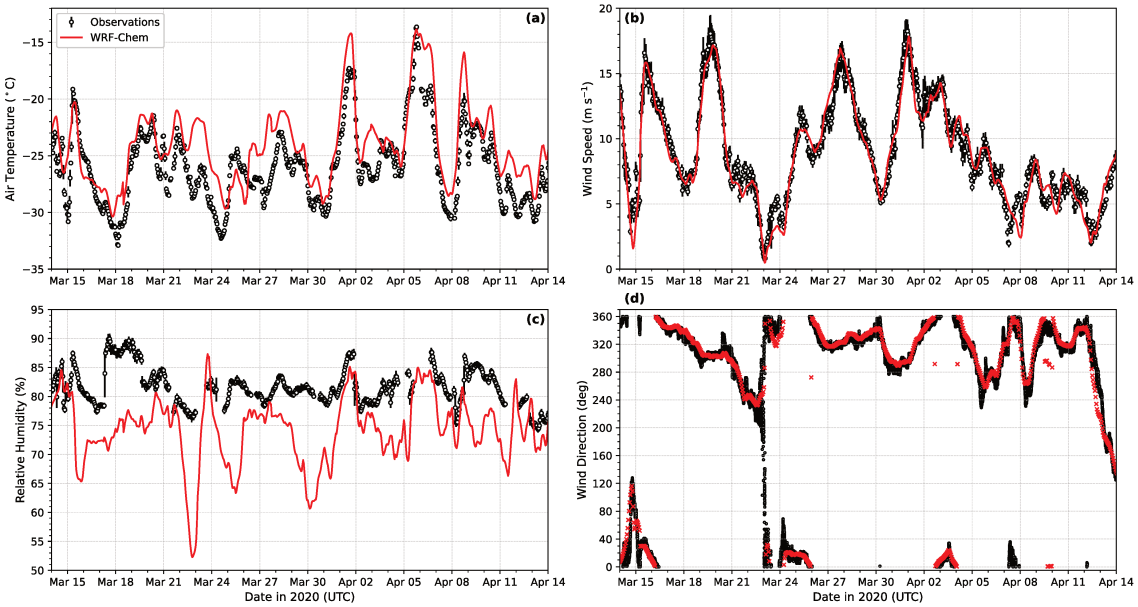

Figure 5.3: Model comparison of meteorological variables with MOSAiC observations. Hourly averages of observed (black) and simulated (red) boundary layer meteorology of (a) air temperature (29 m asl); (b) wind speed (39 m asl); (c) relative humidity (29 m asl); and (d) wind direction (39 m asl, 1-minute measurements plotted) during MOSAiC. Standard deviation of the observations are shown by the black bars. Simulated values are extracted at the closest grid cell to the shiptrack.

were launched from the ship up to four times a day at regular intervals: 05:00, 11:00, 17:00, and 23:00 UTC (to the nearest hour). In total, 119 radiosondes were launched during the simulated period. Figure 5.4 shows the comparison between the mean observed and simulated temperature profiles. For this, we have interpolated the model output to the hour/location of the sonde releases and we averaged all profiles available for each daily release time (05:00, 11:00, 18:00, 23:00 UTC) and show the lowest two kilometers of the atmosphere to focus on the near surface atmosphere representation in the model. The purpose of this comparison is to provide an indication of overall model performance in simulating the vertical structure of the polar boundary layer. At each time interval, the model shows good agreement with the mean observed vertical temperature profiles, within the standard deviation range of the observations. In the lowest 250 m, we find a positive bias of 1–2 °C in the model, consistent with the warm bias in Figure 5.3a. This warm bias can be associated with the presence of near-surface temperature inversions, common in the Arctic. The difficulty in capturing these inversions is however not unique to our model, and is a challenge facing many models and reanalyses (Graham et al., 2019).

Similar comparisons between modelled and observed vertical profiles of winds and relative humidity (Figures B.3, B.4, and B.5) also show good model performance in simulating the vertical structure of the boundary layer, despite some differences in the lowest 250 m. Overall, we show that the model performs well in simulating the observed springtime meteorology in the central Arctic, necessary for modelling boundary layer chemistry.

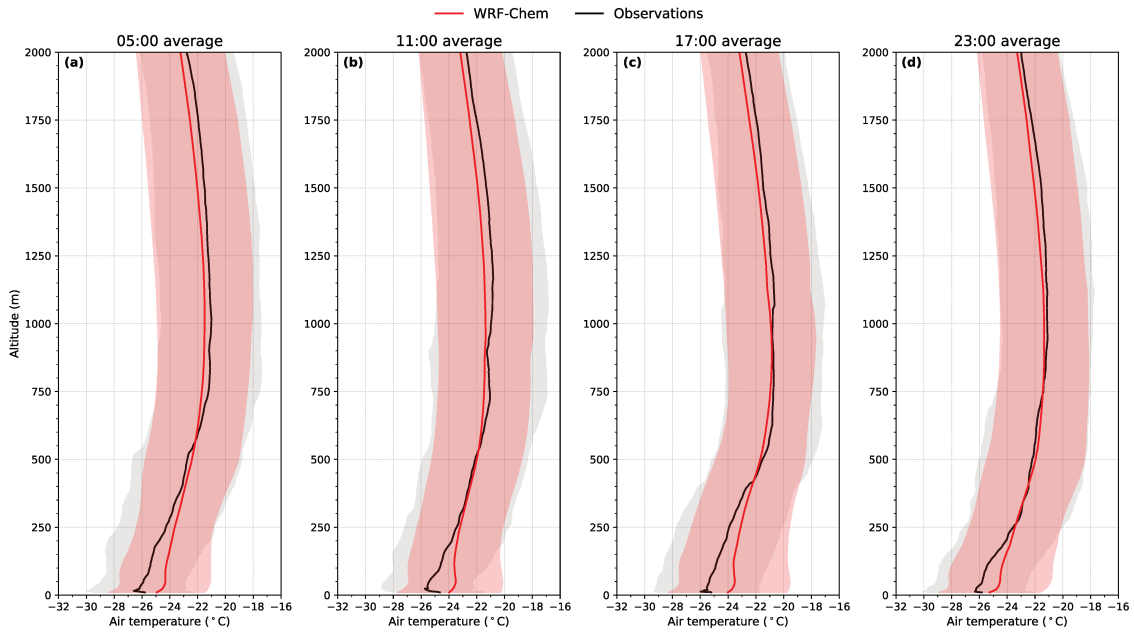

Figure 5.4: Model comparison of vertical temperature profiles with MOSAiC radiosonde observations. Mean vertical air temperature profile from radiosonde observations (black) released above the MOSAiC shiptrack and simulated by WRF-Chem (red) during the simulation period (March 14 – April 14, 2020). Model values are extracted at the closest grid cell to the location of each radiosonde flight path. Data are averaged by time interval during the simulated period (to the nearest hour) at (a) 05:00 UTC, (b) 11:00 UTC, (c) 17:00 UTC, and (d) 23:00 UTC. Shaded areas represent the standard deviation of the observed and model averages.

5.4.2 Mercury, ozone, and bromine evaluation with MOSAiC observations

To evaluate the model, we compare modelled surface Hg(0), O_3, and BrO with observations made onboard the Polarstern in Figure 5.5.

Performance metrics are shown in Table 5.3. We also note here that a two week model spin-up time was selected based on the time needed to stabilize the chemical state of Hg(0) and O_3 in the central Arctic (Figure 5.5, grey shaded area). Observations of

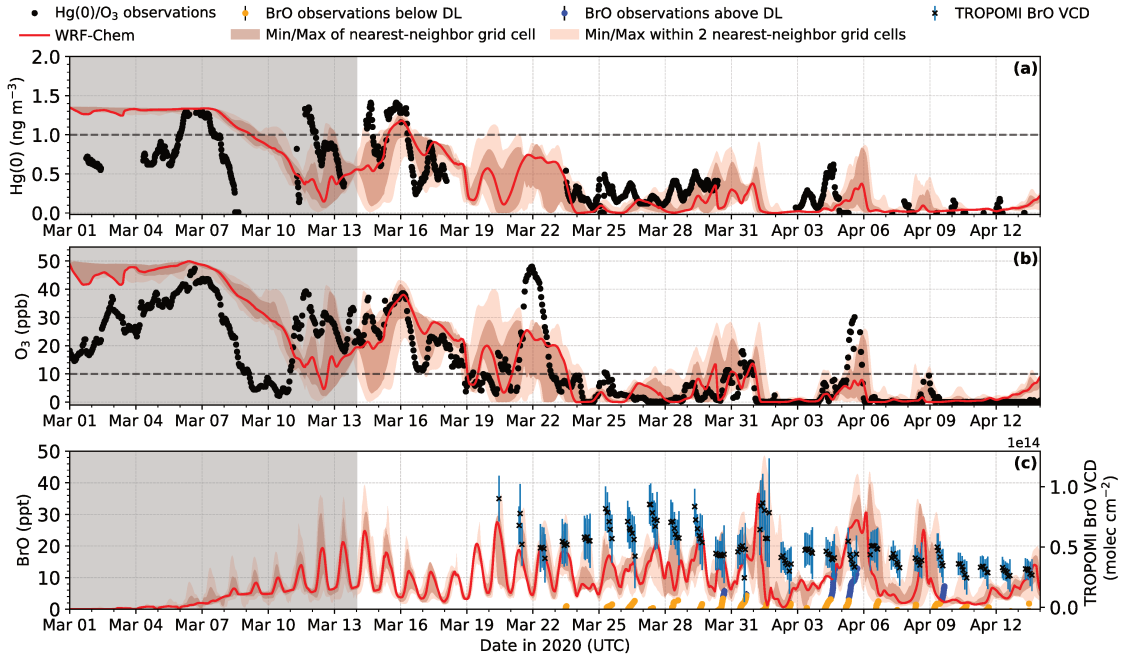

Figure 5.5: Model comparison of chemical species measured during MOSAiC. Surface measurements during MOSAiC (black) of (a) 30-min averaged Hg(0) concentration and (b) hourly averaged O_3 concentration. Simulated concentrations by WRF-Chem plotted in red. (c) BrO observed by MAX-DOAS (left axis, yellow: below detection limit (DL) and blue: above DL) and TROPOMI (right axis) during MOSAiC and simulated by WRF-Chem ($0-1$ km average). TROPOMI data are the total tropospheric column plotted as the average values recorded within 150 km of the MOSAiC shiptrack with standard deviation shown by the error bars. WRF-Chem simulated values are extracted at the closest grid cell to the shiptrack. Grey dashed lines represent the values of Hg(0) and O_3 depletion events ($<$1.0 ng m^{-3} and $<$10 ppb, respectively). Red shaded areas represent the minimum and maximum values simulated by WRF-Chem around the shiptrack grid cell in a 3×3 and 5×5 grid. Dark grey shaded areas represent the model spin-period excluded from the analysis.

Hg(0) (Figure 5.5a) show extended periods of depletion (defined as Hg(0) $<$ 1 ng m^{-3}, Angot et al. (2016)) and concentrations were frequently recorded below 0.5 ng m^{-3}. Similarly, intense depletion of ozone was observed (Figure 5.5b), where O_3 was regularly below 10 ppb and depletion lasted multiple days, particularly in late March/early April. This level of Hg(0) and O_3 depletion is indicative of enhanced surface chemistry and emissions of bromine from sea ice, capable of sustaining the depletion over an extended period of time. There is also a strong correlation between the observations of Hg(0) and O_3 (r = 0.91), suggesting depletion of both species is driven by bromine, as reported in a previous Arctic measurement study (Wang et al., 2019). Hg(0) concentrations during

periods of missing measurement data (e.g., 18 – 23 March and 31 March – 3 April) are therefore likely to be consistent with O_3 concentrations, which exhibit regular depletion during these periods. Our model predicts substantial depletion of both Hg(0) and O_3, in relatively good agreement with the observations ($r = 0.81$ and $r = 0.82$ for Hg(0) and O_3, respectively). In particular, the model is able to capture the prolonged periods of Hg(0) and O_3 depletion in late March/early April. However, simulated Hg(0) has a small negative bias (MBE = -0.09 ng m^{-3}), potentially due to high bromine-initiated oxidation, and the model also underestimates certain periods of ozone recovery (e.g., March 21 – 23). Comparing the simulated time series of Hg(0) and O_3, we find a very strong correlation ($r = 0.99$), indicating oxidation by Br is the major process in the model.

To further assess the extent of bromine-initiated oxidation of Hg(0) and O_3, we compare in Figure 5.5c the average modelled BrO in the lowest 1 km of the atmosphere to MAX-DOAS observations. We also show the TROPOMI tropospheric column BrO along the MOSAiC ship track as a reference for comparison (Figure 5.5c, right axis). We highlight here that there is some uncertainty in directly comparing the lowest 1 km of model data with the MAX-DOAS measurements, however, this uncertainty is difficult to quantify. Our model predicts high BrO concentrations above the shiptrack of up to 40 ppt. The observed concentrations are up to a factor of 5 times smaller than the model predicted estimates ($r = 0.42$, MBE = 9.78 ppt), with many periods of BrO below the detection limit and uncertainty typically below 1 pptv. The average concentrations in the lowest 1 km of our WRF-Chem simulation are, however, consistent with timing and relative abundance of BrO from the total tropospheric column retrieved from TROPOMI (Figure 5.5c). Putting these measurement data in the context of previous Arctic BrO observations, this is much lower than peak levels of around 50 pptv recorded from satellite and ground-based observations (Hönninger and Platt, 2002; Peterson et al., 2017; Simpson et al., 2017; Wagner et al., 2001). It should be noted that these observations of BrO during the MOSAiC spring season are mainly during periods when ozone was near complete depletion. It is well known that reactive bromine can be present even when there are low BrO concentrations, due to the fact that BrO formation cannot occur when O_3 is depleted. There are several possible causes for the difference between modelled and observed BrO. The main

loss of BrO is via reaction with hydroperoxyl radicals (HO_2), forming HOBr. Inaccurate HO_2 concentrations from VOC oxidation may result in insufficient HOBr production, which could maintain high concentrations of BrO. In addition, our description of bromine activation assumes an infinite bromide reservoir from snow on both first year sea ice (FYI) and multi-year sea ice (MYI) (Herrmann et al., 2022). This assumption may overestimate bromine activation from MYI regions, where measurements of bromide in snow on Arctic MYI have recorded lower concentrations than on FYI (Krnavek et al., 2012; Peterson et al., 2019). Uncertainties related to the BrO retrievals that allow for calculation of the BrO concentrations from the MAX-DOAS observations may also contribute to these differences. Finally, heterogeneous recycling on aerosols may sustain reactive bromine concentrations above the surface, independent of snowpack activation (Peterson et al., 2017). An overestimation in modelled aerosol concentrations, or a high reactive uptake probability of bromine, may therefore contribute to an enhancement of bromine recycling and BrO concentrations at altitudes above the surface.

In summary, the model is able to simulate Hg(0) and O_3 depletion in the central Arctic, in good agreement with the observations. There is strong correlation between the Hg(0) and O_3 time series (observed and modelled), indicating oxidation of both species is driven by bromine. However, modelled BrO quantities are overestimated compared to the observations, which may positively bias oxidation of Hg(0) and O_3 by bromine. A recent study, based on reactive bromine and iodine measurements, has attributed a large contribution of ozone destruction to iodine chemistry, on a level comparable with bromine (Benavent et al., 2022). These measurements were made during MOSAiC, at the same time and location modelled in this study, and are the first measurements of iodine monoxide (IO) in the central Arctic. In this work, we did not include iodine chemistry in our model and our halogen descriptions are limited to bromine and chlorine cycling. Future investigations could aim to extend our model chemical mechanism to include descriptions of this chemistry, and, explore its impact on ozone depletion. However, for this work which is focused on the mercury cycle, the impact of iodine chemistry is expected to be minimal on mercury oxidation and deposition.

5.5 Model evaluation of regional Arctic mercury, ozone, and bromine chemistry

5.5.1 Model evaluation at Arctic stations and with satellite retrievals

In addition to the model comparison with MOSAiC observations, we further evaluate the model with measurement data at other Arctic locations. Here, we compare the simulated surface Hg and O_3 concentrations to observations at Arctic stations, as well as modelled tropospheric BrO vertical column density (VCD) with satellite-derived measurements. An additional comparison of meteorology at 3 Arctic stations is also provided in Figures B.6, B.7, and B.8.

Hg(0) at Arctic stations

Figure 5.6 compares modelled surface Hg(0) to hourly averaged observations at Villum (Greenland) and Zeppelin (Svalbard), and 3h averaged observations at Alert (Canada). Overall, we find relatively good agreement between the model and observations in capturing the timing of AMDEs at each measurement site. There is a general negative bias in the simulated Hg(0) time series compared to the observations (Table 5.4), suggesting either too much net Hg(0) oxidation (via high bromine concentrations) or low/missing sources (including re-emission from snow, open ocean sources, and transport from mid-latitudes).

At Villum (Figure 5.6a), the model is able to simulate key features of the observed Hg(0) time series ($r = 0.50$), with some discrepancies discussed below. During the simulated period, six AMDEs were observed (March 27, March 30 – 31, April 2 – 4, April 9 – 10, April 10 – 13, and April 14). The model is able to simulate most features (timing and intensity) of five out of the six events. On April 2, a depletion event lasting approximately two days was observed, where Hg(0) concentrations fell below 0.5 ng m^{-3}. The intensity and duration of this event is captured by the model, although recovery to background levels in the model lags by approximately one day, possibly suggesting low re-emission from snow in the model. The model incorrectly predicts a depletion event between March 24 and March 29 which was not observed. These differences can partly be explained by

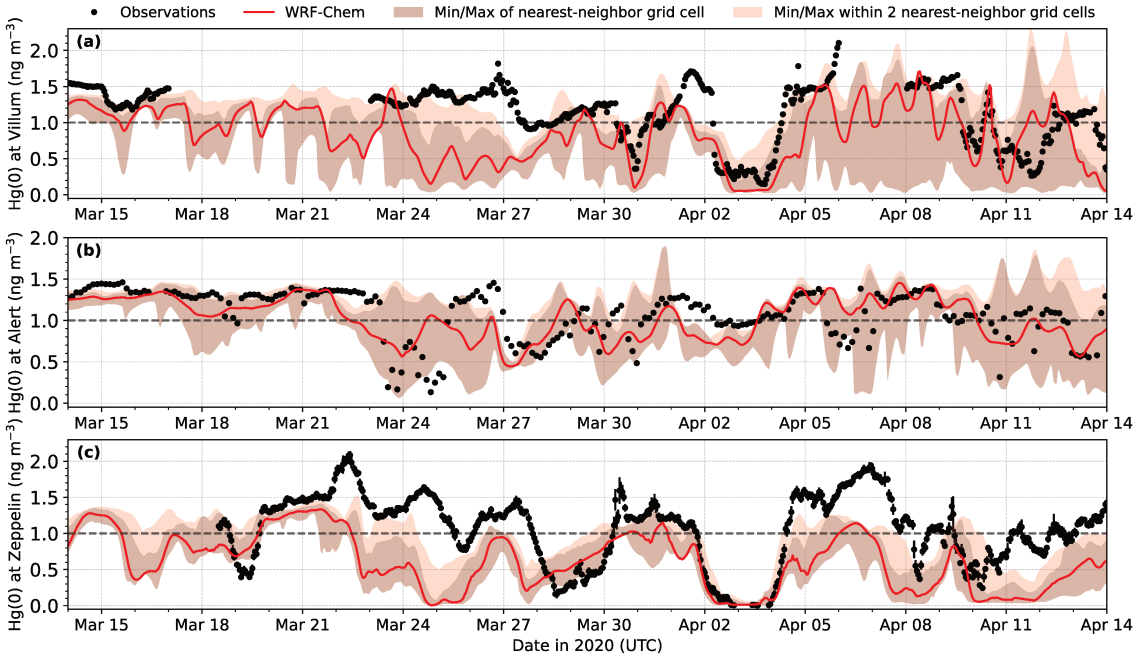

Figure 5.6: Model comparison of surface Hg(0) concentrations with observations from coastal Arctic stations. Surface Hg(0) observed (black) and simulated by WRF-Chem (red) at (a) Villum, Greenland (hourly average); (b) Alert, Canada (2h average); and (c) Zeppelin, Svalbard (hourly average). Grey dashed lines represent the value of Hg(0) depletion events (<1.0 ng m^{-3}). Red shaded areas represent the minimum and maximum values simulated by WRF-Chem around the station grid cell in a 3×3 and 5×5 grid.

the coarse horizontal resolution of the model (100 km). Due to the proximity of Villum to sea ice, this grid cell may partly factor in emissions of bromine from sea ice. We therefore also show in Figure 5.6 the minimum and maximum Hg(0) values within the two nearest neighbour grid cells (shaded regions). The large variability of Hg(0) concentration within neighbouring grid cells highlights the marked differences in emissions and chemistry of Hg(0) over land-based snow and sea ice.

At Alert (Figure 5.6b), Hg(0) is regularly close to background levels (∼1.4 ng m^{-3}), with some intermittent periods of Hg(0) depletion. Simulated Hg(0) shows reasonable agreement with the observations (r = 0.54) with a small negative bias (MBE = −0.05 ng m^{-3}). Speciated Hg measurements at Alert were also available during this period and are evaluated in more detail in Section 5.5.2. Observations at Zeppelin (Figure 5.6c) recorded several depletion events lasting between 1–3 days. There is a broad underestimation of modelled Hg(0) compared to the observations (r = 0.53), which could in part be explained

by low/missing land-based sources (including re-emission from snow). Limitations in model resolution may also contribute to this negative bias by poorly representing the local mountain meteorology at Zeppelin. Chemistry, emissions, and transport at this site can therefore all be impacted as a consequence. Despite the mean negative bias (MBE = -0.49 ng m^{-3}), the timing of depletion and replenishment of Hg(0) are often captured by the model at Zeppelin.

Overall, the model is generally able to reproduce the behaviour of Hg(0) at these sites, with the timing of depletion events often simulated correctly by the model, but underestimating Hg(0) concentrations. The negative bias in modelled Hg(0) concentration is likely a factor of the coarse horizontal resolution of the model, resulting in high bromine oxidation and low Hg(0) re-emission at these sites. Higher resolution model runs are therefore desirable to discern the contributions of bromine oxidation and Hg(0) re-emission from land-based snow and from sea ice at coastal Arctic stations.

Ozone at Arctic stations

Figure 5.7 compares modelled and hourly averaged observations of surface O_3 at six Arctic stations: Villum (Greenland), Alert (Canada), Zeppelin (Svalbard), Utqiaġvik (Alaska), Summit (Greenland), and Eureka (Canada). Model performance metrics are listed in Table 5.4. At Villum (Figure 5.7a), observations of O_3 are correlated with the Hg(0) time series ($r = 0.93$), shown in Figure 5.6a. Modelled O_3 is in reasonable agreement with the observations ($r = 0.54$), with similar features and discrepancies as previously shown in the modelled Hg(0) time series. In particular, an ODE between April 2–4 was observed coinciding with depletion of Hg(0), which is reproduced by the model. However, the model also incorrectly predicts depletion of O_3 between March 23 and March 31, indicating an overestimation of bromine. Modelled O_3 at Alert (Figure 5.7b), is relatively well captured by the model ($r = 0.64$). The observed time series of O_3 and Hg(0) also show very similar features, with a depletion event recorded for both species between March 23–25. At Zeppelin (Figure 5.7c), multiple ODEs were observed and O_3 concentrations exhibit a strong correlation with the Hg(0) measurements ($r = 0.88$). The timing and intensity of these ODEs are mostly captured by the model ($r = 0.56$). However, there is

Table 5.4: Goodness-of-fit statistics between model and observations for Hg and O_3 variables observed at Arctic sites. Correlation coefficients (r), root mean square error (RMSE) and mean bias error (MBE).

Station	Variable	r	RMSE	MBE
Villum	Hg(0)	0.50	0.53 ng m^{-3}	-0.35 ng m^{-3}
	O_3	0.54	19.1 ppb	-15.1 ppb
Alert	Hg(0)	0.54	0.27 ng m^{-3}	-0.05 ng m^{-3}
	Hg(II)	-0.08	59.0 pg m^{-3}	43.2 pg m^{-3}
	Hg(p)	0.26	150 pg m^{-3}	53.9 pg m^{-3}
	O_3	0.64	8.15 ppb	-2.49 ppb
Zeppelin	Hg(0)	0.53	0.64 ng m^{-3}	-0.49 ng m^{-3}
	O_3	0.56	14.4 ppb	-7.61 ppb
Utqiaġvik	O_3	0.52	16.6 ppb	-11.3 ppb
Summit	O_3	0.64	9.01 ppb	6.67 ppb
Eureka	O_3	0.52	11.9 ppb	-0.10 ppb

an overall mean negative bias in the model (MBE = -7.61 ppb), with a marked underestimation between March 23 and March 26 (as in the Hg(0) comparison). This again is suggestive of an overestimation in bromine activation during this period. Comparing the modelled O_3 and Hg(0) time series at these three stations, we find very strong correlation at each site (Villum $r = 0.73$, Alert $r = 0.88$, and Zeppelin $r = 0.99$), indicating that bromine is also the major Hg(0) oxidant in the coastal Arctic.

Ozone measurements at Utqiaġvik show several ODEs which the model is only partially able to capture (Figure 5.7d). In general, the model overpredicts ozone depletion indicating highly active bromine chemistry ($r = 0.52$, MBE = -11.3 ppb). At Summit (Figure 5.7e), no depletion events were observed or simulated by the model due to the location of the station ($r = 0.64$). Summit is situated at a high altitude ($\sim$ 3216 m above

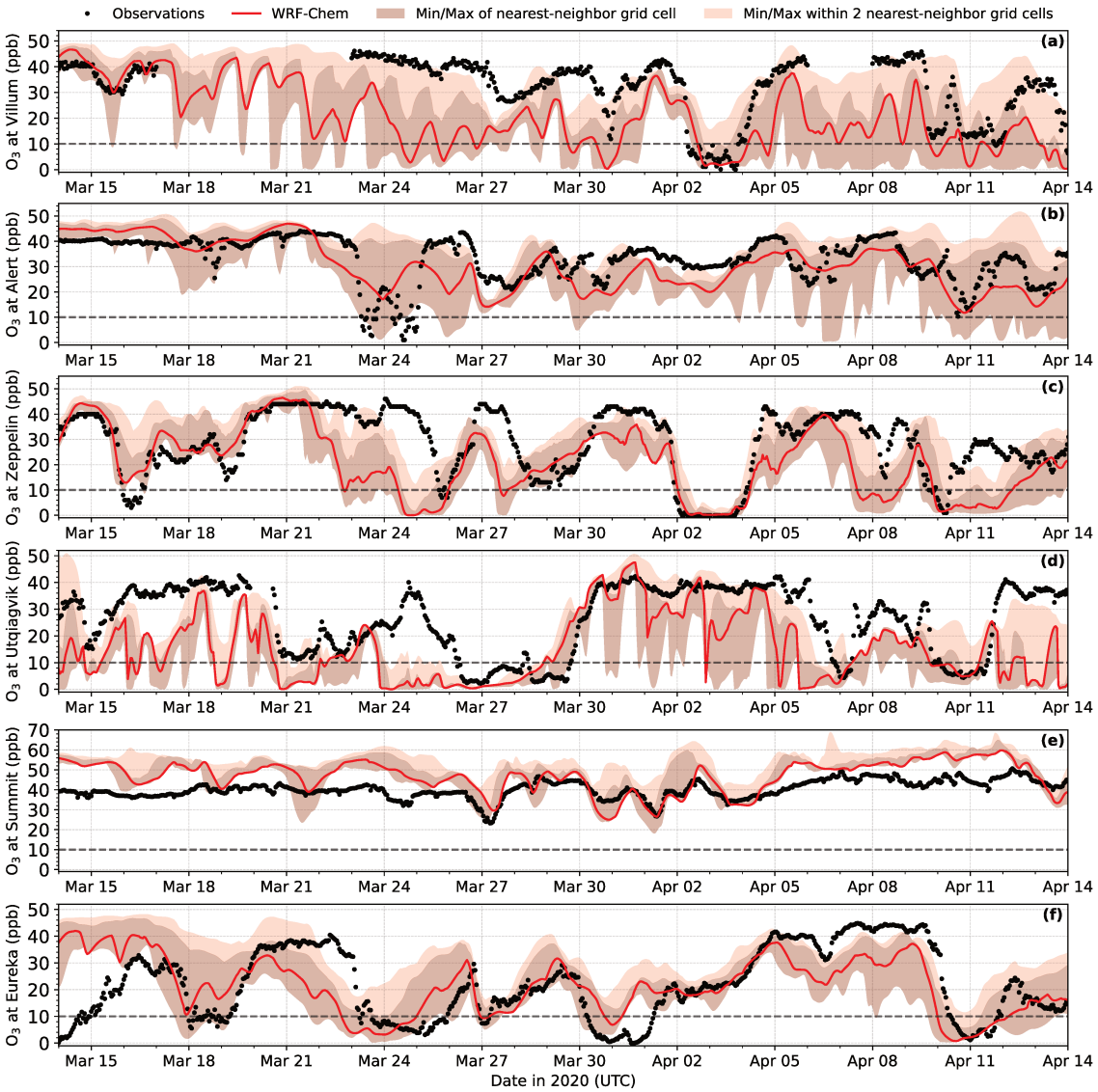

Figure 5.7: Model comparison of surface ozone concentrations with observations from Arctic stations. Hourly average of surface O_3 observations (black) and simulated O_3 by WRF-Chem (red) at (a) Villum, Greenland; (b) Alert, Canada, (c) Zeppelin, Svalbard; (d) Utqiaġvik, Alaska; (e) Summit, Greenland; and (f) Eureka, Canada. Grey dashed lines represent the value of O_3 depletion events ($<$10 ppb). Red shaded areas represent the minimum and maximum values simulated by WRF-Chem around the station grid cell in a 3$\times$3 and 5$\times$5 grid.

sea level) in central Greenland and is therefore largely unaffected by air masses originating over sea ice. There is an overall positive bias in modelled O_3 concentrations (MBE = 6.67 ppb), indicating that the difference may be due to local meteorology (e.g., boundary layer stability) rather than differences in chemistry. At Eureka station (Figure 5.7f), multiple ODEs were observed typically lasting between 1–2 days. For most of the simulated

period (March 18 – April 14), the model performs very well to capture the timing and intensity of ODEs observed at this site ($r = 0.52$). However, ozone concentrations in the first week of the simulation are overpredicted and the depletion is completely missed by the model.

Figure 5.8 shows the average surface O_3 concentration during the simulation period. On the whole, we find good representation of ozone in the model at several coastal and non-coastal Arctic stations. Most ODEs (including the timing, intensity, and duration) are captured by model, with the exception of some events which are missed (e.g., at Eureka) or overpredicted by the model (e.g., at Villum). For coastal sites, there is a general negative bias in O_3 suggesting an overestimation in bromine-initiated oxidation. Increased horizontal resolution could again potentially address some of the disparities between model and observations at all sites.

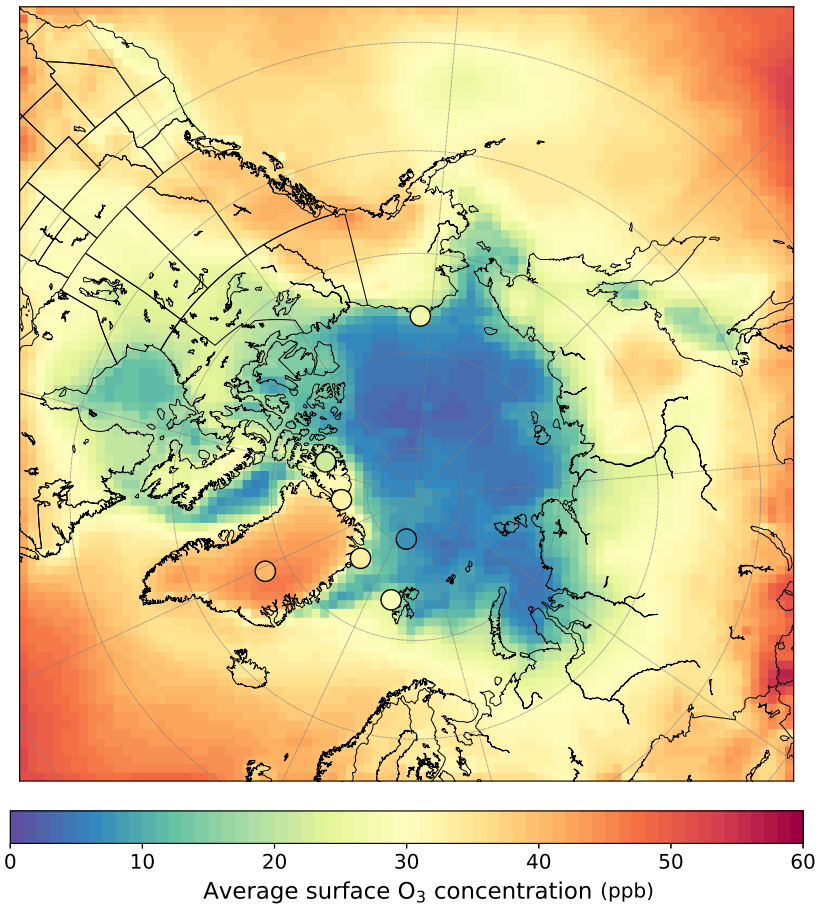

Figure 5.8: Simulated mean surface ozone concentration. Surface ozone concentration is averaged for the full simulation period (March 14 – April 14, 2020). Observational averages for the same period are shown by markers with the same colour scale.

BrO compared to TROPOMI satellite retrieval

We compare in Figure 5.9 the modelled and observed mean tropospheric BrO vertical column densities (VCD) for the simulation period. Satellite observations from TROPOMI on Sentinel-5p are corrected to exclude the stratospheric contribution (see section 5.3.3).

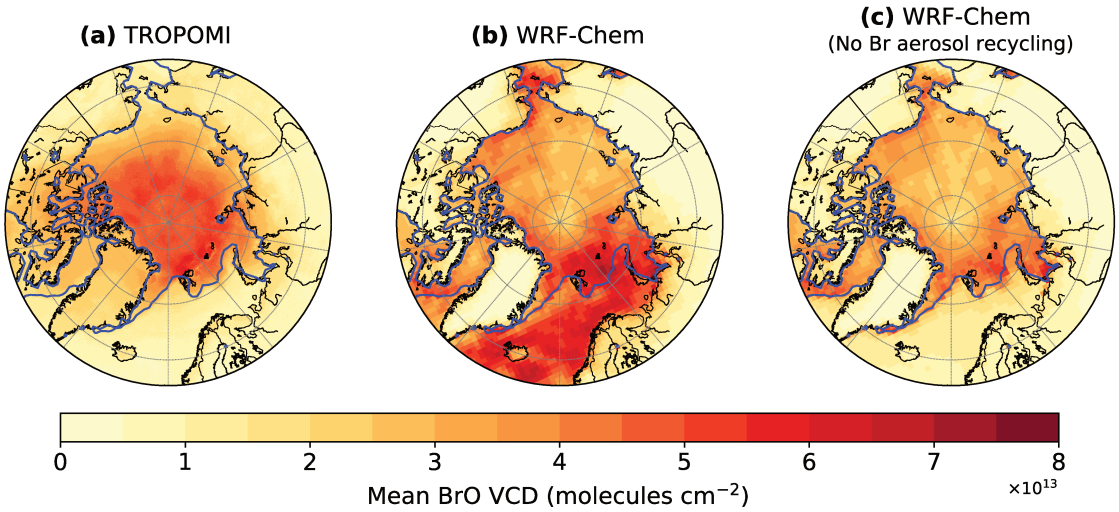

Figure 5.9: Observed and simulated mean tropospheric BrO vertical column density (VCD). Mean BrO VCDs are averaged for the full the simulation period (March 14 – April 14, 2020) from (a) TROPOMI on Sentinel-5p and (b) WRF-Chem. (c) WRF-Chem BrO VCD with no heterogeneous recycling of reactive bromine on aerosols. Blue contour lines represent the sea ice fraction above 75 % coverage at the beginning of the simulation.

The first striking difference between TROPOMI (Figure 5.9a) and the modelled BrO (Figure 5.9b) is the different total columns outside the central Arctic, over primarily open ocean regions (south-east of Greenland and between Alaska and Russia). This can be partly explained by the fact that over open oceans, the sensitivity of satellite observations to boundary layer BrO is largely reduced due to low albedo and cloud effects (Seo et al., 2019), and therefore satellite columns may be too low. The difference also points to the fact that the BrO lifetime in our model may be too long and allows for transport outside the sea ice covered source region for initial bromine activation or the fact that we have to much bromine recycling on surfaces outside sea ice covered regions. Peterson et al. (2017) reported observations of BrO in the Arctic boundary layer sustained by heterogeneous recycling on aerosols, which is one way that reactive bromine can be sustained in air away from the surface. Reactive bromine concentrations are sustained on aerosols

and transported to higher altitudes in the free troposphere where they can be transported longer distances away from the original emissions sources over sea ice covered regions. However, the rate of recycling and re-emissions on aerosols remains uncertain. To explore the effect of recycling on aerosols away from the surface and its impact on sustaining BrO activation away from sea ice, we have completed a sensitivity run with aerosol bromine recycling turned off. The result of this run (Figure 5.9c) is in better agreement with BrO VCD observed, with an underestimation in BrO abundances. This is clearly not a realistic representation of bromine aerosol chemistry, but provides valuable information regarding the role of bromine activation and transport via recycling aerosols in the Arctic. This shows the need for future work on both evaluating modelled aerosol concentrations and/or inaccuracies in the treatment of heterogeneous bromine chemistry.

There are also differences in the central Arctic between TROPOMI (Figure 5.9a) and the modeled BrO (Figure 5.9b) VCDs, over the sea ice covered regions, for example at the north pole (90° N). Here and over other sea ice covered regions the model under predicts the total BrO column compared to the satellite VCD. There are several possible reasons for this, including the fact that the model under predicts total BrO due to uncertainties in emissions, vertical transport, and recycling on aerosols (discussed in the last paragraph). A key issue that may control BrO abundance near the surface in the model is the ability to replenish ozone-rich air from above the surface down to the key bromine emission sources near the surface, which are snow on sea ice and sea salt aerosols. When ozone is depleted, BrO cannot form even if there is activated bromine radicals present. The under prediction of central Arctic BrO VCDs by the model can also be due to the inaccurate representation of vertical transport of activated bromine away from the surface into the free troposphere, where large quantities of ozone are available for reaction to form BrO. The simulated boundary layer (Figure B.9) was often below 700 m, which indicates the volume in which emitted bromine is in direct contact with the surface and can be recycled on surface snow and aerosols. BrO formed near the surface was found to be mixed above the boundary layer height (Figure B.10), with ozone depletion extending up to 2 km above the surface (Figure B.11). While aloft, recycling of bromine is limited to aerosol surfaces as shown in Peterson et al. (2017), resulting in less frequent events of elevated BrO aloft above the

boundary layer height.

5.5.2 Mercury speciation in the Arctic

In Figure 5.10, we plot the modelled chemical speciation of surface Hg(0), Hg(II), and Hg(p) averaged over the simulation period. Observational averages from Arctic stations (where possible) and the MOSAiC shiptrack are also plotted for the same period. Modelled Hg(0) (Figure 5.10a) shows depletion in the central Arctic, due to bromine emissions from sea ice, with higher Hg(0) concentrations over land. The simulated surface average is in good agreement with the available observations, and, predicts a latitudinal gradient with increasing Hg(0) concentrations at lower latitudes. Simulated surface gaseous Hg(II) (Figure 5.10b) concentrations are in the range of 0–100 pg m^{-3}, with the highest concentrations around the coasts and minima over the central Arctic. The five major contributing species in the model are HgX (gaseous Hg(II) volatilized from aerosols), HgOHOH, HgBrOH, HgBrBrO, and $HgBr_2$, indicating high bromine oxidation (Table 5.1). Measurements at Alert report an average Hg(II) concentration of approximately 10 pg m^{-3} during this period, lower than the model average of 48 pg m^{-3}. Modelled Hg(p) concentrations (Figure 5.10c) are close to an order of magnitude greater than Hg(II). During the simulated period, the mean Hg(p) concentration observed at Alert was 125 pg m^{-3}, with the model average in close agreement (158 pg m^{-3}). The tropospheric budget of Hg (Table 5.1) shows that approximately 63% of all oxidized mercury in the model is present as Hg(p), indicating high aerosol processing. We note here that we do not include the photoreduction of Hg(p) on organic aerosols to Hg(0), as in previous Hg modelling studies (e.g., Shah et al., 2021; Zhang and Zhang, 2022), as this photolysis rate is still poorly constrained. By including this process we could expect to see a decrease in the modelled average Hg(p) concentration, and an increase in mean surface Hg(0) concentrations. Overall, the mean modelled Hg(0), Hg(II), and Hg(p) concentrations show reasonable agreement with Arctic observations, within the measurement uncertainty.

We discuss these results in the context of previous Hg speciation measurements in the Arctic during spring. Observations have consistently shown greater Hg(p) concentrations than gaseous Hg(II) in early spring, over both tundra and sea ice (Cobbett et al., 2007;

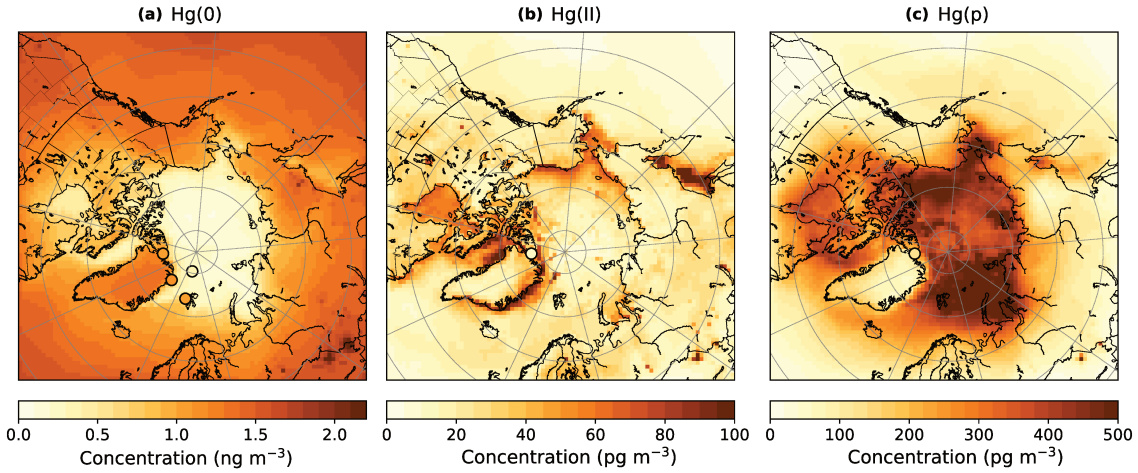

Figure 5.10: Simulated mean surface mercury speciation. Mercury concentrations are averaged for the full simulation period (March 14 – April 14, 2020) for surface (a) Hg(0), (b) gaseous Hg(II), and (c) Hg(p) concentrations. Observational averages for the same period are shown by markers with the same colour scale.

MacSween et al., 2022; Manca et al., 2013; Steffen et al., 2013, 2014). Long-term observations of Hg at Alert (2002–2011) reported average Hg(II) concentrations of 11 pg m^{-3} and 34 pg m^{-3} and Hg(p) concentrations of 137 pg m^{-3} and 150 pg m^{-3} during March and April, respectively (Steffen et al., 2014). These amounts are within the range of our model results, demonstrating a higher fraction of modelled Hg(p) during early spring. From the same long-term dataset, Hg(p) concentrations reached an annual maximum in April, whilst Hg(II) concentrations peaked during May. The reason for the springtime peak in Hg(p) has been investigated and associated with several variables. Low temperatures have been shown to increase the transition of gaseous Hg(II) to Hg(p), as well as a high fraction of organic and chloride containing aerosols (Amos et al., 2012; Steffen et al., 2014; Xu et al., 2020). In addition, the transport of air pollution from mid-latitudes to the Arctic during winter and spring (known as Arctic haze) brings high aerosol concentrations, contributing to the predominance of Hg(p) in spring. Our results are in agreement with these findings, with maximum Hg(p) simulated in the central Arctic, indicating the influence of high aerosol concentrations and low temperatures on Hg(II)/Hg(p) partitioning. Furthermore, Steffen et al. (2013) reported mean concentrations of 30 pg m^{-3} and 393 pg m^{-3} for Hg(II) and Hg(p) respectively, over Arctic sea ice in spring 2009. Observations of Hg(0) made concurrently over both snow-covered tundra and sea ice, showed

that Hg(0) was often significantly higher over tundra than over sea ice, indicating higher re-emission (Steffen et al., 2013). This finding is consistent with the observations in 2020 (Figure 5.10a) as well as the model prediction, where Hg(0) concentrations over continental snow are higher than over sea ice. Further discussion of Hg(0) re-emission over land-based snow and sea ice is provided in section 5.5.4.

Figure 5.11 shows the time series of simulated and 3h averaged observations of gaseous Hg(II), Hg(p), and total Hg at Alert (Canada). The model overestimates Hg(II) at this site (Figure 5.11a), and for Hg(p), we find relatively good agreement with the observations during March, but overestimated Hg(p) concentrations in April (Figure 5.11b). Several factors may contribute to this overestimation. Firstly, uncertainties in the measurements may partially explain some of this difference (Gustin et al., 2015). There is growing evidence that Hg speciation measurements may be biased low by a factor of 1.5–12 (e.g., Gustin et al., 2013, 2015; Huang et al., 2013; Osterwalder et al., 2021) due to analytical challenges. Whether measurements in high latitudes are biased low or not is, however, still a matter of discussion as relative humidity and ozone levels (both shown to influence the collection efficiency of the denuders) are typically low. Model inaccuracies in Hg gas-particle partitioning and other relevant processes are also likely to contribute. As shown previously in Figure 5.6b, modelled Hg(0) concentrations at Alert are in good agreement with the observations. Additionally, the total Hg concentration is well reproduced by the model (Figure 5.11c), suggesting that high Hg(II) and Hg(p) concentrations are unlikely to be solely caused by an overestimation in Hg(0) oxidation or re-emissions. Consequently, this indicates a potential underestimation in the loss of Hg(II) and Hg(p) via deposition. The relative amounts of atmospheric Hg(II) and Hg(p) have been shown to directly impact snow Hg concentrations in the Arctic (Steffen et al., 2014). Mercury deposition to snow and sea ice is discussed further in section 5.5.3). Finally, we once again note the potential role of coarse model resolution on differences between the model and observations, with large variation shown for Hg(II) and Hg(p) in neighbouring grid cells (shaded regions in Figure 5.6).

Overall, the model is capable of simulating the average springtime speciation of Hg(0), Hg(II), and Hg(p) over snow and sea ice compared to observations. Hg(II)/Hg(p)

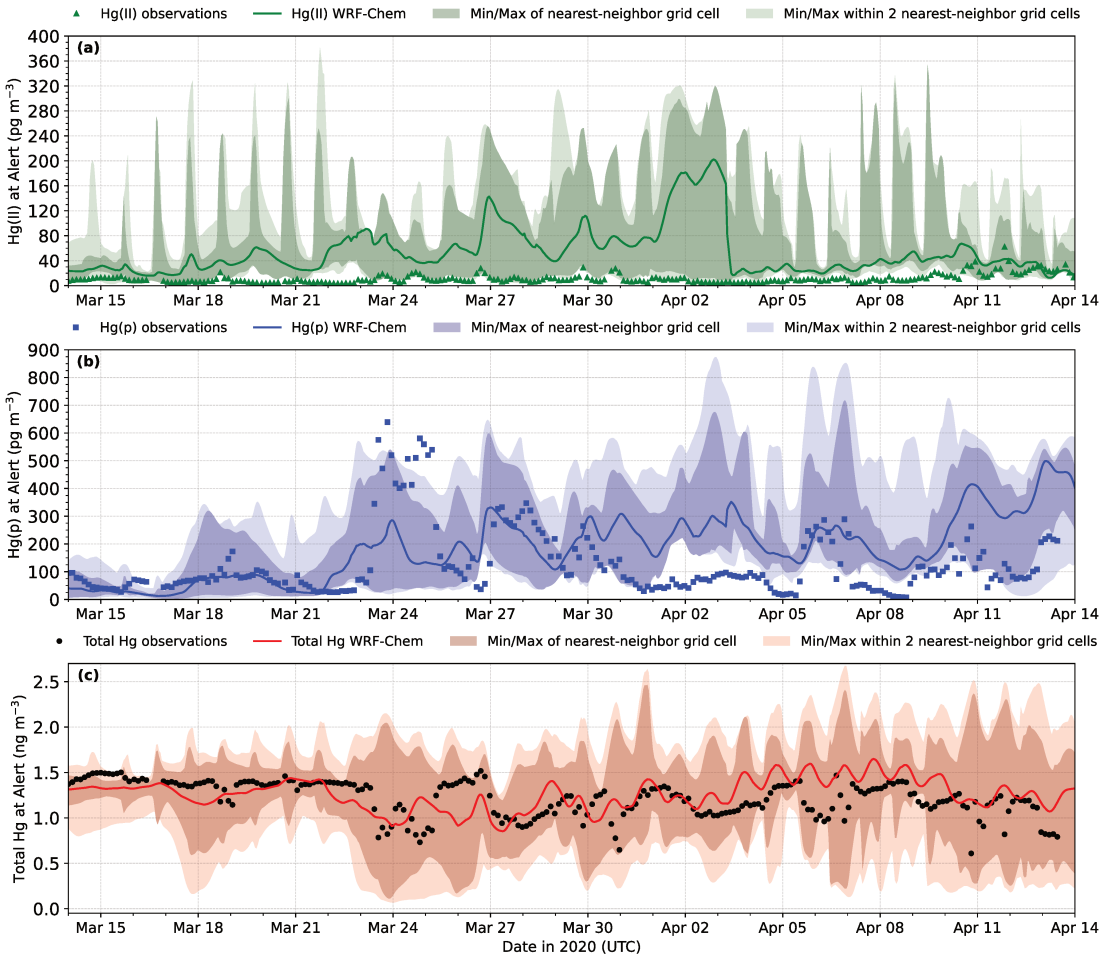

Figure 5.11: Model comparison of surface speciated mercury with observations from Alert, Canada. (a) gaseous Hg(II), (b) Hg(p), and (c) total atmospheric Hg (Hg(0)+Hg(II)+Hg(p)) at Alert, Canada.

partitioning at Alert was not fully captured by the model and more work is needed to refine/test the relevant processes including Hg(II) and Hg(p) deposition, sensitivity of Hg(II) uptake to aerosols, photoreduction of Hg(p), and uncertainties in the gas-particle partitioning equilibrium. Recent analysis of trends in Arctic Hg speciation over the past 20 years suggests that the composition and timing of AMDEs are changing (MacSween et al., 2022). Therefore, more observations of speciated Hg at high latitudes are also necessary to better evaluate models and to monitor shifts in springtime Hg chemistry.

5.5.3 Mercury deposition in the Arctic

Modelled Hg deposition fluxes (dry and wet) are presented in Figure 5.12. We find that dry deposition (Figure 5.12a) is the main Hg deposition process over land and sea ice. The majority of dry deposited Hg in the model is from Hg(II) and Hg(p), accounting for 88 % of total Hg dry deposition, with only 12 % from Hg(0). Over sea ice, the model predicts an even greater fraction of dry deposition from RM ($\sim$ 98 %). The percentage contribution of RM to dry deposition is consistent with the higher fraction of RM during spring, compared with other seasons. For wet removal (Figure 5.12b), the model predicts maximum wet deposition over the open ocean, consistent with previous Hg modelling studies (Holmes et al., 2010; Horowitz et al., 2017; Shah et al., 2021; Travnikov et al., 2017; Zhang and Zhang, 2022). We also find minimal wet deposition of Hg in the central Arctic and over land. This is unsurprising as the Arctic typically exhibits low precipitation rates (snow and rain) during spring, and consequently low wet deposition. To contextualize these results, we compare our modelled deposition fluxes with previous observational and modelling results in the Arctic.

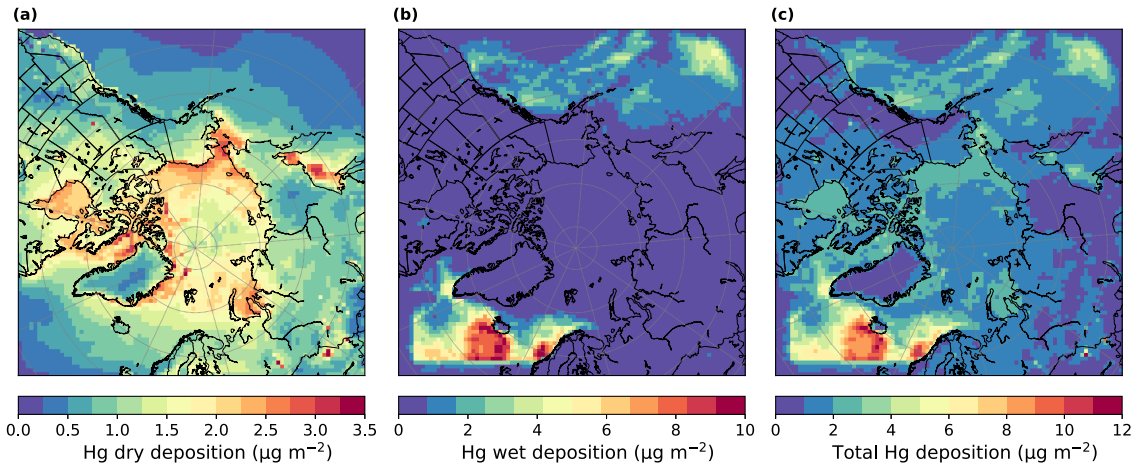

Figure 5.12: Accumulated model mercury deposition during the simulation period. (a) Hg dry deposition, (b) Hg wet deposition, and (c) total Hg deposition between March 14 – April 14, 2020.

Annually averaged observations of Hg wet deposition fluxes in the Arctic and sub-Arctic have been reported in the range of 0–5 μg/m^2/year (Pearson et al., 2019; Sanei et al., 2010; Sprovieri et al., 2017). In Alaska, mean annual Hg wet deposition fluxes of 2–5 μg/m^2/year were recorded at 5 different locations, over several years (2008–2015)

(Pearson et al., 2019). Sprovieri et al. (2017) also reported multi-year (2012–2015) mean fluxes of Hg wet deposition of 0.8–1.7 μg/m^2/year at Ny-Ålesund, Svalbard. Furthermore, measurements from two Canadian sub-Arctic sites have shown wet deposition fluxes of 0.5–2.0 μg/m^2/year (Sanei et al., 2010). Direct comparison between the model and observations is not entirely feasible, as the simulation is not temporally consistent with the observations, thus ignoring seasonal variation in precipitation rates, chemistry, and deposition. Measurement challenges also introduce some uncertainty in these values as the collection efficiency of samplers can be affected by the type of precipitation (rain vs. snow) (Prestbo and Gay, 2009; Rasmussen et al., 2012). However, these observations can still serve as a good indicator of general model performance.

Compared to the reported measurements above, the model underestimates Hg wet deposition over all of these locations, predicting a negligible amount of Hg wet deposition. One explanation is the seasonal differences in precipitation rates, with trends showing an annual peak in the Arctic during summer, likely contributing to greater Hg wet deposition. During the simulated period, our model predicts low precipitation above 60° N, with a cumulative average of 78 mm. Cumulative snowfall measurements from MOSAiC reported estimates of 72–107 mm, between 31 October 2019 and 26 April 2020, giving evidence to the low precipitation rates in the central Arctic (Wagner et al., 2022). Another possibility is the model implementation of Hg(II) wet deposition. This is currently treated by considering the solubility of Hg(II) equal to that of HNO_3, however, this assumption is a broad simplification and should be addressed in future model developments. The model-predicted average of total Hg deposition in the Arctic ($>$ 60° N) is 1.65 μg/m^2 (Figure 5.12c). This value is on the lower range of the recent model-ensemble predictions of Dastoor et al. (2022a) (10.5$\pm$5.0 μg/m^2/year, between March–May). However, our modelled deposition rates are not truly representative of the entire spring season, and would expect higher deposition rates in late spring as a result of the transition from high Hg(p) to high Hg(II) in the Arctic (Steffen et al., 2014). There is also a large variability in simulated springtime deposition fluxes between models (e.g., Angot et al., 2016; Dastoor et al., 2022a), due to differences in model performance of simulating AMDEs. Further evaluation of modelled Hg deposition fluxes with springtime measurements are

needed, particularly at Arctic sites where observations are limited. Alternatively, a year-long model simulation could provide a better comparison with observations, however, additional model developments would be required (e.g., improved description of Hg(II) and Hg(p) wet deposition) before this can be performed.

5.5.4 Hg(0) re-emission from snow and sea ice

Figure 5.13 shows the simulated mean Hg(0) re-emission flux, based on deposited RM to snow and sea ice. Mean Hg(0) re-emission fluxes up to 2.5 ng m^{-2} h^{-1} are predicted over coastal snow-covered regions, whereas re-emission from sea ice is considerably lower ($\sim$ 0.1 ng m^{-2} h^{-1}). In the context of Arctic observations, Hg(0) re-emission fluxes from snow have been reported with large variability, ranging from mean net negative fluxes (e.g., Brooks et al., 2006; Cobbett et al., 2007; Manca et al., 2013; Steen et al., 2009) to mean positive fluxes up to 534 ng m^{-2} h^{-1} during spring (Ferrari et al., 2005, 2008; Kamp et al., 2018; Mann et al., 2015b; Schroeder et al., 2003; Sommar et al., 2007; Steen et al., 2009). Direct comparison between reported values and the modelled fluxes is difficult due to differences in measurement techniques, sampling locations, AMDE frequency, and time of year, resulting in different atmospheric conditions and snowpack properties. As a broad assessment however, the simulated re-emission fluxes here (0 – 2.5 ng m^{-2} h^{-1}) are within the ranges reported by many Arctic and sub-Arctic measurement studies (Dommergue et al., 2003; Ferrari et al., 2005, 2008; Mann et al., 2015b; Schroeder et al., 2003; Sommar et al., 2007). Caution should also be taken when evaluating mean fluxes as studies have shown large re-emission fluxes immediately following AMDEs, often several times greater than the average springtime re-emission flux (e.g., Ferrari et al., 2008; Kamp et al., 2018; Manca et al., 2013). A subsequent investigation of Hg(0) re-emission following AMDEs in the model is therefore useful to assess re-emission flux variability during the spring season, and, potentially complement location-based measurement studies. Measurement data of Hg(0) re-emission from sea ice are even more scarce, making it difficult to assess the model values against observations. Additional measurements of snowpack Hg(0) re-emission fluxes over sea ice are particularly desirable to better evaluate and refine the current Hg(0) re-emission parameterization in the central Arctic.

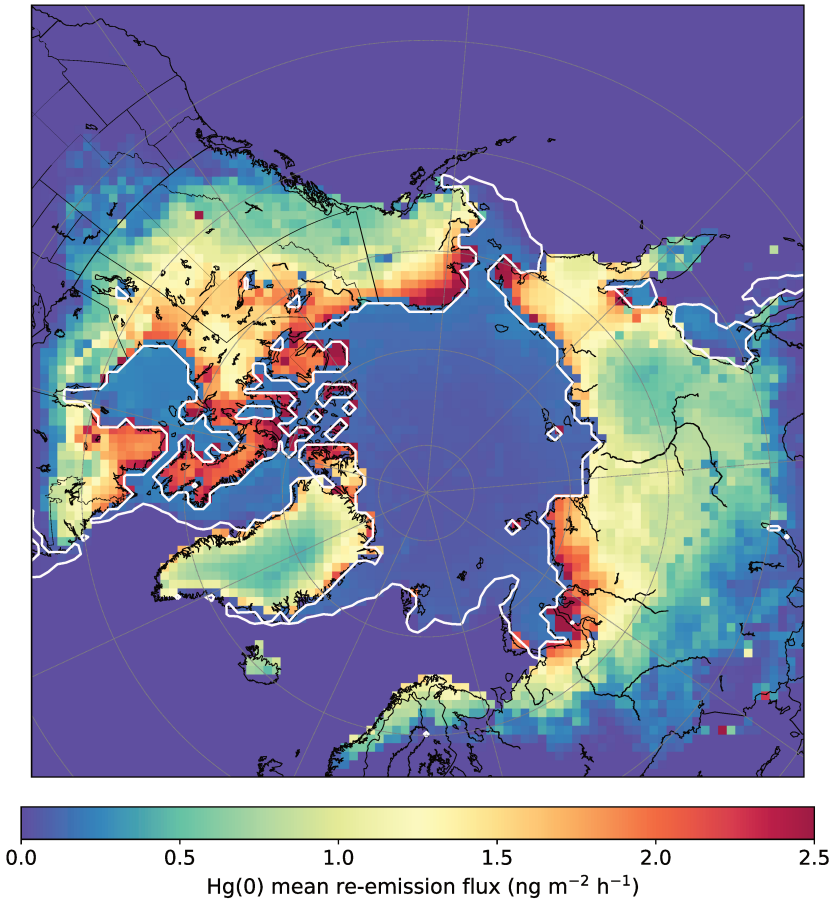

Figure 5.13: Simulated average Hg(0) re-emission flux from snow and sea ice. Simulated mercury re-emission flux is averaged for the full simulation period (March 14 – April 14, 2020). White contour line represents the sea ice fraction above 75 % coverage at the beginning of the simulation.

To understand the transfer of Hg between air and snow in the model, we calculate the fraction of deposited Hg re-emitted from snow and sea ice for the entire simulation period. Above 60° N, approximately 40 % of deposited Hg is re-emitted back to the atmosphere, with 60 % remaining within the snowpack. Over land-based snow, 74 % of deposited Hg is re-emitted, whereas only 4 % of deposited Hg over sea ice is released back into the atmosphere. We note that we apply a smaller photoreduction rate (k_{red}) of RM on sea ice than for land-based snow (see Section 5.2.1), based on the hypothesis that Hg(0) re-emission is comparatively smaller over Arctic sea ice than the continental snowpack (Steffen et al., 2013). Hg(0) observations over Arctic tundra have shown large peaks following depletion which were not observed with the same intensity over sea ice, suggesting lower re-emission rates (Steffen et al., 2013). The presence of chloride in snow has also

been hypothesized to increase Hg retention via stabilisation of Hg(II) and a suppression of photoreduction (Hintelmann et al., 2007; Lehnherr and St. Louis, 2009; Poulain et al., 2004). Recent experimental evidence has supported this hypothesis, showing a negative relationship between chloride concentrations and the amount of photoreduced Hg in snow (Mann et al., 2018). In the context of the Arctic, snow on sea ice is overall more likely to retain mercury than land-based snow as sea ice regions are typically more enriched with chloride (Krnavek et al., 2012; Peterson et al., 2019). The exact mechanism of Hg stabilization by chloride in snow remains unclear, with theories proposing the formation of photostable chlorocomplexes, or by increased Hg(p) concentration in snow considered to be more stable against photoreduction (Brooks et al., 2006; Hintelmann et al., 2007; Poulain et al., 2007). For this study, we assumed deposited Hg(p) to be equally photoreducible as Hg(II), however, this assumption may need to be revisited as future work refines our knowledge of the fate of Hg in snow.

We also assess the sensitivity of our assumption that 60 % of deposited RM to snow and sea ice is available for re-emission by performing a simulation where 100 % of deposited RM is assumed to be photoreducible (Figure 5.14)). Results from this sensitivity test show minimal change to the re-emission fluxes from land-based snow, but re-emissions over sea ice increase by approximately 60–70 %. The uncertainty associated with the rate and magnitude of RM photoreduction in snow remains large, motivating more observational and modelling studies to improve our understanding of these processes. Future model development could also look to refine these parameterizations by testing for different seasons, particularly during summer when Hg(0) re-emissions are known reach their annual maximum (Araujo et al., 2022).

5.6 Summary and future perspectives

This study presents a comprehensive development of the WRF-Chem model, including Hg gas-phase and aerosol chemistry, deposition, and re-emission processes in the Arctic. The recently improved mercury chemical mechanism of Shah et al. (2021) is added to a version of WRF-Chem that includes polar bromine emissions from surface snow and blowing snow together (Marelle et al., 2021), and tested in a dedicated regional Arctic

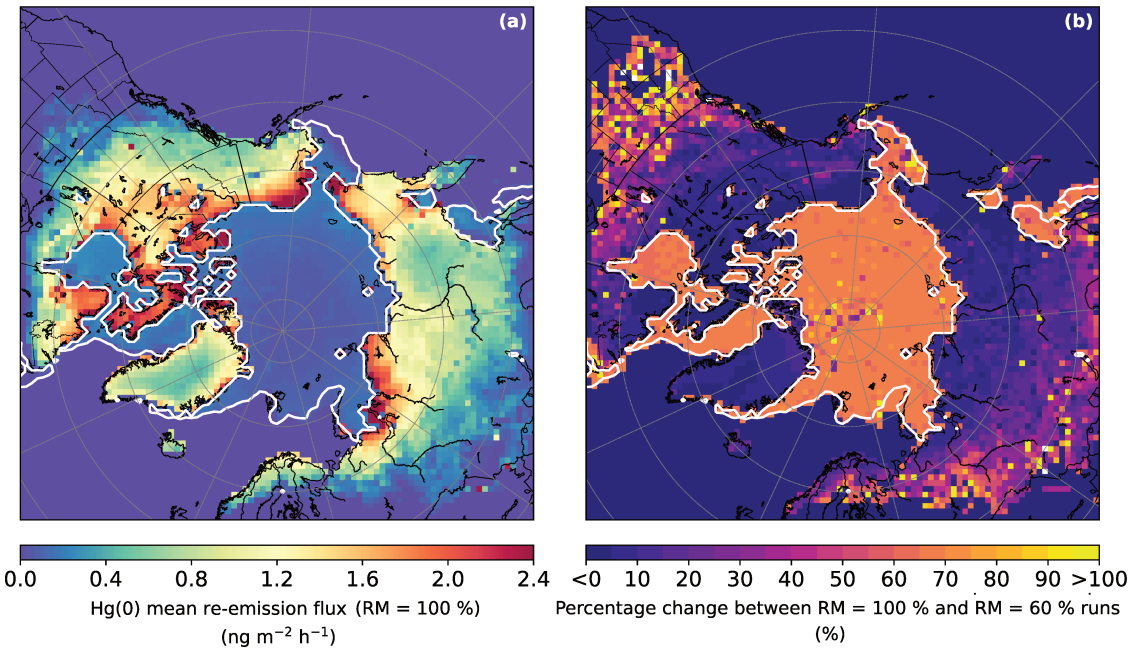

Figure 5.14: Simulated average Hg(0) re-emission flux in the re-emission sensitivity run. (a) Simulation average (March 14 – April 14, 2020) of Hg(0) re-emission flux from snow and sea ice of the sensitivity run, with 100% of deposited reactive mercury (RM) assumed to be photoreducible. (b) Percentage change of Hg(0) re-emission between the sensitivity run assuming 100% and run assuming 60% (Figure 5.13) of RM available for re-emission. White contour lines represent the sea ice fraction above 75 % coverage at the beginning of the simulation.

modelling study for the first time. This new model development allows us to simulate springtime Arctic ozone and mercury depletion on an hourly timescale, with modelled oxidant concentrations calculated online. Model results are evaluated with simultaneous measurements of Hg(0), O_3, and BrO from the central Arctic during MOSAiC and from Arctic stations. The main results of this study can be summarized as follows:

- Model predictions of Hg(0) and O_3 show extended periods of depletion in the central Arctic during spring, in agreement with observations from MOSAiC. Our model results also indicate that bromine is the major Hg(0) oxidant in the Arctic, driving springtime Hg(0) depletion.

- Oxidized mercury (Hg(II) and Hg(p)) in the model is evaluated to understand the speciation and spatial distribution of Hg. We find high aerosol processing of Hg during spring, with Hg(p) accounting for approximately 63 % of all Hg(II) species. Measurements of speciated Hg remain sparse and uncertain. A focus on reduced

uncertainty in Hg(II) and Hg(p) observations, additional measurement campaigns, and long term observations are needed to better evaluate the model.

- Both deposition fluxes of oxidized mercury and re-emission fluxes of Hg(0) from snow/ice remain uncertain. Despite this, the balance of oxidation, deposition, and re-emission predicted here provides reasonable modelled quantities of gas-phase Hg(0) compared to measurements. Based on experimental evidence, we can expect an average systematic uncertainty of $\sim$ 10 %, and in extreme cases up to 20 %, for Hg(0) measurements (Slemr et al., 2015).

- For our modelled period, only 4 % of deposited Hg(II) and Hg(p) over the Arctic Ocean is re-emitted compared to 96 % that remains trapped in snow/ice. Over snow-covered land, the percentage of re-emitted Hg(0) is higher (74 % re-emitted vs. 26 % retained in the snowpack). The implications of this for Arctic Hg(0) summertime re-emission (Araujo et al., 2022), and under long-term environmental changes (e.g., sea ice loss), are important to consider in future work.

This work serves as a basis for future studies to explore some key questions regarding Arctic Hg chemistry. For example, the contribution of the Arctic Ocean to summertime Hg(0) re-emission is an outstanding research question which could be tested using this model. Additionally, the broader impacts of future climate scenarios on Hg chemistry, emissions, and deposition in the Arctic may also be assessed. Overall, this could enable better predictions on the long-term implications of climate change on Hg contamination of Arctic ecosystems. Finally, we note below the key processes for mercury included in the model that remain uncertain:

- **Chemical kinetics** – Identification of Hg(II) species is a top priority to improve our understanding of mercury redox chemistry. This requires additional theoretical, experimental, and modelling studies to reduce uncertainties in the reaction rates of mercury. In particular, photoreduction of Hg(II) and Hg(p) should be investigated further to better constrain the contribution of reduction kinetics to atmospheric Hg chemistry.

- **Dry and wet deposition** – Model descriptions of Hg dry and wet deposition should be revised in future work to more accurately determine the transfer of Hg to snow and ice surfaces.

- **Gas-particle partitioning** – Better understanding of the main model parameters (e.g., heterogeneous uptake rate, partitioning coefficient) that control Hg gas-particle partitioning is needed. An evaluation of modelled aerosol concentrations using observations is needed to refine bromine and mercury heterogeneous recycling on aerosols.

- **Re-emission fluxes from snow and snow on sea-ice** – Hg(0) emissions from snow and ice remain difficult to constrain in models due to the complexity of processes that contribute to them and the difficulty of measuring fluxes. Model assumptions (e.g., 60 % reducible Hg in snow, photoreduction rate constants from snow and snow on sea ice) need additional testing. A more accurate representation of factors which influence Hg(0) re-emission (e.g., snowpack chloride concentration) will also likely be needed in future work.

Data availability

The updated WRF-Chem model code used in this study is available on Zenodo at Ahmed et al. (2022a), https://doi.org/10.5281/zenodo.7137482. The surface meteorology measurements made onboard the *Polarstern* can be accessed at Schmithüsen (2021). The MOSAiC radiosonde data are available at Maturilli et al. (2021). The elemental mercury dataset from MOSAiC is available at Angot et al. (2022a). The merged ozone dataset from MOSAiC is available at Angot et al. (2022c). BrO MAX-DOAS measurement data are available at Mahajan (2022). Surface elemental mercury data at Villum (Greenland) are available at the EBAS website (https://ebas.nilu.no/). Surface ozone data at Villum (Greenland) and Zeppelin (Svalbard) were also retrieved from the EBAS database. The surface Hg measurement dataset at Alert (Canada) is available upon request by contacting the co-authors A. Steffen and G. Stupple. Surface elemental mercury data at Zeppelin (Svalbard) are available upon request by contacting the

co-author K. Pfaffhuber. Surface ozone data at Utqiaġvik (Alaska), Summit (Greenland), and Eureka (Canada) were provided by the NOAA Global Monitoring Laboratory (https://www.esrl.noaa.gov/gmd/ozwv/surfoz/data.html). Surface ozone measurements from Alert (Canada) are provided from the Canadian Air and Precipitation Monitoring Network (CAPMoN). Satellite BrO VCD data from TROPOMI are available upon request by contacting the co-authors A. Richter and B. Zilker.

Author contributions

Conceptualization, design, and initial draft of the manuscript: SA, JLT, ADo, HA, RL, JSt. **Model developments:** SA, JLT, LM. **Model simulations:** SA. **Data acquisition:** HA, SDA, A-MB, BB, IB, LB, MB, NB, JHC, ADa, SD, DHo, DHe, H-WJ, TJ, TL, ASM, KP, KAP, LLJQ, ARin, ARy, ARic, AS, AS-L, GS, HS, JSc, OT, BZ. **Editing and revision of the manuscript:** All authors

Acknowledgements

We would like to thank the following individuals for their contributions during MOSAiC: Jacques Hueber, Matthew D. Shupe, Marion Maturilli, and Holger Schmithüsen. We also thank all those who contributed to MOSAiC and made this endeavour possible (Nixdorf et al., 2021). We thank all those involved in the operation and maintenance of the *Polarstern* research vessel (Knust, 2017). Computer analyses benefited from access to IDRIS HPC resources (GENCI allocation A011017141) and the IPSL mesoscale computing center. Some observations used here were provided by the Atmospheric Radiation Measurement (ARM) Climate Research Facility, a US Department of Energy (DOE) Office of Science User Facility sponsored by the Office of Biological and Environmental Research. We thank the many ARM operators who supported the field observations. We also thank the Dr. Neil Trivett Global Atmosphere Watch Observatory at Alert for technical support.

Funding information

This work was supported by the Ecole Doctorale Sciences de la Terre, de l'Environnement et des Planètes (ED105) of Université Grenoble Alpes. JLT is funded by the European Union's Horizon 2020 research and innovation programme under grant agreement No 101003826 via project CRiceS (Climate Relevant interactions and feedbacks: the key role of sea ice and Snow in the polar and global climate system). JLT and SA also acknowledge support by the CNRS INSU LEFE-CHAT program under the grant BROM-ARC. Some of the observational data reported in this manuscript were produced as part of the Multidisciplinary drifting Observatory for the Study of Arctic Climate (MOSAiC) expedition with the tag MOSAiC20192020, with activities supported by Polarstern expedition AWI_PS122_00. Data acquisition during the MOSAiC expedition was funded by the US National Science Foundation (NSF) (award OPP 1914781 and award OPP 1807163), the Swiss National Science Foundation (grant 200021_188478), the Swiss Polar Institute, the DOE Atmospheric System Research Program (DE-SC0019251), and the US National Oceanic and Atmospheric Administration (NOAA) Physical Sciences Laboratory. Part of this project was also funded by the European Research Council (ERC), H2020 European Research Council (GASPARCON (grant No. 714621)), and the Academy of Finland Flagship funding (grant No. 337552). JS holds the Ingvar Kamprad chair for extreme environments research, sponsored by Ferring Pharmaceuticals. The measurements at Villum Research Station was financially supported by the Danish Environmental Protection Agency with Funds for Environmental Support to the Arctic Region (Project No. J.nr. 2021 – 60333). Measurements in Alert are supported by the Northern Contaminants Program (Crown-Indigenous Relations and Northern Affairs Canada). Satellite BrO data analysis was supported by the Deutsche Forschungsgemeinschaft (project no. 268020496 – TRR 172) within the Transregional Collaborative Research Center 'ArctiC Amplification: Climate Relevant Atmospheric and SurfaCe Processes, and Feedback Mechanisms (AC)3' in subproject C03. ARin was partly supported by the European Union's Horizon 2020 research and innovation framework programme under Grant agreement no. 101003590 (PolarRES).

Chapter 6

Conclusions & Perspectives

This work has aimed to better understand Arctic halogen atmospheric chemistry and its impacts on the ozone and mercury chemical cycles. Several questions were posed at the beginning of this thesis and each are individually answered below. The future perspectives of this work are also presented in this chapter.

1. **Using Lagrangian transport models, what can we learn about the geographical origin and transport pathways of observed ozone-depleted and mercury-enriched air masses in the Arctic? What is the influence of exposure to sea ice on atmospheric mercury and ozone?**

   Atmospheric transport modelling was first used (FLEXPART-WRF and HYSPLIT) to analyse air mass histories, based on coastal Arctic observations of ozone and mercury. Two particular case studies were investigated. First, measurements of surface ozone in the coastal Arctic showed several instances of ODEs during April 2012. Air mass trajectories during these depletion events showed highest potential emission sensitivities from regions over sea ice, with little influence from land. Additionally, in the 7 days preceding the ozone measurements, ozone-depleted air travelled much closer to the surface on average (less than 750 m), compared to ozone-rich air which originated from much higher in the free troposphere (up to 1500 m). Air masses during ozone-depleted periods were therefore much more sensitive to surface and blowing snow emissions of bromine from sea ice. This

analysis was in contribution to the study of Marelle et al. (2021).

In the second case study, I performed an analysis on back trajectory model output from the HYSPLIT model, in contribution to Araujo et al. (2022). This work was done to understand the emission source regions of the summertime maximum in Hg(0), recorded at three coastal Arctic sites during summer 2018. In June 2018, back trajectory analysis indicated approximately 62 % of boundary layer air resided over sea ice and land based snow. During the summer Hg(0) maximum in July 2018, approximately 39% of boundary layer air was associated with sea ice and snow-covered land, suggesting a cryospheric source for the summertime Hg(0) maximum observed in the Arctic. This is in contradiction with previous studies (e.g., Fisher et al., 2012; Sonke et al., 2018; Zhang et al., 2015), which did not assess air mass origins, as presented in this thesis. In both case studies, observations of ODE occurrence and Hg(0) re-emission can be directly linked to the cryosphere, with important implications on future trends under Arctic warming scenarios.

2. **What are the quantifiable impacts of halogen emissions from snow on boundary layer chemistry and oxidative capacity? What combination of emissions, chemistry, and transport can explain surface chlorine and VOC observations in the Arctic?**

   To address this question, I first needed to develop the 1-D model, PACT-1D, to include a new parameterization describing molecular halogen emissions of Cl_2 and Br_2 from surface snow. I then used PACT-1D to study the impacts of halogen emissions on the oxidative capacity of the polar boundary layer during spring. Model results were evaluated using observations from the 2009 OASIS campaign at Utqiaġvik, Alaska, focused on a two-day period between 18–19 March 2009. The model shows good performance in capturing surface measurements of various halogen species, including Cl_2, Br_2, BrO, and HOBr. Modelled Cl_2 and Br_2 emission fluxes are also within a reasonable range of previously measured and simulated snowpack halogen emission fluxes (Custard et al., 2017; Wang and Pratt, 2017).

The model-predicted impact of halogen emissions on oxidative chemistry can be summarized as follows. With surface halogen emissions active, HO_x concentrations increased by up to a factor of 30 at the surface (1.5 m above ground level). This increase was largely driven by Cl-initiated oxidation of CH_4, forming CH_3O_2 and converted to HO_2 via reaction with NO. As a consequence, surface VOC lifetimes with respect to OH were reduced by approximately 43 % in the presence of halogens at the surface, compared to when halogen emissions were deactivated. Therefore, surface reactivity was significantly enhanced with the inclusion of halogen emissions, both directly via Cl-driven oxidation, and indirectly through increased HO_x concentrations.

3. **What is the vertical extent of bromine and chlorine chemistry in the Arctic boundary layer?**

   The next step of this investigation was to assess the vertical extent of halogen chemistry and the impacts on reactivity within the boundary layer. During the simulated period, Cl_2 was confined to approximately the lowest 15 m of the atmosphere, with negligible concentrations of Cl_2 above this height. As a result, a strong vertical reactivity gradient was predicted by the model. Chemical lifetimes of VOCs showed negligible change at altitudes above 50 m, with respect to OH, when emissions of halogens were active or deactivated. These results suggest that the vertical extent of this highly oxidizing layer may only extend up to 15 m above the surface. In the case of bromine, Br_2 was found to be present up to and above the surface inversion height ($\sim$ 40 m), due to heterogeneous activation on aerosols. Finally, the work presented in Chapter 4 was published in *Journal of Geophysical Research: Atmospheres* (Ahmed et al., 2022c). The model is also publicly available to encourage other research work using this newly developed tool (Ahmed et al., 2022b).

4. **Can regional modelling be used to accurately represent springtime ozone and mercury depletion events in the central Arctic on an hourly timescale?**

Following the 1-D model investigation, I explored the regional impacts of spring-time halogen chemistry on ozone and mercury using the 3-D regional model WRF-Chem. At the start of my thesis, there was a lack of chemical transport models suited to investigate the coupled cycles of halogens, ozone, and mercury in the Arctic simultaneously and at sufficient resolution. In this work, I implemented a major development to the WRF-Chem model to include Hg redox chemistry, based on recently improved mechanistic descriptions from Shah et al. (2021). This new chemical mechanism was then applied to an Arctic-focused study for the first time. These developments also extend the recent work of Marelle et al. (2021) which included polar bromine emission sources in WRF-Chem. Therefore, the model study presented in this thesis is also the first to simulate Hg chemistry using bromine emission descriptions from both surface snow and blowing snow simultaneously in the Arctic. This model version is published online, freely available for the wider use of the atmospheric research community (Ahmed et al., 2022a).

I performed simulations with updated WRF-Chem model for spring 2020, during the MOSAiC expedition. Model results of Hg(0) and O_3 showed good agreement with the MOSAiC observations, capturing the extended periods (up to several weeks) of depletion in the central Arctic. The model predicted widespread depletion of both Hg(0) and O_3 in the central Arctic, associated with bromine emissions from sea ice. It is also predicted by the model that bromine is the major oxidant of Hg(0) in the Arctic, consistent with previous Arctic observations (Wang et al., 2019). These results highlight the importance of using online-calculated concentrations of bromine in models, needed to accurately simulate oxidation chemistry and depletion events during spring.

5. **How does mercury redox chemistry impact deposition rates in the Arctic? What are the relative amounts of mercury re-emission and retention in the Arctic snowpack?**

   By including a better representation of Hg oxidation chemistry, it is now possible to more accurately simulate its deposition to the cryosphere and ocean. Model

predicted deposition rates indicated that the majority of deposited Hg in the Arctic during spring was via dry deposition of oxidized Hg (88 %). Once deposited, I also included descriptions of Hg(0) re-emission from snow and sea ice, following photoreduction. Model predictions indicated that approximately 40 % of deposited Hg during spring was re-emitted to the atmosphere, and 60 % was retained in the snowpack (land-based and snow on sea ice). This has important implications for the transfer of atmospheric Hg to the cryosphere and Arctic Ocean, where it can be transformed into toxic methylmercury, as well as for the summer re-emission maximum of Hg(0) during the melt period. These results are presented in Chapter 5, which is currently in preparation to be submitted for publication in *Elementa: Science of the Anthropocene*.

Perspectives

This thesis makes an important contribution to our understanding of Arctic halogen chemistry and its impacts on ozone and mercury. However, there are several limitations which could help advance this work. Here, I propose several improvements and broader research topics to be addressed in future work:

1. **Snowpack emissions in WRF-Chem:** As demonstrated in this thesis, snowpack halogen emissions greatly influence the oxidative capacity of the boundary layer. This is an important component of polar atmospheric chemistry that is often neglected or simplified by 3-D models. The parameterizations of snowpack emissions for molecular halogens, developed in PACT-1D, could be included in WRF-Chem (or other 3-D models) and tested on a regional scale. In addition, this work did not assess the emission of BrCl from snow. Recent measurements in the Arctic have shown that BrCl was produced in snowpack interstitial air, together with Cl_2 and Br_2 (Custard et al., 2017). Including snow emissions of BrCl in PACT-1D could also be tested to assess its contribution to reactive halogen chemistry.

2. **Modelling snow and aqueous-phase chemistry:** A limitation of the PACT-1D

model is that the snowpack is not explicitly represented. This simplification neglects many of the chemical reactions occurring within the snowpack on ice and snow grain surfaces. These multiphase reactions are particularly important for regulating halide concentrations (e.g. HCl and HBr) in the snow and therefore halogen emission fluxes. Additionally, transport processes between the snow interstitial air and overlying atmosphere (e.g. wind pumping) are not accounted for here which may affect the magnitude of snowpack emission fluxes and consequently surface layer atmospheric chemistry. Therefore, including descriptions of aqueous chemistry and snowpack processes would further extend the work in this thesis, building a more realistic representation of the interactions between the snow and atmosphere. These developments could follow similar approaches used in previous 1-D modelling studies (e.g., Thomas et al., 2011; Toyota et al., 2014b) to advance the PACT-1D model in future work.

3. **Modelling iodine chemistry:** Iodine chemistry is not included as part of the current chemical mechanisms in either PACT-1D or WRF-Chem. Although quantities of iodine (I_2) in the Arctic are low, I_2 is highly reactive and therefore important to polar atmospheric chemistry, including ODEs (Raso et al., 2017). Recent measurements of iodine monoxide (IO) in the central Arctic have shown that iodine can contribute to ODEs on a level comparable to bromine (Benavent et al., 2022). Testing this in the version of WRF-Chem used in this thesis would help to further understand the contributions of iodine and bromine to ozone depletion in the Arctic.

4. **Arctic winter/summer modelling:** This thesis was mainly focused on atmospheric chemistry during Arctic springtime. WRF-Chem could also be used to study Arctic atmospheric chemistry during different seasons and conditions (e.g. polar night (winter) and polar day (summer)). For example, investigating potential nocturnal sources of reactive bromine precursors could be important in understanding the onset of bromine activation during polar sunrise (Simpson et al., 2018). Additionally, testing Hg(0) re-emission processes from cryospheric sources during summer

could help to better understand the summertime maximum in Hg(0) concentrations (Araujo et al., 2022)

Finally, there are two broader perspectives that I wish to highlight:

1. **Arctic model intercomparison:** Since the most recent polar model intercomparison project (POLMIP, Emmons et al. (2015)), many models have improved their descriptions of different aspects of Arctic atmospheric chemistry (e.g., Fernandez et al., 2019; Herrmann et al., 2021; Huang et al., 2020; Marelle et al., 2021; Yang et al., 2020). A new Arctic model intercomparison study could evaluate the state-of-the-art in polar atmospheric chemistry modelling, allowing a direct evaluation between the treatment of halogen-driven processes in different models. The recent measurement data from MOSAiC also provides a good opportunity to assess model performances in the central Arctic.

2. **Representation of sea ice leads in models:** Sea ice leads are important features of the Arctic which impact convective mixing of gases in the polar boundary layer (Moore et al., 2014). However, the representation of sea ice leads in atmospheric chemistry models are difficult to accurately capture. Therefore, efforts to couple cryosphere-atmosphere models will be crucial to consider the impacts of Arctic sea ice changes on atmospheric chemistry in a warming climate.

Appendix A

Supplementary material for Chapter 4

This appendix contains supplementary material to Chapter 4, including 1 table with model performance statistics and 8 figures displaying the measurement data from OASIS and results from the sensitivity runs. Table A.1 contains goodness-of-fit statistics between the PACT-1D model and observations made during OASIS. Model results from the sensitivity tests performed with PACT-1D, based on the chlorine and bromine emission parameterizations, are shown in Figures A.1, A.2, and A.3. The full OASIS timeseries of observations used to select the model time period is shown in Figure A.4. A comparison of the calculated surface inversion height derived from two different expressions is plotted in Figure A.5. Modelled differences between the halogen vertical distributions in the AERO and BASE runs are shown in Figure A.6. The vertical distribution of Cl_2 and Br_2 in the BLD sensitivity run is shown in Figure A.7, and finally, vertical distributions and transport rates for BrO and HOBr in the BASE run are plotted in Figure A.8.

Table A.1: Goodness-of-fit statistics between PACT-1D model simulation (BASE run) and OASIS observations. Correlation coefficients (r), root mean square error (RMSE), and mean bias error (MBE).

Variable	***r***	**RMSE**	**MBE**
Cl_2	0.69	36.6 pptv	7.1 pptv
Br_2	0.83	2.0 pptv	0.5 pptv
BrO	0.72	4.4 pptv	-2.6 pptv
HOBr	0.55	5.8 pptv	-3.0 pptv
NO_2	-0.15	139.3 pptv	-68.9 pptv
NO	0.12	45.0 pptv	-22.5 pptv
HCHO	0.58	158.3 pptv	59.8 pptv
O_3	-0.22	12.0 ppbv	-2.4 ppbv
HO_2	0.79	1.8 pptv	-0.5 pptv

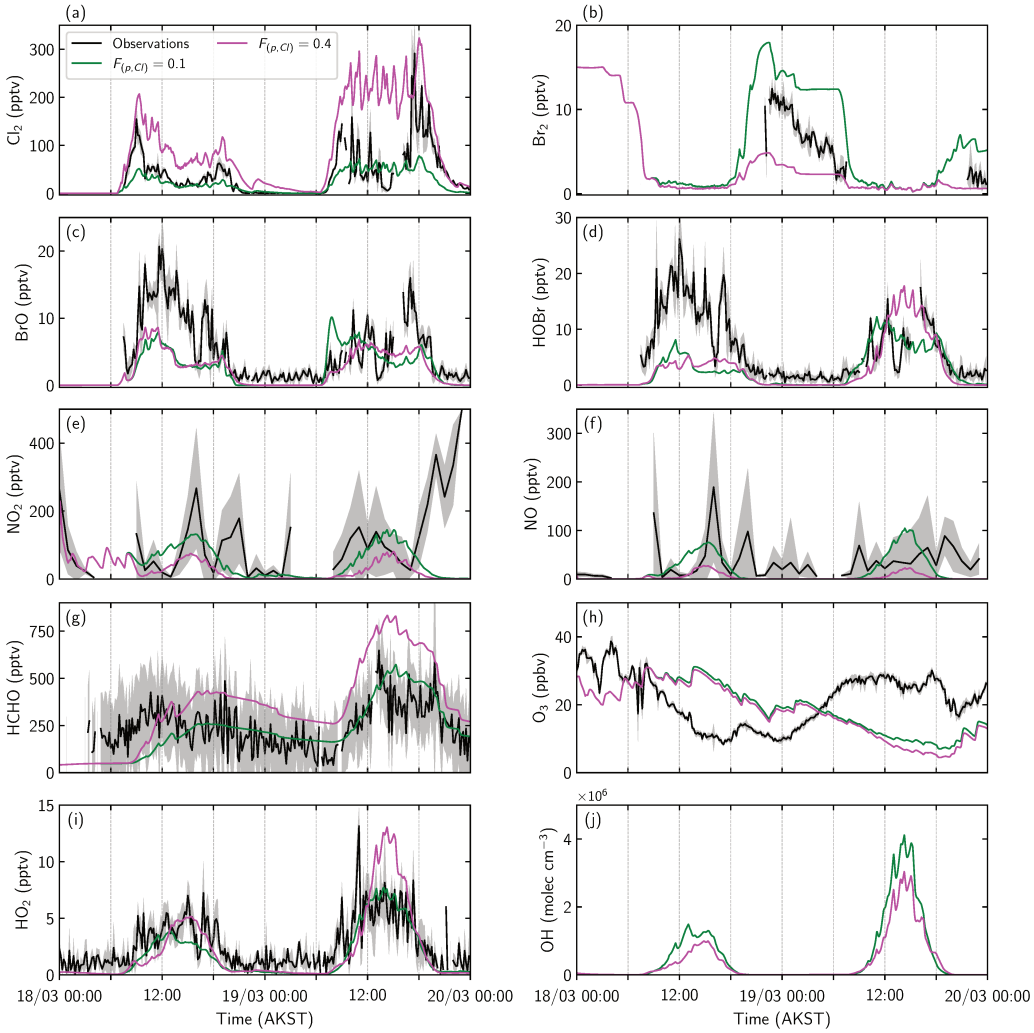

Figure A.1: Model comparison of the primary chlorine emission sensitivity runs with observations at 1.5 m above ground level during 18 and 19 March 2009. Values of $F_{(p,Cl)} = 0.1$ (green) and $F_{(p,Cl)} = 0.4$ (magenta) were tested and are compared with the 10-minute averaged measurements (black). NO_x measurements are plotted as an hourly average. Grey shaded areas represent the standard deviation of the average from the instantaneous measurements.

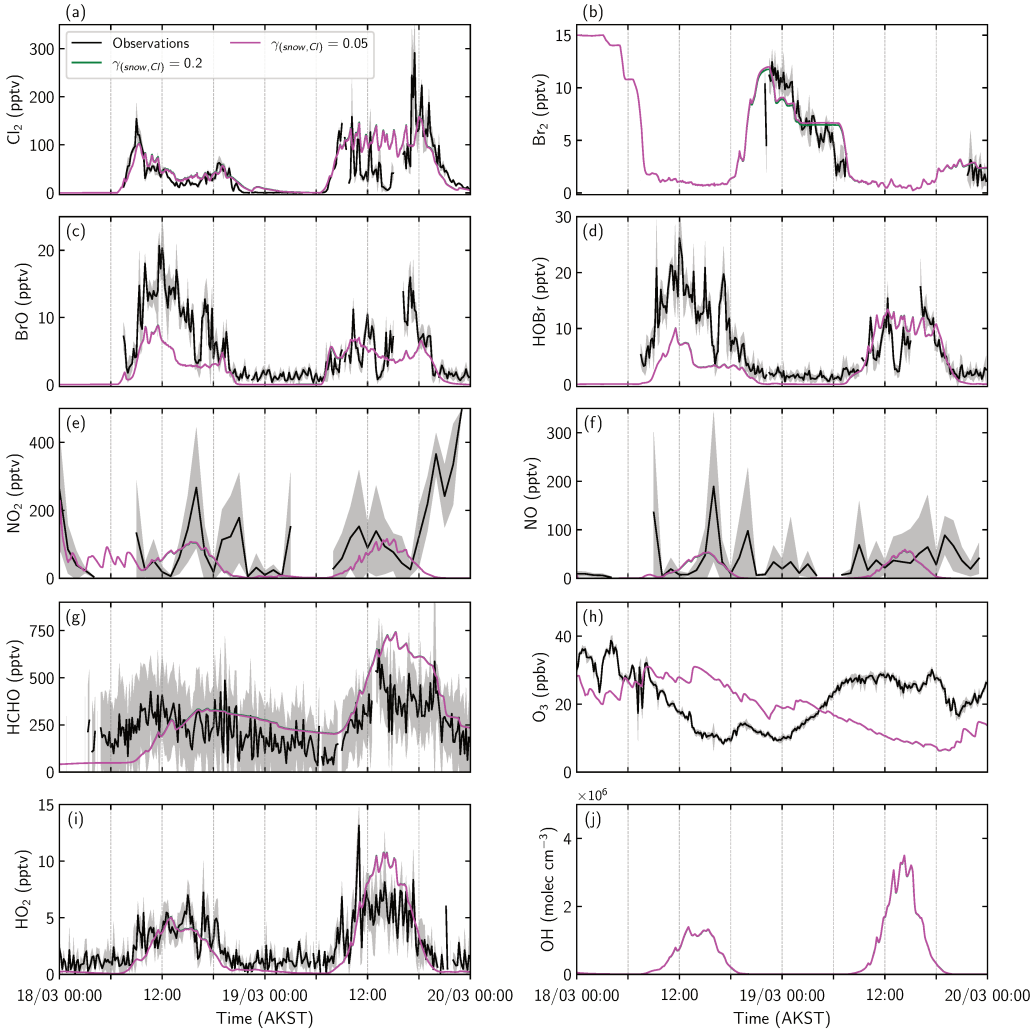

Figure A.2: Model comparison of the snow-surface chlorine recycling sensitivity runs with observations at 1.5 m above ground level during 18 and 19 March 2009. Values of $\gamma_{(snow,Cl)} = 0.05$ (magenta) and $\gamma_{(snow,Cl)} = 0.2$ (green) were tested and are compared with the 10-minute averaged measurements (black). NO_x measurements are plotted as an hourly average. Grey shaded areas represent the standard deviation of the average from the instantaneous measurements.

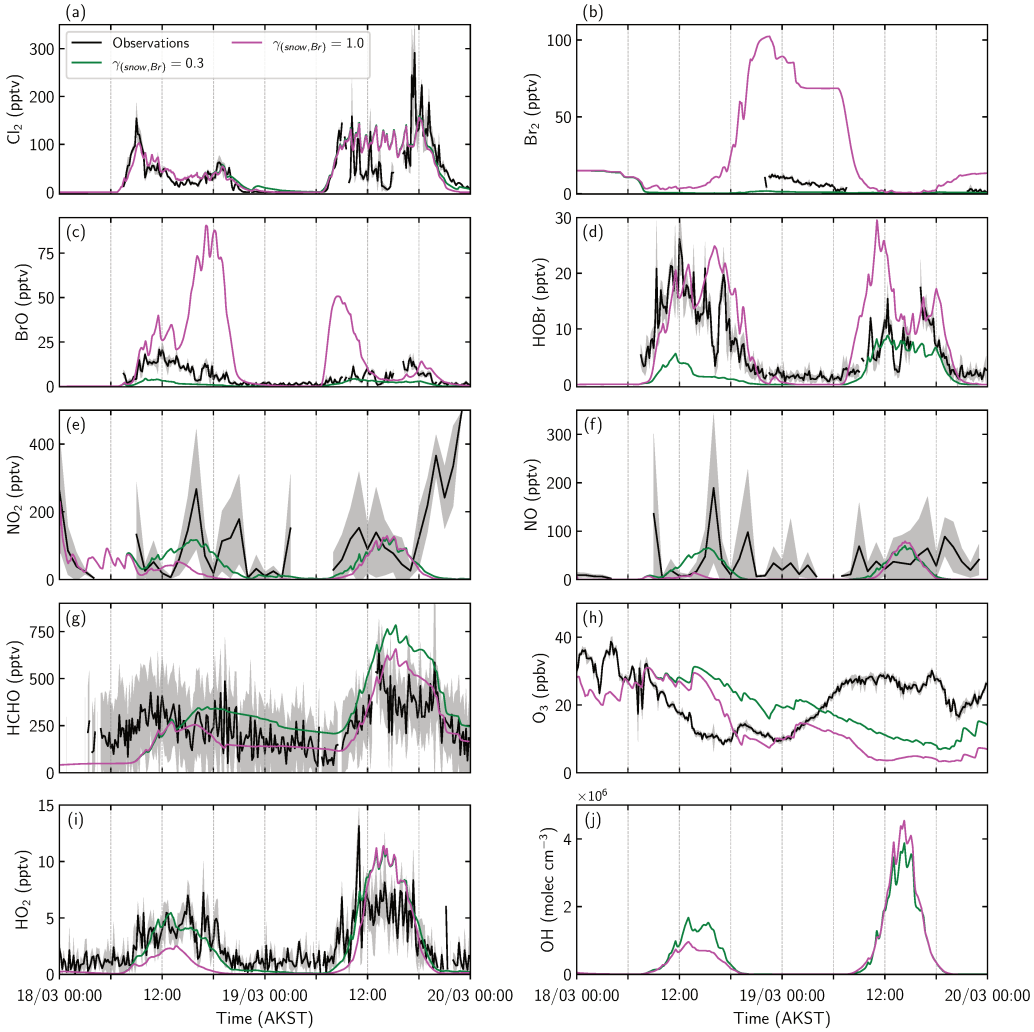

Figure A.3: Model comparison of the snow-surface bromine recycling sensitivity runs with observations at 1.5 m above ground level during 18 and 19 March 2009. Values of $\gamma_{(snow,Br)} = 0.3$ (magenta) and $\gamma_{(snow,Br)} = 1.0$ (green) were tested and are compared with the 10-minute averaged measurements (black). NO_x measurements are plotted as an hourly average. Grey shaded areas represent the standard deviation of the average from the instantaneous measurements.

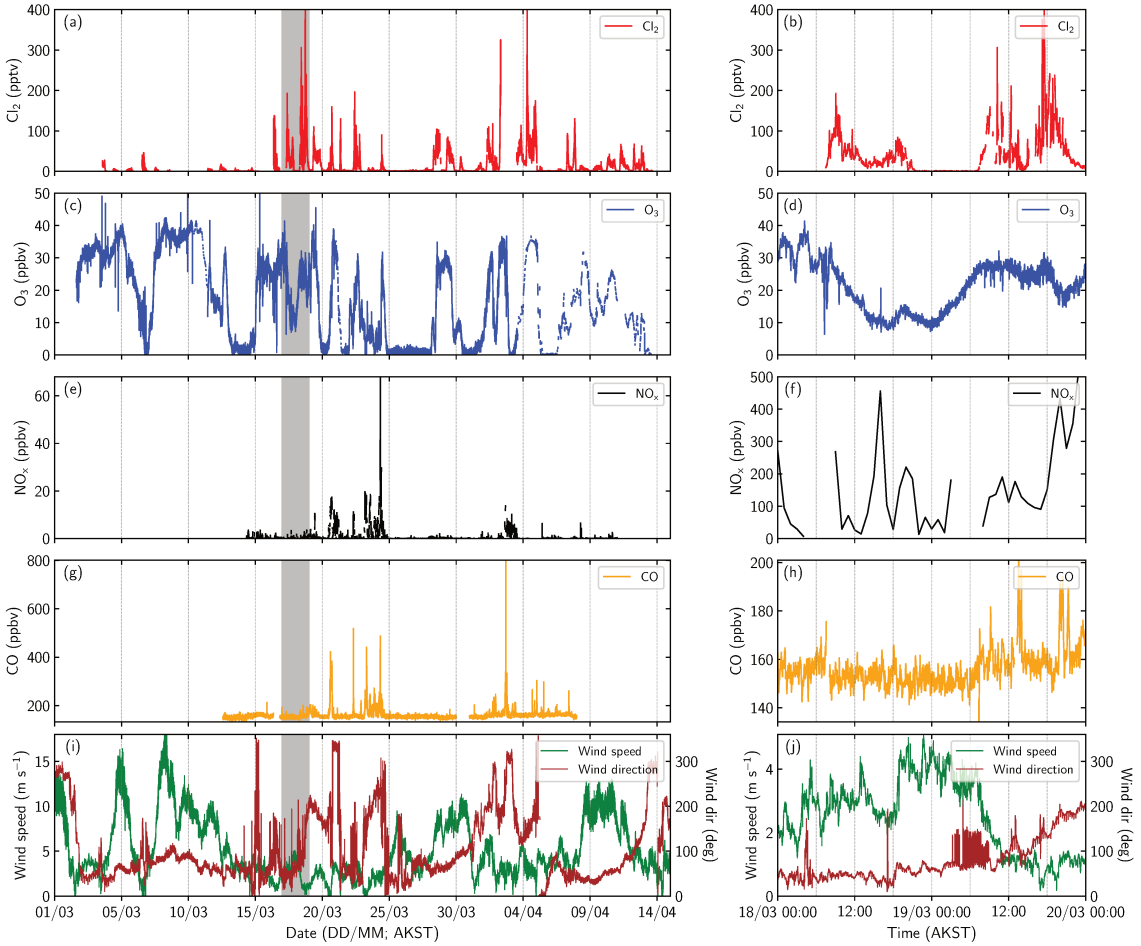

Figure A.4: OASIS observations of selected species (left column) for the entire measurement period and (right column) for the simulation period, 18–19 March 2009. The grey shaded areas on the left plots indicate the modelling time period shown on the right plots. Note the different vertical scales on the left and right plots. Shown are 1-minute averages of the observed data with the exception of (f) which is a one-hour average.

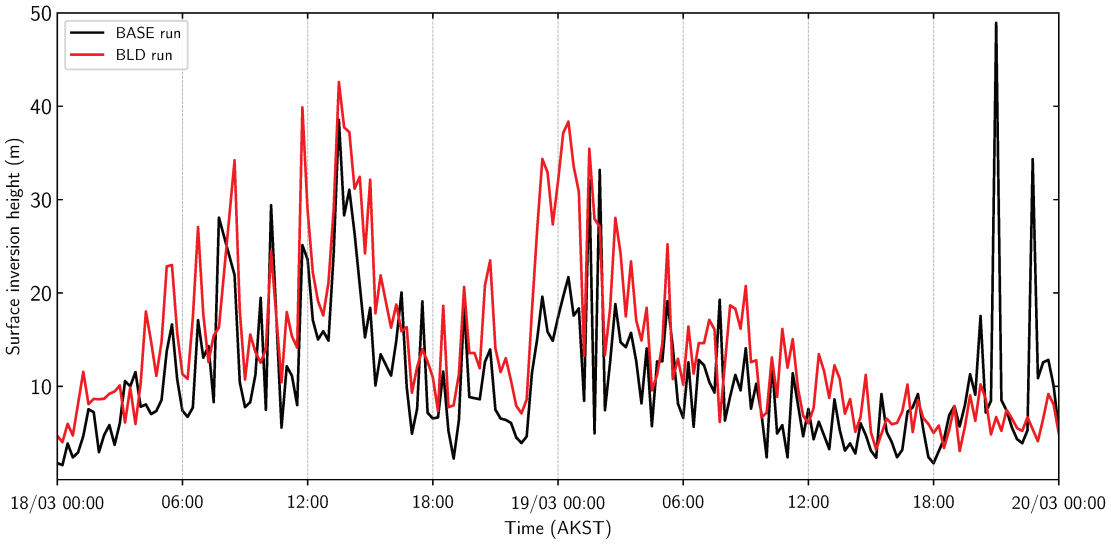

Figure A.5: Surface inversion height estimates calculated from turbulent flux measurements during OASIS Boylan et al. (2014) used in the BASE (black) and BLD (red) runs. The expression used to calculate the surface inversion height in the BASE run is from Zilitinkevich et al. (2002) and Zilitinkevich and Baklanov (2002), and in the BLD run (red), Pollard et al. (1973).

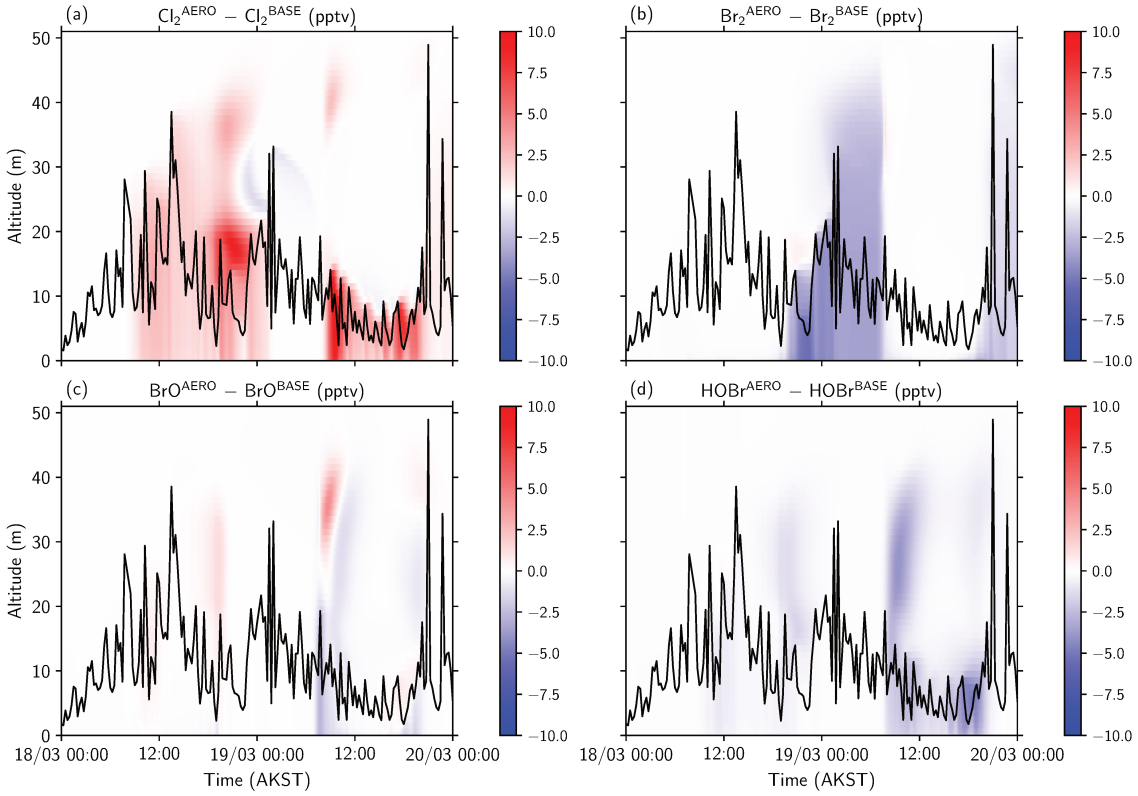

Figure A.6: Differences in the modelled vertical distributions of (a) Cl_2, (b) Br_2, (c) BrO, and (d) HOBr between the AERO and BASE runs during 18 and 19 March 2009. Black trace indicates the model prescribed surface inversion height.

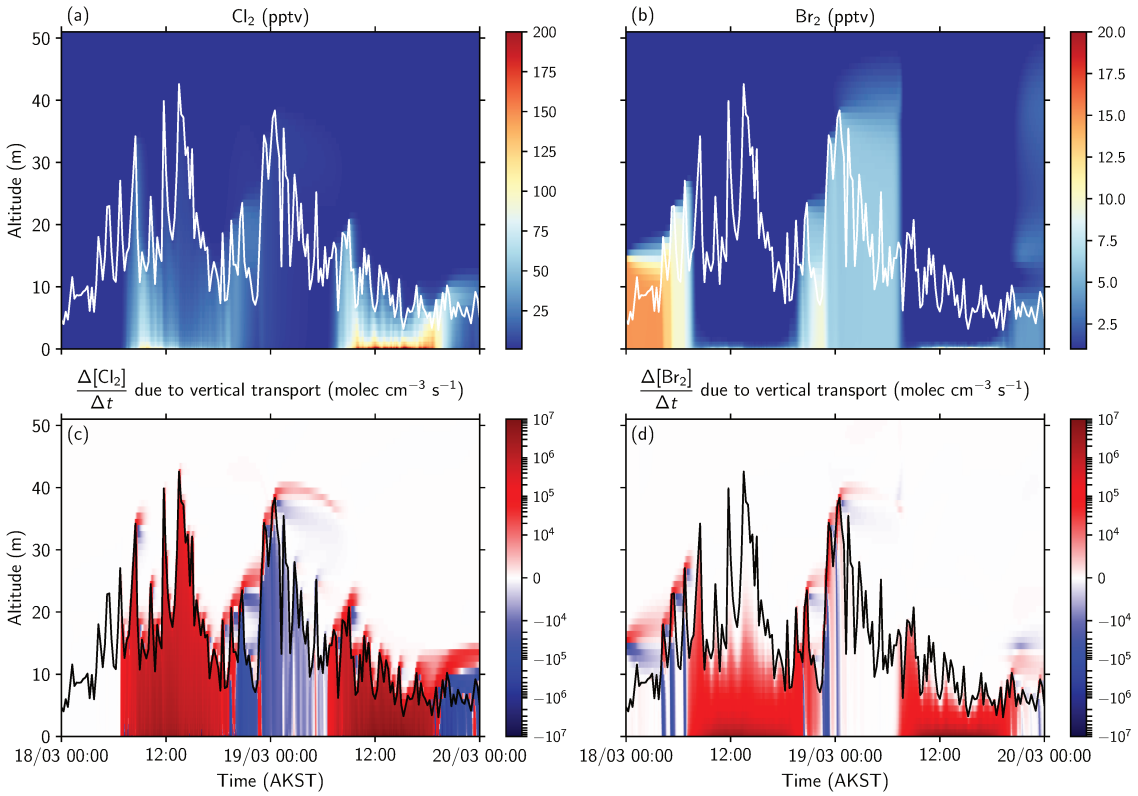

Figure A.7: Modelled vertical distributions of (a) Cl_2 and (b) Br_2 during 18 and 19 March 2009 in the BLD run. White trace indicates the model prescribed surface inversion height. Modelled concentration change of (c) Cl_2 and (d) Br_2 due to vertical transport and deposition with respect to time. Black trace indicates the prescribed surface inversion height. Positive values represent upward transport and negative values indicate downward transport.

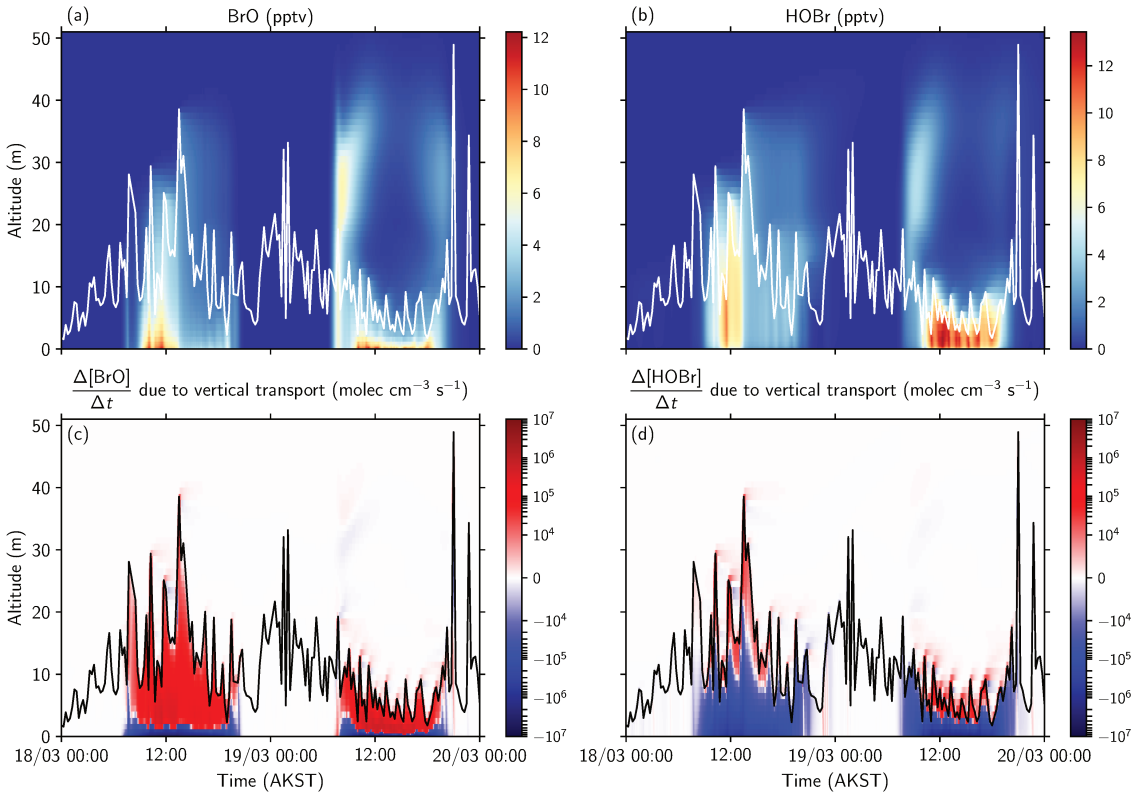

Figure A.8: Modelled vertical distributions of (a) BrO and (b) HOBr during 18 and 19 March 2009 in the BASE run. White trace indicates the model prescribed surface inversion height. Modelled concentration change of (c) BrO and (d) HOBr due to vertical transport and deposition with respect to time. Black trace indicates the prescribed surface inversion height. Positive values represent upward transport and negative values indicate downward transport.

Appendix B

Supplementary material for Chapter 5

This appendix contains supplementary material to Chapter 5, including 1 table with MAX-DOAS retrieval settings and 11 figures displaying additional WRF-Chem model output. Table A.1 contains the MAX-DOAS retrieval settings used to record BrO concentrations during MOSAiC. Figure B.1 shows the WRF-Chem calculated cloud properties. The BrO Differential Slant Column Densities (DSCDs) retrieved during the MOSAiC campaign are plotted in Figure B.2. Figures B.3, B.4, and B.5 show the modelled and observed vertical profiles of relative humidity, wind speed, and wind direction above the MOSAiC shiptrack. Modelled meteorology at Utqiaġvik (Alaska), Summit (Greenland), and Zeppelin Observatory (Svalbard), are compared with observations in Figures B.6, B.7, and B.8, respectively. The simulated planetary boundary layer height above the MOSAiC shiptrack is presented in Figure B.9. Finally, the WRF-Chem simulated vertical distributions of BrO and O_3 above the MOSAiC shiptrack are shown in Figures B.10 and B.11, respectively.

Table B.1: DOAS retrieval settings used in this study.

Parameter	**O_4 (UV)**	**BrO**
Fitting window	338 – 370 nm	338 – 357 nm
O_4 (Thalman and Volkamer, 2013)	✓	✓
BrO (Fleischmann et al., 2004)	✓	✓
NO_2 294 K (Vandaele et al., 1998)	✓	✓
NO 220 K (Vandaele et al., 1998)	✓	✓
O_3 223 K (Serdyuchenko et al., 2014)	✓	✓
O_3 270 K (Serdyuchenko et al., 2014)	✓	✓
HCHO (Meller and Moortgat, 2000)	✓	✓
OClO (Bogumil et al., 2003)		✓
Ring (Chance and Spurr, 1997)	✓	✓
Polynomial order	5	2
Intensity offset	Order 0	Order 0

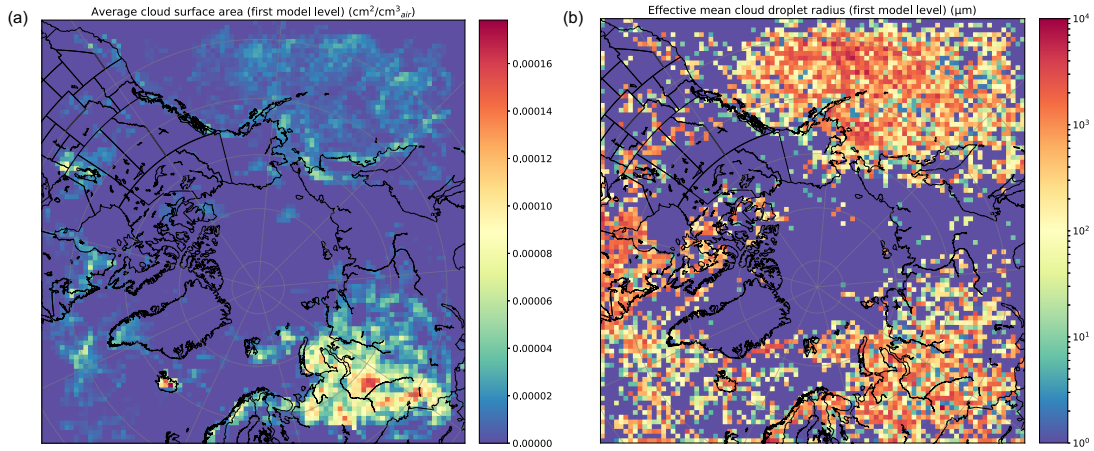

Figure B.1: Model calculated cloud properties. (a) Average cloud surface area for the lowest model level. (b) Effective mean cloud droplet radius for the lowest model level.

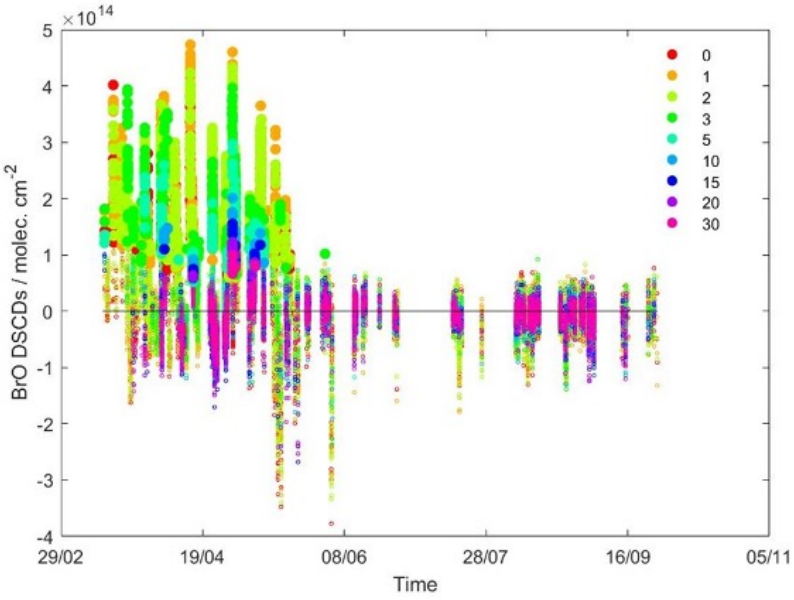

Figure B.2: BrO Differential Slant Column Densities (DSCDs) retrieved during the MOSAiC campaign. Coloured points represent the different elevation angles (in degrees). BrO above the detection limit (filled circles) was only observed during the springtime.

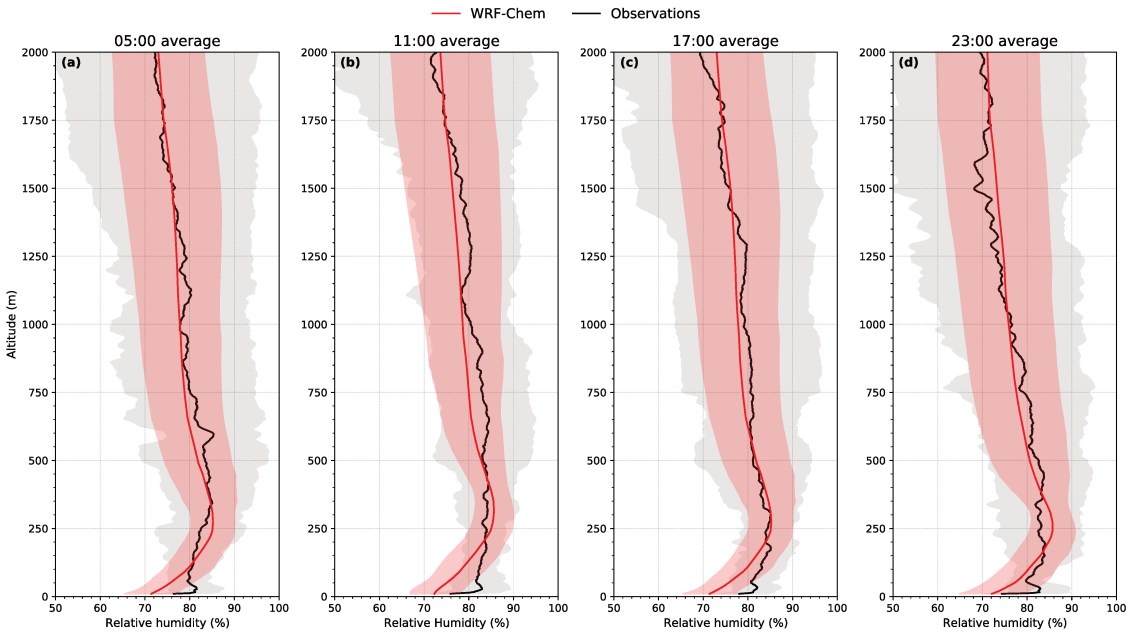

Figure B.3: Modelled and observed vertical profiles of relative humidity for MOSAiC radiosondes. Mean vertical relative humidity profile from radiosonde observations (black) released above the MOSAiC shiptrack and simulated by WRF-Chem (red) during the simulation period (March 14 – April 14, 2020). Model values are extracted at the closest grid cell to the location of each radiosonde flight path. Data are averaged by time interval during the simulated period (to the nearest hour) at (a) 05:00 UTC, (b) 11:00 UTC, (c) 17:00 UTC, and (d) 23:00 UTC. Shaded areas represent the standard deviation of the observed and model averages.

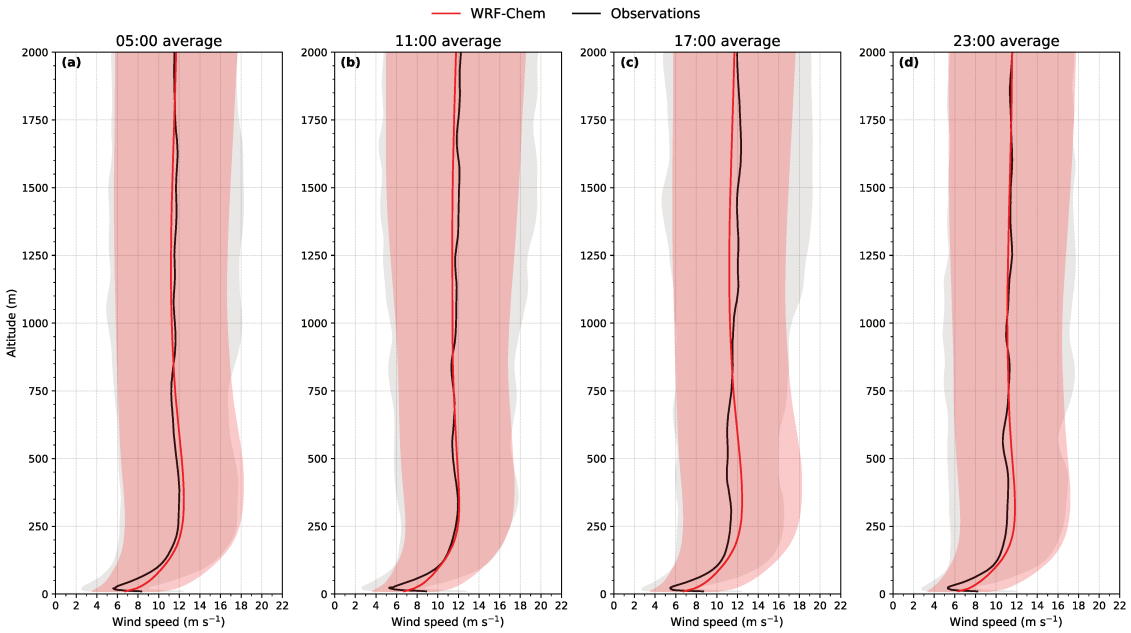

Figure B.4: Modelled and observed vertical profiles of wind speed with MOSAiC radiosondes. Mean vertical wind speed profile from radiosonde observations (black) released above the MOSAiC shiptrack and simulated by WRF-Chem (red) during the simulation period (March 14 – April 14, 2020). Model values are extracted at the closest grid cell to the location of each radiosonde flight path. Data are averaged by time interval during the simulated period (to the nearest hour) at (a) 05:00 UTC, (b) 11:00 UTC, (c) 17:00 UTC, and (d) 23:00 UTC. Shaded areas represent the standard deviation of the observed and model averages.

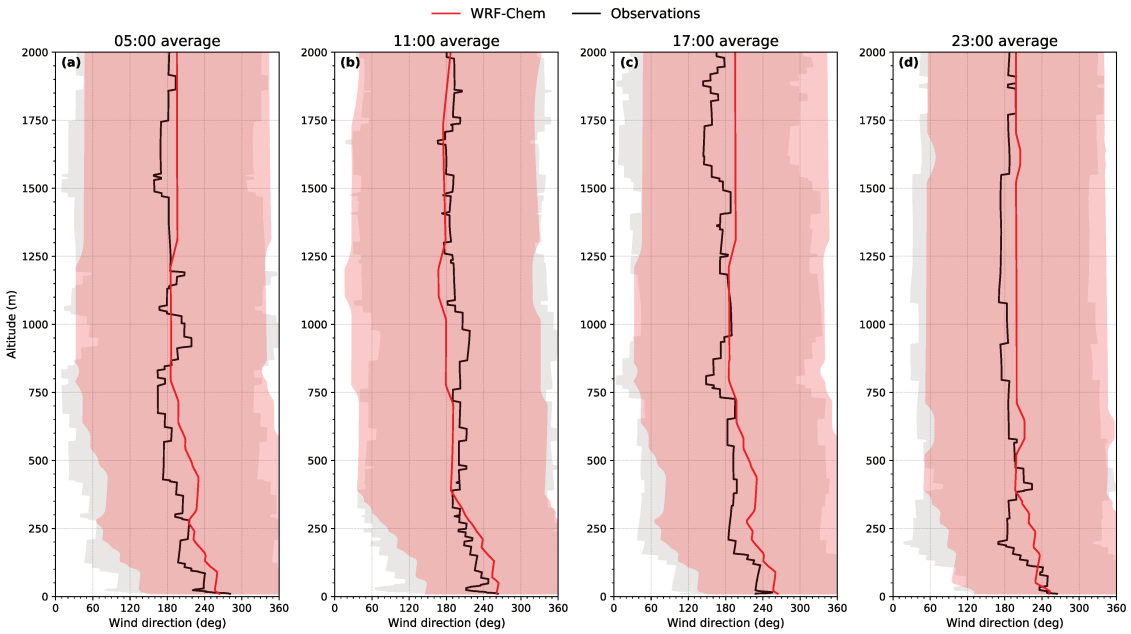

Figure B.5: Modelled and observed vertical profiles of wind direction with MOSAiC radiosondes. Mean vertical wind direction profile from radiosonde observations (black) released above the MOSAiC shiptrack and simulated by WRF-Chem (red) during the simulation period (March 14 – April 14, 2020). Model values are extracted at the closest grid cell to the location of each radiosonde flight path. Data are averaged by time interval during the simulated period (to the nearest hour) at (a) 05:00 UTC, (b) 11:00 UTC, (c) 17:00 UTC, and (d) 23:00 UTC. Shaded areas represent the standard deviation of the observed and model averages.

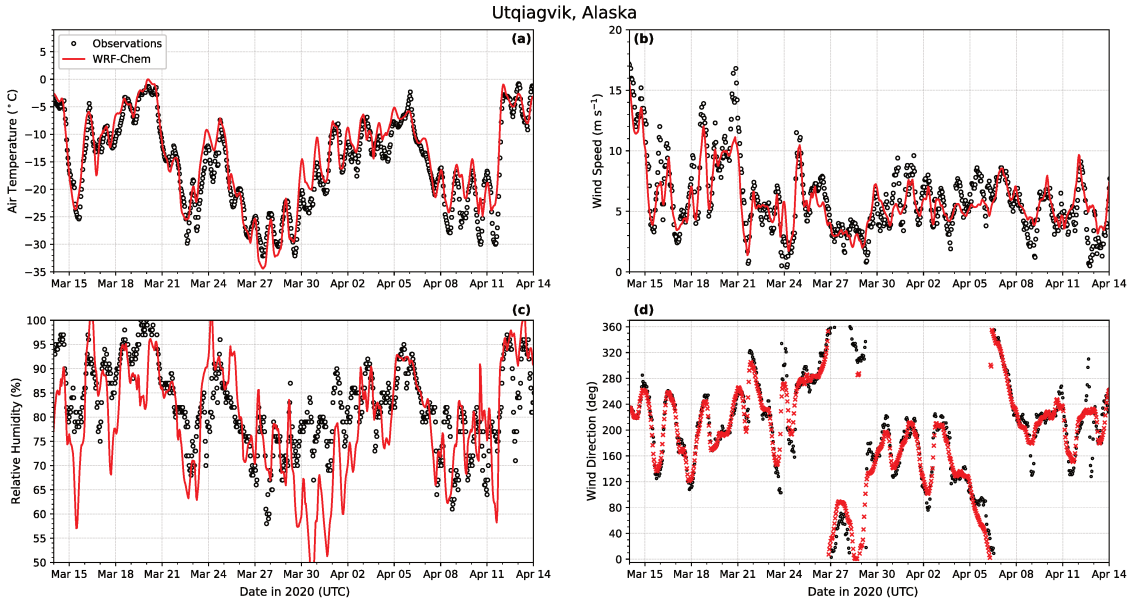

Figure B.6: Model comparison of meteorological variables to observations at Utqiagvik, Alaska. Hourly averages of observed (black) and simulated (red) boundary layer meteorology of (a) air temperature; (b) wind speed; (c) relative humidity; and (d) wind direction (1-minute measurements plotted). Simulated values are extracted at the closest grid cell to the station and interpolated to the height of the station.

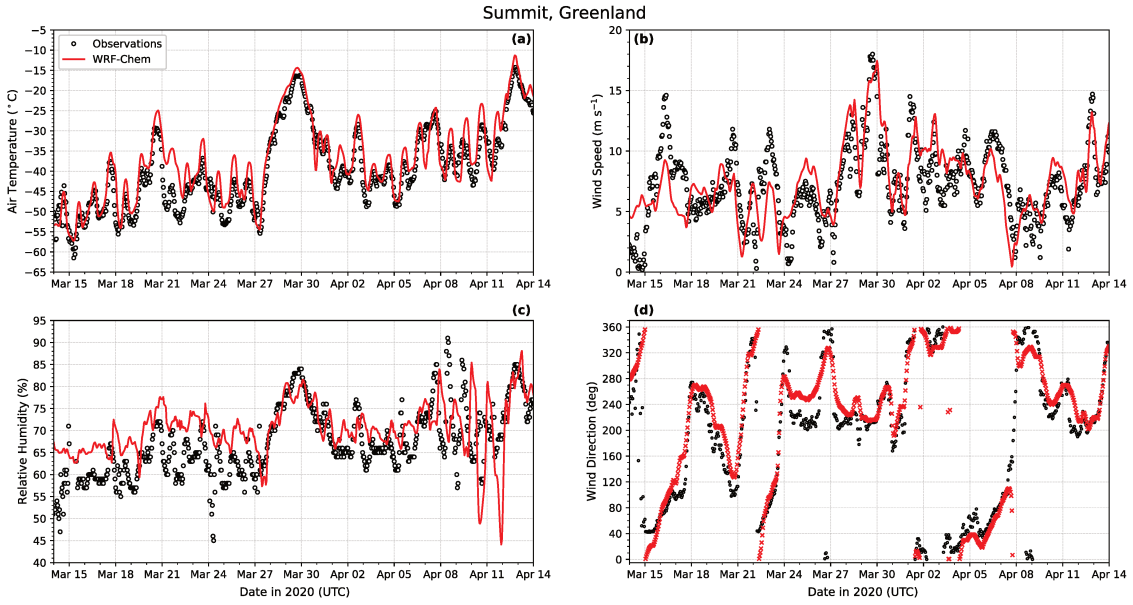

Figure B.7: Same as Figure B.6 plotted for Summit, Greenland.

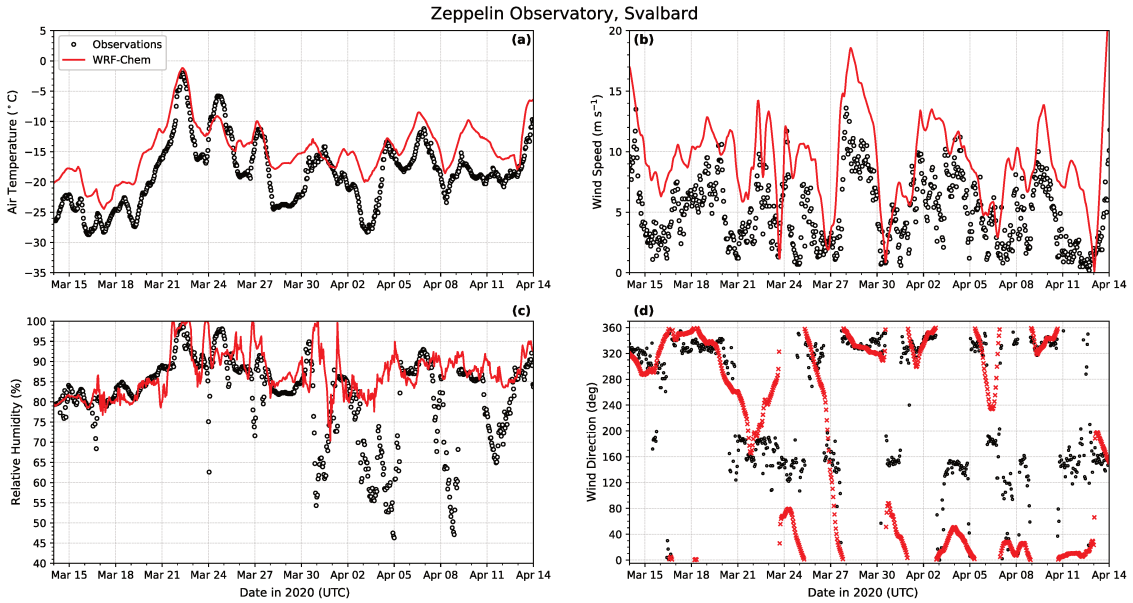

Figure B.8: Same as Figure B.6 plotted for Zeppelin Observatory, Svalbard. Simulated values are extracted at the closest grid cell to the station and interpolated to the height of the station (472 m above sea level).

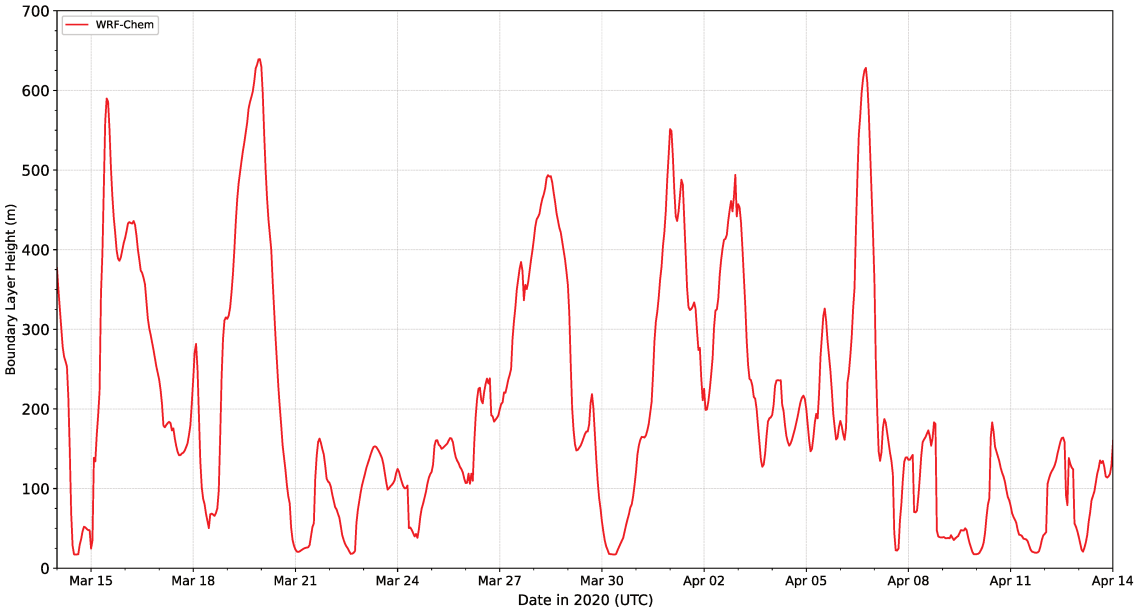

Figure B.9: Simulated boundary layer height above the MOSAiC shiptrack. The boundary layer scheme used in WRF-Chem is the Mellor–Yamada Nakanishi Niino (MYNN) Level 2.5 Scheme which defines the PBL height using a turbulent kinetic energy (TKE) threshold.

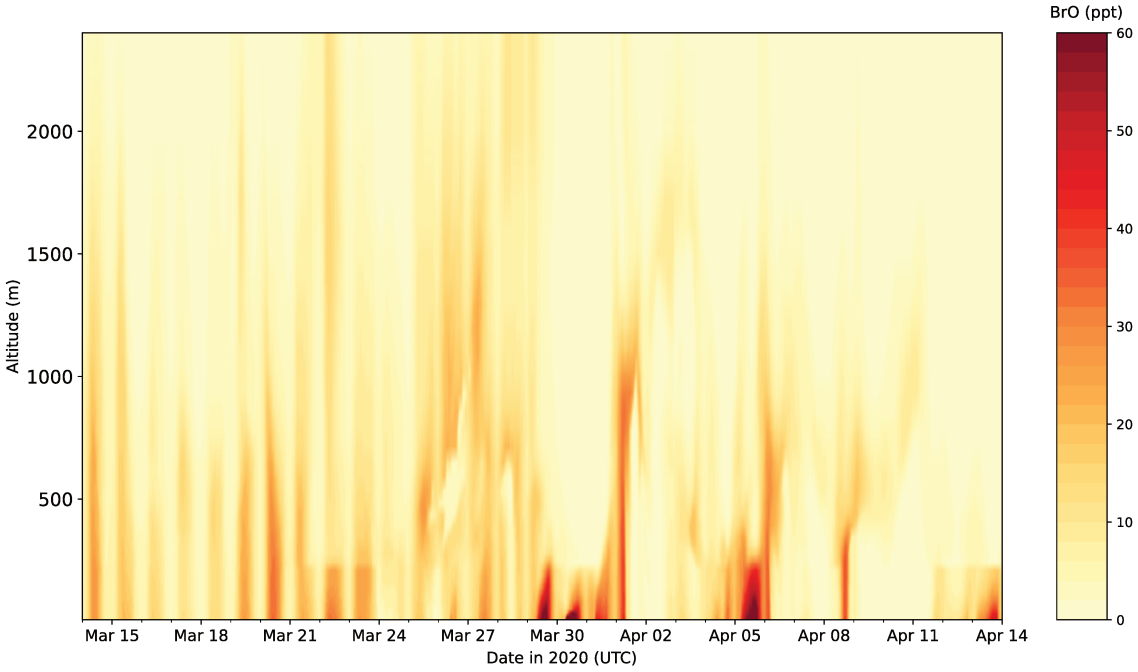

Figure B.10: Simulated vertical BrO concentration above the MOSAiC shiptrack.

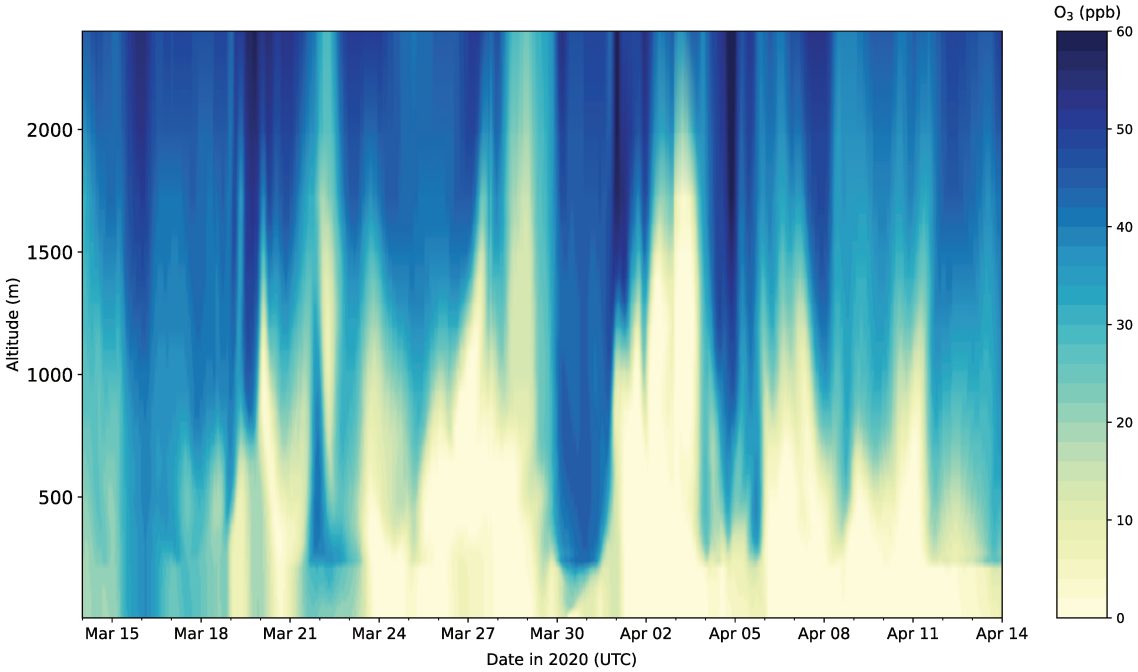

Figure B.11: Simulated vertical ozone concentration above the MOSAiC shiptrack.

Bibliography

Abbatt, J. P. D., Thomas, J. L., Abrahamsson, K., Boxe, C., Granfors, A., Jones, A. E., King, M. D., Saiz-Lopez, A., Shepson, P. B., Sodeau, J., Toohey, D. W., Toubin, C., von Glasow, R., Wren, S. N., and Yang, X. (2012). Halogen activation via interactions with environmental ice and snow in the polar lower troposphere and other regions. *Atmospheric Chemistry and Physics*, 12(14):6237–6271. doi: 10.5194/acp-12-6237-2012.

Aguzzi, A. and J. Rossi, M. (1999). The kinetics of the heterogeneous reaction of $BrONO_2$ with solid alkali halides at ambient temperature. A comparison with the interaction of $ClONO_2$ on NaCl and KBr. *Physical Chemistry Chemical Physics*, 1:4337–4346. doi: 10.1039/A904611I.

Ahmed, S., Thomas, J. L., and Marelle, L. (2022a). Regional-Modeling-LATMOS-IGE/WRF-Chem-Polar: WRF-Chem 4.3.3 including mercury chemistry. doi: 10.5281/zenodo.7137482.

Ahmed, S., Thomas, J. L., Tuite, K., and Stutz, J. (2022b). PACT-1D model (v1.1) including polar chlorine and bromine emission mechanisms. doi: 10.5281/zenodo.6045999.

Ahmed, S., Thomas, J. L., Tuite, K., Stutz, J., Flocke, F., Orlando, J. J., Hornbrook, R. S., Apel, E. C., Emmons, L. K., Helmig, D., Boylan, P., Huey, L. G., Hall, S. R., Ullmann, K., Cantrell, C. A., and Fried, A. (2022c). The Role of Snow in Controlling Halogen Chemistry and Boundary Layer Oxidation During Arctic Spring: A 1D Modeling Case

Study. *Journal of Geophysical Research: Atmospheres*, 127(5):e2021JD036140. doi: 10.1029/2021JD036140.

Aiuppa, A., Franco, A., von Glasow, R., Allen, A. G., D'Alessandro, W., Mather, T. A., Pyle, D. M., and Valenza, M. (2007). The tropospheric processing of acidic gases and hydrogen sulphide in volcanic gas plumes as inferred from field and model investigations. *Atmospheric Chemistry and Physics*, 7(5):1441–1450. doi: 10.5194/acp-7-1441-2007.

AMAP (2011). AMAP Assessment 2011: Mercury in the Arctic. Arctic Monitoring and Assessment Programme (AMAP). Oslo, Norway, 194 pp.

AMAP (2015). AMAP Assessment 2015: Human Health in the Arctic. Arctic Monitoring and Assessment Programme (AMAP), Oslo, Norway. 165 pp.

AMAP (2021). Arctic Monitoring and Assessment Programme (AMAP), Tromsø, Norway. 326 pp.

AMAP/UN Environment (2019). Technical Background Report for the Global Mercury Assessment 2018. Arctic Monitoring and Assessment Programme, Oslo, Norway/UN Environment Programme, Chemicals and Health Branch, Geneva, Switzerland. viii + 426 pp.

Ammann, M., Cox, R. A., Crowley, J. N., Jenkin, M. E., Mellouki, A., Rossi, M. J., Troe, J., and Wallington, T. J. (2013). Evaluated kinetic and photochemical data for atmospheric chemistry: Volume VI – heterogeneous reactions with liquid substrates. *Atmospheric Chemistry and Physics*, 13(16):8045–8228. doi: 10.5194/acp-13-8045-2013.

Amos, H. M., Jacob, D. J., Holmes, C. D., Fisher, J. A., Wang, Q., Yantosca, R. M., Corbitt, E. S., Galarneau, E., Rutter, A. P., Gustin, M. S., Steffen, A., Schauer, J. J., Graydon, J. A., Louis, V. L. S., Talbot, R. W., Edgerton, E. S., Zhang, Y., and Sunderland, E. M. (2012). Gas-particle partitioning of atmospheric Hg(II) and its effect on global mercury deposition. *Atmospheric Chemistry and Physics*, 12(1):591–603. doi: 10.5194/acp-12-591-2012.

Anderson, P. S. and Neff, W. D. (2008). Boundary layer physics over snow and ice. *Atmospheric Chemistry and Physics*, 8(13):3563–3582. doi: 10.5194/acp-8-3563-2008.

Anenberg, S. C., Horowitz, L. W., Tong, D. Q., and West, J. J. (2010). An Estimate of the Global Burden of Anthropogenic Ozone and Fine Particulate Matter on Premature Human Mortality Using Atmospheric Modeling. *Environmental Health Perspectives*, 118(9):1189–1195. doi: 10.1289/ehp.0901220.

Angot, H., Archer, S., Bariteau, L., Blomquist, B., Helmig, D., Howard, D., Hueber, J., Jacobi, H.-W., and Posman, K. (2022a). Gaseous elemental mercury concentrations measured in the University of Colorado container during the 2019-2020 MOSAiC (Multidisciplinary drifting Observatory for the Study of Arctic Climate) expedition. Arctic Data Center. doi: 10.18739/A2C824G3G.

Angot, H., Blomquist, B., Howard, D., Archer, S., Bariteau, L., Beck, I., Boyer, M., Crotwell, M., Helmig, D., Hueber, J., Jacobi, H.-W., Jokinen, T., Kulmala, M., Lan, X., Laurila, T., Madronich, M., Neff, D., Petäjä, T., Posman, K., Quéléver, L., Shupe, M. D., Vimont, I., and Schmale, J. (2022b). Year-round trace gas measurements in the central Arctic during the MOSAiC expedition. *Scientific Data*, 9(1):723. doi: 10.1038/s41597-022-01769-6.

Angot, H., Blomquist, B., Howard, D., Archer, S., Bariteau, L., Beck, I., Boyer, M., Helmig, D., Hueber, J., Jacobi, H.-W., Jokinen, T., Laurila, T., Posman, K., Quéléver, Lauriane, Shupe, M. D., and Schmale, J. (2022c). Ozone dry air mole fractions measured during MOSAiC 2019/2020 (merged dataset). Pangaea. doi: 10.1594/PANGAEA.944393.

Angot, H., Dastoor, A., De Simone, F., Gårdfeldt, K., Gencarelli, C. N., Hedgecock, I. M., Langer, S., Magand, O., Mastromonaco, M. N., Nordstrøm, C., Pfaffhuber, K. A., Pirrone, N., Ryjkov, A., Selin, N. E., Skov, H., Song, S., Sprovieri, F., Steffen, A., Toyota, K., Travnikov, O., Yang, X., and Dommergue, A. (2016). Chemical cycling and deposition of atmospheric mercury in polar regions: review of recent measurements and

comparison with models. *Atmospheric Chemistry and Physics*, 16(16):10735–10763. doi: 10.5194/acp-16-10735-2016.

Apel, E. C. (2009). VOC measurements during OASIS Barrow field intensive Spring 2009. Arctic Data Center. Accessed on 08/24/2021. doi: 10.5065/D6DB7ZXF.

Araujo, B. F., Osterwalder, S., Szponar, N., Lee, D., Petrova, M. V., Pernov, J. B., Ahmed, S., Heimbürger-Boavida, L.-E., Laffont, L., Teisserenc, R., Tananaev, N., Nordstrom, C., Magand, O., Stupple, G., Skov, H., Steffen, A., Bergquist, B., Pfaffhuber, K. A., Thomas, J. L., Scheper, S., Petäjä, T., Dommergue, A., and Sonke, J. E. (2022). Mercury isotope evidence for Arctic summertime re-emission of mercury from the cryosphere. *Nature Communications*, 13(1):4956. doi: 10.1038/s41467-022-32440-8.

Ariya, P. A., Amyot, M., Dastoor, A., Deeds, D., Feinberg, A., Kos, G., Poulain, A., Ryjkov, A., Semeniuk, K., Subir, M., and Toyota, K. (2015). Mercury Physicochemical and Biogeochemical Transformation in the Atmosphere and at Atmospheric Interfaces: A Review and Future Directions. *Chemical Reviews*, 115(10):3760–3802. doi: 10.1021/cr500667e.

Atkinson, R., Baulch, D. L., Cox, R. A., Crowley, J. N., Hampson, R. F., Hynes, R. G., Jenkin, M. E., Rossi, M. J., Troe, J., and IUPAC Subcommittee (2006). Evaluated kinetic and photochemical data for atmospheric chemistry: Volume II – gas phase reactions of organic species. *Atmospheric Chemistry and Physics*, 6(11):3625–4055. doi: 10.5194/acp-6-3625-2006.

Balabanov, N. B., Shepler, B. C., and Peterson, K. A. (2005). Accurate Global Potential Energy Surface and Reaction Dynamics for the Ground State of $HgBr_2$. *The Journal of Physical Chemistry A*, 109(39):8765–8773. doi: 10.1021/jp053415l.

Barret, M., Domine, F., Houdier, S., Gallet, J.-C., Weibring, P., Walega, J., Fried, A., and Richter, D. (2011). Formaldehyde in the Alaskan Arctic snowpack: Partitioning and physical processes involved in air-snow exchanges. *Journal of Geophysical Research: Atmospheres*, 116(D14). doi: 10.1029/2011JD016038.

Barrie, L. A. (1986). Arctic air pollution: An overview of current knowledge. *Atmospheric Environment*, 20(4):643–663. doi: 10.1016/0004-6981(86)90180-0.

Barrie, L. A., Bottenheim, J. W., Schnell, R. C., Crutzen, P. J., and Rasmussen, R. A. (1988). Ozone destruction and photochemical reactions at polar sunrise in the lower Arctic atmosphere. *Nature*, 334(6178):138–141. doi: 10.1038/334138a0.

Barrie, L. A. and Platt, U. (1997). Reactive halogen chemistry in the troposphere. *Chemical Society Reviews*, 41:6448–6472. doi: 10.3402/tellusb.v49i5.15984.

Bartels-Rausch, T., Jacobi, H.-W., Kahan, T. F., Thomas, J. L., Thomson, E. S., Abbatt, J. P. D., Ammann, M., Blackford, J. R., Bluhm, H., Boxe, C., Domine, F., Frey, M. M., Gladich, I., Guzmán, M. I., Heger, D., Huthwelker, T., Klán, P., Kuhs, W. F., Kuo, M. H., Maus, S., Moussa, S. G., McNeill, V. F., Newberg, J. T., Pettersson, J. B. C., Roeselová, M., and Sodeau, J. R. (2014). A review of air–ice chemical and physical interactions (AICI): liquids, quasi-liquids, and solids in snow. *Atmospheric Chemistry and Physics*, 14(3):1587–1633. doi: 10.5194/acp-14-1587-2014.

Benavent, N. (2020). Desarrollo de un instrumento MAX-DOAS para medidas urbanas de calidad del aire y de gases traza en la atmósfera polar. doi: 10.20868/UPM.thesis.65998.

Benavent, N., Mahajan, A. S., Li, Q., Cuevas, C. A., Schmale, J., Angot, H., Jokinen, T., Quéléver, L. L. J., Blechschmidt, A.-M., Zilker, B., Richter, A., Serna, J. A., Garcia-Nieto, D., Fernandez, R. P., Skov, H., Dumitrascu, A., Simões Pereira, P., Abrahamsson, K., Bucci, S., Duetsch, M., Stohl, A., Beck, I., Laurila, T., Blomquist, B., Howard, D., Archer, S. D., Bariteau, L., Helmig, D., Hueber, J., Jacobi, H.-W., Posman, K., Dada, L., Daellenbach, K. R., and Saiz-Lopez, A. (2022). Substantial contribution of iodine to Arctic ozone destruction. *Nature Geoscience*. doi: 10.1038/s41561-022-01018-w.

Berg, L. K., Shrivastava, M., Easter, R. C., Fast, J. D., Chapman, E. G., Liu, Y., and Ferrare, R. A. (2015). A new WRF-Chem treatment for studying regional-scale impacts

of cloud processes on aerosol and trace gases in parameterized cumuli. *Geoscientific Model Development*, 8(2):409–429. doi: 10.5194/gmd-8-409-2015.

Berg, L. K. and Stull, R. B. (2005). A Simple Parameterization Coupling the Convective Daytime Boundary Layer and Fair-Weather Cumuli. *Journal of Atmospheric Sciences*, 62(6):1976–1988. doi: 10.1175/JAS3437.1.

Berg, T., Pfaffhuber, K. A., Cole, A. S., Engelsen, O., and Steffen, A. (2013). Ten-year trends in atmospheric mercury concentrations, meteorological effects and climate variables at Zeppelin, Ny-Ålesund. *Atmospheric Chemistry and Physics*, 13(13):6575–6586. doi: 10.5194/acp-13-6575-2013.

Blechschmidt, A.-M., Richter, A., Burrows, J. P., Kaleschke, L., Strong, K., Theys, N., Weber, M., Zhao, X., and Zien, A. (2016). An exemplary case of a bromine explosion event linked to cyclone development in the Arctic. *Atmospheric Chemistry and Physics*, 16(3):1773–1788. doi: 10.5194/acp-16-1773-2016.

Bogumil, K., Orphal, J., Homann, T., Voigt, S., Spietz, P., Fleischmann, O., Vogel, A., Hartmann, M., Kromminga, H., Bovensmann, H., Frerick, J., and Burrows, J. (2003). Measurements of molecular absorption spectra with the SCIAMACHY pre-flight model: instrument characterization and reference data for atmospheric remote-sensing in the 230–2380 nm region. *Journal of Photochemistry and Photobiology A: Chemistry*, 157(2):167–184. doi: 10.1016/S1010-6030(03)00062-5.

Bottenheim, J. W., Barrie, L. A., Atlas, E., Heidt, L. E., Niki, H., Rasmussen, R. A., and Shepson, P. B. (1990). Depletion of lower tropospheric ozone during Arctic spring: The Polar Sunrise Experiment 1988. *Journal of Geophysical Research: Atmospheres*, 95(D11):18555–18568. doi: 10.1029/JD095iD11p18555.

Bottenheim, J. W. and Chan, E. (2006). A trajectory study into the origin of spring time Arctic boundary layer ozone depletion. *Journal of Geophysical Research: Atmospheres*, 111(D19). doi: 10.1029/2006JD007055.

Bottenheim, J. W., Gallant, A. G., and Brice, K. A. (1986). Measurements of NO_y spe-

cies and O_3 at 82° N latitude. *Geophysical Research Letters*, 13(2):113–116. doi: 10.1029/GL013i002p00113.

Bottenheim, J. W., Netcheva, S., Morin, S., and Nghiem, S. V. (2009). Ozone in the boundary layer air over the Arctic Ocean: measurements during the TARA transpolar drift 2006–2008. *Atmospheric Chemistry and Physics*, 9(14):4545–4557. doi: 10.5194/acp-9-4545-2009.

Bougoudis, I., Blechschmidt, A.-M., Richter, A., Seo, S., Burrows, J. P., Theys, N., and Rinke, A. (2020). Long-term time series of Arctic tropospheric BrO derived from UV–VIS satellite remote sensing and its relation to first-year sea ice. *Atmospheric Chemistry and Physics*, 20(20):11869–11892. doi: 10.5194/acp-20-11869-2020.

Boylan, P., Helmig, D., Staebler, R., Turnipseed, A., Fairall, C., and Neff, W. (2014). Boundary layer dynamics during the Ocean-Atmosphere-Sea-Ice-Snow (OASIS) 2009 experiment at Barrow, AK. *Journal of Geophysical Research: Atmospheres*, 119(5):2261–2278. doi: 10.1002/2013JD020299.

Brasseur, G. P. and Jacob, D. J. (2017). *Modeling of Atmospheric Chemistry*. Cambridge University Press. doi: 10.1017/9781316544754.

Brioude, J., Arnold, D., Stohl, A., Cassiani, M., Morton, D., Seibert, P., Angevine, W., Evan, S., Dingwell, A., Fast, J. D., Easter, R. C., Pisso, I., Burkhart, J., and Wotawa, G. (2013). The Lagrangian particle dispersion model FLEXPART-WRF version 3.1. *Geoscientific Model Development*, 6(6):1889–1904. doi: 10.5194/gmd-6-1889-2013.

Brooks, S. B., Saiz-Lopez, A., Skov, H., Lindberg, S. E., Plane, J. M. C., and Goodsite, M. E. (2006). The mass balance of mercury in the springtime arctic environment. *Geophysical Research Letters*, 33(13). doi: 10.1029/2005GL025525.

Buchholz, R. R., Emmons, L. K., Tilmes, S., and The CESM2 Development Team (2019a). CESM2.1/CAM-chem Instantaneous Output for Boundary Conditions. UCAR/NCAR - Atmospheric Chemistry Observations and Modeling Laboratory. Subset used Lat: 50 to 90, Lon: 120 to 250, 18 March 2009 - 18 March 2009, Accessed: 09/07/2020. doi: 10.5065/NMP7-EP60.

Buchholz, R. R., Emmons, L. K., Tilmes, S., and The CESM2 Development Team (2019b). CESM2.1/CAM-chem Instantaneous Output for Boundary Conditions. UCAR/NCAR - Atmospheric Chemistry Observations and Modeling Laboratory. Subset used Lat: 0 to 90, Lon: 0 to 360, March 2020 - May 2020, Accessed: 1 May 2020. doi: 10.5065/NMP7-EP60.

Burd, J. A., Peterson, P. K., Nghiem, S. V., Perovich, D. K., and Simpson, W. R. (2017). Snowmelt onset hinders bromine monoxide heterogeneous recycling in the Arctic. *Journal of Geophysical Research: Atmospheres*, 122(15):8297–8309. doi: 10.1002/2017JD026906.

Burkholder, J. B., Sander, S. P., Abbatt, J., Barker, J. R., Cappa, C., Crounse, J. D., Dibble, T. S., Huie, R. E., Kolb, C. E., Kurylo, M. J., Orkin, V. L., Percival, C. J., Wilmouth, D. M., and Wine, P. H. (2019). Chemical Kinetics and Photochemical Data for Use in Atmospheric Studies, Evaluation No. 19,. `http://jpldataeval.jpl.nasa.gov/`.

Calvert, J. G., Orlando, J. J., Stockwell, W. R., and Wallington, T. J. (2015). *The Mechanisms of Reactions Influencing Atmospheric Ozone*. Oxford University Press.

Cantrell, C. A. (2009). HO_2 and RO_2 measurements during OASIS Barrow field intensive Spring 2009. Arctic Data Center. Accessed on 08/24/2021. doi: 10.5065/D6GH9G2J.

Cao, L., Platt, U., and Gutheil, E. (2016). Role of the boundary layer in the occurrence and termination of the tropospheric ozone depletion events in polar spring. *Atmospheric Environment*, 132:98–110. doi: 10.1016/j.atmosenv.2016.02.034.

Carpenter, L. J. (2003). Iodine in the Marine Boundary Layer. *Chemical Reviews*, 103(12):4953–4962. doi: 10.1021/cr0206465.

Carter, W. P. L. (2000). Documentation of the SAPRC-99 chemical mechanism for VOC reactivity assessment. *Final Report to California Air Resources Board*, 92(329):95–308.

Chance, K. (1998). Analysis of BrO measurements from the Global Ozone Mon-

itoring Experiment. *Geophysical Research Letters*, 25(17):3335–3338. doi: 10.1029/98GL52359.

Chance, K. V. and Spurr, R. J. D. (1997). Ring effect studies: Rayleigh scattering, including molecular parameters for rotational Raman scattering, and the Fraunhofer spectrum. *Appl. Opt.*, 36(21):5224–5230. doi: 10.1364/AO.36.005224.

Clever, H. L., Johnson, S. A., and Derrick, M. E. (1985). The Solubility of Mercury and Some Sparingly Soluble Mercury Salts in Water and Aqueous Electrolyte Solutions. *Journal of Physical and Chemical Reference Data*, 14(3):631–680. doi: 10.1063/1.555732.

Cobbett, F. D., Steffen, A., Lawson, G., and Van Heyst, B. J. (2007). GEM fluxes and atmospheric mercury concentrations (GEM, RGM and Hgp) in the Canadian Arctic at Alert, Nunavut, Canada (February–June 2005). *Atmospheric Environment*, 41(31):6527–6543. doi: 10.1016/j.atmosenv.2007.04.033.

Corbett, J. J., Lack, D. A., Winebrake, J. J., Harder, S., Silberman, J. A., and Gold, M. (2010). Arctic shipping emissions inventories and future scenarios. *Atmospheric Chemistry and Physics*, 10(19):9689–9704. doi: 10.5194/acp-10-9689-2010.

Crutzen, P. J. (1970). The influence of nitrogen oxides on the atmospheric ozone content. *Quarterly Journal of the Royal Meteorological Society*, 96(408):320–325. doi: 10.1002/qj.49709640815.

Custard, K. D., Pratt, K. A., Wang, S., and Shepson, P. B. (2016). Constraints on Arctic Atmospheric Chlorine Production through Measurements and Simulations of Cl_2 and ClO. *Environmental Science & Technology*, 50(22):12394–12400. doi: 10.1021/acs.est.6b03909.

Custard, K. D., Raso, A. R. W., Shepson, P. B., Staebler, R. M., and Pratt, K. A. (2017). Production and Release of Molecular Bromine and Chlorine from the Arctic Coastal Snowpack. *ACS Earth and Space Chemistry*, 1(3):142–151. doi: 10.1021/acsearthspacechem.7b00014.

Custard, K. D., Thompson, C. R., Pratt, K. A., Shepson, P. B., Liao, J., Huey, L. G., Orlando, J. J., Weinheimer, A. J., Apel, E., Hall, S. R., Flocke, F., Mauldin, L., Hornbrook, R. S., Pöhler, D., General, S., Zielcke, J., Simpson, W. R., Platt, U., Fried, A., Weibring, P., Sive, B. C., Ullmann, K., Cantrell, C., Knapp, D. J., and Montzka, D. D. (2015). The NO_x dependence of bromine chemistry in the Arctic atmospheric boundary layer. *Atmospheric Chemistry and Physics*, 15(18):10799–10809. doi: 10.5194/acp-15-10799-2015.

Dada, L., Angot, H., Beck, I., Baccarini, A., Quéléver, L. L. J., Boyer, M., Laurila, T., Brasseur, Z., Jozef, G., de Boer, G., Shupe, M. D., Henning, S., Bucci, S., Dütsch, M., Stohl, A., Petäjä, T., Daellenbach, K. R., Jokinen, T., and Schmale, J. (2022). A central arctic extreme aerosol event triggered by a warm air-mass intrusion. *Nature Communications*, 13(1):5290. doi: 10.1038/s41467-022-32872-2.

Dastoor, A., Angot, H., Bieser, J., Christensen, J. H., Douglas, T. A., Heimbürger-Boavida, L.-E., Jiskra, M., Mason, R. P., McLagan, D. S., Obrist, D., Outridge, P. M., Petrova, M. V., Ryjkov, A., St. Pierre, K. A., Schartup, A. T., Soerensen, A. L., Toyota, K., Travnikov, O., Wilson, S. J., and Zdanowicz, C. (2022a). Arctic mercury cycling. *Nature Reviews Earth & Environment*, 3(4):270–286. doi: 10.1038/s43017-022-00269-w.

Dastoor, A., Wilson, S. J., Travnikov, O., Ryjkov, A., Angot, H., Christensen, J. H., Steenhuisen, F., and Muntean, M. (2022b). Arctic atmospheric mercury: Sources and changes. *Science of The Total Environment*, 839:156213. doi: 10.1016/j.scitotenv.2022.156213.

Deiber, G., George, C., Le Calvé, S., Schweitzer, F., and Mirabel, P. (2004). Uptake study of $ClONO_2$ and $BrONO_2$ by Halide containing droplets. *Atmospheric Chemistry and Physics*, 4(5):1291–1299. doi: 10.5194/acp-4-1291-2004.

Dibble, T. S., Tetu, H. L., Jiao, Y., Thackray, C. P., and Jacob, D. J. (2020). Modeling the OH-Initiated Oxidation of Mercury in the Global Atmosphere without Viol-

ating Physical Laws. *The Journal of Physical Chemistry A*, 124(2):444–453. doi: 10.1021/acs.jpca.9b10121.

Dibble, T. S., Zelie, M. J., and Mao, H. (2012). Thermodynamics of reactions of ClHg and BrHg radicals with atmospherically abundant free radicals. *Atmospheric Chemistry and Physics*, 12(21):10271–10279. doi: 10.5194/acp-12-10271-2012.

Domine, F., Albert, M., Huthwelker, T., Jacobi, H.-W., Kokhanovsky, A. A., Lehning, M., Picard, G., and Simpson, W. R. (2008). Snow physics as relevant to snow photochemistry. *Atmospheric Chemistry and Physics*, 8(2):171–208. doi: 10.5194/acp-8-171-2008.

Domine, F., Bock, J., Voisin, D., and Donaldson, D. J. (2013). Can We Model Snow Photochemistry? Problems with the Current Approaches. *The Journal of Physical Chemistry A*, 117(23):4733–4749. doi: 10.1021/jp3123314.

Dommergue, A., Bahlmann, E., Ebinghaus, R., Ferrari, C., and Boutron, C. (2007). Laboratory simulation of Hg(0) emissions from a snowpack. *Analytical and Bioanalytical Chemistry*, 388(2):319–327. doi: 10.1007/s00216-007-1186-2.

Dommergue, A., Ferrari, C. P., Poissant, L., Gauchard, P.-A., and Boutron, C. F. (2003). Diurnal Cycles of Gaseous Mercury within the Snowpack at Kuujjuarapik/Whapmagoostui, Québec, Canada. *Environmental Science & Technology*, 37(15):3289–3297. doi: 10.1021/es026242b.

Dommergue, A., Larose, C., Faïn, X., Clarisse, O., Foucher, D., Hintelmann, H., Schneider, D., and Ferrari, C. P. (2010). Deposition of Mercury Species in the Ny-Ålesund Area (79 °N) and Their Transfer during Snowmelt. *Environmental Science & Technology*, 44(3):901–907. doi: 10.1021/es902579m.

Douglas, T. A. and Blum, J. D. (2019). Mercury Isotopes Reveal Atmospheric Gaseous Mercury Deposition Directly to the Arctic Coastal Snowpack. *Environmental Science & Technology Letters*, 6(4):235–242. doi: 10.1021/acs.estlett.9b00131.

Douglas, T. A., Loseto, L. L., Macdonald, R. W., Outridge, P., Dommergue, A., Poulain, A., Amyot, M., Barkay, T., Berg, T., Chételat, J., Constant, P., Evans, M., Ferrari, C., Gantner, N., Johnson, M. S., Kirk, J., Kroer, N., Larose, C., Lean, D., Nielsen, T. G., Poissant, L., Rognerud, S., Skov, H., Sørensen, S., Wang, F., Wilson, S., and Zdanowicz, C. M. (2012). The fate of mercury in Arctic terrestrial and aquatic ecosystems, a review. *Environmental Chemistry*, 9(4):321–355. doi: 10.1071/EN11140.

Driscoll, C. T., Mason, R. P., Chan, H. M., Jacob, D. J., and Pirrone, N. (2013). Mercury as a Global Pollutant: Sources, Pathways, and Effects. *Environmental Science & Technology*, 47(10):4967–4983. doi: 10.1021/es305071v.

Durnford, D. and Dastoor, A. (2011). The behavior of mercury in the cryosphere: A review of what we know from observations. *Journal of Geophysical Research: Atmospheres*, 116(D6). doi: 10.1029/2010JD014809.

Durnford, D., Dastoor, A., Figueras-Nieto, D., and Ryjkov, A. (2010). Long range transport of mercury to the Arctic and across Canada. *Atmospheric Chemistry and Physics*, 10(13):6063–6086. doi: 10.5194/acp-10-6063-2010.

Durnford, D., Dastoor, A., Ryzhkov, A., Poissant, L., Pilote, M., and Figueras-Nieto, D. (2012). How relevant is the deposition of mercury onto snowpacks? – Part 2: A modeling study. *Atmospheric Chemistry and Physics*, 12(19):9251–9274. doi: 10.5194/acp-12-9251-2012.

Durre, I., Vose, R. S., and Wuertz, D. B. (2006). Overview of the Integrated Global Radiosonde Archive. *Journal of Climate*, 19(1):53–68. doi: 10.1175/JCLI3594.1.

Easter, R. C., Ghan, S. J., Zhang, Y., Saylor, R. D., Chapman, E. G., Laulainen, N. S., Abdul-Razzak, H., Leung, L. R., Bian, X., and Zaveri, R. A. (2004). MIRAGE: Model description and evaluation of aerosols and trace gases. *Journal of Geophysical Research: Atmospheres*, 109(D20). doi: 10.1029/2004JD004571.

Ebinghaus, R., Kock, H. H., Temme, C., Einax, J. W., Löwe, A. G., Richter, A., Burrows, J. P., and Schroeder, W. H. (1998). Antarctic Springtime Depletion of At-

mospheric Mercury. *Environmental Science & Technology*, 36(6):1238–1244. doi: 10.1021/es015710z.

Emmons, L. K., Arnold, S. R., Monks, S. A., Huijnen, V., Tilmes, S., Law, K. S., Thomas, J. L., Raut, J.-C., Bouarar, I., Turquety, S., Long, Y., Duncan, B., Steenrod, S., Strode, S., Flemming, J., Mao, J., Langner, J., Thompson, A. M., Tarasick, D., Apel, E. C., Blake, D. R., Cohen, R. C., Dibb, J., Diskin, G. S., Fried, A., Hall, S. R., Huey, L. G., Weinheimer, A. J., Wisthaler, A., Mikoviny, T., Nowak, J., Peischl, J., Roberts, J. M., Ryerson, T., Warneke, C., and Helmig, D. (2015). The POLARCAT Model Intercomparison Project (POLMIP): overview and evaluation with observations. *Atmospheric Chemistry and Physics*, 15(12):6721–6744. doi: 10.5194/acp-15-6721-2015.

Emmons, L. K., Schwantes, R. H., Orlando, J. J., Tyndall, G., Kinnison, D., Lamarque, J.-F., Marsh, D., Mills, M. J., Tilmes, S., Bardeen, C., Buchholz, R. R., Conley, A., Gettelman, A., Garcia, R., Simpson, I., Blake, D. R., Meinardi, S., and Pétron, G. (2020). The Chemistry Mechanism in the Community Earth System Model Version 2 (CESM2). *Journal of Advances in Modeling Earth Systems*, 12(4):e2019MS001882. doi: 10.1029/2019MS001882.

E.U. Copernicus Marine Service Information (2022). Arctic Ocean Physics Reanalysis. doi: 10.48670/moi-00007.

Falk, S. and Sinnhuber, B.-M. (2018). Polar boundary layer bromine explosion and ozone depletion events in the chemistry–climate model EMAC v2.52: implementation and evaluation of AirSnow algorithm. *Geoscientific Model Development*, 11(3):1115–1131. doi: 10.5194/gmd-11-1115-2018.

Fast, J. D., Gustafson Jr., W. I., Easter, R. C., Zaveri, R. A., Barnard, J. C., Chapman, E. G., Grell, G. A., and Peckham, S. E. (2000). Evolution of ozone, particulates, and aerosol direct radiative forcing in the vicinity of Houston using a fully coupled meteorology-chemistry-aerosol model. *Journal of Geophysical Research: Atmospheres*, 111(D21):245–282. doi: 10.1029/2005JD006721.

Fayt, C., De Smedt, I., Letocart, V., Merlaud, A., Pinardi, G., and Van Roozendael, M. (2011). QDOAS 1.00 Software user manual. *Belgian Institute for Space Aeronomy*.

Fernandez, R. P., Carmona-Balea, A., Cuevas, C. A., Barrera, J. A., Kinnison, D. E., Lamarque, J.-F., Blaszczak-Boxe, C., Kim, K., Choi, W., Hay, T., Blechschmidt, A.-M., Schönhardt, A., Burrows, J. P., and Saiz-Lopez, A. (2019). Modeling the Sources and Chemistry of Polar Tropospheric Halogens (Cl, Br, and I) Using the CAM-Chem Global Chemistry-Climate Model. *Journal of Advances in Modeling Earth Systems*, 11(7):2259–2289. doi: 10.1029/2019MS001655.

Ferrari, C. P., Gauchard, P.-A., Aspmo, K., Dommergue, A., Magand, O., Bahlmann, E., Nagorski, S., Temme, C., Ebinghaus, R., Steffen, A., Banic, C., Berg, T., Planchon, F., Barbante, C., Cescon, P., and Boutron, C. F. (2005). Snow-to-air exchanges of mercury in an Arctic seasonal snow pack in Ny-Ålesund, Svalbard. *Atmospheric Environment*, 39(39):7633–7645. doi: 10.1016/j.atmosenv.2005.06.058.

Ferrari, C. P., Padova, C., Faïn, X., Gauchard, P.-A., Dommergue, A., Aspmo, K., Berg, T., Cairns, W., Barbante, C., Cescon, P., Kaleschke, L., Richter, A., Wittrock, F., and Boutron, C. (2008). Atmospheric mercury depletion event study in Ny-Ålesund (Svalbard) in spring 2005. Deposition and transformation of Hg in surface snow during springtime. *Science of The Total Environment*, 397(1):167–177. doi: 10.1016/j.scitotenv.2008.01.064.

Fetterer, F., Knowles, K., Meier, W. N., Savoie, M., and Windnagel, A. K. (2017). Sea Ice Index, Version 3. National Snow and Ice Data Center. doi: 10.7265/N5K072F8.

Finlayson-Pitts, B. and Pitts, J. (1999). *Chemistry of the Upper and Lower Atmosphere: Theory, Experiments, and Applications*. Elsevier Science.

Finlayson-Pitts, B. J., Ezell, M. J., and Pitts, J. N. (1989). Formation of chemically active chlorine compounds by reactions of atmospheric NaCl particles with gaseous N_2O_5 and $ClONO_2$. *Nature*, 337(6204):241–244. doi: 10.1038/337241a0.

Fisher, J. A., Jacob, D. J., Soerensen, A. L., Amos, H. M., Corbitt, E. S., Streets, D. G., Wang, Q., Yantosca, R. M., and Sunderland, E. M. (2013). Factors driving mercury

variability in the Arctic atmosphere and ocean over the past 30 years. *Global Biogeochemical Cycles*, 27(4):1226–1235. doi: 10.1002/2013GB004689.

Fisher, J. A., Jacob, D. J., Soerensen, A. L., Amos, H. M., Steffen, A., and Sunderland, E. M. (2012). Riverine source of Arctic Ocean mercury inferred from atmospheric observations. *Nature Geoscience*, 5(7):499–504. doi: 10.1038/ngeo1478.

Fleischmann, O. C., Hartmann, M., Burrows, J. P., and Orphal, J. (2004). New ultraviolet absorption cross-sections of BrO at atmospheric temperatures measured by time-windowing Fourier transform spectroscopy. *Journal of Photochemistry and Photobiology A: Chemistry*, 168(1):117–132. doi: 10.1016/j.jphotochem.2004.03.026.

Fleming, Z. L., Monks, P. S., and Manning, A. J. (2012). Review: Untangling the influence of air-mass history in interpreting observed atmospheric composition. *Atmospheric Research*, 104–105:1–39. doi: 10.1016/j.atmosres.2011.09.009.

Foster, K. L., Plastridge, R. A., Bottenheim, J. W., Shepson, P. B., Finlayson-Pitts, B. J., and Spicer, C. W. (2001). The Role of Br_2 and BrCl in Surface Ozone Destruction at Polar Sunrise. *Science*, 291(5503). doi: 10.1126/science.291.5503.471.

Francés-Monerris, A., Carmona-García, J., Acuña, A. U., Dávalos, J. Z., Cuevas, C. A., Kinnison, D. E., Francisco, J. S., Saiz-Lopez, A., and Roca-Sanjuán, D. (2020). Photodissociation Mechanisms of Major Mercury(II) Species in the Atmospheric Chemical Cycle of Mercury. *Angewandte Chemie International Edition*, 59(19):7605–7610. doi: 10.1002/anie.201915656.

Frey, M. M., Roscoe, H. K., Kukui, A., Savarino, J., France, J. L., King, M. D., Legrand, M., and Preunkert, S. (2015). Atmospheric nitrogen oxides (NO and NO_2) at Dome C, East Antarctica, during the OPALE campaign. *Atmospheric Chemistry and Physics*, 15(14):7859–7875. doi: 10.5194/acp-15-7859-2015.

Fried, A. (2009). Formaldehyde measurements during OASIS Barrow field intensive Spring 2009. Arctic Data Center. Accessed on 08/24/2021. doi: 10.5065/D63B5X7H.

Fuchs, N. and Sutugin, A. (1971). *High-dispersed aerosols*. Pergamon, Boston, MA. doi: 10.1016/B978-0-08-016674-2.50006-6.

Gencarelli, C. N., De Simone, F., Hedgecock, I. M., Sprovieri, F., and Pirrone, N. (2014). Development and application of a regional-scale atmospheric mercury model based on WRF/Chem: a Mediterranean area investigation. *Environmental Science and Pollution Research*, 21(6):4095–4109. doi: 10.1007/s11356-013-2162-3.

Goliff, W. S., Stockwell, W. R., and Lawson, C. V. (2013). The regional atmospheric chemistry mechanism, version 2. *Atmospheric Environment*, 68:174–185. doi: 10.1016/j.atmosenv.2012.11.038.

Gómez Martín, J. C., Lewis, T. R., Douglas, K. M., Blitz, M. A., Saiz-Lopez, A., and Plane, J. M. C. (2022). The reaction between HgBr and O_3: kinetic study and atmospheric implications. *Physical Chemistry Chemical Physics*, 24:12419–12432. doi: 10.1039/D2CP00754A.

Goodsite, M. E., Plane, J. M. C., and Skov, H. (2004). A Theoretical Study of the Oxidation of Hg0 to $HgBr_2$ in the Troposphere. *Environmental Science & Technology*, 38(6):1772–1776. doi: 10.1021/es034680s.

Goodsite, M. E., Plane, J. M. C., and Skov, H. (2012). Correction to A Theoretical Study of the Oxidation of Hg0 to $HgBr_2$ in the Troposphere. *Environmental Science & Technology*, 46(9):5262–5262. doi: 10.1021/es301201c.

Graham, R. M., Cohen, L., Ritzhaupt, N., Segger, B., Graversen, R. G., Rinke, A., Walden, V. P., Granskog, M. A., and Hudson, S. R. (2019). Evaluation of Six Atmospheric Reanalyses over Arctic Sea Ice from Winter to Early Summer. *Journal of Climate*, 32(14):4121–4143. doi: 10.1175/JCLI-D-18-0643.1.

Grannas, A. M., Jones, A. E., Dibb, J., Ammann, M., Anastasio, C., Beine, H. J., Bergin, M., Bottenheim, J., Boxe, C. S., Carver, G., Chen, G., Crawford, J. H., Dominé, F., Frey, M. M., Guzmán, M. I., Heard, D. E., Helmig, D., Hoffmann, M. R., Honrath, R. E., Huey, L. G., Hutterli, M., Jacobi, H. W., Klán, P., Lefer, B., McConnell, J., Plane,

J., Sander, R., Savarino, J., Shepson, P. B., Simpson, W. R., Sodeau, J. R., von Glasow, R., Weller, R., Wolff, E. W., and Zhu, T. (2007). An overview of snow photochemistry: evidence, mechanisms and impacts. *Atmospheric Chemistry and Physics*, 7(16):4329–4373. doi: 10.5194/acp-7-4329-2007.

Grell, G. A., Peckham, S. E., Schmitz, R., McKeen, S. A., Frost, G., Skamarock, W. C., and Eder, B. (2005). Fully coupled "online" chemistry within the WRF model. *Atmospheric Environment*, 39(37):6957–6975. doi: 10.1016/j.atmosenv.2005.04.027.

Guenther, A. B. (2009). Meteorology measurements during OASIS Barrow field intensive Spring 2009. Arctic Data Center. Accessed on 08/24/2021. doi: 10.5065/D62J6902.

Guenther, A. B., Jiang, X., Heald, C. L., Sakulyanontvittaya, T., Duhl, T., Emmons, L. K., and Wang, X. (2012). The Model of Emissions of Gases and Aerosols from Nature version 2.1 (MEGAN2.1): an extended and updated framework for modeling biogenic emissions. *Geoscientific Model Development*, 5(6):1471–1492. doi: 10.5194/gmd-5-1471-2012.

Gustin, M. S., Amos, H. M., Huang, J., Miller, M. B., and Heidecorn, K. (2015). Measuring and modeling mercury in the atmosphere: a critical review. *Atmospheric Chemistry and Physics*, 15(10):5697–5713. doi: 10.5194/acp-15-5697-2015.

Gustin, M. S., Dunham-Cheatham, S. M., Huang, J., Lindberg, S., and Lyman, S. N. (2021). Development of an Understanding of Reactive Mercury in Ambient Air: A Review. *Atmosphere*, 12(1). doi: 10.3390/atmos12010073.

Gustin, M. S., Huang, J., Miller, M. B., Peterson, C., Jaffe, D. A., Ambrose, J., Finley, B. D., Lyman, S. N., Call, K., Talbot, R., Feddersen, D., Mao, H., and Lindberg, S. E. (2013). Do We Understand What the Mercury Speciation Instruments Are Actually Measuring? Results of RAMIX. *Environmental Science & Technology*, 47(13):7295–7306. doi: 10.1021/es3039104.

Halfacre, J. W., Knepp, T. N., Shepson, P. B., Thompson, C. R., Pratt, K. A., Li, B., Peterson, P. K., Walsh, S. J., Simpson, W. R., Matrai, P. A., Bottenheim, J. W.,

Netcheva, S., Perovich, D. K., and Richter, A. (2014). Temporal and spatial characteristics of ozone depletion events from measurements in the Arctic. *Atmospheric Chemistry and Physics*, 14(10):4875–4894. doi: 10.5194/acp-14-4875-2014.

Hall, S. R. (2009). Actinic Flux measurements during OASIS Barrow field intensive Spring 2009. Arctic Data Center. Accessed on 08/24/2021. doi: 10.5065/D6GB2260.

Hausmann, M. and Platt, U. (1994). Spectroscopic measurement of bromine oxide and ozone in the high Arctic during Polar Sunrise Experiment 1992. *Journal of Geophysical Research: Atmospheres*, 99(D12):25399–25413. doi: 10.1029/94JD01314.

Helmig, D., Boylan, P., Johnson, B., Oltmans, S., Fairall, C., Staebler, R., Weinheimer, A., Orlando, J., Knapp, D. J., Montzka, D. D., Flocke, F., Frieß, U., Sihler, H., and Shepson, P. B. (2012). Ozone dynamics and snow-atmosphere exchanges during ozone depletion events at Barrow, Alaska. *Journal of Geophysical Research: Atmospheres*, 117:D20303. doi: 10.1029/2012JD017531.

Herrmann, M., Cao, L., Sihler, H., Platt, U., and Gutheil, E. (2019). On the contribution of chemical oscillations to ozone depletion events in the polar spring. *Atmospheric Chemistry and Physics*, 19(15):10161–10190. doi: 10.5194/acp-19-10161-2019.

Herrmann, M., Schöne, M., Borger, C., Warnach, S., Wagner, T., Platt, U., and Gutheil, E. (2022). Ozone depletion events in the Arctic spring of 2019: a new modeling approach to bromine emissions. *Atmospheric Chemistry and Physics*, 22(20):13495–13526.

Herrmann, M., Sihler, H., Frieß, U., Wagner, T., Platt, U., and Gutheil, E. (2021). Time-dependent 3D simulations of tropospheric ozone depletion events in the Arctic spring using the Weather Research and Forecasting model coupled with Chemistry (WRF-Chem). *Atmospheric Chemistry and Physics*, 21(10):7611–7638. doi: 10.5194/acp-21-7611-2021.

Hintelmann, H., Graydon, J. A., Kirk, J. L., Barker, J., Dimock, B., Sharp, M. J., and Lehnherr, I. (2007). Methylated Mercury Species in Canadian High Arctic Marine Surface Waters and Snowpacks. *Environmental Science & Technology*, 41(18):6433–6441. doi: 10.1021/es070692s.

Hirdman, D., Aspmo, K., Burkhart, J. F., Eckhardt, S., Sodemann, H., and Stohl, A. (2009). Transport of mercury in the Arctic atmosphere: Evidence for a spring-time net sink and summer-time source. *Geophysical Research Letters*, 36(12). doi: 10.1029/2009GL038345.

Holmes, C. D., Jacob, D. J., Corbitt, E. S., Mao, J., Yang, X., Talbot, R., and Slemr, F. (2010). Global atmospheric model for mercury including oxidation by bromine atoms. *Atmospheric Chemistry and Physics*, 10(24):12037–12057. doi: 10.5194/acp-10-12037-2010.

Hönninger, G. and Platt, U. (2002). Observations of BrO and its vertical distribution during surface ozone depletion at Alert. *Atmospheric Environment*, 36(15):2481–2489. doi: 10.1016/S1352-2310(02)00104-8.

Honrath, R. E., Lu, Y., Peterson, M. C., Dibb, J. E., Arsenault, M. A., Cullen, N. J., and Steffen, K. (2002). Vertical fluxes of NO_x, HONO, and HNO_3 above the snowpack at Summit, Greenland. *Atmospheric Environment*, 36(15):2629–2640. doi: 10.1016/S1352-2310(02)00132-2.

Honrath, R. E., Peterson, M. C., Guo, S., Dibb, J. E., Shepson, P. B., and Campbell, B. (1999). Evidence of NO_x production within or upon ice particles in the Greenland snowpack. *Geophysical Research Letters*, 26(6):695–698. doi: 10.1029/1999GL900077.

Hornbrook, R. S., Crawford, J. H., Edwards, G. D., Goyea, O., Mauldin III, R. L., Olson, J. S., and Cantrell, C. A. (2011). Measurements of tropospheric HO_2 and RO_2 by oxygen dilution modulation and chemical ionization mass spectrometry. *Atmospheric Measurement Techniques*, 4(4):735–756. doi: 10.5194/amt-4-735-2011.

Hornbrook, R. S., Hills, A. J., Riemer, D. D., Abdelhamid, A., Flocke, F. M., Hall, S. R., Huey, L. G., Knapp, D. J., Liao, J., Mauldin III, R. L., Montzka, D. D., Orlando, J. J., Shepson, P. B., Sive, B., Staebler, R. M., Tanner, D. J., Thompson, C. R., Turnipseed, A., Ullmann, K., Weinheimer, A. J., and Apel, E. C. (2016). Arctic springtime observa-

tions of volatile organic compounds during the OASIS-2009 campaign. *Journal of Geophysical Research: Atmospheres*, 121(16):9789–9813. doi: 10.1002/2015JD024360.

Horowitz, H. M., Jacob, D. J., Zhang, Y., Dibble, T. S., Slemr, F., Amos, H. M., Schmidt, J. A., Corbitt, E. S., Marais, E. A., and Sunderland, E. M. (2017). A new mechanism for atmospheric mercury redox chemistry: implications for the global mercury budget. *Atmospheric Chemistry and Physics*, 17(10):6353–6371. doi: 10.5194/acp-17-6353-2017.

Hu, J. H., Shi, Q., Davidovits, P., Worsnop, D. R., Zahniser, M. S., and Kolb, C. E. (1995). Reactive Uptake of $Cl_{2(g)}$ and $Br_{2(g)}$ by Aqueous Surfaces as a Function of Br^- and I^- Ion Concentration: The Effect of Chemical Reaction at the Interface. *The Journal of Physical Chemistry*, 99(21):8768–8776. doi: 10.1021/j100021a050.

Huang, J. and Jaeglé, L. (2017). Wintertime enhancements of sea salt aerosol in polar regions consistent with a sea ice source from blowing snow. *Atmospheric Chemistry and Physics*, 17(5):3699–3712. doi: 10.5194/acp-17-3699-2017.

Huang, J., Jaeglé, L., Chen, Q., Alexander, B., Sherwen, T., Evans, M. J., Theys, N., and Choi, S. (2020). Evaluating the impact of blowing-snow sea salt aerosol on springtime BrO and O_3 in the Arctic. *Atmospheric Chemistry and Physics*, 20(12):7335–7358. doi: 10.5194/acp-20-7335-2020.

Huang, J., Jaeglé, L., and Shah, V. (2018). Using CALIOP to constrain blowing snow emissions of sea salt aerosols over Arctic and Antarctic sea ice. *Atmospheric Chemistry and Physics*, 18(22):16253–16269. doi: 10.5194/acp-18-16253-2018.

Huang, J., Miller, M. B., Weiss-Penzias, P., and Gustin, M. S. (2013). Comparison of Gaseous Oxidized Hg Measured by KCl-Coated Denuders, and Nylon and Cation Exchange Membranes. *Environmental Science & Technology*, 47(13):7307–7316. doi: 10.1021/es4012349.

Hynes, A. J., Donohoue, D. L., Goodsite, M. E., and Hedgecock, I. M. (2009). *Our current understanding of major chemical and physical processes affecting mercury dy-*

namics in the atmosphere and at the air-water/terrestrial interfaces, pages 427–457. Springer US, Boston, MA. doi: 10.1007/978-0-387-93958-2_14.

Iacono, M. J., Delamere, J. S., Mlawer, E. J., Shephard, M. W., Clough, S. A., and Collins, W. D. (2008). Radiative forcing by long-lived greenhouse gases: Calculations with the AER radiative transfer models. *Journal of Geophysical Research: Atmospheres*, 113(D1303). doi: 10.1029/2008JD009944.

IUPAC (2009). IUPAC Task Group on Atmospheric Chemical Kinetic Data Evaluation. `https://iupac-aeris.ipsl.fr/`.

Jacob, D. J. (1999). *Introduction to atmospheric chemistry*. Princeton University Press.

Jacob, D. J. (2000). Heterogeneous chemistry and tropospheric ozone. *Atmospheric Environment*, 34(12):2131–2159. doi: 10.1016/S1352-2310(99)00462-8.

Jacobi, H.-W., Morin, S., and Bottenheim, J. W. (2010). Observation of widespread depletion of ozone in the springtime boundary layer of the central Arctic linked to mesoscale synoptic conditions. *Journal of Geophysical Research: Atmospheres*, 115(D17). doi: 10.1029/2010JD013940.

Jaffe, D. A., Lyman, S., Amos, H. M., Gustin, M. S., Huang, J., Selin, N. E., Levin, L., ter Schure, A., Mason, R. P., Talbot, R., Rutter, A., Finley, B., Jaeglé, L., Shah, V., McClure, C., Ambrose, J., Gratz, L., Lindberg, S., Weiss-Penzias, P., Sheu, G.-R., Feddersen, D., Horvat, M., Dastoor, A., Hynes, A. J., Mao, H., Sonke, J. E., Slemr, F., Fisher, J. A., Ebinghaus, R., Zhang, Y., and Edwards, G. (2014). Progress on Understanding Atmospheric Mercury Hampered by Uncertain Measurements. *Environmental Science & Technology*, 48(13):7204–7206. doi: 10.1021/es5026432.

Kahl, J. D. (1990). Characteristics of the low-level temperature inversion along the Alaskan Arctic coast. *International Journal of Climatology*, 10(5):537–548. doi: 10.1002/joc.3370100509.

Kain, J. S. (2004). The Kain–Fritsch Convective Parameterization: An Up-

date. *Journal of Applied Meteorology*, 43(1):170–181. doi: 10.1175/1520-0450(2004)043<0170:TKCPAU>2.0.CO;2.

Kain, J. S. and Fritsch, J. M. (2004). A One-Dimensional Entraining/Detraining Plume Model and Its Application in Convective Parameterization. *Journal of Atmospheric Sciences*, 47(23):2784–2802. doi: 10.1175/1520-0469(1990)047<2784:AODEPM>2.0.CO;2.

Kalnay, E., Kanamitsu, M., Kistler, R., Collins, W., Deaven, D., Gandin, L., Iredell, M., Saha, S., White, G., Woollen, J., Zhu, Y., Chelliah, M., Ebisuzaki, W., Higgins, W., Janowiak, J., Mo, K. C., Ropelewski, C., Wang, J., Leetmaa, A., Reynolds, R., Jenne, R., and Joseph, D. (1996). The NCEP/NCAR 40-Year Reanalysis Project. *Bulletin of the American Meteorological Society*, 77(3):437–472. doi: 10.1175/1520-0477(1996)077¡0437:TNYRP¿2.0.CO;2.

Kamp, J., Skov, H., Jensen, B., and Sørensen, L. L. (2018). Fluxes of gaseous elemental mercury (GEM) in the High Arctic during atmospheric mercury depletion events (AMDEs). *Atmospheric Chemistry and Physics*, 18(9):6923–6938. doi: 10.5194/acp-18-6923-2018.

Khiri, D., Louis, F., Černušák, I., and Dibble, T. S. (2020). BrHgO*+ CO: Analogue of OH + CO and Reduction Path for Hg(II) in the Atmosphere. *ACS Earth and Space Chemistry*, 4(10):1777–1784. doi: 10.1021/acsearthspacechem.0c00171.

Kirk, J. L., St. Louis, V. L., and Sharp, M. J. (2006). Rapid Reduction and Reemission of Mercury Deposited into Snowpacks during Atmospheric Mercury Depletion Events at Churchill, Manitoba, Canada. *Environmental Science & Technology*, 40(24):7590–7596. doi: 10.1021/es061299+.

Klimont, Z., Kupiainen, K., Heyes, C., Purohit, P., Cofala, J., Rafaj, P., Borken-Kleefeld, J., and Schöpp, W. (2017). Global anthropogenic emissions of particulate matter including black carbon. *Atmospheric Chemistry and Physics*, 17(14):8681–8723. doi: 10.5194/acp-17-8681-2017.

Knepp, T. N., Bottenheim, J., Carlsen, M., Carlson, D., Donohoue, D., Friederich, G., Matrai, P. A., Netcheva, S., Perovich, D. K., Santini, R., Shepson, P. B., Simpson, W., Valentic, T., Williams, C., and Wyss, P. J. (2010). Development of an autonomous sea ice tethered buoy for the study of ocean-atmosphere-sea ice-snow pack interactions: the O-buoy. *Atmospheric Measurement Techniques*, 3(1):249–261. doi: 10.5194/amt-3-249-2010.

Knipping, E. M., Lakin, M. J., Foster, K. L., Jungwirth, P., Tobias, D. J., Gerber, R. B., Dabdub, D., and Finlayson-Pitts, B. J. (2000). Experiments and Simulations of Ion-Enhanced Interfacial Chemistry on Aqueous NaCl Aerosols. *Science*, 288(5464):301–306. doi: 10.1126/science.288.5464.301.

Knust, R. (2017). Polar Research and Supply Vessel POLARSTERN Operated by the Alfred-Wegener-Institute. *Journal of large-scale research facilities*, 3:A119. doi: 10.17815/jlsrf-3-163.

Koo, J.-H., Wang, Y., Kurosu, T. P., Chance, K., Rozanov, A., Richter, A., Oltmans, S. J., Thompson, A. M., Hair, J. W., Fenn, M. A., Weinheimer, A. J., Ryerson, T. B., Solberg, S., Huey, L. G., Liao, J., Dibb, J. E., Neuman, J. A., Nowak, J. B., Pierce, R. B., Natarajan, M., and Al-Saadi, J. (2012). Characteristics of tropospheric ozone depletion events in the Arctic spring: analysis of the ARCTAS, ARCPAC, and ARCIONS measurements and satellite BrO observations. *Atmospheric Chemistry and Physics*, 12(20):9909–9922. doi: 10.5194/acp-12-9909-2012.

Krnavek, L., Simpson, W. R., Carlson, D., Domine, F., Douglas, T. A., and Sturm, M. (2012). The chemical composition of surface snow in the Arctic: Examining marine, terrestrial, and atmospheric influences. *Atmospheric Environment*, 50:349–359. doi: 10.1016/j.atmosenv.2011.11.033.

Lalonde, J. D., Amyot, M., Doyon, M.-R., and Auclair, J.-C. (2003). Photo-induced Hg(II) reduction in snow from the remote and temperate Experimental Lakes Area (Ontario, Canada). *Journal of Geophysical Research: Atmospheres*, 108(D6). doi: 10.1029/2001JD001534.

Lalonde, J. D., Poulain, A. J., and Amyot, M. (2002). The Role of Mercury Redox Reactions in Snow on Snow-to-Air Mercury Transfer. *Environmental Science & Technology*, 36(2):174–178. doi: 10.1021/es010786g.

Lana, A., Bell, T. G., Simó, R., Vallina, S. M., Ballabrera-Poy, J., Kettle, A. J., Dachs, J., Bopp, L., Saltzman, E. S., Stefels, J., Johnson, J. E., and Liss, P. S. (2011). An updated climatology of surface dimethlysulfide concentrations and emission fluxes in the global ocean. *Global Biogeochemical Cycles*, 5(1). doi: 10.1029/2010GB003850.

Laskin, A., Wang, H., Robertson, W. H., Cowin, J. P., Ezell, M. J., and Finlayson-Pitts, B. J. (2006). A New Approach to Determining Gas-Particle Reaction Probabilities and Application to the Heterogeneous Reaction of Deliquesced Sodium Chloride Particles with Gas-Phase Hydroxyl Radicals. *The Journal of Physical Chemistry A*, 110(36):10619–10627. doi: 10.1021/jp063263+.

Lee, J.-Y., Marotzke, J., Bala, G., Cao, L., Corti, S., Dunne, J., Engelbrecht, F., Fischer, E., Fyfe, J., Jones, C., Maycock, A., Mutemi, J., Ndiaye, O., Panickal, S., and Zhou, T. (2021). *Future Global Climate: Scenario-Based Projections and Near-Term Information*, page 553–672. Cambridge University Press, Cambridge, United Kingdom and New York, NY, USA. doi: 10.1017/9781009157896.006.

Lehnherr, I. and St. Louis, V. L. (2009). Importance of Ultraviolet Radiation in the Photodemethylation of Methylmercury in Freshwater Ecosystems. *Environmental Science & Technology*, 43(15):5692–5698. doi: 10.1021/es9002923.

Lehrer, E., Hönninger, G., and Platt, U. (2004). A one dimensional model study of the mechanism of halogen liberation and vertical transport in the polar troposphere. *Atmospheric Chemistry and Physics*, 4:2427–2440. doi: 10.5194/acp-4-2427-2004.

Lelieveld, J., Gromov, S., Pozzer, A., and Taraborrelli, D. (2016). Global tropospheric hydroxyl distribution, budget and reactivity. *Atmospheric Chemistry and Physics*, 16(19):12477–12493. doi: 10.5194/acp-16-12477-2016.

Liang, Q., Rodriguez, J. M., Douglass, A. R., Crawford, J. H., Olson, J. R., Apel, E., Bian, H., Blake, D. R., Brune, W., Chin, M., Colarco, P. R., da Silva, A., Diskin, G. S.,

Duncan, B. N., Huey, L. G., Knapp, D. J., Montzka, D. D., Nielsen, J. E., Pawson, S., Riemer, D. D., Weinheimer, A. J., and Wisthaler, A. (2011). Reactive nitrogen, ozone and ozone production in the Arctic troposphere and the impact of stratosphere-troposphere exchange. *Atmospheric Chemistry and Physics*, 11(24):13181–13199. doi: 10.5194/acp-11-13181-2011.

Liao, J., Huey, L. G., Liu, Z., Tanner, D. J., Cantrell, C. A., Orlando, J. J., Flocke, F. M., Shepson, P. B., Weinheimer, A. J., Hall, S. R., Ullmann, K., Beine, H. J., Wang, Y., Ingall, E. D., Stephens, C. R., Hornbrook, R. S., Apel, E. C., Riemer, D., Fried, A., Mauldin, R. L., Smith, J. N., Staebler, R. M., Neuman, J. A., and Nowak, J. B. (2014). High levels of molecular chlorine in the Arctic atmosphere. *Nature Geoscience*, 7(2):91–94. doi: 10.1038/ngeo2046.

Liao, J., Huey, L. G., Scheuer, E., Dibb, J. E., Stickel, R. E., Tanner, D. J., Neuman, J. A., Nowak, J. B., Choi, S., Wang, Y., Salawitch, R. J., Canty, T., Chance, K., Kurosu, T., Suleiman, R., Weinheimer, A. J., Shetter, R. E., Fried, A., Brune, W., Anderson, B., Zhang, X., Chen, G., Crawford, J., Hecobian, A., and Ingall, E. D. (2012a). Characterization of soluble bromide measurements and a case study of BrO observations during ARCTAS. *Atmospheric Chemistry and Physics*, 12(3):1327–1338. doi: 10.5194/acp-12-1327-2012.

Liao, J., Huey, L. G., Tanner, D. J., Flocke, F. M., Orlando, J. J., Neuman, J. A., Nowak, J. B., Weinheimer, A. J., Hall, S. R., Smith, J. N., Fried, A., Staebler, R. M., Wang, Y., Koo, J.-H., Cantrell, C. A., Weibring, P., Walega, J., Knapp, D. J., Shepson, P. B., and Stephens, C. R. (2012b). Observations of inorganic bromine (HOBr, BrO, and Br_2) speciation at Barrow, Alaska, in spring 2009. *Journal of Geophysical Research: Atmospheres*, 117:D00R16. doi: 10.1029/2011JD016641.

Liao, J., Sihler, H., Huey, L. G., Neuman, J. A., Tanner, D. J., Friess, U., Platt, U., Flocke, F. M., Orlando, J. J., Shepson, P. B., Beine, H. J., Weinheimer, A. J., Sjostedt, S. J., Nowak, J. B., Knapp, D. J., Staebler, R. M., Zheng, W., Sander, R., Hall, S. R., and Ullmann, K. (2011). A comparison of Arctic BrO measurements by chemical ionization

mass spectrometry and long path-differential optical absorption spectroscopy. *Journal of Geophysical Research: Atmospheres*, 116:D00R02. doi: 10.1029/2010JD014788.

Lindberg, S. E., Brooks, S., Lin, C.-J., Scott, K., Meyers, T., Chambers, L., Landis, M., and Stevens, R. (2001). Formation of Reactive Gaseous Mercury in the Arctic: Evidence of Oxidation of Hg°to Gas-Phase Hg-II Compounds after Arctic Sunrise. *Water, Air and Soil Pollution: Focus*, 1(5):295–302. doi: 10.1023/A:1013171509022.

Lindberg, S. E., Brooks, S., Lin, C. J., Scott, K. J., Landis, M. S., Stevens, R. K., Goodsite, M., and Richter, A. (2002). Dynamic Oxidation of Gaseous Mercury in the Arctic Troposphere at Polar Sunrise. *Environmental Science & Technology*, 36(6):1245–1256. doi: 10.1021/es0111941.

Lindberg, S. E. and Stratton, W. J. (1998). Atmospheric Mercury Speciation: Concentrations and Behavior of Reactive Gaseous Mercury in Ambient Air. *Environmental Science & Technology*, 32(1):49–57. doi: 10.1021/es970546u.

Lindqvist, O. and Rodhe, H. (1985). Atmospheric mercury—a review. *Tellus B*, 37B(3):136–159. doi: 10.1111/j.1600-0889.1985.tb00062.x.

Liu, X., Qu, H., Huey, L. G., Wang, Y., Sjostedt, S., Zeng, L., Lu, K., Wu, Y., Hu, M., Shao, M., Zhu, T., and Zhang, Y. (2017). High Levels of Daytime Molecular Chlorine and Nitryl Chloride at a Rural Site on the North China Plain. *Environmental Science & Technology*, 51(17):9588–9595. doi: 10.1021/acs.est.7b03039.

Lohberger, F., Hönninger, G., and Platt, U. (2004). Ground-based imaging differential optical absorption spectroscopy of atmospheric gases. *Applied Optics*, 43(24):4711–4717. doi: 10.1364/AO.43.004711.

Lu, J. Y., Schroeder, W. H., Barrie, L. A., Steffen, A., Welch, H. E., Martin, K., Lockhart, L., Hunt, R. V., Boila, G., and Richter, A. (2001). Magnification of atmospheric mercury deposition to polar regions in springtime: The link to tropospheric ozone depletion chemistry. *Geophysical Research Letters*, 28(17):3219–3222. doi: 10.1029/2000GL012603.

MacSween, K., Stupple, G., Aas, W., Kyllönen, K., Pfaffhuber, K. A., Skov, H., Steffen, A., Berg, T., and Mastromonaco, M. N. (2022). Updated trends for atmospheric mercury in the Arctic: 1995–2018. *Science of The Total Environment*, 837:155802. doi: 10.1016/j.scitotenv.2022.155802.

Madronich, S. and Flocke, S. (1999). *The Role of Solar Radiation in Atmospheric Chemistry*, pages 1–26. Springer Berlin Heidelberg, Berlin, Heidelberg. doi: 10.1007/978-3-540-69044-3_1.

Mahajan, A. S. (2022). Substantial contribution of iodine to Arctic ozone destruction - data. Mendeley Data, V1. doi: 10.17632/bn7ytz4mfz.1.

Manca, G., Ammoscato, I., Esposito, G., Ianniello, A., Nardino, M., and Sprovieri, F. (2013). Dynamics of snow-air mercury exchange at Ny Ålesund during springtime 2011. *E3S Web of Conferences*, 1:03010. doi: 10.1051/e3sconf/20130103010.

Mann, E., Mallory, M., Ziegler, S., Tordon, R., and O'Driscoll, N. (2015a). Mercury in Arctic snow: Quantifying the kinetics of photochemical oxidation and reduction. *Science of The Total Environment*, 509–510:115–132. doi: 10.1016/j.scitotenv.2014.07.056.

Mann, E., Mallory, M. L., Ziegler, S. E., Avery, T. S., Tordon, R., and O'Driscoll, N. (2015b). Photoreducible Mercury Loss from Arctic Snow Is Influenced by Temperature and Snow Age. *Environmental Science & Technology*, 49(20):12120–12126. doi: 10.1021/acs.est.5b01589.

Mann, E., Ziegler, S., Mallory, M., and O'Driscoll, N. (2014). Mercury photochemistry in snow and implications for Arctic ecosystems. *Environmental Reviews*, 22(4):331–345. doi: 10.1139/er-2014-0006.

Mann, E., Ziegler, S., Steffen, A., and O'Driscoll, N. (2018). Increasing chloride concentration causes retention of mercury in melted Arctic snow due to changes in photoreduction kinetics. *Journal of Environmental Sciences*, 68:122–129. doi: 10.1016/j.jes.2018.01.006.

Marelle, L., Raut, J.-C., Law, K. S., Berg, L. K., Fast, J. D., Easter, R. C., Shrivastava, M., and Thomas, J. L. (2017). Improvements to the WRF-Chem 3.5.1 model for quasi-hemispheric simulations of aerosols and ozone in the Arctic. *Geoscientific Model Development*, 10(10):3661–3677. doi: 10.5194/gmd-10-3661-2017.

Marelle, L., Thomas, J. L., Ahmed, S., Tuite, K., Stutz, J., Dommergue, A., Simpson, W. R., Frey, M. M., and Baladima, F. (2021). Implementation and impacts of surface and blowing snow sources of Arctic bromine activation within WRF-Chem 4.1.1. *Journal of Advances in Modeling Earth Systems*, 13:e2020MS002391. doi: 10.1029/2020MS002391.

Marelle, L., Thomas, J. L., Raut, J.-C., Law, K. S., Jalkanen, J.-P., Johansson, L., Roiger, A., Schlager, H., Kim, J., Reiter, A., and Weinzierl, B. (2016). Air quality and radiative impacts of Arctic shipping emissions in the summertime in northern Norway: from the local to the regional scale. *Atmospheric Chemistry and Physics*, 16(4):2359–2379. doi: 10.5194/acp-16-2359-2016.

Maturilli, M., Holdridge, D. J., Dahlke, S., Graeser, J., Sommerfeld, A., Jaiser, R., Deckelmann, H., and Schulz, A. (2021). Initial radiosonde data from 2019-10 to 2020-09 during project MOSAiC. PANGAEA. doi: 10.1594/PANGAEA.928656.

Mauldin III, R. L., Frost, G. J., Chen, G., Tanner, D. J., Prevot, A. S. H., Davis, D. D., and Eisele, F. L. (1998). OH measurements during the First Aerosol Characterization Experiment (ACE 1): Observations and model comparisons. *Journal of Geophysical Research: Atmospheres*, 103(D13):16713–16729. doi: 10.1029/98JD00882.

McNamara, S. M., Chen, Q., Edebeli, J., Kulju, K. D., Mumpfield, J., Fuentes, J. D., Bertman, S. B., and Pratt, K. A. (2021). Observation of N_2O_5 Deposition and $ClNO_2$ Production on the Saline Snowpack. *ACS Earth and Space Chemistry*, 5(5):1020–1031. doi: 10.1021/acsearthspacechem.0c00317.

McNamara, S. M., Garner, N. M., Wang, S., Raso, A. R. W., Thanekar, S., Barget, A. J., Fuentes, J. D., Shepson, P. B., and Pratt, K. A. (2020). Bromine Chloride in the Coastal

Arctic: Diel Patterns and Production Mechanisms. *ACS Earth and Space Chemistry*, 4(4):620–630. doi: 10.1021/acsearthspacechem.0c00021.

McNamara, S. M., Raso, A. R. W., Wang, S., Thanekar, S., Boone, E. J., Kolesar, K. R., Peterson, P. K., Simpson, W. R., Fuentes, J. D., Shepson, P. B., and Pratt, K. A. (2019). Springtime Nitrogen Oxide-Influenced Chlorine Chemistry in the Coastal Arctic. *Environmental Science & Technology*, 53(14):8057–8067. doi: 10.1021/acs.est.9b01797.

McNeill, V. F., Grannas, A. M., Abbatt, J. P. D., Ammann, M., Ariya, P., Bartels-Rausch, T., Domine, F., Donaldson, D. J., Guzman, M. I., Heger, D., Kahan, T. F., Klán, P., Masclin, S., Toubin, C., and Voisin, D. (2012). Organics in environmental ices: sources, chemistry, and impacts. *Atmospheric Chemistry and Physics*, 12(20):9653–9678. doi: 10.5194/acp-12-9653-2012.

Meller, R. and Moortgat, G. K. (2000). Temperature dependence of the absorption cross sections of formaldehyde between 223 and 323 K in the wavelength range 225–375 nm. *Journal of Geophysical Research: Atmospheres*, 105(D6):7089–7101. doi: 10.1029/1999JD901074.

Monks, S. A., Arnold, S. R., Emmons, L. K., Law, K. S., Turquety, S., Duncan, B. N., Flemming, J., Huijnen, V., Tilmes, S., Langner, J., Mao, J., Long, Y., Thomas, J. L., Steenrod, S. D., Raut, J. C., Wilson, C., Chipperfield, M. P., Diskin, G. S., Weinheimer, A., Schlager, H., and Ancellet, G. (2015). Multi-model study of chemical and physical controls on transport of anthropogenic and biomass burning pollution to the Arctic. *Atmospheric Chemistry and Physics*, 15(6):3575–3603. doi: 10.5194/acp-15-3575-2015.

Moore, C. W., Obrist, D., Steffen, A., Staebler, R. M., Douglas, T. A., Richter, A., and Nghiem, S. V. (2014). Convective forcing of mercury and ozone in the Arctic boundary layer induced by leads in sea ice. *Nature*, 506(7486):81–84. doi: 10.1038/nature12924.

Morrison, H., Thompson, G., and Tatarskii, V. (2009). Impact of Cloud Microphysics on the Development of Trailing Stratiform Precipitation in a Simulated Squall Line: Com-

parison of One- and Two-Moment Schemes. *Monthly Weather Review*, 137(3):991–1007. doi: 10.1175/2008MWR2556.1.

Mudryk, L. R., Dawson, J., Howell, S. E. L., Derksen, C., Zagon, T. A., and Brady, M. (2021). Impact of 1, 2 and 4 °C of global warming on ship navigation in the Canadian Arctic. *Nature Climate Change*, 11(8):673–679. doi: 10.1038/s41558-021-01087-6.

Myhre, G., Shindell, D., Bréon, F.-M., Collins, W., Fuglestvedt, J., Huang, J., Koch, D., Lamarque, J.-F., Lee, D., Mendoza, B., Nakajima, T., Robock, A., Stephens, G., Takemura, T., and Zhang, H. (2013). *Anthropogenic and natural radiative forcing*, pages 659–740. Cambridge University Press, Cambridge, UK. doi: 10.1017/CBO9781107415324.018.

Nakanishi, M. (2001). Improvement Of The Mellor–Yamada Turbulence Closure Model Based On Large-Eddy Simulation Data. *Boundary-Layer Meteorology*, 99(3):349–378. doi: 10.1023/A:1018915827400.

Nakanishi, M. and Niino, H. (2009). Development of an Improved Turbulence Closure Model for the Atmospheric Boundary Layer. *Journal of the Meteorological Society of Japan*, 87(5):895–912. doi: 10.2151/jmsj.87.895.

National Centers for Environmental Prediction (2000). NCEP FNL Operational Model Global Tropospheric Analyses, continuing from July 1999. Research Data Archive at the National Center for Atmospheric Research, Computational and Information Systems Laboratory. doi: 10.5065/D6M043C6.

Neff, W., Helmig, D., Grachev, A., and Davis, D. (2008). A study of boundary layer behavior associated with high NO concentrations at the South Pole using a minisodar, tethered balloon, and sonic anemometer. *Atmospheric Environment*, 42(12):2762–2779. doi: 10.1016/j.atmosenv.2007.01.033.

Neuman, J. A., Nowak, J. B., Huey, L. G., Burkholder, J. B., Dibb, J. E., Holloway, J. S., Liao, J., Peischl, J., Roberts, J. M., Ryerson, T. B., Scheuer, E., Stark, H., Stickel, R. E., Tanner, D. J., and Weinheimer, A. (2010). Bromine measurements in ozone depleted

air over the Arctic Ocean. *Atmospheric Chemistry and Physics*, 10(14):6503–6514. doi: 10.5194/acp-10-6503-2010.

Nicolaus, M., Perovich, D. K., Spreen, G., Granskog, M. A., von Albedyll, L., Angelopoulos, M., Anhaus, P., Arndt, S., Belter, H. J., Bessonov, V., Birnbaum, G., Brauchle, J., Calmer, R., Cardellach, E., Cheng, B., Clemens-Sewall, D., Dadic, R., Damm, E., de Boer, G., Demir, O., Dethloff, K., Divine, D. V., Fong, A. A., Fons, S., Frey, M. M., Fuchs, N., Gabarró, C., Gerland, S., Goessling, H. F., Gradinger, R., Haapala, J., Haas, C., Hamilton, J., Hannula, H.-R., Hendricks, S., Herber, A., Heuzé, C., Hoppmann, M., Høyland, K. V., Huntemann, M., Hutchings, J. K., Hwang, B., Itkin, P., Jacobi, H.-W., Jaggi, M., Jutila, A., Kaleschke, L., Katlein, C., Kolabutin, N., Krampe, D., Kristensen, S. S., Krumpen, T., Kurtz, N., Lampert, A., Lange, B. A., Lei, R., Light, B., Linhardt, F., Liston, G. E., Loose, B., Macfarlane, A. R., Mahmud, M., Matero, I. O., Maus, S., Morgenstern, A., Naderpour, R., Nandan, V., Niubom, A., Oggier, M., Oppelt, N., Pätzold, F., Perron, C., Petrovsky, T., Pirazzini, R., Polashenski, C., Rabe, B., Raphael, I. A., Regnery, J., Rex, M., Ricker, R., Riemann-Campe, K., Rinke, A., Rohde, J., Salganik, E., Scharien, R. K., Schiller, M., Schneebeli, M., Semmling, M., Shimanchuk, E., Shupe, M. D., Smith, M. M., Smolyanitsky, V., Sokolov, V., Stanton, T., Stroeve, J., Thielke, L., Timofeeva, A., Tonboe, R. T., Tavri, A., Tsamados, M., Wagner, D. N., Watkins, D., Webster, M., and Wendisch, M. (2022). Overview of the MOSAiC expedition: Snow and sea ice. *Elementa: Science of the Anthropocene*, 10(1). doi: 10.1525/elementa.2021.000046.

Nightingale, P. D., Malin, G., Law, C. S., Watson, A. J., Liss, P. S., Liddicoat, M. I., Boutin, J., and Upstill-Goddard, R. C. (2000). In situ evaluation of air-sea gas exchange parameterizations using novel conservative and volatile tracers. *Global Biogeochemical Cycles*, 14(1):373–387. doi: 10.1029/1999GB900091.

Nixdorf, U., Dethloff, K., Rex, M., Shupe, M., Sommerfeld, A., Perovich, D., Nicolaus, M., Heuzé, C., Rabe, B., Loose, B., Damm, E., Gradinger, R., Fong, A., Maslowski, W., Rinke, A., Kwok, R., Spreen, G., Wendisch, M., Herber, A., Hirsekorn, M., Mohaupt, V., Frickenhaus, S., Immerz, A., Weiss-Tuider, K., König, B., Mengedoht, D.,

Regnery, J., Gerchow, P., Ransby, D., Krumpen, T., Morgenstern, A., Haas, C., Kanzow, T., Rack, F. R., Saitzev, V., Sokolov, V., Makarov, A., Schwarze, S., Wunderlich, T., Wurr, K., and Antje, B. (2021). MOSAiC Extended Acknowledgement. Zenodo. doi: 10.5281/zenodo.5541624.

Oltmans, S. J. (1981). Surface ozone measurements in clean air. *Journal of Geophysical Research: Oceans*, 86(C2):1174–1180. doi: 10.1029/JC086iC02p01174.

Oltmans, S. J., Johnson, B. J., and Harris, J. M. (2012). Springtime boundary layer ozone depletion at Barrow, Alaska: Meteorological influence, year-to-year variation, and long-term change. *Journal of Geophysical Research: Atmospheres*, 117:D00R18. doi: 10.1029/2011JD016889.

Oltmans, S. J. and Komhyr, W. D. (1986). Surface ozone distributions and variations from 1973–1984: Measurements at the NOAA Geophysical Monitoring for Climatic Change Baseline Observatories. *Journal of Geophysical Research: Atmospheres*, 91(D4):5229–5236. doi: 10.1029/JD091iD04p05229.

Osterwalder, S., Dunham-Cheatham, S. M., Ferreira Araujo, B., Magand, O., Thomas, J. L., Baladima, F., Pfaffhuber, K. A., Berg, T., Zhang, L., Huang, J., Dommergue, A., Sonke, J. E., and Gustin, M. S. (2021). Fate of Springtime Atmospheric Reactive Mercury: Concentrations and Deposition at Zeppelin, Svalbard. *ACS Earth and Space Chemistry*, 5(11):3234–3246. doi: 10.1021/acsearthspacechem.1c00299.

Parrish, D. D., Holloway, J. S., and Fehsenfeld, F. C. (1994). Routine, Continuous Measurement of Carbon Monoxide with Parts per Billion Precision. *Environmental Science & Technology*, 28(9):1615–1618. doi: 10.1021/es00058a013.

Pearson, C., Howard, D., Moore, C., and Obrist, D. (2019). Mercury and trace metal wet deposition across five stations in Alaska: controlling factors, spatial patterns, and source regions. *Atmospheric Chemistry and Physics*, 19(10):6913–6929. doi: 10.5194/acp-19-6913-2019.

Petäjä, T., Duplissy, E.-M., Tabakova, K., Schmale, J., Altstädter, B., Ancellet, G., Arshinov, M., Balin, Y., Baltensperger, U., Bange, J., Beamish, A., Belan, B., Berchet,

A., Bossi, R., Cairns, W. R. L., Ebinghaus, R., El Haddad, I., Ferreira-Araujo, B., Franck, A., Huang, L., Hyvärinen, A., Humbert, A., Kalogridis, A.-C., Konstantinov, P., Lampert, A., MacLeod, M., Magand, O., Mahura, A., Marelle, L., Masloboev, V., Moisseev, D., Moschos, V., Neckel, N., Onishi, T., Osterwalder, S., Ovaska, A., Paasonen, P., Panchenko, M., Pankratov, F., Pernov, J. B., Platis, A., Popovicheva, O., Raut, J.-C., Riandet, A., Sachs, T., Salvatori, R., Salzano, R., Schröder, L., Schön, M., Shevchenko, V., Skov, H., Sonke, J. E., Spolaor, A., Stathopoulos, V. K., Strahlendorff, M., Thomas, J. L., Vitale, V., Vratolis, S., Barbante, C., Chabrillat, S., Dommergue, A., Eleftheriadis, K., Heilimo, J., Law, K. S., Massling, A., Noe, S. M., Paris, J.-D., Prévôt, A. S. H., Riipinen, I., Wehner, B., Xie, Z., and Lappalainen, H. K. (2020). Overview: Integrative and Comprehensive Understanding on Polar Environments (iCUPE) – concept and initial results. *Atmospheric Chemistry and Physics*, 20(14):8551–8592.

Peterson, P. K., Hartwig, M., May, N. W., Schwartz, E., Rigor, I., Ermold, W., Steele, M., Morison, J. H., Nghiem, S. V., and Pratt, K. A. (2019). Snowpack measurements suggest role for multi-year sea ice regions in Arctic atmospheric bromine and chlorine chemistry. *Elementa Science of the Anthropocene*, 7(14). doi: 10.1525/elementa.352.

Peterson, P. K., Pöhler, D., Sihler, H., Zielcke, J., General, S., Frieß, U., Platt, U., Simpson, W. R., Nghiem, S. V., Shepson, P. B., Stirm, B. H., Dhaniyala, S., Wagner, T., Caulton, D. R., Fuentes, J. D., and Pratt, K. A. (2017). Observations of bromine monoxide transport in the Arctic sustained on aerosol particles. *Atmospheric Chemistry and Physics*, 17(12):7567–7579. doi: 10.5194/acp-17-7567-2017.

Peterson, P. K., Simpson, W. R., Pratt, K. A., Shepson, P. B., Frieß, U., Zielcke, J., Platt, U., Walsh, S. J., and Nghiem, S. V. (2015). Dependence of the vertical distribution of bromine monoxide in the lower troposphere on meteorological factors such as wind speed and stability. *Atmospheric Chemistry and Physics*, 15(4):2119–2137. doi: 10.5194/acp-15-2119-2015.

Pielke, R. A. and Mahrer, Y. (1975). Representation of the Heated Planetary Boundary Layer in Mesoscale Models with Coarse Vertical Resolution.

Journal of the Atmospheric Sciences, 32:2288–2308. doi: 10.1175/1520-0469(1975)032<2288:ROTHPB>2.0.CO;2.

Piot, M. and von Glasow, R. (2008). The potential importance of frost flowers, recycling on snow, and open leads for ozone depletion events. *Atmospheric Chemistry and Physics*, 8(9):2437–2467. doi: 10.5194/acp-8-2437-2008.

Piot, M. and von Glasow, R. (2009). Modelling the multiphase near-surface chemistry related to ozone depletions in polar spring. *Journal of Atmospheric Chemistry*, 64(2):77–105. doi: 10.1007/s10874-010-9170-1.

Plane, J. M. and Saiz-Lopez, A. (2006). *UV-Visible Differential Optical Absorption Spectroscopy (DOAS)*, pages 147–188. John Wiley & Sons, Ltd. doi: 10.1002/9780470988510.ch3.

Platt, S. M., Hov, Ø., Berg, T., Breivik, K., Eckhardt, S., Eleftheriadis, K., Evangeliou, N., Fiebig, M., Fisher, R., Hansen, G., Hansson, H.-C., Heintzenberg, J., Hermansen, O., Heslin-Rees, D., Holmén, K., Hudson, S., Kallenborn, R., Krejci, R., Krognes, T., Larssen, S., Lowry, D., Lund Myhre, C., Lunder, C., Nisbet, E., Nizzetto, P. B., Park, K.-T., Pedersen, C. A., Aspmo Pfaffhuber, K., Röckmann, T., Schmidbauer, N., Solberg, S., Stohl, A., Ström, J., Svendby, T., Tunved, P., Tørnkvist, K., van der Veen, C., Vratolis, S., Yoon, Y. J., Yttri, K. E., Zieger, P., Aas, W., and Tørseth, K. (2022). Atmospheric composition in the European Arctic and 30 years of the Zeppelin Observatory, Ny-Ålesund. *Atmospheric Chemistry and Physics*, 22(5):3321–3369. doi: 10.5194/acp-22-3321-2022.

Platt, U. and Hönninger, G. (2003). The role of halogen species in the troposphere. *Chemosphere*, 52(2):325–338. doi: 10.1016/S0045-6535(03)00216-9.

Platt, U. and Stutz, J. (2008). *Differential Absorption Spectroscopy*, pages 135–174. Springer Berlin Heidelberg, Berlin, Heidelberg. doi: 10.1007/978-3-540-75776-4_6.

Poissant, L., Pilote, M., Xu, X., Zhang, H., and Beauvais, C. (2004). Atmospheric mercury speciation and deposition in the Bay St. François wetlands. *Journal of Geophysical Research: Atmospheres*, 109(D11).

Pollard, R. T., Rhines, P. B., and Thompson, R. O. R. Y. (1973). The deepening of the wind-Mixed layer. *Geophysical Fluid Dynamics*, 4(4):381–404. doi: 10.1080/03091927208236105.

Poulain, A. J., Garcia, E., Amyot, M., Campbell, P. G., and Ariya, P. A. (2007). Mercury distribution, partitioning and speciation in coastal vs. inland High Arctic snow. *Geochimica et Cosmochimica Acta*, 71(14):3419–3431. doi: 10.1016/j.gca.2007.05.006.

Poulain, A. J., Lalonde, J. D., Amyot, M., Shead, J. A., Raofie, F., and Ariya, P. A. (2004). Redox transformations of mercury in an Arctic snowpack at springtime. *Atmospheric Environment*, 38(39):6763–6774. doi: 10.1016/j.atmosenv.2004.09.013.

Prados-Roman, C., Cuevas, C. A., Hay, T., Fernandez, R. P., Mahajan, A. S., Royer, S.-J., Galí, M., Simó, R., Dachs, J., Großmann, K., Kinnison, D. E., Lamarque, J.-F., and Saiz-Lopez, A. (2015). Iodine oxide in the global marine boundary layer. *Atmospheric Chemistry and Physics*, 15(2). doi: 10.5194/acp-15-583-2015.

Pratt, K. A., Custard, K. D., Shepson, P. B., Douglas, T. A., Pöhler, D., General, S., Zielcke, J., Simpson, W. R., Platt, U., Tanner, D. J., Gregory Huey, L., Carlsen, M., and Stirm, B. H. (2013). Photochemical production of molecular bromine in Arctic surface snowpacks. *Nature Geoscience*, 6(5):351–356. doi: 10.1038/ngeo1779.

Pratte, P. and Rossi, M. J. (2006). The heterogeneous kinetics of HOBr and HOCl on acidified sea salt and model aerosol at 40–90% relative humidity and ambient temperature. *Physical Chemistry Chemical Physics*, 8:3988–4001. doi: 10.1039/B604321F.

Prestbo, E. M. and Gay, D. A. (2009). Wet deposition of mercury in the U.S. and Canada, 1996–2005: Results and analysis of the NADP mercury deposition network (MDN). *Atmospheric Environment*, 43(27):4223–4233. doi: 10.1016/j.atmosenv.2009.05.028.

Quinn, P. K., Shaw, G., Andrews, E., Dutton, E. G., Ruoho-Airola, T., and Gong, S. L. (2007). Arctic haze: current trends and knowledge gaps. *Tellus B*, 59(1):99–114. doi: 10.1111/j.1600-0889.2006.00238.x.

Rabe, B., Heuzé, C., Regnery, J., Aksenov, Y., Allerholt, J., Athanase, M., Bai, Y., Basque, C., Bauch, D., Baumann, T. M., Chen, D., Cole, S. T., Craw, L., Davies, A., Damm, E., Dethloff, K., Divine, D. V., Doglioni, F., Ebert, F., Fang, Y.-C., Fer, I., Fong, A. A., Gradinger, R., Granskog, M. A., Graupner, R., Haas, C., He, H., He, Y., Hoppmann, M., Janout, M., Kadko, D., Kanzow, T., Karam, S., Kawaguchi, Y., Koenig, Z., Kong, B., Krishfield, R. A., Krumpen, T., Kuhlmey, D., Kuznetsov, I., Lan, M., Laukert, G., Lei, R., Li, T., Torres-Valdés, S., Lin, L., Lin, L., Liu, H., Liu, N., Loose, B., Ma, X., McKay, R., Mallet, M., Mallett, R. D. C., Maslowski, W., Mertens, C., Mohrholz, V., Muilwijk, M., Nicolaus, M., O'Brien, J. K., Perovich, D., Ren, J., Rex, M., Ribeiro, N., Rinke, A., Schaffer, J., Schuffenhauer, I., Schulz, K., Shupe, M. D., Shaw, W., Sokolov, V., Sommerfeld, A., Spreen, G., Stanton, T., Stephens, M., Su, J., Sukhikh, N., Sundfjord, A., Thomisch, K., Tippenhauer, S., Toole, J. M., Vredenborg, M., Walter, M., Wang, H., Wang, L., Wang, Y., Wendisch, M., Zhao, J., Zhou, M., and Zhu, J. (2022). Overview of the MOSAiC expedition: Physical oceanography. *Elementa: Science of the Anthropocene*, 10(1). doi: 10.1525/elementa.2021.00062.

Rasmussen, R., Baker, B., Kochendorfer, J., Meyers, T., Landolt, S., Fischer, A. P., Black, J., Thériault, J. M., Kucera, P., Gochis, D., Smith, C., Nitu, R., Hall, M., Ikeda, K., and Gutmann, E. (2012). How Well Are We Measuring Snow: The NOAA/FAA/NCAR Winter Precipitation Test Bed. *Bulletin of the American Meteorological Society*, 93(6):811–829. doi: 10.1175/BAMS-D-11-00052.1.

Raso, A. R. W., Custard, K. D., May, N. W., Tanner, D., Newburn, M. K., Walker, L., Moore, R. J., Huey, L. G., Alexander, L., Shepson, P. B., and Pratt, K. A. (2017). Active molecular iodine photochemistry in the Arctic. *Proceedings of the National Academy of Sciences*, 114(38):10053–10058. doi: 10.1073/pnas.1702803114.

Rhodes, R. H., Yang, X., Wolff, E. W., McConnell, J. R., and Frey, M. M. (2017). Sea ice as a source of sea salt aerosol to Greenland ice cores: a model-based study. *Atmospheric Chemistry and Physics*, 17(15):9417–9433. doi: 10.5194/acp-17-9417-2017.

Richter, A., Wittrock, F., Eisinger, M., and Burrows, J. P. (1998). GOME observations

of tropospheric BrO in northern hemispheric spring and summer 1997. *Geophysical Research Letters*, 25(14):2683–2686. doi: 10.1029/98GL52016.

Ridley, B. A., Atlas, E. L., Montzka, D. D., Browell, E. V., Cantrell, C. A., Blake, D. R., Blake, N. J., Cinquini, L., Coffey, M. T., Emmons, L. K., Cohen, R. C., DeYoung, R. J., Dibb, J. E., Eisele, F. L., Flocke, F. M., Fried, A., Grahek, F. E., Grant, W. B., Hair, J. W., Hannigan, J. W., Heikes, B. J., Lefer, B. L., Mauldin, R. L., Moody, J. L., Shetter, R. E., Snow, J. A., Talbot, R. W., Thornton, J. A., Walega, J. G., Weinheimer, A. J., Wert, B. P., and Wimmers, A. J. (2003). Ozone depletion events observed in the high latitude surface layer during the TOPSE aircraft program. *Journal of Geophysical Research: Atmospheres*, 108(D4). doi: 10.1029/2001JD001507.

Rolph, G., Stein, A., and Stunder, B. (2017). Real-time Environmental Applications and Display sYstem: READY. *Environmental Modelling & Software*, 95:210–228. doi: 10.1016/j.envsoft.2017.06.025.

Rudolph, J., Ru Fu, B., Thompson, A., Anlauf, K., and Bottenheim, J. (1999). Halogen atom concentrations in the Arctic Troposphere derived from hydrocarbon measurements: Impact on the budget of formaldehyde. *Geophysical Research Letters*, 26(19):2941–2944. doi: 10.1029/1999GL010869.

Saiz-Lopez, A., Acuña, A. U., Trabelsi, T., Carmona-García, J., Dávalos, J. Z., Rivero, D., Cuevas, C. A., Kinnison, D. E., Sitkiewicz, S. P., Roca-Sanjuán, D., and Francisco, J. S. (2019). Gas-Phase Photolysis of Hg(I) Radical Species: A New Atmospheric Mercury Reduction Process. *Journal of the American Chemical Society*, 141(22):8698–8702. doi: 10.1021/jacs.9b02890.

Saiz-Lopez, A., Fernandez, R. P., Ordóñez, C., Kinnison, D. E., Gómez Martín, J. C., Lamarque, J.-F., and Tilmes, S. (2014). Iodine chemistry in the troposphere and its effect on ozone. *Atmospheric Chemistry and Physics*, 14(23):13119–13143. doi: 10.5194/acp-14-13119-2014.

Saiz-Lopez, A., Plane, J. M. C., Baker, A. R., Carpenter, L. J., von Glasow, R., Gómez Martín, J. C., McFiggans, G., and Saunders, R. W. (2012). Atmospheric Chem-

istry of Iodine. *Tellus B: Chemical and Physical Meteorology*, 112(3):1773–1804. doi: 10.1021/cr200029u.

Saiz-Lopez, A., Sitkiewicz, S. P., Roca-Sanjuán, D., Oliva-Enrich, J. M., Dávalos, J. Z., Notario, R., Jiskra, M., Xu, Y., Wang, F., Thackray, C. P., Sunderland, E. M., Jacob, D. J., Travnikov, O., Cuevas, C. A., Acuña, A. U., Rivero, D., Plane, J. M. C., Kinnison, D. E., and Sonke, J. E. (2018). Photoreduction of gaseous oxidized mercury changes global atmospheric mercury speciation, transport and deposition. *Nature Communications*, 9(1):4796. doi: 10.1038/s41467-018-07075-3.

Saiz-Lopez, A. and von Glasow, R. (2012). Arctic tropospheric chemistry: an overview. *Tellus B: Chemical and Physical Meteorology*, 49(5):450–454. doi: 10.1039/C2CS35208G.

Salawitch, R. J., Canty, T., Kurosu, T., Chance, K., Liang, Q., da Silva, A., Pawson, S., Nielsen, J. E., Rodriguez, J. M., Bhartia, P. K., Liu, X., Huey, L. G., Liao, J., Stickel, R. E., Tanner, D. J., Dibb, J. E., Simpson, W. R., Donohoue, D., Weinheimer, A., Flocke, F., Knapp, D., Montzka, D., Neuman, J. A., Nowak, J. B., Ryerson, T. B., Oltmans, S., Blake, D. R., Atlas, E. L., Kinnison, D. E., Tilmes, S., Pan, L. L., Hendrick, F., Van Roozendael, M., Kreher, K., Johnston, P. V., Gao, R. S., Johnson, B., Bui, T. P., Chen, G., Pierce, R. B., Crawford, J. H., and Jacob, D. J. (2010). A new interpretation of total column BrO during Arctic spring. *Geophysical Research Letters*, 37(21). doi: 10.1029/2010GL043798.

Saltzman, E. S., King, D. B., Holmen, K., and Leck, C. (1993). Experimental determination of the diffusion coefficient of dimethylsulfide in water. *Journal of Geophysical Research: Oceans*, 93(C9):16481–16486. doi: 10.1029/93JC01858.

Sand, M., Samset, B. H., Balkanski, Y., Bauer, S., Bellouin, N., Berntsen, T. K., Bian, H., Chin, M., Diehl, T., Easter, R., Ghan, S. J., Iversen, T., Kirkevåg, A., Lamarque, J.-F., Lin, G., Liu, X., Luo, G., Myhre, G., Noije, T. V., Penner, J. E., Schulz, M., Seland, Ø., Skeie, R. B., Stier, P., Takemura, T., Tsigaridis, K., Yu, F., Zhang, K., and Zhang, H. (2017). Aerosols at the poles: an AeroCom Phase II multi-model evaluation. *At-*

mospheric Chemistry and Physics, 17(19):12197–12218. doi: 10.5194/acp-17-12197-2017.

Sandu, A. and Sander, R. (2006). Technical note: Simulating chemical systems in Fortran90 and Matlab with the Kinetic PreProcessor KPP-2.1. *Atmospheric Chemistry and Physics*, 6(1):187–195. doi: 10.5194/acp-6-187-2006.

Sanei, H., Outridge, P., Goodarzi, F., Wang, F., Armstrong, D., Warren, K., and Fishback, L. (2010). Wet deposition mercury fluxes in the Canadian sub-Arctic and southern Alberta, measured using an automated precipitation collector adapted to cold regions. *Atmospheric Environment*, 44(13):1672–1681. doi: 10.1016/j.atmosenv.2010.01.030.

Schmithüsen, H. (2021). Continuous meteorological surface measurement during POLARSTERN cruise PS122/3. PANGAEA. doi: 10.1594/PANGAEA.935223.

Schroeder, W. H., Anlauf, K. G., Barrie, L. A., Lu, J. Y., Steffen, A., Schneeberger, D. R., and Berg, T. (1998). Arctic springtime depletion of mercury. *Nature*, 394(6691):331–332. doi: 10.1038/28530.

Schroeder, W. H., Steffen, A., Scott, K., Bender, T., Prestbo, E., Ebinghaus, R., Lu, J. Y., and Lindberg, S. E. (2003). Summary report: first international Arctic atmospheric mercury research workshop. *Atmospheric Environment*, 37(18):2551–2555. doi: 10.1016/S1352-2310(03)00153-5.

Schwartz, S. E. (1986). Mass-Transport Considerations Pertinent to Aqueous Phase Reactions of Gases in Liquid-Water Clouds. In Jaeschke, W., editor, *Chemistry of Multiphase Atmospheric Systems*, pages 415–471, Berlin, Heidelberg. Springer Berlin Heidelberg.

Seigneur, C., Vijayaraghavan, K., Lohman, K., Karamchandani, P., and Scott, C. (2004). Global Source Attribution for Mercury Deposition in the United States. *Environmental Science & Technology*, 38(2):555–569. doi: 10.1021/es034109t.

Seinfeld, J. and Pandis, S. (2006). *Atmospheric Chemistry and Physics: From Air Pollution to Climate Change*. Wiley, 2nd edition.

Seisel, S., Flückiger, B., and Rossi, M. J. (1998). The heterogeneous reaction of N_2O_5 with HBr on Ice comparison with N_2O_5+HCl. *Berichte der Bunsengesellschaft für physikalische Chemie*, 102(6):811–820. doi: 10.1002/bbpc.19981020604.

Selin, N. E. (2009). Global Biogeochemical Cycling of Mercury: A Review. *Annual Review of Environment and Resources*, 34(1):43–63. doi: 10.1146/annurev.environ.051308.084314.

Selin, N. E., Jacob, D. J., Yantosca, R. M., Strode, S., Jaeglé, L., and Sunderland, E. M. (2008). Global 3-D land-ocean-atmosphere model for mercury: Present-day versus preindustrial cycles and anthropogenic enrichment factors for deposition. *Global Biogeochemical Cycles*, 22(2). doi: 10.1029/2007GB003040.

Seo, S., Richter, A., Blechschmidt, A.-M., Bougoudis, I., and Burrows, J. P. (2019). First high-resolution BrO column retrievals from TROPOMI. *Atmospheric Measurement Techniques*, 12(5):2913–2932. doi: 10.5194/amt-12-2913-2019.

Serdyuchenko, A., Gorshelev, V., Weber, M., Chehade, W., and Burrows, J. P. (2014). High spectral resolution ozone absorption cross-sections – Part 2: Temperature dependence. *Atmospheric Measurement Techniques*, 7(2):625–636. doi: 10.5194/amt-7-625-2014.

Shah, V., Jacob, D. J., Thackray, C. P., Wang, X., Sunderland, E. M., Dibble, T. S., Saiz-Lopez, A., Černušák, I., Kellö, V., Castro, P. J., Wu, R., and Wang, C. (2021). Improved Mechanistic Model of the Atmospheric Redox Chemistry of Mercury. *Environmental Science & Technology*, 55(21):14445–14456. doi: 10.1021/acs.est.1c03160.

Shapiro, M. A., Hampel, T., and Krueger, A. J. (1987). The Arctic Tropopause Fold. *Monthly Weather Review*, 115(2):444–454. doi: 10.1175/1520-0493(1987)115<0444:TATF>2.0.CO;2.

Sherman, L. S., Blum, J. D., Johnson, K. P., Keeler, G. J., Barres, J. A., and Douglas, T. A. (2011). Mass-independent fractionation of mercury isotopes in Arctic snow driven by sunlight. *Nature Geoscience*, 3(3):173–177. doi: 10.1038/ngeo758.

Shetter, R. E. and Müller, M. (1999). Photolysis frequency measurements using actinic flux spectroradiometry during the PEM-Tropics mission: Instrumentation description and some results. *Journal of Geophysical Research: Atmospheres*, 104(D5):5647–5661. doi: 10.1029/98JD01381.

Shupe, M. D., Rex, M., Blomquist, B., Persson, P. O. G., Schmale, J., Uttal, T., Althausen, D., Angot, H., Archer, S., Bariteau, L., Beck, I., Bilberry, J., Bucci, S., Buck, C., Boyer, M., Brasseur, Z., Brooks, I. M., Calmer, R., Cassano, J., Castro, V., Chu, D., Costa, D., Cox, C. J., Creamean, J., Crewell, S., Dahlke, S., Damm, E., de Boer, G., Deckelmann, H., Dethloff, K., Dütsch, M., Ebell, K., Ehrlich, A., Ellis, J., Engelmann, R., Fong, A. A., Frey, M. M., Gallagher, M. R., Ganzeveld, L., Gradinger, R., Graeser, J., Greenamyer, V., Griesche, H., Griffiths, S., Hamilton, J., Heinemann, G., Helmig, D., Herber, A., Heuzé, C., Hofer, J., Houchens, T., Howard, D., Inoue, J., Jacobi, H.-W., Jaiser, R., Jokinen, T., Jourdan, O., Jozef, G., King, W., Kirchgaessner, A., Klingebiel, M., Krassovski, M., Krumpen, T., Lampert, A., Landing, W., Laurila, T., Lawrence, D., Lonardi, M., Loose, B., Lüpkes, C., Maahn, M., Macke, A., Maslowski, W., Marsay, C., Maturilli, M., Mech, M., Morris, S., Moser, M., Nicolaus, M., Ortega, P., Osborn, J., Pätzold, F., Perovich, D. K., Petäjä, T., Pilz, C., Pirazzini, R., Posman, K., Powers, H., Pratt, K. A., Preußer, A., Quéléver, L., Radenz, M., Rabe, B., Rinke, A., Sachs, T., Schulz, A., Siebert, H., Silva, T., Solomon, A., Sommerfeld, A., Spreen, G., Stephens, M., Stohl, A., Svensson, G., Uin, J., Viegas, J., Voigt, C., von der Gathen, P., Wehner, B., Welker, J. M., Wendisch, M., Werner, M., Xie, Z., and Yue, F. (2022). Overview of the MOSAiC expedition: Atmosphere. *Elementa: Science of the Anthropocene*, 10(1). doi: 10.1525/elementa.2021.00060.

Simpson, W. R., Brown, S. S., Saiz-Lopez, A., Thornton, J. A., and von Glasow, R. (2015). Tropospheric Halogen Chemistry: Sources, Cycling, and Impacts. *Chemical Reviews*, 115(10):4035–4062. doi: 10.1021/cr5006638.

Simpson, W. R., Frieß, U., Thomas, J. L., Lampel, J., and Platt, U. (2018). Polar Nighttime Chemistry Produces Intense Reactive Bromine Events. *Geophysical Research Letters*, 45(18):9987–9994. doi: 10.1029/2018GL079444.

Simpson, W. R., Perovich, D., Matrai, P., Shepson, P., and Chavez, F. (2009). The Collaborative O-Buoy Project: Deployment of a Network of Arctic Ocean Chemical Sensors for the IPY and beyond. Arctic Data Center. doi: 10.18739/A2WD4W.

Simpson, W. R., Peterson, P., Frieß, U., Sihler, H., Lampel, J., Platt, U., Moore, C., Pratt, K., Shepson, P., Halfacre, J., and Nghiem, S. (2017). Horizontal and vertical structure of reactive bromine events probed by bromine monoxide MAX-DOAS. *Atmospheric Chemistry and Physics*, 17(15):9291–9309. doi: 10.5194/acp-17-9291-2017.

Simpson, W. R., von Glasow, R., Riedel, K., Anderson, P., Ariya, P., Bottenheim, J., Burrows, J., Carpenter, L. J., Frieß, U., Goodsite, M. E., Heard, D., Hutterli, M., Jacobi, H.-W., Kaleschke, L., Neff, B., Plane, J., Platt, U., Richter, A., Roscoe, H., Sander, R., Shepson, P., Sodeau, J., Steffen, A., Wagner, T., and Wolff, E. (2007). Halogens and their role in polar boundary-layer ozone depletion. *Atmospheric Chemistry and Physics*, 7(16):4375–4418. doi: 10.5194/acp-7-4375-2007.

Sitkiewicz, S. P., Rivero, D., Oliva-Enrich, J. M., Saiz-Lopez, A., and Roca-Sanjuán, D. (2019). Ab initio quantum-chemical computations of the absorption cross sections of HgX_2 and HgXY (X, Y = Cl, Br, and I): molecules of interest in the Earth's atmosphere. *Physical Chemistry Chemical Physics*, 21:455–467. doi: 10.1039/C8CP06160B.

Skamarock, W. C., Klemp, J. B., Dudhia, J., Gill, D. O., Liu, Z., Berner, J., Wang, W., Powers, J. G., Duda, M. G., Barker, D. M., and Huang, X.-Y. (2019). A Description of the Advanced Research WRF Version 4. Technical report. doi: 10.5065/1dfh-6p97.

Skov, H., Brooks, S. B., Goodsite, M. E., Lindberg, S. E., Meyers, T. P., Landis, M. S., Larsen, M. R., Jensen, B., McConville, G., and Christensen, J. (2006). Fluxes of reactive gaseous mercury measured with a newly developed method using relaxed eddy accumulation. *Atmospheric Environment*, 40(28):5452–5463. doi: 10.1016/j.atmosenv.2006.04.061.

Skov, H., Christensen, J. H., Goodsite, M. E., Heidam, N. Z., Jensen, B., Wåhlin, P., and Geernaert, G. (2004). Fate of Elemental Mercury in the Arctic during Atmospheric

Mercury Depletion Episodes and the Load of Atmospheric Mercury to the Arctic. *Environmental Science & Technology*, 38(8):2373–2382. doi: 10.1021/es030080h.

Skov, H., Hjorth, J., Nordstrøm, C., Jensen, B., Christoffersen, C., Bech Poulsen, M., Baldtzer Liisberg, J., Beddows, D., Dall'Osto, M., and Christensen, J. H. (2020). Variability in gaseous elemental mercury at Villum Research Station, Station Nord, in North Greenland from 1999 to 2017. *Atmospheric Chemistry and Physics*, 20(21):13253–13265. doi: 10.5194/acp-20-13253-2020.

Slemr, F., Angot, H., Dommergue, A., Magand, O., Barret, M., Weigelt, A., Ebinghaus, R., Brunke, E.-G., Pfaffhuber, K. A., Edwards, G., Howard, D., Powell, J., Keywood, M., and Wang, F. (2015). Comparison of mercury concentrations measured at several sites in the Southern Hemisphere. *Atmospheric Chemistry and Physics*, 15(6):3125–3133. doi: 10.5194/acp-15-3125-2015.

Smith, J., Sjostedt, S., Abbatt, J., and Wiedensohler, A. (2009). Aerosol measurements during OASIS Barrow field intensive Spring 2009. Arctic Data Center. Accessed on 08/24/2021. doi: 10.5065/D6P8491K.

Sommar, J., Wängberg, I., Berg, T., Gårdfeldt, K., Munthe, J., Richter, A., Urba, A., Wittrock, F., and Schroeder, W. H. (2007). Circumpolar transport and air-surface exchange of atmospheric mercury at Ny-Ålesund (79○ N), Svalbard, spring 2002. *Atmospheric Chemistry and Physics*, 7(1):151–166. doi: 10.5194/acp-7-151-2007.

Song, S., Selin, N. E., Soerensen, A. L., Angot, H., Artz, R., Brooks, S., Brunke, E.-G., Conley, G., Dommergue, A., Ebinghaus, R., Holsen, T. M., Jaffe, D. A., Kang, S., Kelley, P., Luke, W. T., Magand, O., Marumoto, K., Pfaffhuber, K. A., Ren, X., Sheu, G.-R., Slemr, F., Warneke, T., Weigelt, A., Weiss-Penzias, P., Wip, D. C., and Zhang, Q. (2015). Top-down constraints on atmospheric mercury emissions and implications for global biogeochemical cycling. *Atmospheric Chemistry and Physics*, 15(12):7103–7125. doi: 10.5194/acp-15-7103-2015.

Sonke, J. E., Teisserenc, R., Heimbürger-Boavida, L.-E., Petrova, M. V., Marusczak, N., Dantec, T. L., Chupakov, A. V., Li, C., Thackray, C. P., Sunderland, E. M.,

Tananaev, N., and Pokrovsky, O. S. (2018). Eurasian river spring flood observations support net Arctic Ocean mercury export to the atmosphere and Atlantic Ocean. *Proceedings of the National Academy of Sciences*, 115(50):E11586–E11594. doi: 10.1073/pnas.1811957115.

Spicer, C. W., Plastridge, R. A., Foster, K. L., Finlayson-Pitts, B. J., Bottenheim, J. W., Grannas, A. M., and Shepson, P. B. (2002). Molecular halogens before and during ozone depletion events in the Arctic at polar sunrise: concentrations and sources. *Atmospheric Environment*, 36(15). doi: 10.1016/S1352-2310(02)00125-5.

Sprovieri, F., Pirrone, N., Bencardino, M., D'Amore, F., Angot, H., Barbante, C., Brunke, E.-G., Arcega-Cabrera, F., Cairns, W., Comero, S., Diéguez, M. D. C., Dommergue, A., Ebinghaus, R., Feng, X. B., Fu, X., Garcia, P. E., Gawlik, B. M., Hageström, U., Hansson, K., Horvat, M., Kotnik, J., Labuschagne, C., Magand, O., Martin, L., Mashyanov, N., Mkololo, T., Munthe, J., Obolkin, V., Ramirez Islas, M., Sena, F., Somerset, V., Spandow, P., Vardè, M., Walters, C., Wängberg, I., Weigelt, A., Yang, X., and Zhang, H. (2017). Five-year records of mercury wet deposition flux at GMOS sites in the Northern and Southern hemispheres. *Atmospheric Chemistry and Physics*, 17(4):2689–2708. doi: 10.5194/acp-17-2689-2017.

Stauffer, D. R. and Seaman, N. L. (1990). Use of Four-Dimensional Data Assimilation in a Limited-Area Mesoscale Model. Part I: Experiments with Synoptic-Scale Data. *Monthly Weather Review*, 118(6):1250–1277. doi: 10.1175/1520-0493(1990)118<1250:UOFDDA>2.0.CO;2.

Steen, A. O., Berg, T., Dastoor, A. P., Durnford, D. A., Hole, L. R., and Pfaffhuber, K. A. (2009). Dynamic exchange of gaseous elemental mercury during polar night and day. *Atmospheric Environment*, 43(25):5604–5610. doi: 10.1016/j.atmosenv.2009.07.069.

Steenhuisen, F. and Wilson, S. (2019). Development and application of an updated geospatial distribution model for gridding 2015 global mercury emissions. *Atmospheric Environment*, 211:138–150. doi: 10.1016/j.atmosenv.2019.05.003.

Steenhuisen, F. and Wilson, S. J. (2022). Geospatially distributed (gridded) global

mercury emissions to air from anthropogenic sources in 2015. DataverseNL. doi: 10.34894/SZ2KOI.

Steffen, A., Bottenheim, J., Cole, A., Douglas, T. A., Ebinghaus, R., Friess, U., Netcheva, S., Nghiem, S., Sihler, H., and Staebler, R. (2013). Atmospheric mercury over sea ice during the OASIS-2009 campaign. *Atmospheric Chemistry and Physics*, 13(14):7007–7021. doi: 10.5194/acp-13-7007-2013.

Steffen, A., Bottenheim, J., Cole, A., Ebinghaus, R., Lawson, G., and Leaitch, W. R. (2014). Atmospheric mercury speciation and mercury in snow over time at Alert, Canada. *Atmospheric Chemistry and Physics*, 14(5):2219–2231. doi: 10.5194/acp-14-2219-2014.

Steffen, A., Douglas, T., Amyot, M., Ariya, P., Aspmo, K., Berg, T., Bottenheim, J., Brooks, S., Cobbett, F., Dastoor, A., Dommergue, A., Ebinghaus, R., Ferrari, C., Gardfeldt, K., Goodsite, M. E., Lean, D., Poulain, A. J., Scherz, C., Skov, H., Sommar, J., and Temme, C. (2008). A synthesis of atmospheric mercury depletion event chemistry in the atmosphere and snow. *Atmospheric Chemistry and Physics*, 8(6):1445–1482. doi: 10.5194/acp-8-1445-2008.

Steffen, A., Schroeder, W., Bottenheim, J., Narayan, J., and Fuentes, J. D. (2002). Atmospheric mercury concentrations: measurements and profiles near snow and ice surfaces in the Canadian Arctic during Alert 2000. *Atmospheric Environment*, 36(15):2653–2661. doi: 10.1016/S1352-2310(02)00112-7.

Steffen, A., Schroeder, W., Macdonald, R., Poissant, L., and Konoplev, A. (2005). Mercury in the Arctic atmosphere: An analysis of eight years of measurements of GEM at Alert (Canada) and a comparison with observations at Amderma (Russia) and Kuujjuarapik (Canada). *Science of The Total Environment*, 342(1):185–198. doi: 10.1016/j.scitotenv.2004.12.048.

Stein, A. F., Draxler, R. R., Rolph, G. D., Stunder, B. J. B., Cohen, M. D., and Ngan, F. (2015). NOAA's HYSPLIT Atmospheric Transport and Dispersion Modeling System.

Bulletin of the American Meteorological Society, 96:2059–2077. doi: 10.1175/BAMS-D-14-00110.1.

Stephens, C. R., Shepson, P. B., Steffen, A., Bottenheim, J. W., Liao, J., Huey, L. G., Apel, E., Weinheimer, A., Hall, S. R., Cantrell, C., Sive, B. C., Knapp, D. J., Montzka, D. D., and Hornbrook, R. S. (2012). The relative importance of chlorine and bromine radicals in the oxidation of atmospheric mercury at Barrow, Alaska. *Journal of Geophysical Research: Atmospheres*, 117(D14). doi: 10.1029/2011JD016649.

Stephenson, S. R., Wang, W., Zender, C. S., Wang, H., Davis, S. J., and Rasch, P. J. (2018). Climatic Responses to Future Trans-Arctic Shipping. *Geophysical Research Letters*, 45(18):9898–9908. doi: 10.1029/2018GL078969.

Stull, R. B. (1988). *An introduction to boundary layer meteorology*, volume 13. Springer Dordrecht. doi: 10.1007/978-94-009-3027-8.

Subir, M., Ariya, P. A., and Dastoor, A. P. (2011). A review of uncertainties in atmospheric modeling of mercury chemistry I. Uncertainties in existing kinetic parameters – Fundamental limitations and the importance of heterogeneous chemistry. *Atmospheric Environment*, 45(32):5664–5676. doi: 10.1016/j.atmosenv.2011.04.046.

Subir, M., Ariya, P. A., and Dastoor, A. P. (2012). A review of the sources of uncertainties in atmospheric mercury modeling II. Mercury surface and heterogeneous chemistry – A missing link. *Atmospheric Environment*, 46:1–10. doi: 10.1016/j.atmosenv.2011.07.047.

Swanson, W. F., Holmes, C. D., Simpson, W. R., Confer, K., Marelle, L., Thomas, J. L., Jaeglé, L., Alexander, B., Zhai, S., Chen, Q., Wang, X., and Sherwen, T. (2022). Comparison of model and ground observations finds snowpack and blowing snow both contribute to Arctic tropospheric reactive bromine. *Atmospheric Chemistry and Physics Discussions*, 2022:1–38. doi: 10.5194/acp-2022-44.

Tanner, D. J., Jefferson, A., and Eisele, F. L. (1997). Selected ion chemical ionization mass spectrometric measurement of OH. *Journal of Geophysical Research: Atmospheres*, 102(D5):6415–6425. doi: 10.1029/96JD03919.

Tewari, M., Chen, F., Wang, W., Dudhia, J., LeMone, M. A., Gayno, G., Wegiel, J., and Cuenca, R. H. (2004). Implementation and verification of the unified Noah land surface model in the WRF model. In *20th Conference on Weather Analysis and Forecasting/16th Conference on Numerical Weather Prediction*, pages 11–15.

Thalman, R. and Volkamer, R. (2013). Temperature dependent absorption cross-sections of O_2–O_2 collision pairs between 340 and 630 nm and at atmospherically relevant pressure. *Phys. Chem. Chem. Phys.*, 15:15371–15381. doi: 10.1039/C3CP50968K.

Theys, N., Van Roozendael, M., Hendrick, F., Yang, X., De Smedt, I., Richter, A., Begoin, M., Errera, Q., Johnston, P. V., Kreher, K., and De Mazière, M. (2011). Global observations of tropospheric BrO columns using GOME-2 satellite data. *Atmospheric Chemistry and Physics*, 11(4):1791–1811. doi: 10.5194/acp-11-1791-2011.

Thomas, J. L., Dibb, J. E., Huey, L. G., Liao, J., Tanner, D., Lefer, B., von Glasow, R., and Stutz, J. (2012). Modeling chemistry in and above snow at Summit, Greenland – Part 2: Impact of snowpack chemistry on the oxidation capacity of the boundary layer. *Atmospheric Chemistry and Physics*, 12(14):6537–6554. doi: 10.5194/acp-12-6537-2012.

Thomas, J. L., Stutz, J., Lefer, B., Huey, L. G., Toyota, K., Dibb, J. E., and von Glasow, R. (2011). Modeling chemistry in and above snow at Summit, Greenland – Part 1: Model description and results. *Atmospheric Chemistry and Physics*, 11(10):4899–4914. doi: 10.5194/acp-11-4899-2011.

Thompson, C. R., Shepson, P. B., Liao, J., Huey, L. G., Apel, E. C., Cantrell, C. A., Flocke, F., Orlando, J., Fried, A., Hall, S. R., Hornbrook, R. S., Knapp, D. J., Mauldin III, R. L., Montzka, D. D., Sive, B. C., Ullmann, K., Weibring, P., and Weinheimer, A. (2015). Interactions of bromine, chlorine, and iodine photochemistry during ozone depletions in Barrow, Alaska. *Atmospheric Chemistry and Physics*, 15(16):9651–9679. doi: 10.5194/acp-15-9651-2015.

Toyota, K., Dastoor, A. P., and Ryzhkov, A. (2014a). Air–snowpack exchange of bromine, ozone and mercury in the springtime Arctic simulated by the 1-D model PHANTAS –

Part 2: Mercury and its speciation. *Atmospheric Chemistry and Physics*, 14(8):4135–4167. doi: 10.5194/acp-14-4135-2014.

Toyota, K., McConnell, J. C., Lupu, A., Neary, L., McLinden, C. A., Richter, A., Kwok, R., Semeniuk, K., Kaminski, J. W., Gong, S.-L., Jarosz, J., Chipperfield, M. P., and Sioris, C. E. (2011). Analysis of reactive bromine production and ozone depletion in the Arctic boundary layer using 3-D simulations with GEM-AQ: inference from synoptic-scale patterns. *Atmospheric Chemistry and Physics*, 11(8):3949–3979. doi: 10.5194/acp-11-3949-2011.

Toyota, K., McConnell, J. C., Staebler, R. M., and Dastoor, A. P. (2014b). Air–snowpack exchange of bromine, ozone and mercury in the springtime Arctic simulated by the 1-D model PHANTAS – Part 1: In-snow bromine activation and its impact on ozone. *Atmospheric Chemistry and Physics*, 14(8):4101–4133. doi: 10.5194/acp-14-4101-2014.

Travnikov, O., Angot, H., Artaxo, P., Bencardino, M., Bieser, J., D'Amore, F., Dastoor, A., De Simone, F., Diéguez, M. D. C., Dommergue, A., Ebinghaus, R., Feng, X. B., Gencarelli, C. N., Hedgecock, I. M., Magand, O., Martin, L., Matthias, V., Mashyanov, N., Pirrone, N., Ramachandran, R., Read, K. A., Ryjkov, A., Selin, N. E., Sena, F., Song, S., Sprovieri, F., Wip, D., Wängberg, I., and Yang, X. (2017). Multi-model study of mercury dispersion in the atmosphere: atmospheric processes and model evaluation. *Atmospheric Chemistry and Physics*, 17(8):5271–5295. doi: 10.5194/acp-17-5271-2017.

Tuckermann, M., Ackermann, R., Gölz, C., Lorenzen-Schmidt, H., Senne, T., Stutz, J., Trost, B., Unold, W., and Platt, U. (1997). DOAS-observation of halogen radical-catalysed arctic boundary layer ozone destruction during the ARCTOC-campaigns 1995 and 1996 in Ny-Ålesund, Spitsbergen. *Tellus B: Chemical and Physical Meteorology*, 49(5):533–555. doi: 10.3402/tellusb.v49i5.16005.

Tuite, K., Thomas, J. L., Veres, P. R., Roberts, J. M., Stevens, P. S., Griffith, S. M., Dusanter, S., Flynn, J. H., Ahmed, S., Emmons, L., Kim, S.-W., Washenfelder, R.,

Young, C., Tsai, C., Pikelnaya, O., and Stutz, J. (2021). Quantifying nitrous acid formation mechanisms using measured vertical profiles during the CalNex 2010 campaign and 1D column modeling. *Journal of Geophysical Research: Atmospheres*, 126:e2021JD034689. doi: 10.1029/2021JD034689.

United Nations Environment Programme (2013). Global Mercury Assessment 2013: Sources, emissions, releases, and environmental transport.

Vandaele, A., Hermans, C., Simon, P., Carleer, M., Colin, R., Fally, S., Mérienne, M., Jenouvrier, A., and Coquart, B. (1998). Measurements of the NO_2 absorption cross-section from 42000 cm^{-1} to 10000 cm^{-1} (238–1000 nm) at 220 K and 294 K. *Journal of Quantitative Spectroscopy and Radiative Transfer*, 59(3):171–184. doi: 10.1016/S0022-4073(97)00168-4.

Villena, G., Wiesen, P., Cantrell, C. A., Flocke, F., Fried, A., Hall, S. R., Hornbrook, R. S., Knapp, D., Kosciuch, E., Mauldin III, R. L., McGrath, J. A., Montzka, D., Richter, D., Ullmann, K., Walega, J., Weibring, P., Weinheimer, A., Staebler, R. M., Liao, J., Huey, L. G., and Kleffmann, J. (2011). Nitrous acid (HONO) during polar spring in Barrow, Alaska: A net source of OH radicals? *Journal of Geophysical Research: Atmospheres*, 116:D00R07. doi: 10.1029/2011JD016643.

von Glasow, R., Sander, R., Bott, A., and Crutzen, P. J. (2002a). Modeling halogen chemistry in the marine boundary layer 1. Cloud-free MBL. *Journal of Geophysical Research: Atmospheres*, 107(D17). doi: 10.1029/2001JD000942.

von Glasow, R., Sander, R., Bott, A., and Crutzen, P. J. (2002b). Modeling halogen chemistry in the marine boundary layer 2. Interactions with sulfur and the cloud-covered MBL. *Journal of Geophysical Research: Atmospheres*, 107(D17). doi: 10.1029/2001JD000943.

von Storch, H., Langenberg, H., and Feser, F. (2000). A Spectral Nudging Technique for Dynamical Downscaling Purposes. *Monthly Weather Review*, 128(10):3664–3673. doi: 10.1175/1520-0493(2000)128<3664:ASNTFD>2.0.CO;2.

Wagner, D. N., Shupe, M. D., Cox, C., Persson, O. G., Uttal, T., Frey, M. M., Kirchgaessner, A., Schneebeli, M., Jaggi, M., Macfarlane, A. R., Itkin, P., Arndt, S., Hendricks, S., Krampe, D., Nicolaus, M., Ricker, R., Regnery, J., Kolabutin, N., Shimanshuck, E., Oggier, M., Raphael, I., Stroeve, J., and Lehning, M. (2022). Snowfall and snow accumulation during the MOSAiC winter and spring seasons. *The Cryosphere*, 16(6):2373–2402. doi: 10.5194/tc-16-2373-2022.

Wagner, T., Leue, C., Wenig, M., Pfeilsticker, K., and Platt, U. (2001). Spatial and temporal distribution of enhanced boundary layer BrO concentrations measured by the GOME instrument aboard ERS-2. *Journal of Geophysical Research: Atmospheres*, 106(D20):24225–24235. doi: 10.1029/2000JD000201.

Wang, S., McNamara, S. M., Kolesar, K. R., May, N. W., Fuentes, J. D., Cook, R. D., Gunsch, M. J., Mattson, C. N., Hornbrook, R. S., Apel, E. C., and Pratt, K. A. (2020). Urban Snowpack $ClNO_2$ Production and Fate: A One-Dimensional Modeling Study. *ACS Earth and Space Chemistry*, 4(7):1140–1148. doi: 10.1021/acsearthspacechem.0c00116.

Wang, S., McNamara, S. M., Moore, C. W., Obrist, D., Steffen, A., Shepson, P. B., Staebler, R. M., Raso, A. R. W., and Pratt, K. A. (2019). Direct detection of atmospheric atomic bromine leading to mercury and ozone depletion. *Proceedings of the National Academy of Sciences*, 116(29):14479–14484. doi: 10.1073/pnas.1900613116.

Wang, S. and Pratt, K. A. (2017). Molecular Halogens Above the Arctic Snowpack: Emissions, Diurnal Variations, and Recycling Mechanisms. *Journal of Geophysical Research: Atmospheres*, 122(21):11,991–12,007. doi: 10.1002/2017JD027175.

Weibring, P., Richter, D., Walega, J. G., and Fried, A. (2007). First demonstration of a high performance difference frequency spectrometer on airborne platforms. *Optics Express*, 15(21):13476–13495. doi: 10.1364/OE.15.013476.

Weibring, P., Richter, D., Walega, J. G., Rippe, L., and Fried, A. (2010). Difference frequency generation spectrometer for simultaneous multispecies detection. *Optics Express*, 18(26):27670–27681. doi: 10.1364/OE.18.027670.

Weinheimer, A. J. (2009). Ozone, NO_x, and NO_y measurements during OASIS Barrow field intensive Spring 2009. Arctic Data Center. Accessed on 08/24/2021. doi: 10.5065/D6RJ4GK6.

Weinheimer, A. J., Montzka, D. D., Campos, T. L., Walega, J. G., Ridley, B. A., Donnelly, S. G., Keim, E. R., Del Negro, L. A., Proffitt, M. H., Margitan, J. J., Boering, K. A., Andrews, A. E., Daube, B. C., Wofsy, S. C., Anderson, B. E., Collins, J. E., Sachse, G. W., Vay, S. A., Elkins, J. W., Wamsley, P. R., Atlas, E. L., Flocke, F., Schauffler, S., Webster, C. R., May, R. D., Loewenstein, M., Podolske, J. R., Bui, T. P., Chan, K. R., Bowen, S. W., Schoeberl, M. R., Lait, L. R., and Newman, P. A. (1998). Comparison between DC-8 and ER-2 species measurements in the tropical middle troposphere: NO, NO_y, O_3, CO_2, CH_4, and N_2O. *Journal of Geophysical Research: Atmospheres*, 103(D17):22087–22096. doi: 10.1029/98JD01421.

Wesely, M. (1989). Parameterization of surface resistances to gaseous dry deposition in regional-scale numerical models. *Atmospheric Environment*, 23(6):1293–1304. doi: 10.1016/0004-6981(89)90153-4.

Wessel, S., Aoki, S., Winkler, P., Weller, R., Herber, A., Gernandt, H., and Schrems, O. (1998). Tropospheric ozone depletion in polar regions A comparison of observations in the Arctic and Antarctic. *Tellus B: Chemical and Physical Meteorology*, 50(1):34–50. doi: 10.3402/tellusb.v50i1.16020.

Wiedinmyer, C., Akagi, S. K., Yokelson, R. J., Emmons, L. K., Al-Saadi, J. A., Orlando, J. J., and Soja, A. J. (2011). The Fire INventory from NCAR (FINN): a high resolution global model to estimate the emissions from open burning. *Geoscientific Model Development*, 4(3):625–641. doi: 10.5194/gmd-4-625-2011.

Wiedinmyer, C., Kimura, Y., McDonald-Buller, E., Seto, K., Emmons, L., Tang, W., Buchholz, R., and Orlando, J. (2022). The Fire INventory from NCAR version 2 (FINNv2): updates to a high resolution global fire emissions model. *Journal of Advances in Modeling Earth Systems*. (In preparation).

Wild, O., Zhu, X., and Prather, M. J. (2000). Fast-J: Accurate Simulation of In- and

Below-Cloud Photolysis in Tropospheric Chemical Models. *Journal of Atmospheric Chemistry*, 37(3):245–282. doi: 10.1023/A:1006415919030.

Willmes, S. and Heinemann, G. (2015). Daily pan-Arctic sea-ice lead maps for 2003-2015, with links to maps in NetCDF format. doi: 10.1594/PANGAEA.854411.

Willmes, S. and Heinemann, G. (2016). Sea-Ice Wintertime Lead Frequencies and Regional Characteristics in the Arctic, 2003–2015. *Remote Sensing*, 8(1). doi: 10.3390/rs8010004.

Woo, K. S., Chen, D. R., Pui, D. Y. H., and McMurry, P. H. (2001). Measurement of Atlanta Aerosol Size Distributions: Observations of Ultrafine Particle Events. *Aerosol Science and Technology*, 34(1):75–87. doi: 10.1080/02786820120056.

Wren, S. N., Donaldson, D. J., and Abbatt, J. P. D. (2013). Photochemical chlorine and bromine activation from artificial saline snow. *Atmospheric Chemistry and Physics*, 13(19):9789–9800. doi: 10.5194/acp-13-9789-2013.

Xu, L., Zhang, Y., Tong, L., Chen, Y., Zhao, G., Hong, Y., Xiao, H., and Chen, J. (2020). Gas-particle partitioning of atmospheric reactive mercury and its contribution to particle bound mercury in a coastal city of the Yangtze River Delta, China. *Atmospheric Environment*, 239:117744. doi: 10.1016/j.atmosenv.2020.117744.

Yang, X., Blechschmidt, A.-M., Bognar, K., McClure-Begley, A., Morris, S., Petropavlovskikh, I., Richter, A., Skov, H., Strong, K., Tarasick, D., Uttal, T., Vestenius, M., and Zhao, X. (2020). Pan-Arctic surface ozone: modelling vs measurements. *Atmospheric Chemistry and Physics*, 20(4):15937—15967. doi: 10.5194/acp-20-15937-2020.

Yang, X., Frey, M. M., Rhodes, R. H., Norris, S. J., Brooks, I. M., Anderson, P. S., Nishimura, K., Jones, A. E., and Wolff, E. W. (2019). Sea salt aerosol production via sublimating wind-blown saline snow particles over sea ice: parameterizations and relevant microphysical mechanisms. *Atmospheric Chemistry and Physics*, 19(13):8407–8424. doi: 10.5194/acp-19-8407-2019.

Yang, X., Pyle, J. A., and Cox, R. A. (2008). Sea salt aerosol production and bromine release: Role of snow on sea ice. *Geophysical Research Letters*, 35(16). doi: 10.1029/2008GL034536.

Yang, X., Pyle, J. A., Cox, R. A., Theys, N., and Van Roozendael, M. (2010). Snow-sourced bromine and its implications for polar tropospheric ozone. *Atmospheric Chemistry and Physics*, 10(16):7763–7773. doi: 10.5194/acp-10-7763-2010.

Zaveri, R. A., Easter, R. C., Fast, J. D., and Peters, L. K. (2008). Model for Simulating Aerosol Interactions and Chemistry (MOSAIC). *Journal of Geophysical Research: Atmospheres*, 113(D13). doi: 10.1029/2007JD008782.

Zhang, L., Blanchard, P., Gay, D. A., Prestbo, E. M., Risch, M. R., Johnson, D., Narayan, J., Zsolway, R., Holsen, T. M., Miller, E. K., Castro, M. S., Graydon, J. A., Louis, V. L. S., and Dalziel, J. (2012). Estimation of speciated and total mercury dry deposition at monitoring locations in eastern and central North America. *Atmospheric Chemistry and Physics*, 12(9):4327–4340.

Zhang, L., Wright, L. P., and Blanchard, P. (2009). A review of current knowledge concerning dry deposition of atmospheric mercury. *Atmospheric Environment*, 43(37):5853–5864. doi: 10.1016/j.atmosenv.2009.08.019.

Zhang, P. and Zhang, Y. (2022). Earth system modeling of mercury using CESM2 – Part 1: Atmospheric model CAM6-Chem/Hg v1.0. *Geoscientific Model Development*, 15(9):3587–3601. doi: 10.5194/gmd-15-3587-2022.

Zhang, Y., Jacob, D. J., Dutkiewicz, S., Amos, H. M., Long, M. S., and Sunderland, E. M. (2015). Biogeochemical drivers of the fate of riverine mercury discharged to the global and Arctic oceans. *Global Biogeochemical Cycles*, 29(6):854–864. doi: 10.1002/2015GB005124.

Zilitinkevich, S. and Baklanov, A. (2002). Calculation Of The Height Of The Stable Boundary Layer In Practical Applications. *Boundary-Layer Meteorology*, 105(3):389–409. doi: 10.1023/A:1020376832738.

Zilitinkevich, S., Baklanov, A., Rost, J., Smedman, A.-s., Lykosov, V., and Calanca, P. (2002). Diagnostic and prognostic equations for the depth of the stably stratified Ekman boundary layer. *Quarterly Journal of the Royal Meteorological Society*, 128(579):25–46. doi: 10.1256/00359000260498770.